Computer Modeling in
Engineering & Sciences

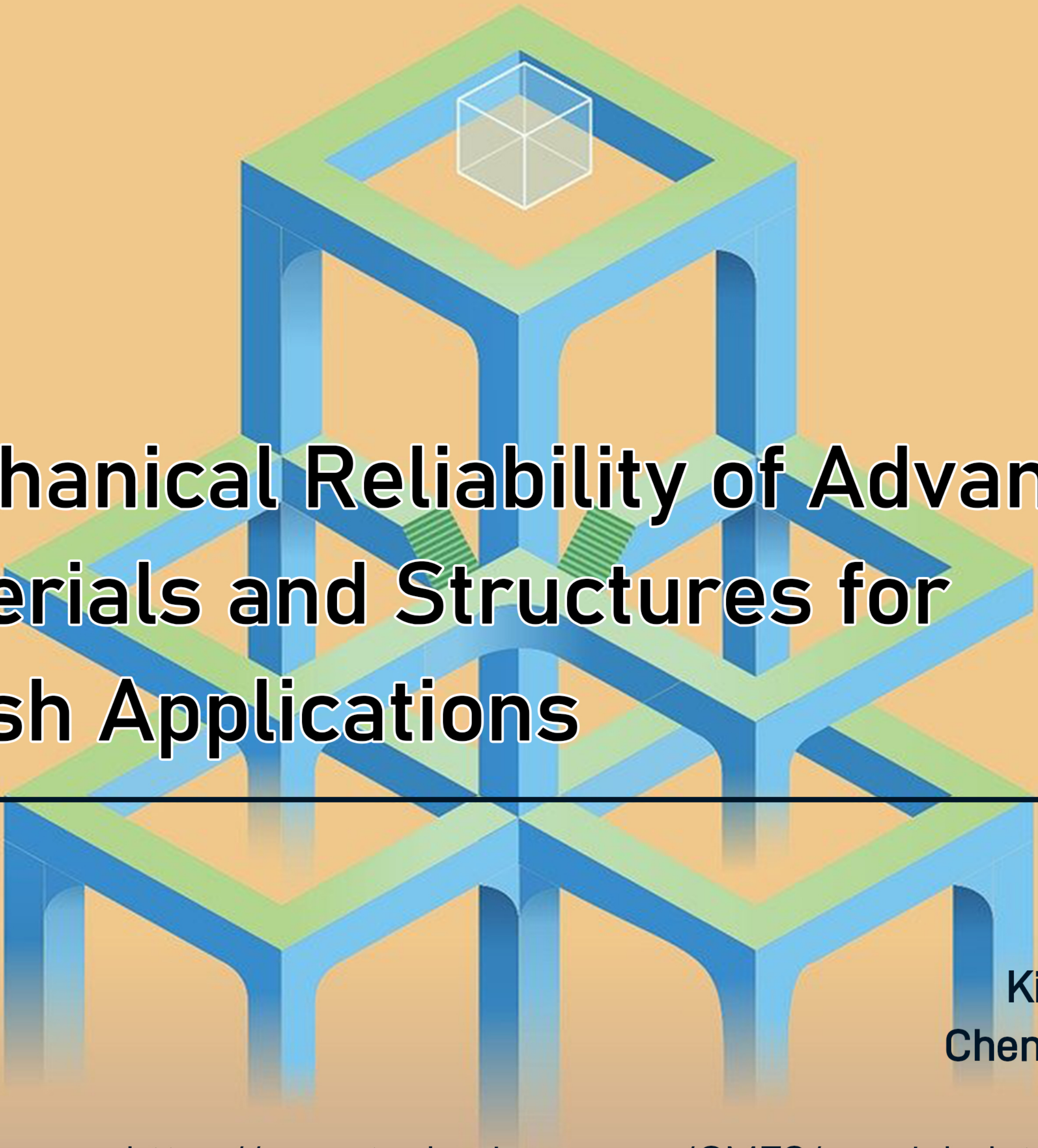

Mechanical Reliability of Advanced Materials and Structures for Harsh Applications

Edited By
Xu Long
Kim S Siow
Chengqing Wu

https://www.techscience.com/CMES/special_detail/amsha

www.techscience.com/journal/CMES

Tech Science Press

Mechanical Reliability of Advanced Materials and Structures for Harsh Applications

Editors

Xu Long
Kim S Siow
Chengqing Wu

Tech Science Press

Editors

Xu Long
Professor
Northwestern Polytechnical University
Xi'an
China

Kim S Siow
Associate Professor
National University of Malaysia
Selangor
Malaysia

Chengqing Wu
Professor
University of Technology
Sydney
Australia

Editorial Office
Tech Science Press
2520 St. Rose Parkway,
Suite 108D, Henderson, Nevada,
89074, USA

This is a reprint of articles from the Special Issue published online in the open access journal *Computer Modeling in Engineering & Sciences* (ISSN 1526-1492 (Print); ISSN 1526-1506 (Online)) (available at: https://www.techscience.com/journal/CMES).

For citation purposes, cite each article independently as indicated on the article page online and as indicated below:

Author AA, Author BB. Title of article. Abbreviated Journal Name. Year; volume(issue):pagination.

ISBN: 979-8-9989030-0-7 (PDF)

CONTENTS

Computer Modeling in
Engineering & Sciences

Tech Science Press

DOI: 10.32604/cmes.2022.018037

ARTICLE

Numerical and Experimental Investigations of the Thermal Fatigue Lifetime of CBGA Packages

Borui Yang[1], **Jun Luo**[2], **Bo Wan**[1,*], **Yutai Su**[1,3], **Guicui Fu**[1] **and Xu Long**[3,*]

[1]School of Reliability and Systems Engineering, Beihang University, Beijing, 100191, China

[2]Sichuan Institute of Solid-State Circuits, China Electronics Technology Group Corporation, Chongqing, 400060, China

[3]School of Mechanics, Civil Engineering and Architecture, Northwestern Polytechnical University, Xi'an, 710072, China

[*]Corresponding Authors: Bo Wan. Email: wanbo@buaa.edu.cn; Xu Long. Email: xulong@nwpu.edu.cn

Received: 24 June 2021 Accepted: 04 August 2021

ABSTRACT

A thermal fatigue lifetime prediction model of ceramic ball grid array (CBGA) packages is proposed based on the Darveaux model. A finite element model of the CBGA packages is established, and the Anand model is used to describe the viscoplasticity of the CBGA solder. The average viscoplastic strain energy density increment ΔWave of the CBGA packages is obtained using a finite element simulation, and the influence of different structural parameters on the ΔWave is analyzed. A simplified analytical model of the ΔWave is established using the simulation data. The thermal fatigue lifetime of CBGA packages is obtained from a thermal cycling test. The Darveaux lifetime prediction model is modified based on the thermal fatigue lifetime obtained from the experiment and the corresponding ΔWave. A validation test is conducted to verify the accuracy of the thermal fatigue lifetime prediction model of the CBGA packages. This proposed model can be used in engineering to evaluate the lifetime of CBGA packages.

KEYWORDS

CBGA packages; lifetime prediction; finite element method; thermal fatigue; Anand model; Darveaux model

1 Introduction

As electronic products have become smaller, lighter, and more reliable, ceramic ball grid array (CBGA) packaging has been increasingly used in electronic products. As a critical component of a stand-alone machine or a system, the failure of the CBGA device will cause the system to malfunction, resulting in high risks to product engineering. Therefore, the lifetime prediction of CBGA packages is essential to the reliability research of electronic products.

CBGA devices are high-density interconnect devices. In CBGA assembly, the device and the printed circuit board (PCB) are connected by soldering to form a component. The solder joints are prone to multiple failure modes during the assembly and subsequent testing under complicated loadings [1]. The failure modes of solder joints include false soldering and solder joint deformation. Failure significantly affects the device's quality and solder joint reliability. These problems are caused primarily by improper control of the temperature and time parameters during soldering. Pang et al. [2] studied the changes in the microstructure of BGA solder joints under thermal cycling conditions and found that thermal cycling increased the grain coarseness. An intermetallic compound was located between the tin-lead solder interface and the pad, decreasing the strength of the solder joint and causing it to fail. Solomon et al. [3] analyzed the fatigue behavior of 60Sn40Pb solder at different temperatures. The research results of Zhang et al. [4] showed that thermal fatigue decreased the reliability of electronic components. Therefore, this article focuses on the number of thermal fatigue life cycles of a CBGA in a thermal cyclic profile. Zuo et al. [5] used the Engelmaier model, a strain-range-based fatigue model, to study the fatigue life of defective solder joints. Wan et al. [6] proposed an improved reliability evaluation method based on PoF technique and maximum entropy (MaxEnt) principle. The results showed that the proposed MaxEnt distributions can generate more reliable reliability evaluation results compared with Weibull distributions. Su et al. [7] conducted fatigue reliability design for Metal Dual Inline Packages under random vibration using finite element analysis, physics of failure model and surface response method. Wang et al. [8] conducted experiments to investigate the thermal behavior, mechanical properties of composite solder alloys and shear fracture behavior of solder joints. The test results reflected that the hardness and modulus of composite solder alloys were enhanced after the addition of Ni-CNTs. Fu et al. [9] analyzed thermal distributions and stress-strain distributions of the SiP by finite element analysis (FEA) tools based on hardware information and lifecycle profile of SiP. With the utilization of PoF models, lifetime matrix of the SiP is obtained.

The Anand viscoplastic model is a common model to describe the constitutive relationships of solders, and the viscoplasticity of solder material in a thermal environment. It uses a single internal variable to describe the resistance of the internal state of the material to plastic flow. This model relates the deformation behavior of viscoplastic materials to the strain rate and temperature. Amagai et al. [10–12] used the Anand model and revised it to investigate the deformation of SnPb series, SnZn series, SnAg series, and SnAgCu series solders at different humidities and strain rates. Wu et al. [13] used the Anand viscoplastic constitutive model to simulate the nano-silver sintered die-attachment in devices under thermal cyclic conditions. The simulation results showed that the bonding layer of the nano-silver paste experienced plastic strain under these conditions, which was the leading cause of the chip connection failure. Similar with previous works with the framework of the unified creep-plasticity model [14,15], Long performed extensive experimental studies with a wide range of temperature and strain rate and parameterized the Anand constitutive model with excellent agreement with measured stress–strain curves [16].

Many scholars have researched the reliability and lifetime prediction methods of solder joints. Che et al. [17] performed a thermal cycle finite element analysis on a plastic BGA package with Sn-3.8Ag-0.7Cu lead-free solder joints. They predicted and compared the fatigue life of solder joints using different 2-D and 3-D finite element analysis models. Wang et al. [18] proposed an advantageous mechanics-based acceleration approach to estimate the thermal fatigue life of BGA solder joints. Li et al. [19] conducted a stress-strain analysis on the simulation results of SnAgCu solder under thermal shock to evaluate different loading conditions and performed crack growth correlation and life prediction. Jiang et al. [20] used an energy-based life prediction model for BGA solder balls under thermal cyclic conditions and verified the correctness of the model and parameters through accelerated life tests. Hu et al. [21] proposed a thermal fatigue life prediction model for BGA solder joints considering the effect of the load sequence. The model improved the usability and accessibility of test data and verified the new failure criterion through experiments and simulations. Lee et al. [22] studied the effect of the size of the plastic-encapsulated BGA device substrate on the failure under thermal cyclic conditions. The study found that the thermal fatigue life of the solder balls had an inverse relationship with the substrate size.

Energy-based lifetime prediction models are also often used. Akay et al. [23] proposed a life prediction model for the number of failure cycles of a device. This model was used to predict the lifetime of a wireframe BGA package. Another energy-based model that considered the effects of elasticity and creep was proposed by Liang et al. [24]. This model is appliable to BGA packages. Darveaux [25] proposed a life prediction model for BGA packages/chip-scale packages (CSP) that is currently widely used. Chen et al. [26] applied the Darveaux model to predict the life of solder balls of stacked die packages under thermal cyclic conditions. The prediction results were used to verify the accuracy of the proposed optimization method. Li et al. [27] also used the Darveaux model to obtain the strain energy distribution during crack initiation in the expansion area of a quad flat package (QFP) using finite element simulation. The results showed that the average strain energy density was similar in the crack initiation zone, but the average strain energy density was different in the crack propagation zone, resulting in similar crack initiation times but different crack growth rates. Marbut et al. [28] simulated mechanical stress caused by shear stress resulting from the thermal expansion of a flip-chip device under thermal cyclic conditions and modified the Darveaux model parameters for lifetime prediction. Sitta et al. [29] used the Anand model and finite element methods to model discrete low-voltage packages and applied the Darveaux model for lifetime prediction. Zhang et al. [30] established a 3D slice model to analyze the reliability of solder joints. The time- and temperature-related creep properties of 63Sn37Pb solder were determined under thermal cyclic conditions. They used the Darveaux model to predict the thermal fatigue life of solder joints and studied the effect of the package size. The research results showed that the larger the chip size, the greater the maximum stress at the boundary was. They also found that the thickness of the bottom plate significantly affected the thermal failure of the package's structure. This study uses the Darveaux model for the lifetime prediction of CBGA packages because the model exhibits good performance for BGA life prediction.

Based on previous research, it can be noticed that the Darveaux model has a very effective application in the field of solder life prediction. Through the Darveaux model, the number of life cycles can be quickly obtained. However, the correlation coefficients of the Darveaux model vary greatly for different structural designs, structural parameters and material characteristics of the package. Therefore, for typical CBGA packages, modification of the Darveaux model is required.

A life prediction model of CBGA packages is established using a finite element model of a CBGA and the Anand constitutive model to characterize the viscoplasticity of the solder. The average viscoplastic strain energy increment ΔW_{ave} is obtained from the finite element simulation, and the influence of different structural parameters on ΔW_{ave} is analyzed. Multiple regression analysis is used to establish a simplified analytical model of ΔW_{ave}. A thermal cyclic test is conducted to modify the parameters of the Darveaux life prediction model. Experiments are conducted to determine the number of thermal fatigue life cycles of a typical CGBA. In addition, a validation test is carried out to verify the accuracy of the life prediction model of CBGA packages.

2 Theory and Model Formulation

2.1 Viscoplastic Constitutive Model

The Anand model [31] is a constitutive equation used to describe the rate-dependent deformation of metals at high temperatures. The Anand model is a unified viscoplastic constitutive model. It comprehensively considers the creep deformation and plastic deformation that occur simultaneously during soldering. The unified constitutive model describes the mechanical behavior of solder in a straightforward manner and uses test data to identify the model parameters.

The Anand model has two basic characteristics: (1) The model does not have a clear yield surface in the stress space; thus, there is no need to provide loading and unloading criteria during deformation. Plastic deformation can occur under all non-zero stress conditions. (2) The model uses the deformation resistance s as a single internal variable. s represents the average resistance of the material's internal state to the macroscopic plastic flow.

The Anand constitutive model describes the relationship between the strain rate and temperature and the deformation behavior of viscoplastic materials, strain hardening, the historical effect of the strain rate, and the dynamic recovery of strain. Initially, the Anand model was primarily used to describe the thermal properties of high-strength aluminum and other structural metals. It is currently widely used to describe the viscoplastic behavior of solder.

In the Anand model, the deformation resistance is proportional to the equivalent stress:

$$\sigma = cs; c < 1, c = \left(T, \varepsilon_p\right) \tag{1}$$

where c is the material parameter, which is expressed as:

$$c = \frac{1}{\xi}\sinh^{-1}\left\{\left[\frac{\varepsilon_P}{A}\exp\left(\frac{Q}{RT}\right)\right]^m\right\} \tag{2}$$

where ϵp is the inelastic strain rate. ξ is the stress multiplier. A is the constant. Q is the activation energy. T is the environmental temperature. R is the gas constant. m is the strain rate sensitivity index.

The flow equation of the viscoplastic Anand model adopts the hyperbolic creep law, which is described as:

$$\varepsilon_P = A\exp\left[-\frac{Q}{RT}\right]\left[\sinh\left(\xi\frac{\sigma}{s}\right)\right]^{\frac{1}{m}} \tag{3}$$

The evolution equation for the internal variable s is:

$$s = h(\sigma, s, T)\,\varepsilon_P \tag{4}$$

where $h(\sigma,s,T)$ is the hardening function, which is related to the dynamic strain hardening and recovery process of the material. The hardening function is given by:

$$h = h_0\left|1 - \frac{s}{s^*}\right|^a sign\left(1 - \frac{s}{s^*}\right) \tag{5}$$

where h_0 and a are the strain-hardening parameters of the performance material. s^* is the saturation value of s and is expressed as follows:

$$s^* = s'\left[\frac{\varepsilon_P}{A}\exp\left(\frac{Q}{RT}\right)\right]^n \tag{6}$$

where s' is the coefficient of the deformation resistance saturation value. n is the strain rate sensitivity. By combining Eqs. (4)–(6), s can be obtained as follows:

$$s = \left[h_0\left|1 - \frac{s}{s^*}\right|^a sign\left(1 - \frac{s}{s^*}\right)\right]\varepsilon_P \tag{7}$$

Accordingly:

$$\sigma^* = \frac{s'}{\xi}\left[\frac{\varepsilon_P}{A}\exp\left(\frac{Q}{RT}\right)\right]^n \sinh^{-1}\left\{\left[\frac{\varepsilon_P}{A}\exp\left(\frac{Q}{RT}\right)\right]^m\right\} \tag{8}$$

Eq. (8) is related to the material's saturation stress, temperature, and strain rate. Under isothermal conditions and if s* > s, the following applies:

$$\frac{d\sigma}{d\varepsilon_P} = ch_0\left|1-\frac{s}{s^*}\right|^a sign\left(1-\frac{s}{s^*}\right), a \geq 1 \tag{9}$$

By integrating the above Eq. (9), the following expression of the stress can be obtained:

$$\sigma = \sigma^* - \left\{\left(\sigma^*-\sigma\right)^{(1-a)} + (a-1)\left[(ch_0)\left(\sigma^*\right)^{-a}\right]\varepsilon_P\right\}^{\frac{1}{1-a}} \tag{10}$$

where $\sigma_0 = cs_0$, and s_0 is the initial value of s.

The stress-strain relationship can be calculated using Eq. (10), and the strain energy can be obtained based on the calculated stress and strain. The viscoplastic strain energy density is defined as the summation of the product of the stress and inelastic strain increment vectors divided by the number of converged subsets. The viscoplastic strain energy can be written as:

$$W_E = \sum_{i=1}^{N}\sigma_i\left(\Delta\varepsilon^{pl}{}_i\right)v_i \tag{11}$$

where W_E is the plastic energy, σ is the stress vector, $\Delta\epsilon^{pl}$ is the plastic strain increment, and v_i is the volume of the integration points. The average of the strain energy density can be written as:

$$W_{ave} = \frac{\sum_{i=1}^{N} v_i W_i}{\sum_{i=1}^{N} v_i} \tag{12}$$

where N is the total number of selected analysis elements. i is the element number. v_i is the element volume with the element number i. W_i is the average viscoplastic strain energy density of the element with the element number i. The average viscoplastic strain energy density increment $\Delta \mathrm{W}_{\mathrm{ave}}$ is given by:

$$\Delta W_{ave} = W_{ave(n)} - W_{ave(n-1)} \tag{13}$$

where n and $n-1$ are the cycle numbers. $\Delta \mathrm{W}_{\mathrm{ave}}$ is used as the input for the subsequent models.

2.2 Energy-Based Darveaux Model

The Darveaux life prediction model [25] is based on energy. This model considers the plastic energy exerted on the device under cyclic load conditions. The plastic energy dissipation can be obtained from the stress-strain hysteresis curve. The area of the curve represents the cumulative fatigue damage of the solder joints during thermal cycling.

The Darveaux life prediction model divides the crack propagation into two parts. In the first part, the model predicts the number of cycles during which cracks are initiated. The predicted number of cycles in this part is given by:

$$N_0 = k_1\left(\Delta W_{ave}\right)^{k_2} \tag{14}$$

where N_0 is the number of cycles during initial crack propagation. k_1 and k_2 are the correlation coefficients related to the solder joint material, the selected model, the thickness of the analysis unit, the grid division, and other parameters.

In the second part, the model uses fracture mechanics to predict the growth rate of the crack and deduce the number of cycles required for the crack to expand and lead to the complete failure of the area. The predicted number of cycles in this part is given by:

$$\frac{da}{dN} = k_3\,(\Delta W_{ave})^{k_4} \tag{15}$$

where k_3 and k_4 are the same correlation coefficients as k_1 and k_2. a is the characteristic fracture length, da/dN is the crack growth rate.

Finally, the two parts are combined to obtain the number of cycles required for component destruction.

$$N_f = N_0 + \frac{a}{da/dN} \tag{16}$$

where N_f is the number of cycles of crack propagation leading to complete failure.

In addition, in Darveaux's energy-based life prediction model, the coefficients $k_1 \sim k_4$ are in English units of measure; thus, unit conversion is required. The unit of ΔW_{ave} is megapascals, which is divided by 0.006895 to convert to pounds per square inch. The millimeter unit of the crack length is divided by 25.4 to convert to inches.

3 Method of Lifetime Prediction

The flowchart of the life prediction methodology for CBGA packages is shown in Fig. 1. First, the CBGA structural model is established according to the sizes of typical CBGA packages, including the chip shell, the array of solder balls, pads, and the PCB substrate. The material properties are obtained, such as the thermal properties and mechanical properties. Based on the CBGA structural model, we set the boundary conditions and select the profile of the thermal cyclic test. The finite element simulation results are obtained after meshing. According to the load applied in the CBGA model, we calculate the displacement, stress, and strain of each finite element based on the thermal expansion equation and the viscoplastic constitutive model. We use Eq. (11) and the stress and plastic strain to obtain the plastic energy dissipation. The structural parameters are changed in the simulation, such as the solder ball diameter, the solder ball pitch, the package size, and the environmental parameters, e.g., the half-cycle dwell time to obtain the value of ΔW_{ave} for different structures and environmental conditions. Consequently, we can calculate ΔW_{ave} of the solder joint using the finite element simulation results. A simplified analytical model of ΔW_{ave} is established through multiple linear regression using the ΔW_{ave} data from the simulation with different values of the independent variables, e.g., the ball diameter, ball pitch, package size, and the thermal profile. Subsequently, we carry out thermal cyclic tests for the four test profiles to derive the thermal fatigue life cycles of the CBGA packages. Finally, the number of cycles to failure, the crack lengths, and the corresponding predicted ΔW_{ave} are used to fit the coefficients of the Darveaux life prediction model to obtain the life prediction model of the CBGA packages. In addition, we perform a validation test of the life prediction model using the same parameters of the CBGA packages. We then compare the actual lifetime with the predicted lifetime to determine the accuracy of the life prediction model of the CBGA packages.

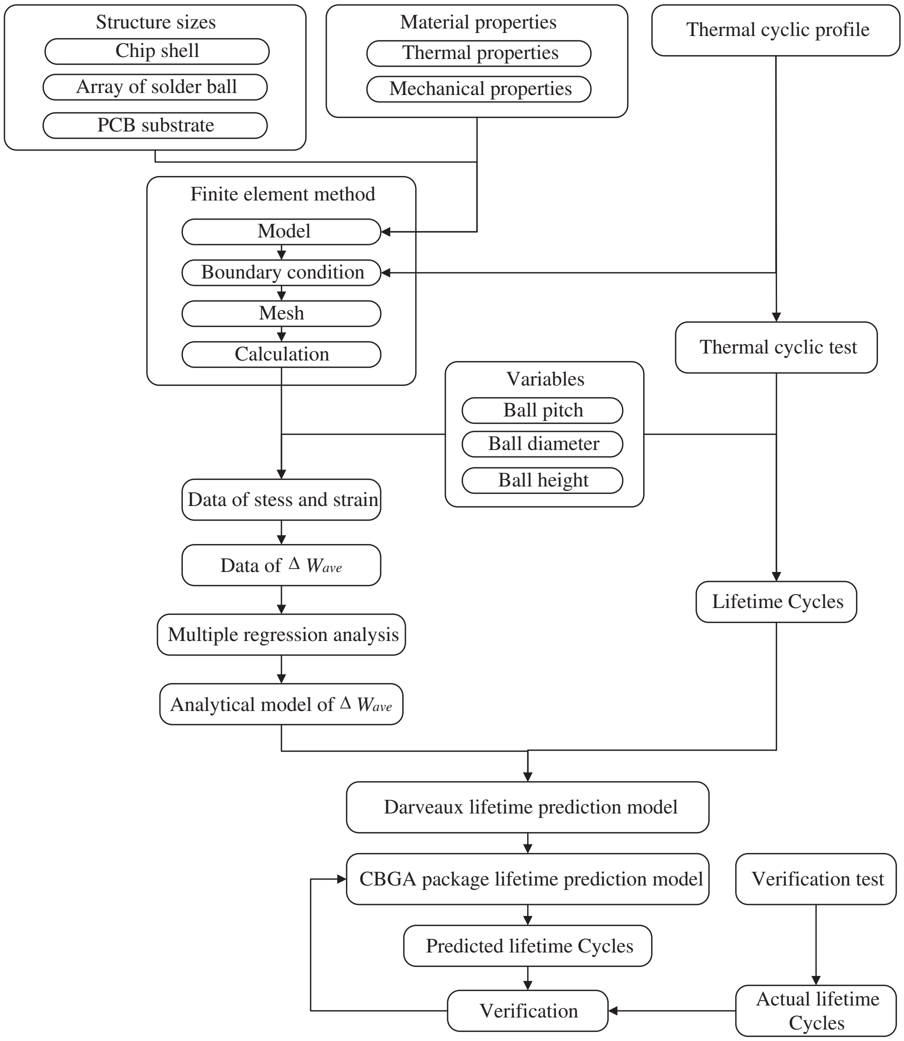

Figure 1: Procedure of lifetime prediction

At present, CBGA packages are widely used in the aerospace field due to their high-density array and ease of assembly. The structural parameters and the material properties of the CBGA packages are determined to establish the finite element model. CBGA packages typically consist of three layers. From top to bottom, the first layer is the chip, the second layer contains the solder balls and solder, and the third layer is the substrate. The structural parameters include the size of the device, the diameter of the solder ball, the pitch of the solder joint, the standoff height of the solder, and other parameters. The typical CBGA structure is shown in Fig. 2.

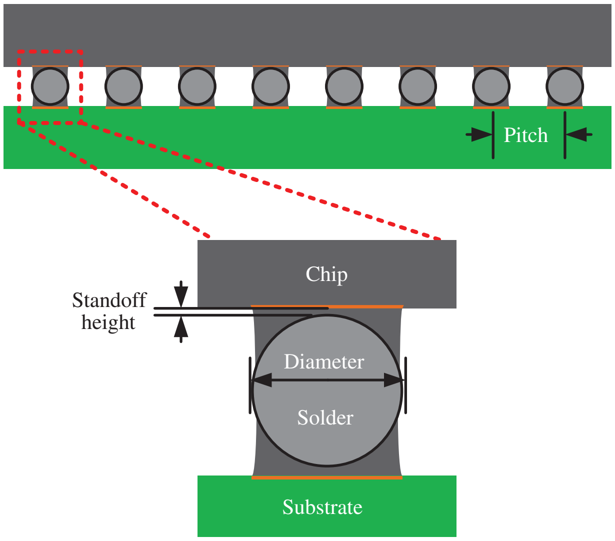

Figure 2: Schematic diagram of a CBGA package used in the finite element simulation

The simulation uses the typical structural parameter values used in a CBGA shown in Table 1. The material properties in this paper mainly refer to the properties related to the thermal cycle of the solder, such as Young's modulus, Poisson's ratio, density, and thermal expansion coefficient. The packaging materials currently used in the production of CBGA are devices with ceramic shells. The solder material is 63Sn37Pb, and the PCB board is FR-4. The material properties used in the simulation are listed in Table 2.

During the thermal cycle, the solder joints will creep. The Anand viscoplastic constitutive model is used to simulate the creep behavior of the solder joints. The 63Sn37Pb Anand model parameters are listed in Table 3.

Table 1: Structural parameters of a CBGA package

Parameter name	Parameter value
Pitch/mm	0.8, 1.0, 1.27
Diameter/mm	0.47/0.42/0.38, 0.64/0.56/0.49, 0.85/0.78/0.72
Size	16 × 16, 18 × 18, 20 × 20, 22 × 22, 24 × 24
Standoff Height/mm	0.07

Table 2: Relevant material parameters for simulation

Material name	Density (kg/mm^3)	CTE (K^{-1})	Young's modulus (MPa)	Poisson's ratio
63Sn37Pb	8.4e^{-6}	2.47e^{-5}	30800	0.35
Ceramic	3.6e^{-6}	7.8e^{-6}	380000	0.25
FR-4	2.27e^{-6}	X-direction 1.6 e^{-5}	X direction 27924	XY direction 0.11
		Y-direction 1.6 e^{-5}	Y direction 27924	YX direction 0.39
		Z-direction 8.4 e^{-5}	Z direction 12204	XZ direction 0.39

Table 3: 63Sn37Pb Anand model parameters

Parameters	Values
Constant A (s^{-1})	26
Constant Q/R(1/K)	5797
Coefficient of deformation resistance saturation value s' (MPa)	83.12
Strain-hardening parameter h_0 (MPa)	92148
Stress factor ξ	10
Strain-rate sensitivity index m	0.256
Strain-rate sensitivity n	0.043
Strain-hardening parameter a	1.24
Initial value of internal variable s_0 (MPa)	37.9

The environmental parameters of the test are based on the temperature profile in the thermal cyclic test described in the ESCC-Q-70-08a standard. The temperature range is −55°C∼100°C. The initial temperature is set to room temperature (22°C). The temperature change rate does not exceed 10° C/min. The maximum temperature is maintained for 15 min, and each cycle lasts 1 h. The temperature profile is shown in Fig. 3.

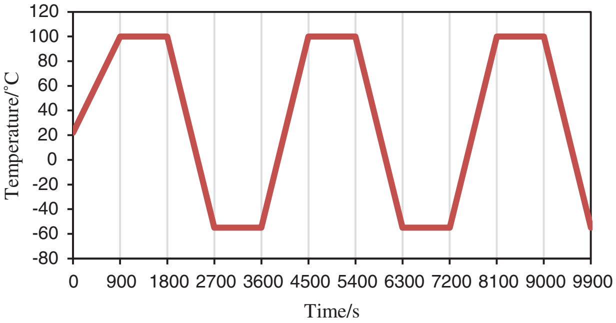

Figure 3: Temperatrue profile in the thermal cyclic test

In the simulation, the model has the same temperature conditions as in the thermal cyclic test profile. Since the CBGA package is centrally symmetric, it is only necessary to establish its 1/4 finite element model, and symmetric boundary conditions are used. The bottom of the model is fixed. After setting the boundary conditions of the displacement constraints shown in Fig. 4, the thermal cyclic simulation of the CBGA model is conducted. The average mesh size of the substrate and the chip shell is 0.9 mm. The average mesh size of the solder paste is 0.15 mm. The average mesh size of the solder ball is 0.08 mm. Mesh number changes according to structural parameters, which is shown in Table 4.

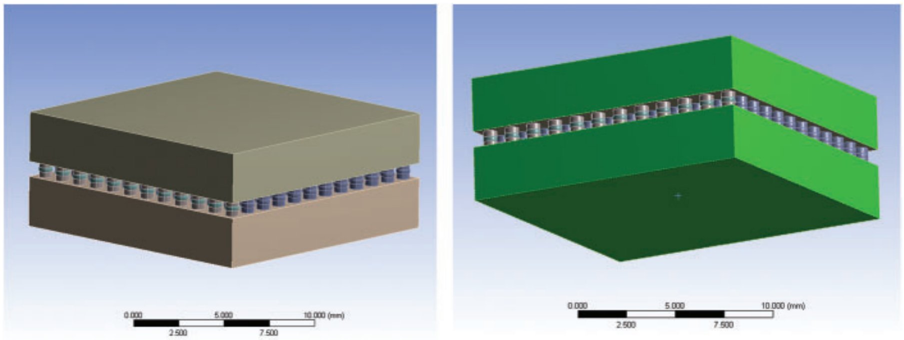

(a) FE model (b) Boundary condition

Figure 4: FE model and boundary condition

4 Numerical Analysis

4.1 Results of FE Simulations

4.1.1 Simulation Results

The simulation is performed with different structural parameter values to predict the lifetime of the structure. The Darveaux model is used, and ΔW_{ave} is obtained from the simulation. The average viscoplastic strain energy density $W_{ave}(n)$ of the previous n cycles is derived by Eq. (12). The average viscoplastic strain energy density increment $\Delta W_{ave}(n)$ is obtained from Eq. (13). Reference [32] found that ΔW_{ave} remained stable after the second thermal cycle. Therefore, the ΔW_{ave} of the third cycle is used as the result.

The simulation results indicate that the maximum stress and plastic strain occur at the corners. Hence, failure is more likely at the corners, as shown in Figs. 5 and 6. The stress is Von Mises stress. The strain is maximum principal strain. Therefore, we select a solder joint at the corner for the analysis and calculate its ΔW_{ave}. The ΔW_{ave} values of five cycles are shown in Fig. 7. It is observed that ΔW_{ave} remains stable after the second thermal cycle.

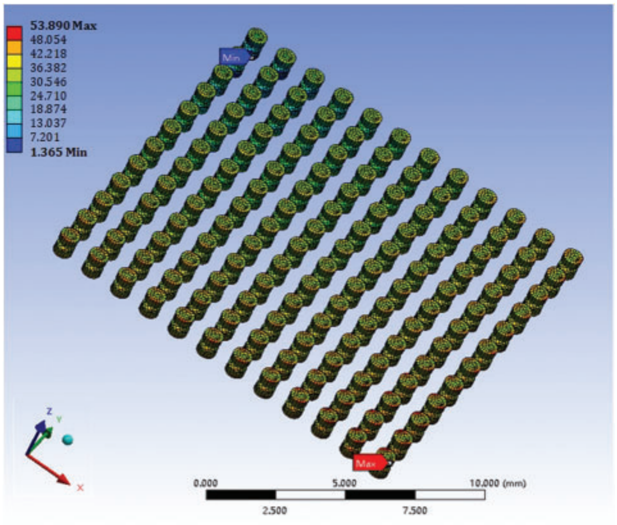

Figure 5: Stress distribution

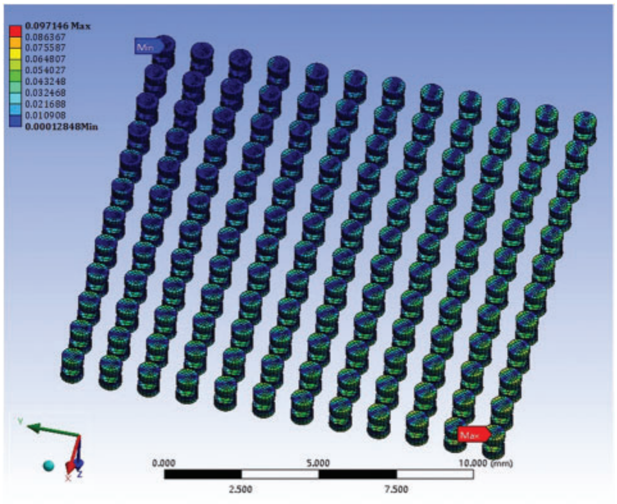

Figure 6: Plastic strain distribution

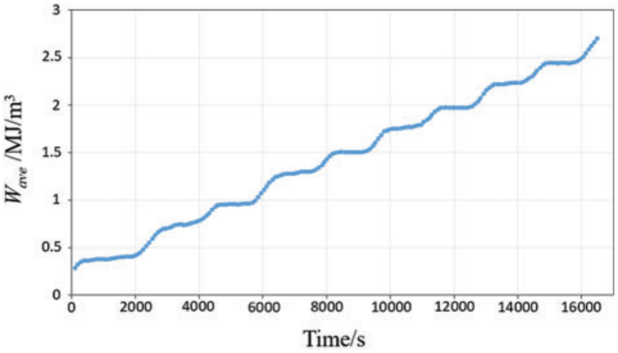

Figure 7: Wave in 5 cycles

4.1.2 Diameter of the Solder Ball

The ΔW_{ave} values for different solder ball diameters are shown in Fig. 8. ΔW_{ave} decreases with an increase in the diameter of the solder ball. The diameter affects the size of the solder ball. It is the most important parameter in the solder ball structure. The change will inevitably affect the strain energy generated by the solder ball. For larger solder balls, it is reasonable that the strain energy for the same thermal profile is smaller.

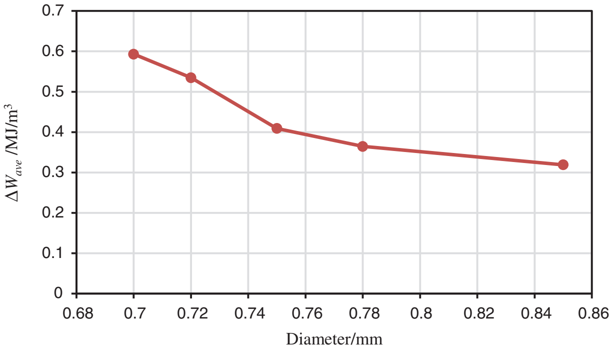

Figure 8: ΔW_{ave} *vs.* the diameter of the solder ball

4.1.3 Standoff Height of the Solder

The values of ΔW_{ave} for different solder standoff heights are shown in Fig. 9. ΔW_{ave} decreases with an increase in the solder standoff height, but the effect is negligible and can be ignored. Compared with the diameter, standoff height is a relatively small structural parameter in the solder ball structure. The failure of the solder ball is mainly caused by the stress in the shear direction. The change of standoff height has little effect on the tangential structure. Therefore, the influence of standoff height is small and this paper choose not to include standoff height in the analytical model of ΔW_{ave}.

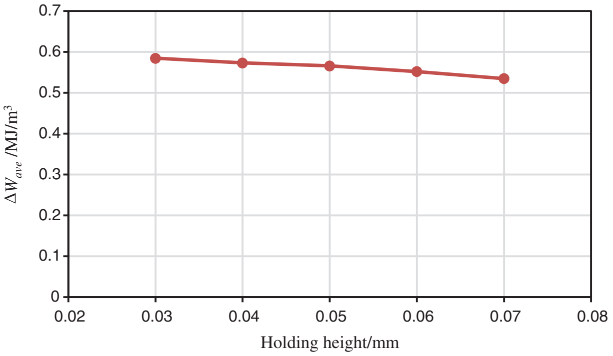

Figure 9: ΔW_{ave} *vs.* the standoff height of the solder

4.1.4 Size of the Package

The ΔW_{ave} values for different package sizes are shown in Fig. 10. The size of the device is determined by the solder ball pitch and the size of the solder ball array. For a given solder ball pitch, ΔW_{ave} increases with an increase in the device size, and the effect is significant. When the size of packages increases, the affected area and volume under the thermal profile will increase. The strain energy increment will increase accordingly.

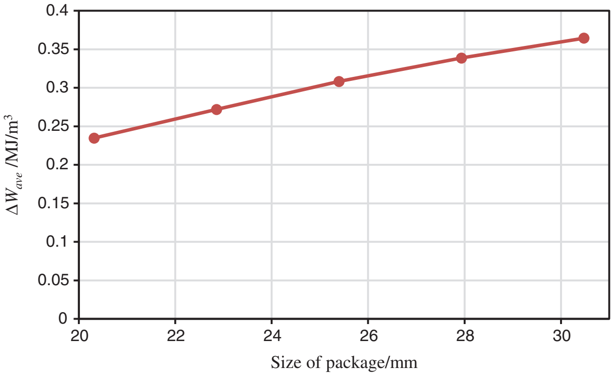

Figure 10: ΔW_{ave} *vs.* the package size

In addition, the pitch of the solder ball should also be considered. However, the range of the solder ball diameter depends on the pitch in practical applications. Thus, it is meaningless to determine the effect of the pitch of solder ball in the simulation.

4.2 Numerical Results of ΔW_{ave}

The ΔW_{ave} results for different values of the structural parameters and mesh numbers obtained from the simulation are listed in Table 4.

Table 4: Simulation results of ΔW_{ave}

No.	Pitch/mm	Diameter/mm	Size/mm	Mesh number	ΔW_{ave}/MJ/m^3
1	1.27	0.85	30.48	293568	0.31897
2	1.27	0.78	30.48	227198	0.364487
3	1.27	0.72	30.48	179025	0.5348
4	1.27	0.85	27.94	246679	0.301893
5	1.27	0.78	27.94	190909	0.338698
6	1.27	0.72	27.94	150431	0.423149
7	1.27	0.85	25.4	203867	0.279362
8	1.27	0.78	25.4	157776	0.308169
9	1.27	0.72	25.4	124323	0.4377
10	1.27	0.85	22.86	165132	0.251078
11	1.27	0.78	22.86	127799	0.271908
12	1.27	0.72	22.86	100701	0.38176
13	1.27	0.85	20.32	130475	0.219764
14	1.27	0.78	20.32	100977	0.234838
15	1.27	0.72	20.32	79567	0.33075
16	1	0.64	30.48	203535	0.42191
17	1	0.56	30.48	137170	0.507009
18	1	0.49	30.48	92711	0.680472
19	1	0.64	27.94	171026	0.38491
20	1	0.56	27.94	115261	0.458203
21	1	0.49	27.94	77903	0.611384
22	1	0.64	25.4	141344	0.34389
23	1	0.56	25.4	95257	0.405
24	1	0.49	25.4	64383	0.537467
25	1	0.64	22.86	114489	0.29895
26	1	0.56	22.86	77158	0.346523
27	1	0.49	22.86	52150	0.457509
28	1	0.64	20.32	90460	0.25259
29	1	0.56	20.32	60965	0.285857
30	1	0.49	20.32	41205	0.378572
31	0.8	0.47	30.48	128292	0.46648
32	0.8	0.42	30.48	92658	0.497254
33	0.8	0.38	30.48	69629	0.632014
34	0.8	0.47	27.94	107801	0.41725
35	0.8	0.42	27.94	77858	0.44113
36	0.8	0.38	27.94	58508	0.561645

(Continued)

Table 4 (Continued)

No.	Pitch/mm	Diameter/mm	Size/mm	Mesh number	$\Delta W_{ave}/MJ/m^3$
37	0.8	0.47	25.4	89092	0.36755
38	0.8	0.42	25.4	64346	0.385988
39	0.8	0.38	25.4	48354	0.492405
40	0.8	0.47	22.86	72164	0.31651
41	0.8	0.42	22.86	52120	0.328559
42	0.8	0.38	22.86	39167	0.42023
43	0.8	0.47	20.32	57019	0.26546
44	0.8	0.42	20.32	41181	0.272178
45	0.8	0.38	20.32	30946	0.348607

MATLAB is used to fit the simplified analytical model of ΔW_{ave} and perform multiple regression analysis for the prediction. Regression analysis provides a life prediction model with good generalization ability. The principle is to establish a prediction model that describes the distribution of the discrete sample points obtained from experiments or simulations. Commonly used regression algorithms include polynomial regression and linear regression. Multiple regression is used to predict the value and trend of the dependent variable using multiple independent variables. In addition, cross-validation is required to establish a life prediction model with a good fit and high predictability. Typically, the data are divided into a training set and a test set. In this study, the 45 sets of samples are divided into 40 sets of training data and 5 sets of test data.

According to the energy law description of the fatigue life of surface solder joints in the IPC-SM-785 standard, the potential cyclic fatigue damage is related to the structural parameters and the thermal profile. Here we use multiple nonlinear regression to fit and normalize the data as follows:

$$\Delta W_{ave} = 0.002201 \times p^{1.889} \times D^{-1.770} \times L^{1.282} \tag{17}$$

where ΔW_{ave} is the average viscoplastic strain energy density increment. p is the pitch of the solder balls. D is the diameter of the solder balls. L is the size of the package. The coefficient of determination is 0.9057, and the mean square error is 0.00766, indicating that the simplified analytical model of ΔW_{ave} has good accuracy.

5 Experimental Results and Discussion

5.1 Experimental Setup

Common CBGA packages were selected for testing. The samples had different sizes, different diameters, and different solder ball pitches. CBGA575 is a large CBGA. Its structure is sensitive, and it is prone to failure. The structural parameters of the CBGA packages used in the test are listed in Table 5.

Table 5: Structural parameters of the CBGA package used in the test

No.	Array	Pitch/mm	Diameter/mm	Size of package/mm
1	26 × 26	1.27	0.76	33.02
2	24 × 24	1.27	0.76	30.48
3	22 × 22	1.27	0.76	27.94
4	18 × 18	1.27	0.76	22.86
5	16 × 16	1.27	0.76	20.32
6	21 × 21	1	0.65	21
7	15 × 15	1	0.65	15
8	14 × 14	1	0.65	14
9	27 × 27	0.8	0.5	13.5
10	24 × 24	0.8	0.5	12
11	21 × 21	0.8	0.5	10.5

In the thermal cyclic test, a common failure monitoring method is the daisy chain monitoring system and crack length monitoring. The daisy chain system is a real-time monitoring method that determines the failure by monitoring the change in the resistance value. When any solder joint in a link cracks and fails, the resistance value of the entire link changes. The daisy chain verification system has the advantages of full coverage and straightforward analysis. The coverage rate of the solder joints tested by this method is 100%. Therefore, the daisy chain monitoring system was used as a failure monitoring method in the test to obtain the lifetime of the CBGA package sample under thermal cyclic conditions. The test equipment is shown in Fig. 11.

Figure 11: Test equipment

The thermal cyclic test profile shown in Fig. 3 was used. The failure criterion of the solder joint is the one used in the IPC-9701 standard. Failure is defined as two conditions. The first condition is that the event of the increase of the daisy chain resistance to 1,000 Ω for a period of one micro-second happens 10 times within 10% of the cycles to initial increase. The second condition is that the resistance increases by more than 20% within five consecutive detections.

5.2 Thermal Cyclic Test Results

During the thermal cycle test, we detect the fluctuation of the resistance of the daisy chain in real-time to evaluate the solder joint cracking of the assembly structure.

The CBGA575 sample is used as an example to illustrate the mapping of the daisy chain resistance changes and the crack growth. The first cracked solder joint we monitored was the first daisy chain link, which was located at the corner. The daisy chain resistance changes with the thermal cycle time, as shown in Fig. 12. From the first to the 235th thermal cycle, the resistance of the daisy chain remains at a normal resistance of about 3 Ω, and the solder joints are in a stable stage, as shown in Fig. 12. From the 236th to the 252nd cycle, the resistance of the daisy chain shows an increase from 20 Ω to about 300 Ω. At this time, the solder joints of the assembly structure are in the crack initiation stage, as shown in Fig. 12. Tiny cracks appear in this stage. In the high-temperature holding stage, the resistance drops to about 3 Ω, and in the low-temperature holding stage, the resistance increases to about 300 Ω. The reason is that the solder expands during the high-temperature stage. Even if the solder joints have cracked, they remain connected and have a small resistance value. As the temperature decreases, the solder shrinks, and the resistance increases. From the 253rd to the 342nd thermal cycle, the resistance of the daisy chain increases irregularly to several hundred Ω. At this time, the solder joint is in the crack propagation stage, as shown in Fig. 12. The resistance value is normal in the high-temperature stage and larger in the low-temperature stage. After the 343rd thermal cycle, the resistance of the daisy chain suddenly increases to around 50,000 Ω, exhibiting high resistance. At this time, the solder joint has completely failed, as shown in Fig. 12.

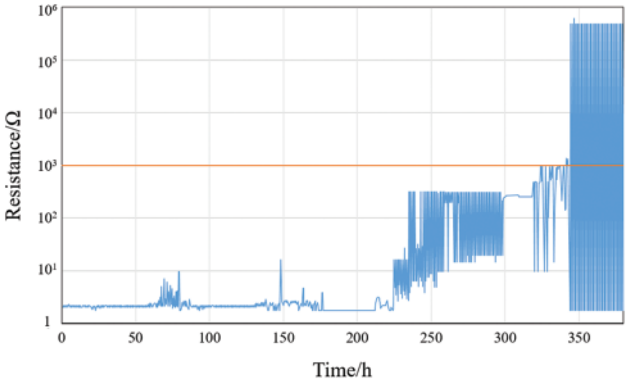

Figure 12: The daisy chain resistance change during the thermal cycling test

The fluctuation of the resistance of the daisy chain detected during the test indicates that the solder joints inside the assembly structure have cracked. The greater the fluctuation, the longer the cracks are between the solder joint and the component. When the high resistance state is reached for the first time, it indicates that the solder joint crack has penetrated, and the assembly structure has failed. As shown in Fig. 13, the cracks occur at the interface of the solder and pad. Hence, we assume that the crack penetration length is the same as the diameter of the interface of the solder and pad. The crack lengths are listed in Table 6, and the test results of the thermal cycle test are listed in Table 7.

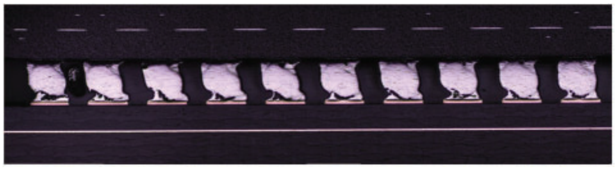

Figure 13: Graph of test samples during crack penetration

Table 6: Crack length

Package name	Crack length (diameter of pad)/mm
CBGA575	0.72
CBGA256	0.635
CBGA160	0.47

Table 7: Results of the thermal cycle test

No.	Crack length/mm	Pitch/mm	Diameter/mm	Size of package/mm	ΔW_{ave}/MJ/m^3	Failure cycles
1	0.72	1.27	0.76	33.02	0.497436	343
2	0.72	1.27	0.76	30.48	0.448924	399
3	0.72	1.27	0.76	27.94	0.401539	419
4	0.72	1.27	0.76	22.86	0.310457	542
5	0.72	1.27	0.76	20.32	0.266946	641
6	0.635	1	0.65	21	0.233802	723
7	0.635	1	0.65	15	0.151884	955
8	0.635	1	0.65	14	0.139027	1019
9	0.635	0.8	0.5	13.5	0.138506	1007
10	0.47	0.8	0.5	12	0.119094	1362
11	0.47	0.8	0.5	10.5	0.100356	1503

5.3 Improved Darveaux Model

The length of the solder joint cracks and the number of failure cycles were obtained from tests, and the ΔW_{ave} values were calculated by Eq. (17). We used the nonlinear fitting function lsqnonlin in MATLAB to determine the coefficient ks of the Darveaux thermal fatigue life prediction model, i.e., the value of the coefficient ks in Eqs. (14) and (15). The modification results are listed in Table 8.

Table 8: Darveaux coefficient of crack growth

Darveaux coefficient	k_1	k_2	k_3	k_4
Value	1.74E4	−0.9789	1.112E−05	0.8111

Therefore, the thermal fatigue life prediction model of the CBGA packages is proposed as follows:

$$N_f = 17400 \times (\Delta W_{ave})^{-0.9789} + \frac{a}{1.112 \times 10^{-5} \times (\Delta W_{ave})^{0.8111}} \tag{18}$$

where ΔW_{ave} is the average strain energy density increment, a is the crack length, and N_f is the number of failure cycles. The degree of fit between the calculated and actual results is shown in Fig. 14. The coefficient of determination is 0.9742, which indicates an excellent fit.

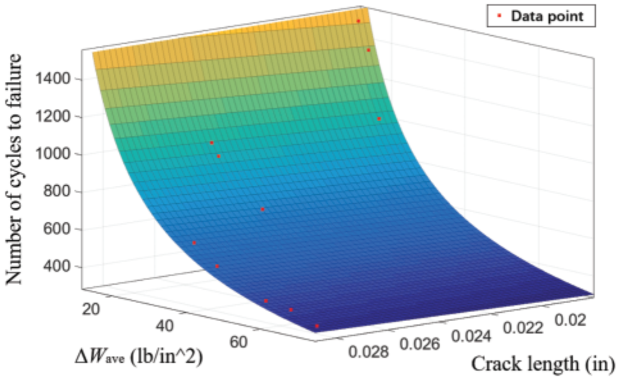

Figure 14: Fitted results of the thermal fatigue life prediction model

This paper establishes an analytical model for life prediction of CBGA Packages. It can quickly solve the lifetime of CBGA. Table 9 is the Darveaux model coefficients obtained by Li et al. [19] based on the test and simulation data of SnAgCu solder under temperature shock conditions using the least squares method. There is a considerable difference in the Darveaux model coefficients compared with this article. This shows that the coefficients of the model vary greatly for different structures, materials, and test types. Therefore, establishing a model for specific test results can make lifetime prediction results more accurate.

The improved Darveaux model is obtained by substituting Eq. (17) into Eq. (18) as follows:

$$\begin{aligned} N_f =& 17400 \times \left(0.002201 \times p^{1.889} \times D^{-1.770} \times L^{1.282}\right)^{-0.9789} \\ &+ \frac{a}{1.112 \times 10^{-5} \times \left(0.002201 \times p^{1.889} \times D^{-1.770} \times L^{1.282}\right)^{0.8111}} \end{aligned} \tag{19}$$

We chose other CBGA575s of the same specification to verify the life prediction model. The example of daisy chain resistance change during the verification tests is shown in Fig. 15.

The failure cycles of tests and the predicted failure cycles of the Darveaux model are listed in Table 10.

Table 9: Darveaux coefficient of crack growth from a reference [19]

Darveaux coefficient	k_1	k_2	k_3	k_4
Value	2.44E−7	−7.90	8.82	1.86

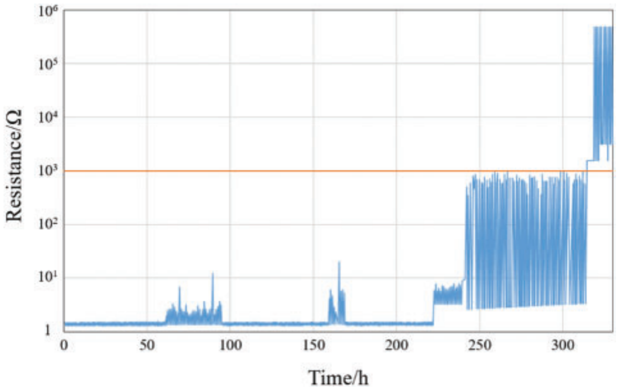

Figure 15: The example of daisy chain resistance change during the verification tests

Table 10: The parameters of CBGA575

No.	Crack length/mm	ΔW_{ave}/MJ/m^3	Failure cycles of tests	Predicted failure cycles	Error/%
1	0.72	0.332739	518	501	3.2
2	0.635	0.307439	539	526	2.4
3	0.47	0.125493	1213	1174	3.2
4	0.72	0.497436	319	343	7.5

The errors between the test results and the prediction results of the Darveaux model are also shown in the table. Three of the errors are below 5%, and the other one is below 10%. They reflect the good accuracy of this life prediction model.

6 Conclusions

Simulations and experiments were used to determine the thermal fatigue lifetime of CBGA packages. A simplified analytical model of the average viscoplastic strain energy density increment ΔW_{ave} was established, and the Darveaux life prediction model of CBGA packages was modified based on the test results. After determining the structural parameters and material properties of the CBGA packages, a finite element simulation was carried out, and the ΔW_{ave} data were obtained. Subsequently, the influence of the different structural parameters on ΔW_{ave} was analyzed. Multiple regression analysis was used to establish a simplified analytical model of ΔW_{ave} using simulation data. Then, a thermal cyclic test was conducted to obtain the thermal fatigue life cycle number of typical CGBAs. We monitored the changes in the resistance value in real-time to evaluate the cracking of the solder joints of the assembly structure. The test results provided information on the thermal fatigue lifetime of typical CBGA packages and were used as part of the input into the Darveaux life prediction model. Meanwhile, the corresponding ΔW_{ave} was calculated using the simplified analytical model of ΔW_{ave}. The Darveaux life prediction model of the CBGA packages was then modified using the number of life cycles and ΔW_{ave}. The accuracy of the life prediction model of the CBGA packages was determined using a validation test. The proposed life prediction model of the CBGA packages is accurate and can be used to calculate the lifetime of CBGA packages in practical engineering applications.

Acknowledgement: The authors thank Ye Wang and Hongyan Leng of Beihang University for their thoughtful discussions and suggestions on writing and experimenting in this study.

Funding Statement: The authors received no specific funding for this study.

Conflicts of Interest: The authors declare that they have no conflicts of interest to report regarding the present study.

References

1. Long, X., Liu, Y., Yao, Y., Jia, F., Zhou, C. et al. (2018). Constitutive behaviour and life evaluation of solder joint under the multi-field loadings. *AIP Advances, 8(8),* 085001. DOI 10.1063/1.5044446.
2. Pang, J., Low, T. H., Xiong, B. S., Xu, L., Neo, C. C. (2004). Thermal cycling aging effects on Sn-Ag-Cu solder joint microstructure, IMC and strength. *Thin Solid Films, 462(3),* 370–375. DOI 10.1016/j.tsf.2004.05.092.
3. Solomon H. D. (1991). Low cycle fatigue of Sn96 solder with reference to eutectic solder and a high Pb solder. *Journal of Electronic Packaging, 113(2),* 102–108. DOI 10.1115/1.2905374.
4. Zhang, X., Lee, S. R., Pao, Y. H. (2000). A damage evolution model for thermal fatigue analysis of solder joints. *Journal of Electronic Packaging, 122(3),* 200–206. DOI 10.1115/1.1286121.
5. Zuo, J., Fu, G., Su, Y., Jiang, M. (2017). Thermal fatigue life analysis of defective solder joints based on engelmaier fatigue model. *IEEE Electrical Design of Advanced Packaging and Systems Symposium,* pp. 1–3. Haining, China.
6. Wan, B., Wang, Y., Su, Y., Fu, G. (2020). Reliability evaluation of multi-mechanism failure for semi-conductor devices using physics-of-failure technique and maximum entropy principle. *IEEE Access, 8,* 188154–188170. DOI 10.1109/ACCESS.2020.3031022.
7. Su, Y., Fu, G., Wan, B., Yu, T., Zhou, W. et al. (2019). Fatigue reliability design for metal dual inline packages under random vibration based on response surface method. *Microelectronics Reliability, 100(7),* 113404. DOI 10.1016/j.microrel.2019.113404.
8. Wang, H., Hu, X., Jiang, X. (2020). Effects of Ni modified MWCNTs on the microstructural evolution and shear strength of Sn-3.0 Ag-0.5 Cu composite solder joints. *Materials Characterization, 163,* 110287. DOI 10.1016/j.matchar.2020.110287.
9. Fu, G., Su, Y., Guo, W., Wan, B., Zhang, Z. et al. (2018). Life prediction methodology of system-in-package based on physics of failure. *Microelectronics Reliability, 88(2),* 173–178. DOI 10.1016/j.microrel.2018.06.119.
10. Amagai, M., Watanabe, M., Omiya, M., Kishimoto, K., Shibuya, T. (2002). Mechanical characterization of Sn-Ag-based lead-free solders. *Microelectronics Reliability, 42(6),* 951–966. DOI 10.1016/S0026-2714(02)00017-3.
11. Xu, C., Gang, C., Sakane, M. (2005). Prediction of stress–strain relationship with an improved Anand constitutive model for lead-free solder Sn-3.5Ag. *IEEE Transactions on Components & Packaging Technologies, 28(1),* 111–116. DOI 10.1109/TCAPT.2004.843157.
12. Chen, X., Chen, G., Sakane, M. (2004). Modified Anand constitutive model for lead-free solder Sn-3.5Ag. *Conference on Thermal & Thermomechanical Phenomena in Electronic Systems,* pp. 447–452. Piscataway: IEEE.
13. Wu, J., Yang, H., Zhang, Y. (2018). The research of low temperature sintering nano-sliver paste based on Anand model. *Proceedings of the International Symposium on Big Data and Artificial Intelligence,* pp. 105–108. Hong Kong: Association for Computing Machinery.

14. Long, X., He, X., Yao, Y. (2017). An improved unified creep-plasticity model for SnAgCu solder under a wide range of strain rates. *Journal of Materials Science, 52(10),* 6120–6137. DOI 10.1007/s10853-017-0851-x.
15. Wang, W. J., Long, X., Du, C. Y., Fu, Y. H., Wu, Y. P. (2020). Enhancement of the unified constitutive model for viscoplastic solders in wide strain rate and temperature ranges. *Strength of Materials, 51(8),* 917–925. DOI 10.1007/s11223-020-00142-5.
16. Long, X., Chen, Z., Wang, W., Fu, Y., Wu, Y. (2020). Parameterized Anand constitutive model under a wide range of temperature and strain rate: Experimental and theoretical studies. *Journal of Materials Science, 55(24),* 10811–10823. DOI 10.1007/s10853-020-04689-1.
17. Che, F. X., Pang, J. H. (2012). Fatigue reliability analysis of Sn-Ag-Cu solder joints subject to thermal cycling. *IEEE Transactions on Device and Materials Reliability, 13(1),* 36–49. DOI 10.1109/TDMR.2012.2195007.
18. Wang, W., Chen, Z., Wang, S., Long, X. (2020). Mechanics-based acceleration for estimating thermal fatigue life of electronic packaging structure. *Microelectronics Reliability, 107(4),* 113616. DOI 10.1016/j.microrel.2020.113616.
19. Li, J., Xu, H., Hokka, J., Mattila, T. T., Chen, H. et al. (2011). Finite element analyses and lifetime predictions for SnAgCu solder interconnections in thermal shock tests. *Soldering & Surface Mount Technology, 23(3),* 161–167. DOI 10.1108/09540911111146917.
20. Jiang, L., Zhu, W., He, H. (2017). Comparison of Darveaux model and Coffin-Manson model for fatigue life prediction of BGA solder joints. *International Conference on Electronic Packaging Technology,* pp. 1474–1477. Piscataway: IEEE.
21. Hu, W., Li, Y., Sun, Y., Mosleh, A. (2016). A model of BGA thermal fatigue life prediction considering load sequence effects. *Materials, 9(10),* 860. DOI 10.3390/ma9100860.
22. Lee, S. R., Ben, H., Kong, Y. H., Baylon, B., Leung, T. et al. (2002). Assessment of board level solder joint reliability for PBGA assemblies with lead-free solders. *Soldering & Surface Mount Technology, 14(3),* 46–50. DOI 10.1108/09540910210444728.
23. Akay, H. U., Liu, Y., Rassaian, M. (2003). Simplification of finite element models for thermal fatigue life prediction of PBGA packages. *Journal of Electronic Packaging, 125(3),* 347–353. DOI 10.1115/1.1569956.
24. Liang, J., Gollhardt, N., Lee, P. S., Heinrich, S., Schroeder, S. (1997). An integrated fatigue life prediction methodology for optimum design and reliability assessment of solder interconnections. *Pacific Rim/ASME International and Intersociety Conference, Electronic and Photonic Packaging,* pp. 1583–1592. Kohala Coast, HI: ASME.
25. Darveaux, R. (2000). Effect of simulation methodology on solder joint crack growth correlation. *Proceedings of the 50th Electronic Components and Technology Conference,* pp. 1048–1058. Las Vegas.
26. Chen, R. S., Huang, C. H., Xie, Y. Z. (2012). Application of optimal design on twin die stacked package by reliability indicator of average SED concept. *Journal of Mechanics, 28(1),* 135–142. DOI 10.1017/jmech.2012.14.
27. Li, L. T., Jing, B., Hu, J. X. (2020). The degradation study for QFP interconnection structure based on PCMD health index and Darveaux model. *Microelectronics Reliability, 109(11),* 113662. DOI 10.1016/j.microrel.2020.113662.
28. Marbut, C. J., Montazeri, M., Huitink, D. R. (2018). Rapid solder interconnect fatigue life test methodology for predicting thermomechanical reliability. *IEEE Transactions on Device and Materials Reliability, 18(3),* 412–421. DOI 10.1109/TDMR.2018.2851541.
29. Sitta, A., Mauromicale, G., Sequenzia, G., Messina, A. A., Renna, M. et al. (2021). Thermo-mechanical finite element simulation and visco-plastic solder fatigue for low voltage discrete package. *22nd International Conference on Thermal, Mechanical and Multi-Physics Simulation and Experiments in Microelectronics and Microsystems (EuroSimE),* pp. 1–6. St. Julian.
30. Zhang, X., Wong, E. H., Lee, C., Chai, T. C., Ma, Y. et al. (2004). Thermo-mechanical finite element analysis in a multichip build up substrate based package design. *Microelectronics Reliability, 44(4),* 611–619. DOI 10.1016/j.microrel.2003.09.006.

31. Anand, L. (1982). Constitutive equations for the rate-dependent deformation of metals at elevated temperatures. *Transactions of the Asme Journal of Engineering Materials & Technology, 104(1),* 12–17. DOI 10.1115/1.3225028.
32. Dauksher, W., Lau, J. (2009). A finite-element-based solder-joint fatigue-life prediction methodology for Sn-Ag–Cu ball-grid-array packages. *IEEE Transactions on Device and Materials Reliability, 9(2),* 231–236. DOI 10.1109/TDMR.2009.2014943.

Computer Modeling in
Engineering & Sciences

Tech Science Press

DOI: 10.32604/cmes.2022.018349

ARTICLE

Reliability Analysis for Retaining Pile in Foundation Pit Based on Bayesian Principle

Yousheng Deng, Chengpu Peng*, Jialin Su, Lingtao Li, Liqing Meng and Long Li

Research Center of Plie-supported Structures, Xi'an University of Science and Technology, Xi'an, 710054, China

*Corresponding Author: Chengpu Peng. Email: 19204053003@stu.xust.edu.cn

Received: 18 July 2021 Accepted: 30 August 2021

ABSTRACT

Moso bamboo has the advantages of high short-term strength and reproducibility, appropriating for temporary supporting structure of shallow foundation pit. According to the displacement of the pile top from an indoor model test, the reliability of the supporting effect of the moso bamboo pile was analyzed. First, the calculation formula of reliability index was deduced based on the mean-value first-order second-moment (MVFOSM)method and probability theory under ultimate limit state and serviceability limit state. Then, the dimensionless bias factor (the ratio of the measured value to the calculated value) was introduced to normalize the displacement. The mathematical characteristics of the displacement were estimated and optimized based on Bayesian theory. Finally, taking 2.5 as the design reliability index, the effect of safety factor, tolerable limit displacement, and the ratio of the ultimate limit displacement to the tolerable on reliability index was analyzed. The results show that the safety level of the supporting pile can be increased by 1–2 levels when the safety factor increases by 0.5. When the coefficient of variation of tolerable limit displacement is less than 0.3, the safety factor can be 2–2.5. And the ratio of the ultimate limit displacement to the tolerable has a great influence on the reliability index, when the soil conditions is well, the ratio can be 1.2–1.3.

KEYWORDS

Moso bamboo pile; shallow foundation pit; reliability; sensitivity; Bayesian theory

1 Introduction

In the process of urban-rural integration construction, there are lots of shallow foundation engineering in the soft soil area. The engineering was not usually supported, because of the effect of excavation length, safety awareness, and engineering cost, causing many safety accidents [1]. To solve the problem and respond to the conception of national green development conception and eco-friendly building, moso bamboo is used as the supporting material for shallow foundation pit. The supporting effect in the shallow foundation pit was verified by an indoor model test [2] and engineering application [3]. To ensure that the supporting piles can meet the requirements of engineering, the reliability analysis will be carried out.

Structural reliability is the ability to complete a specific function during the prescribed time under the prescribed conditions, using reliable degree or failure probability as evaluation indices [4]. At present, relevant scholars at home and abroad have achieved many results in the field of reliability analysis. Bayesian theory has played a certain role in determining the random field parameters and related functions of soil parameters [5]. To reasonably characterize the spatial variability of soil parameters, Yang et al. [6] combined the limit equilibrium method and finite element method to analyze the influence of soil parameters on the displacement of slope. Huang et al. [7] analyzed the influence of the grouting method and soil condition of bearing layer on reliability index according to lots of static test data of drilling piles. Aladejare et al. [8] utilized Bayesian theory to establish probability distribution function, analyzed the effect of the correlation of soil parameters on the reliability index. Soil is a three-phase material, the parameters of soil are discontinuity, so the indeces of soil are difficult to be accurately determined. Fan et al. [9,10] studied the variation of soil characteristics along the pile length. Sun et al. [11] stated that internal friction angle of soil has a great influence on reliability index based on the Monte Carlo (MC) method. Zhang et al. [12] put forward an efficient calculation method of reliability index based on the probability density function and the Bootstrap method to solve the problem of determining mathematical characteristics of geotechnical parameters. Du et al. [13] established four failure models to research the influence of soil parameters on reliability index. Saseendran et al. [14] considered the uncertainty of the system parameters of the pile-slope, used the response surface method to derive the implicit function and to conduct the reliability analysis of its system safety. Jiang et al. [15] established normal distribution random field and lognormal distribution random field and clarified the influence of parameters changes on slope reliability index. Data discretization is an extreme problem in the indoor model test. To solve the problem in processing data is important. Zheng et al. [16,17] used Bayesian theory to optimize data, solving the problem of testing and monitoring data discretization. Xu et al. [18] improved the MVFOSM method, effectively reduced the non-linear iteration process, and established a revised function to ensure the accuracy of calculated results. Xin et al. [19] introduced the Coupula function to analyze the correlation between different parameters based on the problem of data discretization. Liu et al. [20] calculated the autocorrelation distance of soil parameters based on the recursive average method, which reduced the dispersion of parameters and made the calculation more accurate. What is more, Su et al. [21] introduced Gaussian process method in the reliability analysis of a slope, the method has a good accuracy and efficiency. Zhu et al. [22] proposed a novel Gaussian process surface method, constructing random field by Karhunen-Loeve expansion and the limit equilibrium method to evaluate the stability of slopes.

Among the existing research results, Bian et al. [23] analyzed the linear relationship of β_{uls} and β_{sls} (reliability index of pile bearing vertical load, under ultimate limit state and serviceability limit state, respectively). Referring to the above-mentioned methods, according to the model factors and distribution type of displacement, the calculation method of reliability index, used for supporting pile of foundation pit under different limit state, was deduced. The reliability index was calculated by the MVFOSM method, the JC method and the mapping transformation method, and verified by the MC method. Combining Bayesian theory, the effect of safety factor, tolerable limit displacement, and the ratio of the ultimate limit displacement to the tolerable on reliability index was analyzed. The results can provide a reasonable evaluation basis for the design of supporting structure used in foundation pit.

2 Uncertainty Analysis of Limit State

2.1 Serviceability Limit State

According to the failure principle, the limit state of the supporting pile can be divided into ultimate limit state and serviceability limit state. Under the serviceability limit state, the displacement is up to the design value, but the soil around the foundation pit has not failed. And the supporting structure has not been functionally damaged and still has a certain bearing capacity. However, the pile top displacement increases abruptly, and the supporting structure fails in the ultimate limit state. Therefore, the performance function should be established according to the different limit states during the reliability analysis of the supporting pile.

In the design of the supporting structure used in the foundation pit, the warning limit of displacement should be set and less than the ultimate limit value. Once d_m (measured displacement) exceeds the warning limit, the supporting structure should be strengthened, to prevent greater displacement. In the paper, the warning limit is defined as tolerable limit, and the limit state function is named as serviceability limit state function. In the design of the supporting structure, K (safety factor) is usually introduced, defined as the ratio of d_{tol} (tolerable displacement) to d_p (calculated displacement), shown as Eq. (1).

$$K = \frac{\mu_{d_{\mathrm{tol}}}}{\mu_{d_{\mathrm{p}}}} \tag{1}$$

In the Eq. (1), μ_{dtol} and μ_{dp} are the average of the tolerable displacement and the calculated displacement.

The test data in the paper comes from many tests [24]. In the test, soil, moso bamboo pile and mass block used as experimental load are quite different. d_p and d_m of the supporting pile are affected by uncertain factors such as the soil, the loading conditions and the pile materials. The data cannot be compared straightly, and the data is limit under the same test conditions. To increase the sample and eliminate the error in the displacement data of bamboo piles, the collected data are normalized, and the dimensionless bias factor is introduced, defined as the ratio of d_m to d_p, shown as Eq. (2).

$$\lambda = \frac{d_{\mathrm{m}}}{d_{\mathrm{p}}} \tag{2}$$

The significance of introducing the bias factor is to consider the difference of d_p and d_m, and make the expected results clear. Taking the bias factor as the basic parameter, analyze the influence of its mathematical characteristics on the reliability index.

According to the conception of reliability, when $Z = 0$, it means that the supporting pile is in a critical state. While $Z < 0$, d_{tol} is less than d_{m}, it can be judged that the normal use performance is invalid, and further measures need to be taken. The failure probability of the supporting pile can be shown as Eq. (3).

$$\begin{aligned} P &= \Pr(Z < 0) \\ &= \Pr(d_{\mathrm{tol}} < d_{\mathrm{m}}) \end{aligned} \tag{3}$$

When λ, d_{tol}, d_{p}, d_{m} obey lognormal distribution, according to the limit state equation and the MVFOSM method, the failure probability of supporting pile under serviceability limit state can be expressed as Eq. (4). According to the probability limit state method, the reliability index of supporting pile under serviceability limit state can be calculated, shown as Eq. (5).

$$\begin{aligned} p_{f_s} &= P\left(d_{\mathrm{tol}} < d_{\mathrm{m}}\right) \\ &= P\left\{\ln\left[\left(d_{\mathrm{tol}}/d_{\mathrm{p}}\right)\left(d_{\mathrm{p}}/d_{\mathrm{m}}\right) < 0\right]\right\} \\ &= P\left(\ln d_{\mathrm{tol}} - \ln d_{\mathrm{p}} - \ln\lambda < 0\right) \\ &= \Phi\left(-\frac{\mu_{\ln d_{\mathrm{tol}}} - \mu_{\ln d_{\mathrm{p}}} - \mu_{\ln\lambda}}{\sqrt{\sigma^2_{\ln d_{\mathrm{tol}}} + \sigma^2_{\ln d_{\mathrm{p}}} + \sigma^2_{\ln\lambda}}}\right) \end{aligned} \tag{4}$$

$$\begin{aligned} \beta_{\mathrm{sls}} &= \frac{\mu_{\ln d_{\mathrm{tol}}} - \mu_{\ln d_{\mathrm{p}}} - \mu_{\ln\lambda}}{\sqrt{\sigma^2_{\ln d_{\mathrm{tol}}} + \sigma^2_{\ln d_{\mathrm{p}}} + \sigma^2_{\ln\lambda}}} \\ &= \frac{\ln\left[\left(K/\mu_\lambda\right)\sqrt{\left(1+\delta^2_{d_{\mathrm{p}}}\right)\left(1+\delta^2_\lambda\right)/\left(1+\delta^2_{d_{\mathrm{tol}}}\right)}\right]}{\sqrt{\ln\left[\left(1+\delta^2_{d_{\mathrm{tol}}}\right)\left(1+\delta^2_{d_{\mathrm{p}}}\right)\left(1+\delta^2_\lambda\right)\right]}} \end{aligned} \tag{5}$$

In Eqs. (4) and (5), μ_{lndtol}, σ_{lndtol} represent the logarithmic mean value and logarithmic standard deviation of the tolerable displacement, respectively. $\mu_{\ln\lambda}$ and $\sigma_{\ln\lambda}$ represent the logarithmic mean value and logarithmic standard deviation of λ. μ_λ is the mean value of the bias factor. $\delta_{d\mathrm{p}}$, σ_λ, $\sigma_{d\mathrm{tol}}$ is the coefficient of variation of d_p, λ and d_{tol}, respectively.

2.2 Ultimate Limit State

The displacement limit state equation established above takes d_{tol} as a standard for the critical state of the support performance. The reliability analysis based on the basis belongs to the reliability design under the serviceability limit state. When d_{p} exceeds the tolerable limit, it indicates that the supporting capacity has not reached the expected goal, but the supporting capacity has not been lost completely. The failure probability of supporting pile under ultimate limit state can be expressed as Eq. (6).

$$\begin{aligned} p_{f_{\mathrm{u}}} &= P\left(d_{\mathrm{uls}} < d_{\mathrm{m}}\right) \\ &= P\left\{\ln\left[\left(d_{\mathrm{uls}}/d_{\mathrm{tol}}\right)\left(d_{\mathrm{tol}}/d_{\mathrm{p}}\right)\left(d_{\mathrm{p}}/d_{\mathrm{m}}\right)\right] < 0\right\} \\ &= P\left(\ln\lambda_{\mathrm{u}} + \ln d_{\mathrm{tol}} - \ln d_{\mathrm{p}} - \ln\lambda_d < 0\right) \\ &= \Phi\left(-\frac{\mu_{\ln\lambda_{\mathrm{u}}} + \mu_{\ln d_{\mathrm{tol}}} - \mu_{\ln d_{\mathrm{p}}} - \mu_{\ln\lambda_d}}{\sqrt{\sigma^2_{\ln\lambda_{\mathrm{u}}} + \sigma^2_{\ln d_{\mathrm{tol}}} + \sigma^2_{\ln d_{\mathrm{p}}} + \sigma^2_{\ln\lambda_d}}}\right) \end{aligned} \tag{6}$$

During the loading period of the indoor model test, the load was not up to the ultimate bearing capacity of the supporting pile, so the ultimate displacement of the pile top could not be obtained. However, the S-logt failure principle shows that the displacement corresponding to the stage of the steep drop at the end of the curve is the calculated limit displacement. Therefore, the load-displacement data collected from the indoor model test was processed by the *p-d* curve, which is expressed as Eq. (7). The reliability index of supporting pile under the ultimate limit state can be calculated, shown as Eq. (8).

$$P=\frac{d}{a+bd} \tag{7}$$

$$\begin{aligned}\beta_{\text{uls}} &= \frac{\mu_{\ln\lambda_{\text{u}}}+\mu_{\ln d_{\text{tol}}}-\mu_{\ln d_{\text{p}}}-\mu_{\ln\lambda_{d}}}{\sqrt{\sqrt{\sigma^2_{\ln\lambda_{\text{u}}}+\sigma^2_{\ln d_{\text{tol}}}+\sigma^2_{\ln d_{\text{p}}}+\sigma^2_{\ln\lambda_{d}}}}}\\ &= \frac{\ln\left[\left(\mu_{\lambda_{\text{u}}}\cdot\mu_{d_{\text{tol}}}\right)/\left(\mu_{\lambda}\cdot\mu_{d_{\text{p}}}\right)\cdot\sqrt{\left[\left(1+\delta^2_{\lambda_{d}}\right)\left(1+\delta^2_{d_{\text{p}}}\right)\right]/\left[\left(1+\delta^2_{\lambda_{\text{u}}}\right)\left(1+\delta^2_{d_{\text{tol}}}\right)\right]}\right]}{\sqrt{\ln\left[\left(1+\delta^2_{\lambda_{\text{u}}}\right)\left(1+\delta^2_{d_{\text{tol}}}\right)\left(1+\delta^2_{d_{\text{p}}}\right)\left(1+\delta^2_{\lambda_{d}}\right)\right]}}\\ &= C_0\beta_{\text{sls}}+C_1\end{aligned} \tag{8}$$

$$C_0=\frac{\sqrt{\ln\left[\left(1+\delta^2_{d_{\text{tol}}}\right)\left(1+\delta^2_{d_{\text{p}}}\right)\left(1+\delta^2_{\lambda}\right)\right]}}{\sqrt{\ln\left[\left(1+\delta^2_{\lambda_{\text{u}}}\right)\left(1+\delta^2_{d_{\text{tol}}}\right)\left(1+\delta^2_{d_{\text{p}}}\right)\left(1+\delta^2_{\lambda}\right)\right]}}$$

$$C_1=\frac{\ln\left(\left(\mu_{\lambda_{\text{u}}}/\sqrt{\left(1+\delta^2_{\lambda_{\text{u}}}\right)}\right)\right.}{\sqrt{\ln\left[\left(1+\delta^2_{\lambda_{\text{u}}}\right)\left(1+\delta^2_{d_{\text{tol}}}\right)\left(1+\delta^2_{d_{\text{p}}}\right)\left(1+\delta^2_{\lambda}\right)\right]}}$$

In the equation, λ_u is the ratio between the ultimate limit displacement and the tolerable, $\mu_{\lambda u}$ and $\delta_{\lambda u}$ are the mean value and the coefficient of variation of the bias factor.

3 Optimization Based on Bayesian Theory

3.1 Distribution Test of Related Variables

Calculating the reliability index should consider the distribution characteristics of the index. According to d_p and d_m, the bias factor of the supporting pile can be calculated. Based on the K-S test method and the significance level is 0.05, the distribution characteristics of d_{m}, d_{p}, and λ were analyzed to check whether the variables conform to normal distribution, lognormal distribution, or the Gumbel distribution. The distribution test results are shown in Table 1.

Table 1: Results of distribution test

Parameters	d_{m}			d_{p}			λ		
	N	LN	I	N	LN	I	N	LN	I
P value	0.93	0.97	0.74	0.80	0.82	0.53	0.21	0.46	0.40
Statistics	0.16	0.13	0.14	0.18	0.17	0.13	0.18	0.15	0.16
Critical value	0.37	0.34	0.34	0.37	0.37	0.35	0.21	0.21	0.21
Conclusion	Accept	Accept	Accept	Accept	Accept	Accept	Accept	Accept	Accept

In Table 1, N, LN, I represent normal distribution, lognormal distribution, the Gumbel distribution, respectively. The results based on the K-S test show that the statistics of d_m, d_p, and λ are less than the critical values. Therefore, the assumptions of the distribution type of the basic variables can be accepted. In the test results, the lognormal distribution corresponds to the largest similarity, so the samples are more consistent with the lognormal distribution. Consequently, in the following analysis, the distribution of the basic variables is seemed as lognormal distribution to deduct the relative calculated formula.

3.2 Bayesian Optimization Principle

A large amount of accurate test data can effectively reduce the design error. But considering the design and cost of indoor model tests, collecting lots of test data is difficult. Based on the problem, Zheng et al. [16,17] combined mathematical statistics and the Bayesian principle, defined the relative deviation (ζ) of the model factor and proposed the Bayesian optimal estimation of the model factor. The calculation of ζ is shown in Eq. (9).

$$\zeta = \frac{\left|\lambda_d - \mu_{\lambda_d}\right|}{\mu_{\lambda_d}} \tag{9}$$

In the reference [25], according to the relative deviation, the test data can be divided into three levels: good, general and bad. After the division of test data, the general data are optimized by Bayesian optimization estimation. Because the difference between the bad data and other data is too large, the error of reliability of analysis will be caused, so it should be discarded.

The judgment basis of dividing data is as follows:

(1) Good data: $\zeta < 0.25$

(2) General data: $\zeta \leq 0.25 < 0.5$

(3) bad data: $\zeta \geq 0.5$

According to the types of data, the good data are set as the prior distribution. When the data conform to the normal distribution, the prior density function of the variable is as Eq. (10). μ_1 and σ_1 are the mean value and standard deviation of the variables, respectively.

$$f_p(x) = N(\mu_1, \sigma_1) \tag{10}$$

Assuming the general data are a likelihood function, the mean value and standard deviation are μ_2 and σ_2, respectively. So the μ_2 and σ_2 of the posterior distribution of variables are calculated as Eqs. (11) and (12).

$$\mu_3 = \frac{\mu_2\sigma_1^2 + \mu_1(\sigma_2^2/n)}{\sigma_1^2 + \sigma_2^2/n} \tag{11}$$

$$\sigma_3^2 = \sigma_2^2 + \frac{\sigma_1^2(\sigma_2^2/n)}{\sigma_1^2 + (\sigma_2^2/n)} \tag{12}$$

On the basis of the above analysis, the model factor conforms to a lognormal distribution. Therefore, the mean value and standard deviation of the posterior distribution are needed to be transformed, calculated as Eqs. (13) and (14).

$$\mu_4 = \exp\left(\mu_3 + 0.5\sigma_3^2\right) \tag{13}$$

$$\sigma_4 = \mu_4^2\left[\exp\left(\sigma_3^2 - 1\right)\right] \tag{14}$$

3.3 Test Data Processing

Submitting the collected test data into Eq. (8) to calculate the model factor, then calculating the relative deviation of the calculated results according to Eq. (9) and classifying the model factors according to the relative deviation. The classification results are shown in Table 2. In the Table 2, 21 sets are good, 10 sets are general, and only 1 set is bad. The model factor range of 0.91–1.32 is good data, the general data range is 0.81–0.86 and 1.46–1.53. The model factor value of bad data is 0.55.

The bad data is discarded. Using Eqs. (13) and (14) to optimize the remaining data. The statistical analysis of the optimized data is shown in Table 3. The mean value of the raw data is equal to that of the updated data. But the coefficient of variation of the former is twice that of the latter. Therefore, the Bayesian optimal estimation can better solve the problem of data discretization.

Table 2: Classification of model factor

Number	λ	ζ	Type	Numer	λ	ζ	Type
1	1.13	0.03	good	17	0.98	0.16	Good
2	1.20	0.03	good	18	0.97	0.16	Good
3	1.22	0.05	good	19	0.95	0.18	Good
4	1.22	0.05	good	20	0.94	0.19	Good
5	1.09	0.06	good	21	0.91	0.22	Good
6	1.23	0.06	good	22	0.86	0.26	General
7	1.23	0.06	good	23	1.46	0.26	General
8	1.24	0.07	good	24	0.85	0.27	General
9	1.25	0.08	good	25	1.47	0.27	General
10	1.25	0.08	good	26	0.83	0.28	General
11	1.03	0.11	good	27	0.81	0.30	General
12	1.29	0.11	good	28	1.51	0.30	General
13	1.3	0.12	good	29	1.51	0.30	General
14	1.31	0.13	good	30	1.53	0.32	General
15	1.31	0.13	good	31	1.53	0.32	General
16	1.32	0.14	good	32	0.52	0.55	Bad

Table 3: Mathematical characteristics statistics of model factor

Statistic	Raw data	Good data	General data	Updated data
Mean value	1.158	1.151	1.236	1.158
Standard deviation	0.250	0.143	0.344	0.137
Coefficient of variation	0.216	0.124	0.278	0.118

In the light of the mean value, standard deviation, and coefficient of variation of the updated data, the reliability index of supporting pile under serviceability limit state was calculated based on the MVFOSM method, the JC method, the mapping transformation method, and the MC method. The calculated equation of the MVFOSM method is shown as Eq. (4). The coefficient of variation of the calculated displacement (δ_{dp}) was calculated from the test data, $\delta_{dp} = 0.12$. The coefficient of variation of d_{tol} and d_m was the same. The performance function of the JC method and the MC method is calculated as Eq. (15). The reliability indices of each method were calculated in the MATLAB software. The calculated results are shown in Table 4.

$$\begin{aligned} g &= d_{\mathrm{tol}} - d_{\mathrm{m}} \\ &= \frac{d_{\mathrm{tol}}}{d_{\mathrm{p}}} - \lambda = 0 \end{aligned} \tag{15}$$

As known in Table 4, the calculated value using the updated data is higher than the results using the raw data. The mean value of the raw data and the updated data is the same. Because the mean value of the likelihood function is small, and the coefficient of variation is large, so the coefficient of variation of the raw data is large and the calculated reliability index is small. Considering the distribution type of the data, the Bayesian optimal estimation optimizes the mean value and coefficient of variation of likelihood function based on prior distribution function, revises the bad data, and reduces its influence on reliability analysis.

Table 4: Calculated value of reliability index

Data type	MVFOSM method	JC method	Mapping transformation method	MC method
Raw data	2.09	2.19	2.19	2.20
Updated data	2.69	3.07	3.07	3.08

There is a difference in the calculated results between different calculation methods. The difference of using the MVFOSM method is the smallest, only 0.60. The difference between the JC method, the mapping transformation method and the MC method is equal, the value is 0.88. The results of the JC method and the mapping transformation method are higher than the results of the MVFOSM method, the smallest difference is 0.1 and the largest is 0.38. Because the calculated results of the JC method and the mapping transformation method are the same, so the next reliability analysis uses the two methods to calculate the reliability index, and use the MC method to check the calculated results.

4 Parameters Analysis

4.1 Safety Factor

According to the reference [25], the security level is classified by the reliability index, shown in Table 5. In the paper, the designed reliability index is 2.5. According to the *Federal Highway Administration Load and Resistance Factor Design (LRFD) for Highway Bridge Substructures* [26], the safety factor of designing pile structures is specified. The theoretical analysis and static load test of safety factor are 3.5 and 2.0, respectively. Moso bamboo pile is a new material of pile. Compared with the concrete pile, the actual engineering experience and theory are not complete. Therefore, the safety factor is in the range of 2.0–3.5. Using the MVFOSM method, the JC method and the MC method to calculate reliability index β_{sls}, the results are shown in Fig. 1. The influence of safety factors on reliability was analyzed. The range of safety factors was discussed under the condition of ensuring the safety level.

Table 5: Relationship between reliability index and failure probability

Reliability index	Failure probability	Security level
1.0	0.16	–
1.5	0.07	–
2.0	0.023	poor
2.5	0.006	Lower middle
3.0	0.001	Higher middle
4.0	0.00003	Good
5.0	0.0000003	High

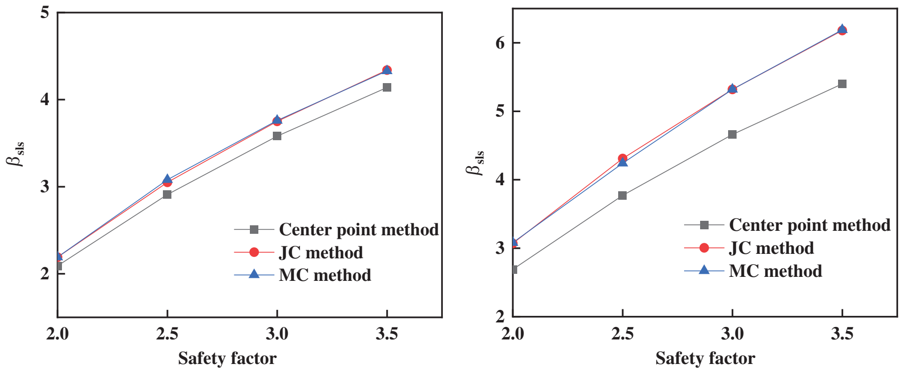

(a) (b)

Figure 1: The influence of safety factor on the reliability index (a) Raw data (b) Updated data

The reliability index increases with the increase of the safety factor. When the safety factor is 2.5, the smallest reliability index is 3.00, the largest is 3.08. As known in Fig. 1, when the reliability index is within 2.5–3.5, the security level is medium. And according to the three methods, the failure probability of supporting pile under serviceability limit state is about 1%. According to the investigation report of the foundation pit accident, the accident probability of foundation pit without a supporting structure is about 21.8% [1]. Comparing with the two sets of data, it is obvious that the use of the Moso bamboo pile as a supporting structure can significantly improve the safety of shallow foundation pits.

As shown in Fig. 1, the calculated reliability index using the updated data is significantly higher than the calculation result based on the raw data. When the safety factor is 2.0, the reliability index of the former is close to the latter when the safety factor is 2.5. The reliability index of using the MVFOSM method is less than the value of using the JC method and the MC method, but the security level is the same and the failure probability is less than 6%. The reliability index keeps substantially increasing with the increase of safety factor. When the safety factor is 2.5, the reliability index of using the MVFOSM method is 3.99, the security level is high, and the failure probability is less than 0.03%. With the same safety factor, the reliability of using the JC method and the MC method is 4.31 and 4.24, the security level is high, and the failure probability is less than 0.0003%. When the safety factor is 3.5, the reliability index is too large, the supporting capacity is excessive, and the cost is too high to meet the economic requirements of the engineering. Therefore, the reliability corresponding to the safety factor is not considered.

Because of the influence of soil parameters, underwater and other uncertain factors, it is difficult to determine the specific limit displacement of the foundation pit. Therefore, in the process of calculating the reliability index under the ultimate limit state, the coefficient of variation of the ratio of the limit displacement to the tolerable ($\delta_{\lambda u}$) is regarded as a random variable, within the range of 0–0.5. Discussing the variation trend of reliability under different coefficient of variation, the calculated results are shown in Fig. 2.

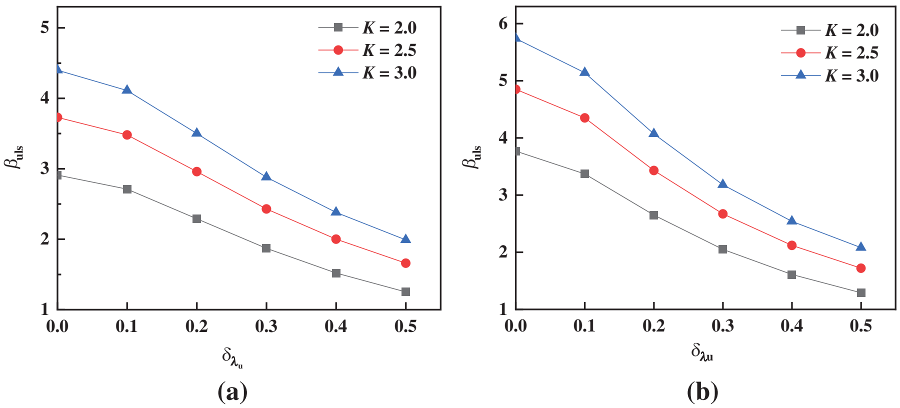

Figure 2: The influence of $\delta_{\lambda u}$ on the β_{uls} (a) Raw data (b) Updated data

As shown in Fig. 2, when the variables are the same, the reliability index of using updated data is higher than the value of using raw data, and the difference is gradually reducing with the increase of $\delta_{\lambda u}$, the correction ability of prior distribution function is weakened. Taking the safety factor of 2.5 as an example, when $\delta_{\lambda u} = 0.1$, the difference of using the two different data is the largest, 0.87. When $\delta_{\lambda u} = 0.5$, the difference is the smallest, only 0.06. When $\delta_{\lambda u} = 0.3$, β_{uls} starts to be smaller than β_{sls}. The main cause of the problem is that $\delta_{\lambda u}$ is too large, resulting in a lot of λ_u being less than 1. It means that the error is too large in calculating the limit displacement of the foundation pit, resulting in the measured limit displacement being less than the tolerable displacement. When $\lambda_u < 1$, the tolerable displacement will also vary. Therefore, judging the limit displacement of soil in the foundation pit is extremely important to the reliability analysis of supporting pile capacity.

β_{uls} decreases with the increase of $\delta_{\lambda u}$. When $\delta_{\lambda u}$ is in the range of 0–0.3, the decreased amplitude of β_{uls} keeps increasing. When $\delta_{\lambda u}$ is in the range of 0.3–0.5, the decreased amplitude starts to decrease, but the variation is small. As known in Fig. 2, when the reliability index is larger than 2.5, the security level is medium. When $\delta_{\lambda u} = 0.3$ and the safety factor is 2.5 or 3.0, the calculated reliability index of using updated data can reach the security level. But the calculated reliability index of using raw data can reach the security level when the safety factor is 3.0. Therefore, in the reliability analysis under the ultimate limit state, the prior distribution function still plays a positive role in correcting the data discretization.

4.2 Tolerable Displacement

Tolerable displacement is a basic variable of the limit state equation and a standard for judging whether the supporting structure meets the normal use. In the design of the supporting structure, the tolerable displacement should be firstly determined according to relative parameters and engineering experience. The target value is determined according to tolerable displacement and safety factor, and the target value is a key index to determine other parameters of the supporting pile. Therefore, d_{tol} is a standard to guide d_p. The deviation of d_{tol} determines whether the designed displacement is reasonable. Taking $\delta_{d\mathrm{tol}}$ as a basic variable, the range is 0–0.5, the influence of d_{tol} on β_{sls} is analyzed. The calculated results are shown in Fig. 3.

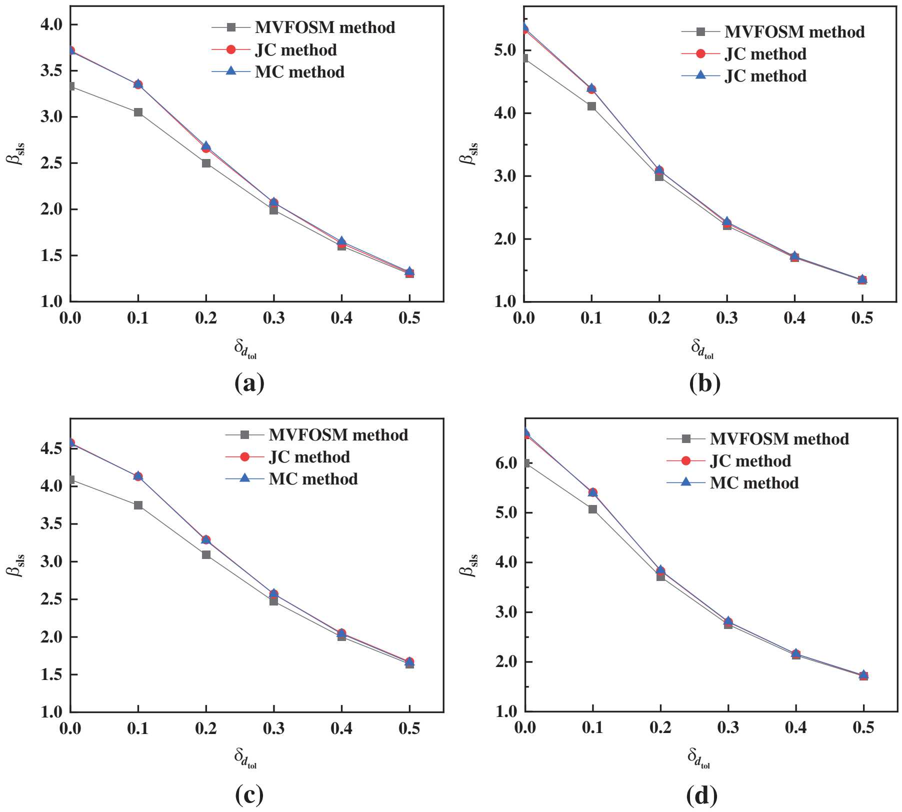

(a) (b)

(c) (d)

Figure 3: The influence of $\delta_{\lambda u}$ on the β_{uls} with different safety factor (a) Raw data ($K = 2.5$) (b) Updated data ($K = 2.5$) (c) Raw data ($K = 3.0$) (d) Updated data ($K = 3.0$)

When $\delta_{d\mathrm{tol}}$ is in the range of 0–0.3, the β_{sls} of using the updated data is significantly higher than the value of using the raw data, the largest difference is 1.91, the smallest is 0.22. the correction performance of the prior distribution function in Bayesian optimal estimation still plays an active role. Taking $\beta_{\mathrm{sls}} \geq 2.5$ as the goal reliability, it means that the security level is medium and above. When $\delta_{d\mathrm{tol}} = 0.2$, the β_{sls} of using the three methods are about 3.0, meeting the design requirement. If the $\delta_{d\mathrm{tol}}$ is too large because of extreme factors, the safety factor can be increased properly.

β_{sls} fluctuates greatly with the change of $\delta_{d\mathrm{tol}}$. Taking $K = 2.5$ as an example, $\delta_{d\mathrm{tol}}$ varies from 0 to 0.5. The β_{sls} based on the raw data and the updated data decreases 2.03 and 3.53, respectively. In the design of the supporting pile, if d_{tol} varies greatly, it will affect the rationality of d_p of foundation pit, indirectly reduce K, and cause the reliability index to drop. Therefore, the d_{tol} is important to K.

β_{uls} decreases greatly with the increase of $\delta_{d\mathrm{tol}}$. When $\delta_{d\mathrm{tol}} = 0.4$, the reliability index of using updated data is still larger than 2.5, the security level is medium and above.

4.3 Ratio of Limit Displacement to Tolerable Displacement

In the design of the supporting structure, the ratio of limit displacement to tolerable displacement (λ_u) is a subjective judgment based on objective factors and experience. λ_u is another safety factor in the reliability analysis under the ultimate limit state. Taking λ_u as a basic variable to calculate β_{uls} based on the MVFOSM method, the influence of $\mu_{\lambda u}$ and $\delta_{\lambda u}$ on β_{uls} are analyzed, the results are shown in Fig. 4.

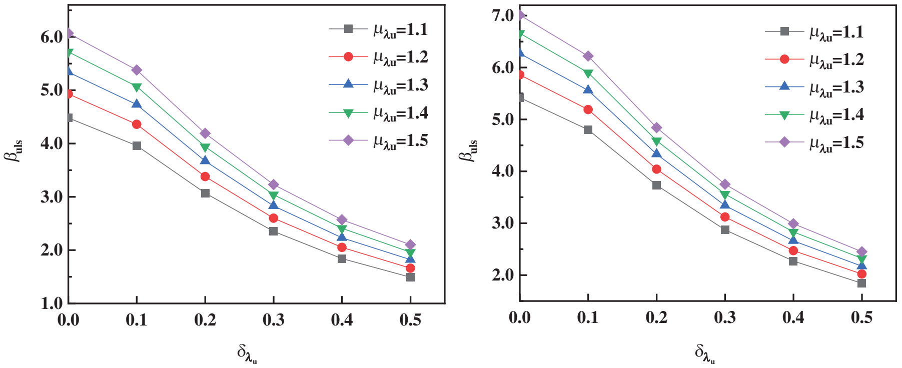

(a) **(b)**

Figure 4: The influence of λu on the reliability index (a) Updated data ($K = 2.5$) (b) Updated data ($K = 3.0$)

The influence of $\delta_{\lambda u}$ on β_{uls} is much higher than that of $\mu_{\lambda u}$. Taking $K = 2.5$ as an example, when $\delta_{\lambda u}$ varies from 0.1 to 0.2, β_{uls} has the fastest declining rate. And the change value is 1.18. β_{uls} keeps increasing with the increase of $\mu_{\lambda u}$. But the variation amplitude is reducing gradually, the largest value is 0.45. The change of the former is 2.62 times that of the latter.

β_{uls} increases gradually with the increase of $\mu_{\lambda u}$, but the variation amplitude is reducing. When the $\delta_{\lambda u}$= 0, $\delta_{\lambda u}$ varies from 1.1 to 1.5, the largest difference of β_{uls} is 1.59. When $\delta_{\lambda u}$= 0.5, the largest difference is 0.61. Taking $K = 2.5$ as an example, when $\delta_{\lambda u} \geq 0.3$, some values of β_{uls} start to be less than 2.5. When $\delta_{\lambda u}$= 0.3, β_{uls} can meet the safety requirement with the increase of $\mu_{\lambda u}$.

5 Conclusion

(1) Using the Bayesian principle to optimize and estimate test data, the mean value of the raw data and the updated data are the same, but the coefficient of variation of the former is two times of the latter. And the β of using the updated data is higher than that of using the raw data. The Bayesian principle can efficiently reduce the influence of test error on relative parameters, and solve the problem of data discretization.

(2) The safety factor increases by 0.5, the safety of the supporting structure can be increased by 1 to 2 levels.

(3) Taking $\beta_{\text{sls}} \geq 2.5$ as the goal reliability, when $\delta_{d\text{tol}} = 0.2$, the β_{sls} based on the updated data is about 3.0, meeting the safety requirement. If the $\delta_{d\text{tol}}$ is too large because of extreme factors, the safety factor can be increased properly to meet safety requirements.

(4) The ratio of limit displacement to tolerable displacement has a great influence on β_{uls}. When $\delta_{\lambda u} = 0.3$, β_{uls} can meet the safety requirement with the increase of $\mu_{\lambda u}$. If $\delta_{\lambda u}$increases continually, the safety factor should be increased simultaneously.

Data Availability: The data used to support the findings of this study are included in the article.

Funding Statement: The research described in the paper was supported by the National Natural Science Foundation of China (No. 51878554) Key projects of Shaanxi Natural Science Basic Research Program (No. 2018JZ5012).

Conflicts of Interest: The authors declare that they have no known competing financial interests or personal relationships that could have appeared to influence the work reported in this paper.

References

1. Li, L. Y., Li, R. Z., Lei, Z. X. (2017). Study on pattern of foundation pit accident based on statistical analysis. *Modern Urban Transit, 12,* 50–55.
2. Deng, Y. S., Wang, H., Yang, M. (2016). Model tests on shallow excavation support through bamboo micropile. *Rock and Soil Mechanics, 37(S2),* 294–300. DOI 10.16285/j.rsm.2016.S2.036.
3. Zhen, G. X. (2014). New building foundation pit supporting technologies with low carbon environmental protection. *Fujian Construction Science & Technology, 2,* 1–5.
4. Zhao, G. F., Gong, J. X., Zhao, S. C. (2000). Developments of reliability research for civil engineering structure in China. *Journal of Dalian University of Technology, 3,* 253–258.
5. Tian, M., Li, D. Q., Cao, Z. J. (2017). Quantification of spatial variability of soil parameters using bayesian approaches. *Rock and Soil Mechanics, 38(11),* 3355–3362. DOI 10.16285/j.rsm.2017.11.035.
6. Xue, Y., Wu, Y. P., Miao, F. S., Li, L. W. (2021). Back analysis of shear strength parameters of sliding surface by using combination method of random field and Bayes theory. *Journal of Zhejiang University (Engineering Science), 55(6),* 1118–1127. DOI 10.3785/j.issn.1008-973X.2021.06.012.
7. Huang, S. G., Shen, J. H., Li, M. (2019). Reliability analysis of bearing capacity of post-grouted bored piles. *Rock and Soil Mechanics, 40,* 1977–1982. DOI 10.16285/j.rsm.2018.0332.
8. Aladejare, A. E., Wang, Y. (2018). Influence of rock property correlation on reliability analysis of rock slope stability: From property characterization to reliability analysis. *Geoscience Frontiers, 9(6),* 1639–1648. DOI 10.1016/j.gsf.2017.10.003.
9. Fan, H. J., Huang, Q. D., Liang, R. (2014). Reliability analysis of piles in spatially varying soils considering multiple failure modes. *Computers and Geotechnics, 57(2),* 97–104. DOI 10.1016/j.compgeo.2014.01.009.
10. Fan, H. J., Liang, R. (2015). Importance sampling based algorithm for efficient reliability analysis of axially loaded piles. *Computers and Geotechnics, 65(2),* 278–284. DOI 10.1016/j.compgeo.2015.01.005.
11. Sun, Y. D. (2017). *Stability analysis of deep excavation based on reliability theory*. China University of Geosicence, Beijing.
12. Zhang, L. S., Li, D. Q., Cao, Z. J., Tang, X. S. (2019). Efficient reliability analysis of excavation deformation considering statistical uncertainty using Monte Carlo simulation. *Engineering Journal of Wuhan University, 52(3),* 207–215. DOI 10.14188/j.1671-8844.2019-03-004.
13. Du, X. L., Cao, X. X., Zhong, Z. L., Hou, B. W. (2020). Robust geotechnical design of soil-pile foundation system considering multiple failure modes. *Chinese Safety Science Journal, 30(6),* 23–30. DOI 10.16265/j.cnki.issn1003-3033.2020.06.004.
14. Saseendran, R., Dodagoudar, G. R. (2020). Reliability analysis of slopes stabilized with piles using response surface method. *Geomechanics and Engineering, 21(6),* 513–525. DOI 10.12989/gae.2020.21.6.513.
15. Jiang, S. H., Liu, S. H., Huang, J. S. (2020). Non-intrusive reliability analysis of unsaturated embankment slopes accounting for spatial variabilities of soil hydraulic and shear strength parameters. *Engineering with Computers, 7,* 1–14. DOI 10.1007/s00366-020-01108-6.

16. Zheng, J. J., Xu, Z. J., Liu, Y. et al. (2012). Bayesian optimization for resistance factor of piles. *Chinese Journal of Geotechnical Engineering, 34,* 1716–17241.
17. Zheng, J. J., Liu, S. Q., Xun, Z. J. (2012). Bayesian estimation of design values of bearing capacity of foundation piles. *Bridge Construction, 42,* 41–45.
18. Xu, Z. J., Han, X., Zheng, J. J. (2020). Study on reliability optimization design method of piles under vertical loads. *Journal of Huazhong University of Science and Technology (Natural Science Edition), 48,* 55–60. DOI 10.13245/j.hust.200511.
19. Xin, J. X., Wu, X. Z., Gao, W. (2016). Copula-based analysis of load-displacement curves of cement-fly ash-gravel pile. *Rock and Soil Mechanics, 37(S1),* 424–434. DOI 10.16285/j.rsm.2016.S1.055.
20. Liu, C., Yuan, Y., Zuo, Z. H. (2020). Pile reliability design considering the influence of soil auto-correlation distance. *Hydrogeology & Engineering Geology, 47(3),* 122–127. DOI 10.16030/j.cnki.issn.1000-3665.201910004.
21. Su, G. S., Xiao, Y. L. (2011). Guassian process method for slope reliability analysis. *Chinese Journal of Geotechnical Engineering, 33(6),* 916–920.
22. Zhu, B., Pei, H. F., Yang, Q. (2019). Gaussian process regression-based response surface method and reliability analysis of slopes. *Chinese Journal of Geotechnical Engineering, 41(s1),* 209–212.
23. Bian, X. Y., Zheng, J. J., Xu, Z. J. et al. (2015). Target reliability index for serviceability limit state of single piles. *Journal of Central South University, 22(1),* 310–316. DOI 10.1007/s11771-015-2523-9.
24. Cheng, Z. H. (2020). *Study on bearing characteristics of dentate bamboo pile-Soil composite support system (Master's Thesis)*. Xi'an University of Science and Technology.
25. Zhen, J. J., Liu, Y., Guo, J. (2009). Probabilistic analysis and reliability assessment for acceptance rate of foundation pile testing. *Chinese Journal of Geotechnical Engineering, 31,* 1660–1664.
26. American Association of State Highway and Transportation Officials (AASHTO) (2007). *Load and resistance factor design (LRFD) for bridge design specifications* (4th ed.). Washington DC: American Association of State Highway and Transportation Officials.

Computer Modeling in
Engineering & Sciences

Tech Science Press

DOI: 10.32604/cmes.2022.018234

ARTICLE

Image Reconstruction for ECT under Compressed Sensing Framework Based on an Overcomplete Dictionary

Xuebin Qin[1,*], Yutong Shen[1], Jiachen Hu[1], Mingqiao Li[1], Peijiao Yang[1], Chenchen Ji[1] and Xinlong Zhu[2]

[1]School of Electrical and Control Engineering, Xi'an University of Science and Technology, Xi'an, 710054, China

[2]Shaanxi Coal and Shaanbei Mining Co., Ltd., Xi'an, 719000, China

[*]Corresponding Author: Xuebin Qin. Email: qinxb@xust.edu.cn

Received: 09 July 2021 Accepted: 02 September 2021

ABSTRACT

Electrical capacitance tomography (ECT) has great application potential in multiphase process monitoring, and its visualization results are of great significance for studying the changes in two-phase flow in closed environments. In this paper, compressed sensing (CS) theory based on dictionary learning is introduced to the inverse problem of ECT, and the K-SVD algorithm is used to learn the overcomplete dictionary to establish a nonlinear mapping between observed capacitance and sparse space. Because the trained overcomplete dictionary has the property to match few features of interest in the reconstructed image of ECT, it is not necessary to rely on the sparsity of coefficient vector to solve the nonlinear mapping as most algorithms based on CS theory. Two-phase flow distribution in a cylindrical pipe was modeled and simulated, and three variations without sparse constraint based on Landweber, Tikhonov, and Newton-Raphson algorithms were used to rapidly reconstruct a 2-D image.

KEYWORDS

Electrical capacitance tomography; dictionary learning; compressed sensing; k-SVD algorithm; overcomplete dictionary; two-phase flow

1 Introduction

In industrial processes, it is often necessary to analyze information about two-phase flow in a pipeline or closed container. Traditional detection methods have been unable to provide accurate measurement because of the complexity of flow motion. In recent decades, with the development of modern measurement technology, electrical tomography (ET), with its advantages of non-invasive, non-damaging characteristics, and simple structure and low cost, has attracted extensive attention from researchers. At present, ET mainly includes electrical resistance tomography [1] (ERT), electrical impedance tomography [2] (EIT), electromagnetic tomography [3] (EMT), and electrical capacitance tomography [4] (ECT). ECT investigated in this study is a technique for visualizing a two-phase medium with phases of different permittivity in a pipe or a closed container. The system is suitable for imaging multicomponent phase flows, such as sand, that are not conductors. ECT technology has shown great potential in many fields, such as multiphase flow measurement [5], combustion imaging [6], and solid particle monitoring in a fluidized bed [7,8].

The objective of ECT is to obtain projection data through a sensor array fixed on the outer wall of a pipe or container, and then use an algorithm to obtain the internal permittivity distribution, which is presented with 2-D or 3-D images. The sensor array is composed of multiple electrodes, and the number of electrodes can be 8, 12, or 16. The mutual capacitances between electrodes are collected to form a capacitance sequence which is the projected data reflecting internal information. Mathematical modeling computes the permittivity distribution from the capacitance sequence, which is an inverse problem model. Many algorithms have been proposed to solve the inverse problem, such as Convolutional Neural Networks (CNN), the linear inverse projection algorithm (LBP), Landweber algorithm, and Tikhonov regularization algorithm. Deep learning has shown great advantages in many fields, especially in image processing [9,10]. Deep learning has many advantages such as strong learning ability, wide coverage, and good portability [11–13]. However, deep learning models are more complex and time-consuming. High, it violates the real-time nature of electrical capacitance tomography. The LBP algorithm has fast computation but low image accuracy. The Landweber algorithm is a simple iterative algorithm, and many scholars have improved its convergence rate [14–16]. The inverse problem is ill-posed, but the Tikhonov regularization algorithm transforms the ill-posed problem into a well-posed problem by adding regularization constraint terms based on the l_2-norm to the target function, and then obtains an effective solution. The reconstructed image is smooth but insensitive to edge contours.

Most algorithms establish approximate linear mapping to replace non-linear mapping because of the “soft field” in ECT, resulting in low accuracy of the reconstructed image. In 2006, Donoho proposed compressive sensing (CS) theory [17], which pointed out that when the signal is sparse or compressible, the original signal can be accurately reconstructed with far fewer samples than that required by Shannon’s theorem. In recent years, Figueiredo and Candes et al. extended CS theory [18–21]. CS theory has been widely applied in the field of imaging, and it can be used for image reconstruction in ECT [22–24].

In CS theory, the transform basis for sparse representation is crucial. For image reconstruction systems in different application fields, the transform basis is generally the specified orthogonal basis, such as discrete Fourier transform (DFT) [25], discrete cosine transform (DCT) [26], or discrete wavelet transform (DWT) [27]. The classical orthonormal basis is better for some features of the image but is negative for two-phase distributions, because two-phase flow is always varied in a complex industrial process. Specifying an orthonormal basis may reflect the permittivity distribution of a flow pattern such as stratified flow. To solve the above problems, this paper introduces the idea of CS and dictionary learning to ECT theory [28,29], which is called D-CS-ECT. Different flow patterns are used to train the transform basis so that it matches the different features of the permittivity distribution as much as possible to improve the accuracy of the reconstructed image [30].

In this paper, the transform basis is an overcomplete dictionary. The overcomplete dictionary is flexible and adaptive. It captures different features of the signal through multiple atoms and improves the redundancy of the transform system to approximate the original signal. There are some features of interest in the image reconstructed by ECT system, which focus on the position and boundary of the two phases. The trained overcomplete dictionary is able to match the features.

This paper is organized as follows: in Section 2, the basic principles of ECT and CS theory based on over-complete dictionaries are introduced. In Section 3, the process of dictionary learning is described, which is mainly the construction of a training sample set and the application of the K-SVD algorithm. The reconstruction results are analyzed and evaluated through simulation in Section 4. Concluding remarks are presented in Section 5.

2 ECT under the Framework of D-CS Theory

2.1 Basic Principles of ECT

The hardware architecture of ECT systems is composed of a sensor array, data acquisition module, and image reconstruction unit. In this study, a sensor array with 12 electrodes is driven by an excitation voltage, as shown in Fig. 1b, and the electrodes are numbered from 1 to 12. Firstly, Electrode 1 is excited with a 1 V voltage while the other electrodes are grounded. The capacitance values between Electrode 1 and Electrodes 2, 3, 4..., 12 are collected and then numbered 1–2, 1–3, 1–4..., 1–12. Secondly, Electrode 2 is excited with a 1 V voltage while the other electrodes are grounded. The capacitance values between Electrode 2 and Electrodes 3, 4, 5..., 12 are collected and then numbered 2–3, 2–4, 2–5..., 2–12. By analogy, capacitance values 3–4, 3–5, 3–6..., 3–12 can be obtained between Electrode 3 and Electrodes 2, 3, 4..., 12. Finally, a total of 66 capacitance values can be collected, and the equation [31] to calculate the number of capacitor sequences can be derived by

$$N = \frac{M \times (M-1)}{2} \tag{1}$$

where N is the number of capacitor sequences, and M is the number of electrodes.

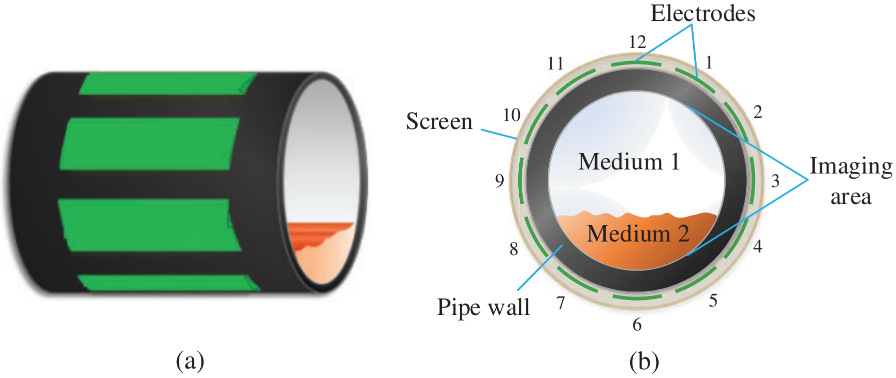

Figure 1: ECT sensor with 12 electrodes for two-phase flow in the pipeline. (a) 3-D structure; (b) 2-D section

For a complex and changeable two-phase flow, the distribution in the pipeline includes seven flow patterns: central bubble flow, eccentric bubble flow, two-bubble flow, three-bubble flow, four-bubble flow, stratified flow, and annular flow, as shown in Fig. 2.

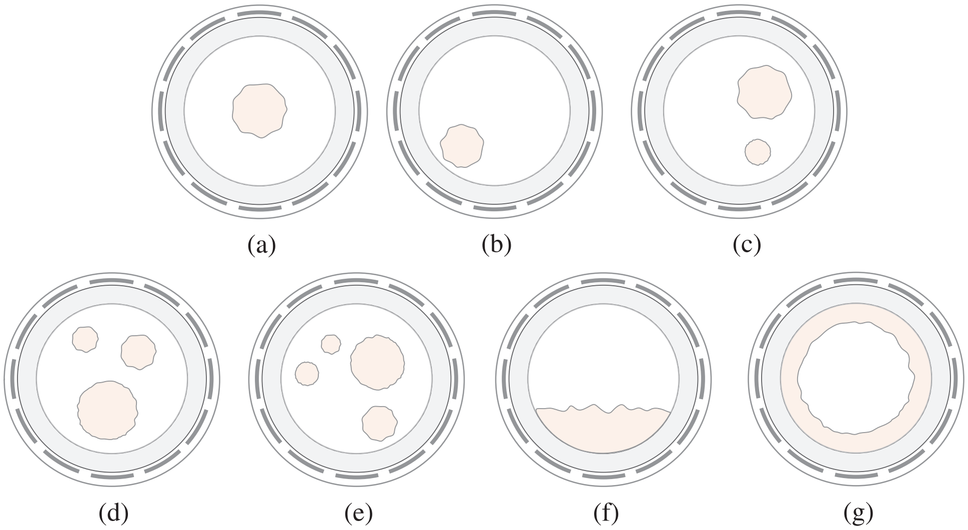

Figure 2: Different flow patterns. (a) Central bubble flow; (b) Eccentric bubble flow; (c) Two-bubble flow; (d) Three-bubble flow; (e) Four-bubble flow; (f) Stratified flow; (g) Annular flow

In ECT, the approximate linear relationship between the capacitance sequence and the permittivity sequence is described by the following equation:

$$\lambda = Sg \tag{2}$$

where $\lambda \in R^{p\times 1}$ is the capacitance vector reflecting the projection of mediums in the imaging area. $g \in R^{n\times 1}$ is the permittivity vector, and is also the pixel vector because the variation trend of permittivity distribution can be reflected by the pixels. $S \in R^{m\times n}$ is the sensitivity matrix, which reflects the sensitivity of the capacitance vector affected by the permittivity distribution.

In Fig. 1b, ε_1 and ε_2 ($\varepsilon_1 > \varepsilon_2$) are the permittivity of medium 1 and medium 2. The state in which the imaging area is filled with medium 1 is called "full field," and C_H denotes the measured capacitance vector under the full field state. The state in which the imaging area is filled with medium 2 is called "empty field," and C_L denotes the measured capacitance vector under the empty field state. In industrial processes, ε_1 and ε_2 are generally known, so C_H and C_L can be obtained in advance. The capacitance vector measured by the ECT system at a certain moment during process monitoring is C_M, and the normalization methods for the capacitance vector at this moment are given in (3) and (4).

$$\lambda = \frac{C_M - C_L}{C_H - C_L} \tag{3}$$

$$\lambda = \frac{1/C_M - 1/C_L}{1/C_H - 1/C_L} \tag{4}$$

where (3) is the parallel normalization method, and (4) is the series normalization method. It can be seen from (3) or (4) that the λ from (2) is actually the difference in capacitance. Both normalization methods have their advantages and disadvantages, and their differences are discussed in [32]. In this study, (3) is selected as the normalization method for the capacitance vector.

S from (2) is the sensitivity matrix of the empty field state. According to the potential distribution in the imaging area [33], the discrete derivation result for S is

$$\begin{cases} S_{i,j}^{k} = \dfrac{\partial C_{i,j}}{\partial \varepsilon_{\mathrm{k}}} = \dfrac{\iint_{\Omega_k} \nabla \phi_i^k \nabla \phi_j^k dxdy}{U^2} \\ \quad 1 \leq \mathrm{i} \leq \mathrm{M}, 1 \leq j \leq \mathrm{M},\ i < j \\ \qquad\quad 1 \leq k \leq n \end{cases} \tag{5}$$

where the number of electrodes is M, the number of pixels distributed in the imaging area is n, and the excitation voltage of the electrode is U=1 V. $C_{i,j}$ is the capacitance scalar between the $i-th$ electrode and the $j-th$ electrode. At the spatial position of the $k-th$ pixel point, $S_{i,j}^{k}$ is the sensitivity scalar relating to the interaction between the $i-th$ electrode and the $j-th$ electrode, ε_{k} is the permittivity scalar, and ϕ_i^k, ϕ_i^k are the potential scalars relating to the excitation of the $i-th$, $i-th$ electrodes.

The normalization method for the sensitivity matrix is given by

$$S_{\mathrm{norm}} = Sdiag\left(\frac{1}{\sqrt{\sum_{j=1}^{n} S_{ij}^2}}\right) \tag{6}$$

where $diag(\cdot)$ is the diagonal matrix operator, and S_{norm} is the normalized sensitivity matrix.

To obtain the image is to solve g. Because the number of the capacitance sequence obtained from the sensor is far lower than the number of pixels in the reconstructed image, S is an ill-posed matrix, and (2) is ill-posed and its solution is not unique. The error function is minimized in the inverse problem of the ECT, that is,

$$\min ||\lambda - Sg||^2 \tag{7}$$

Many existing image reconstruction algorithms for ECT can be improved on the basis of (7), such as adding constraint terms based on the l_2-norm to the target function.

2.2 D-CS-ECT

CS theory mainly includes three parts: the sparse representation of signal, design of the observation matrix, and signal reconstruction. D-CS using a dictionary rather than an orthogonal basis is a branch of CS theory [34]. Proposed the dictionary-restricted isometry property (D-RIP), which is a natural generalization of the restricted isometry property (RIP) [35], proving that the idea of signal reconstruction by a redundant and coherent dictionary is feasible. The mathematical model for D-CS-ECT is given below.

The image signal is represented as a small number of values in sparse space through an overcomplete dictionary. Sparse representation can be expressed as

$$\mathrm{g} = Dx \tag{8}$$

where $g \in R^{n\times 1}$ is the pixel vector. D is an $n \times p$ matrix, with n smaller than p, that represents the redundant overcomplete dictionary, and its column vectors represent atoms. $x \in R^{p\times 1}$ is the coefficient vector. Assuming that x has K non-zero elements, it is called *K-sparse*. Dictionary learning defines D as an "atom library" of matching features of interest. A non-zero element in x is equivalent to the weight of the corresponding atom in "atom library", and different images are represented by selecting different weight sets.

The nonlinear mapping relation between the observed capacitance and the coefficient vector can be written as

$$\lambda = Sg = SDx = A^{D-CS}x \tag{9}$$

where $\lambda \in R^{m\times 1}$ is the capacitance vector. $A^{D-CS} = SD$, and A^{D-CS} is an $m \times p$ sensing matrix. In the case that x is approximately sparse, it can be considered that A^{D-CS} has an approximately sparse property for λ. $S \in R^{m\times n}$ is the observation matrix and also the sensitivity matrix.

The procedure of the reconstruction algorithm is to first solve x according to (9), and then solve g according to (8). Classical signal reconstruction algorithms based on CS theory mainly include greedy algorithms and convex optimization algorithms. In this study, the sparsity adaptive matching pursuit (SAMP) algorithm [36] and the gradient projection for the sparse reconstruction (GPSR) algorithm [37] are used as examples to present the optimization equation.

A mathematics model of an l_0-analysis optimization problem for the SAMP algorithm is given by

$$\begin{cases} x_{opt} = \arg\min ||x||_0 \quad s.t \ \ ||\lambda - SDx||_2 \le \alpha \\ \qquad\qquad g_{opt} = Dx_{opt} \end{cases} \tag{10}$$

The SAMP algorithm, which is an improvement on the orthogonal matching pursuit (OMP) algorithm, is a greedy algorithm. This algorithm avoids taking the number of non-zero elements in x as a priori, and iterates an approximate solution to x within the allowable error range of λ and SDx (α is the upper limit of error).

A mathematical model for the GPSR algorithm can be described as

$$\begin{cases} x_{opt} = \arg\min\{||\lambda - SDx||_2 + \beta||x||_1\} \\ \qquad\qquad g_{opt} = Dx_{opt} \end{cases} \tag{11}$$

The convex optimization problem takes β as the penalty term, which measures the sparsity of x by using l_0-analysis, and approximates the real solution to x by minimizing the objective function.

The above algorithms solve x according to the sparse constraint of x itself, resulting in complex calculation. In D-CS-ECT, x can be solved without the sparse constraint, and two reasonable reasons are given:

(1) In (9), A^{D-CS} has the sparse property for reconstructed images (the sparse property comes from D), which can replace the sparse constraint.

(2) The detection of two-phase flow in an industrial process requires a noiseless binary image, which makes the contact contour of the two mediums obvious and shows that the two-phase distribution is accurate. The few features of interest in the image reconstructed by ECT system work as an indirect factor that solving x is not constrained by sparsity.

According to the above analysis, three variations of the Landweber algorithm, the Tikhonov regularization algorithm, and the improved Newton–Raphson algorithm are used to achieve image reconstruction, which are called Non-Sparse-Landweber, Non-Sparse-Tikhonov, and Non-Sparse Newton-Raphson, and their derivation results are given below.

NS-Landweber:

$$\begin{aligned} &x_{(k+1)} = x_k - \theta (SD)^T (SDx_k - \lambda) \\ &x_{opt} = x_{(k+1)} \quad s.t\ \ x_{(k+1)} - x_k \leq e \\ &g_{opt} = Dx_{opt} \end{aligned} \tag{12}$$

NS-Tikhonov:

$$\begin{aligned} &x_{opt} = [(SD)^T SD + \mu I]^{-1} (SD)^T \lambda \\ &g_{opt} = Dx_{opt} \end{aligned} \tag{13}$$

NS-Newton-Raphson:

$$\begin{aligned} &x_{k+1} = x_k - [(SD)^T SD + \gamma I]^{-1} (SD)^T (SDx_k - \lambda) \\ &x_{opt} = x_{(k+1)} \quad s.t\ \ x_{(k+1)} - x_k \leq e \\ &g_{opt} = Dx_{opt} \end{aligned} \tag{14}$$

where (12) and (14) are iterative algorithms and (12) is a direct algorithm. θ in (12), μ in (13), and γ in (14) are tunable parameters. e in (12) and (14) is the error between adjacent iterations. The appearance of x_{opt} are that elements associated with the features of interest are retained prominently, while other elements associated with the features of non-interest are suppressed (close to zero). Fig. 3 shows the overall idea of the image reconstruction algorithm in D-CS-ECT.

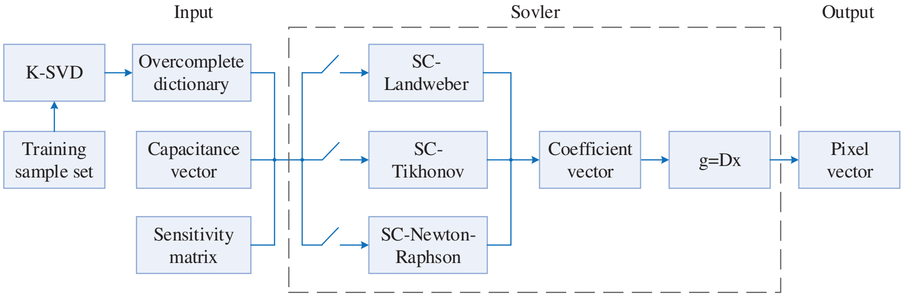

Figure 3: The process of image reconstruction algorithm in ECT

3 Dictionary Learning

Dictionary learning is the precondition of image reconstruction. It mainly includes the establishment of a training sample set and a learning algorithm. The training sample of this experiment is obtained by simulation in COMSOL5.4 software. The dictionary learning model has attracted much attention in the past few decades, and has been used in fields including image processing, signal restoration and pattern recognition. For the input audio feature, when it is represented by a set of over-complete basis, under the condition of satisfying a certain sparsity or reconstruction error, an approximate representation of the original audio segment can be obtained, that is, $Y \approx DX \cdot Y$ is the input Need to get the original frame feature parameters of the sparse representation, the dimension is the feature dimension multiply the number of samples D represents the sparse matrix, each column of it is called an “atom”, X is the obtained sparse representation coefficient of Y with respect to D, and the dimension is a dictionary number of atoms multiply number of samples. The optimization goal is to use as few atoms as possible to represent the signal in a given over-complete dictionary, and get the problem of sparse X. This problem can be described by the following formula:

$$\min_{D,X} \sum_{\mathrm{i}} ||\mathrm{X_i}||_0, s.t||Y - DX||_F^2 \le \varepsilon \tag{15}$$

We need to minimize the error after restoration and make X as sparse as possible to obtain a more concise representation of the signal and reduce the complexity of the model. Sparse dictionary learning includes two stages: one is the dictionary construction stage; the other is the use of the constructed dictionary to represent the sample stage. As an effective tool for sparse representation of signals, dictionaries provide a more meaningful way to extract the essential features of signal hiding. Therefore, obtaining a suitable dictionary is the key to the success of the sparse representation algorithm. In this experiment, we choose to learn the dictionary method to initialize a 16×256-dimensional Discrete Cosine Transform over complete dictionary D, where 16 is the dimension of the features in the sample, and 256 is the number of dictionary atoms. Then use Orthogonal Matching Pursuit (OMP) algorithm for sparse representation of the original audio frame feature data to obtain the coefficient matrix X of the corresponding dictionary, and then use K-Singular Value Decomposition (K-Singular Value Decomposition) according to the coefficient matrix X obtained. Decomposition (K-SVD) algorithm updates the dictionary D column by column quickly [10], and also updates the coefficient matrix X, and calculates the reconstruction error; after K iterations or convergence to the specified error, the dictionary D and coefficients are completed joint optimization of matrix X.

The pixel distribution of the imaging area reflects the accuracy of the real situation inside the pipeline. The sampled number of pixels for the image should be determined before constructing the training sample set. Five different shaped objects are placed in the pipeline that reflect different flow patterns, as shown in Fig. 4a. The “circular” path method is used to form a 961 or 1681 pixel image, and the “square” path method is used to form a 561, 1281 or 5097 pixel image.These different pixel distributions respectively restore images, as shown in Figs. 4b–4f.

Selection of the image mainly depends on the restoration of the outline of the contact between the two mediums. In the “circular” path method, Objects B and D in the restored image are positive, but Objects A, C, and E are not. The “square” path method works for objects of any shape, but the quality of the image depends on the number of pixels. All objects are deformed in the 561-pixel image, and the restoration quality is poor. The 5097-pixel image better reflects the real situation inside the pipeline, but the high number of pixels leads to a time-consuming program for the K-SVD algorithm. The 1281-pixel distribution was selected to restore image because the degree of image restoration and the running speed of the K-SVD program is between Figs. 4d and 4f.

Training samples were created based on the three model examples shown in Fig. 5. Except for the cross-section radius R_1 inside the pipe, the parameters were set randomly. In Fig. 5a, $c_1(x_1, y_1)$ and $c_2(x_2, y_2)$ are the center coordinates of two bubbles, with R_2 and R_3 as their radii. In Fig. 5b, H_1 is the height of the arcs medium. In Fig. 5c, R_3, R_4, and L are the internal radius, external radius, and thickness of the annular medium.

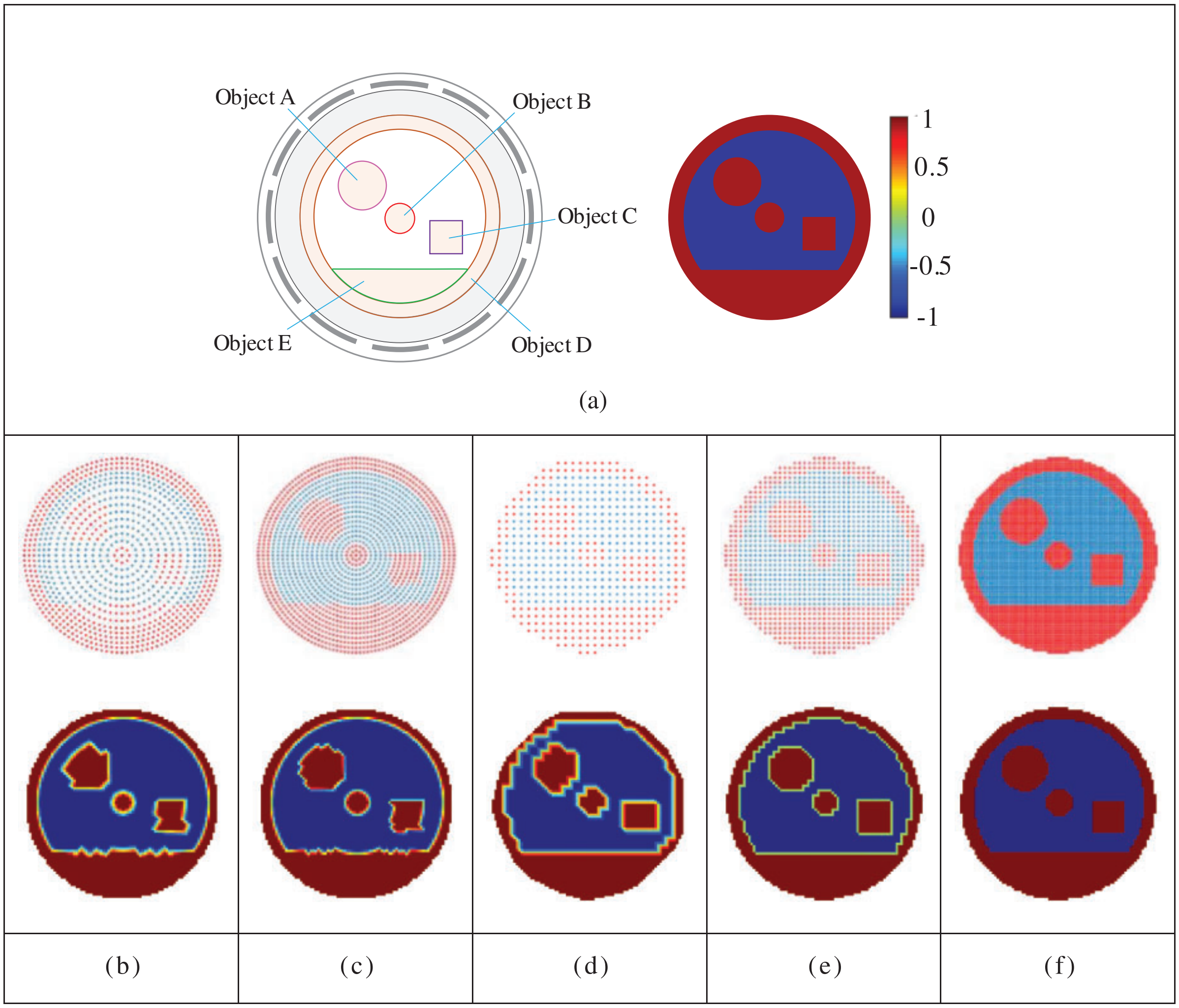

(a)

(b) (c) (d) (e) (f)

Figure 4: Image with different number of pixels. (a) A two-phase distribution which contains object A, B, C, D, E with the same permittivity; The best restored image for this two-phase distribution. (b) The image with 961 pixels. (c) The image with 1681 pixels. (d) The image with 561 pixels. (e) The image with 1281 pixels. (f) The image with 5097 pixels

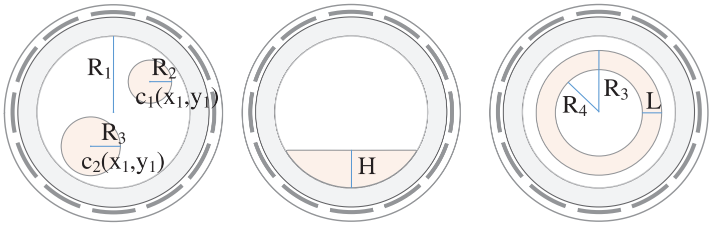

(a) (b) (c)

Figure 5: (a) A model for creating samples with two-bubble distribution, similar models can be used for single-bubble distribution, three-bubble distribution, etc. (b) A model for creating samples with stratified distribution. (c) A model for creating samples with annular distribution

Six types of training samples (a central bubble and an eccentric bubble are collectively called a single bubble) were obtained according to the flow pattern. The distribution for single bubbles, two bubbles, three bubbles, and four bubbles each had 1000 images. 850 images showed stratified distribution, and 863 images showed annular distribution. The training sample set consisted of 5,713 binary images of the internal section of the cylindrical pipe, and some training samples are shown in Fig. 6.

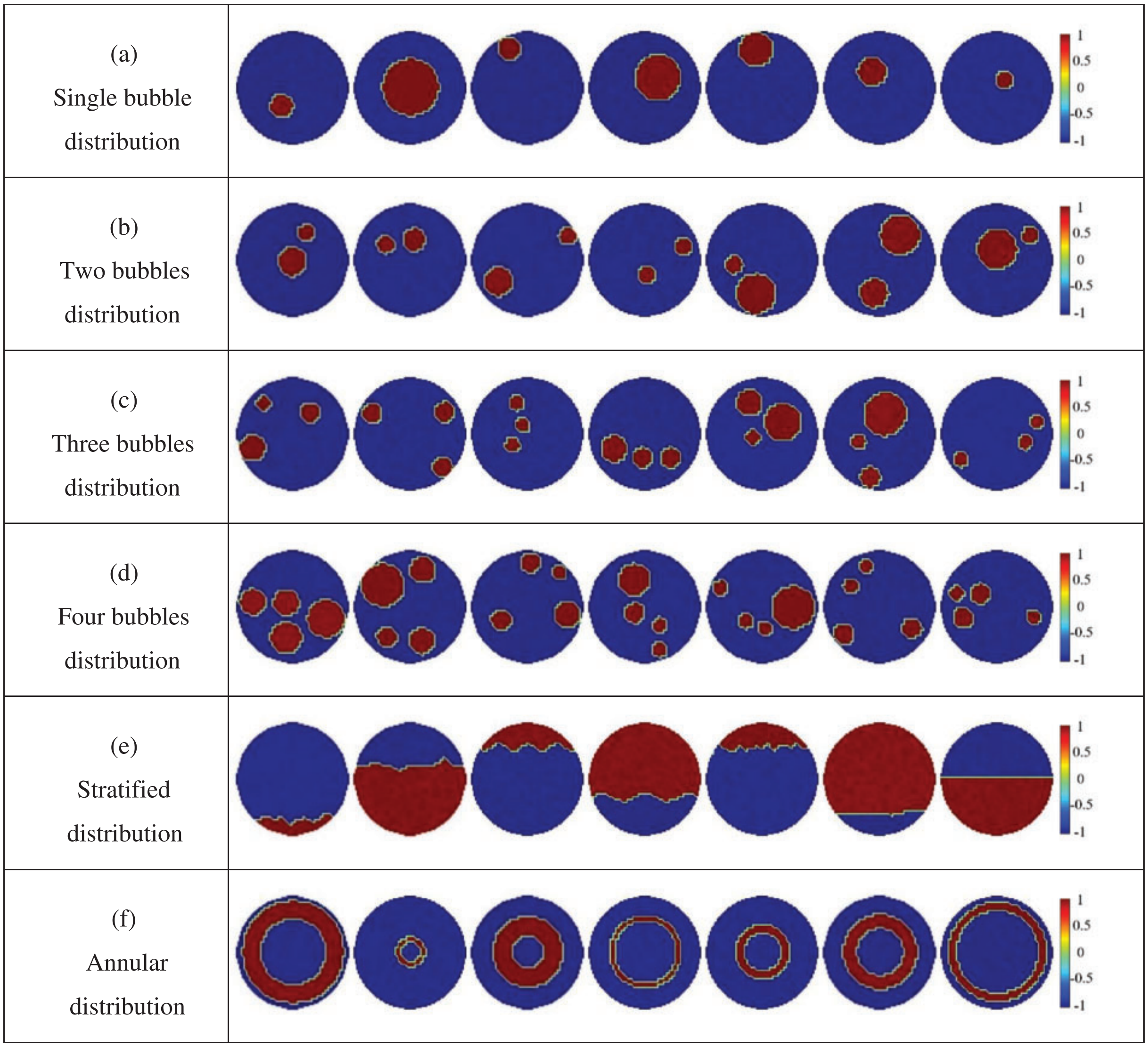

Figure 6: Part of the training sample set

The training samples for the six different distributions were denoted as $G_1, G_2, G_3, G_4, G_5, G_6$, and the total training sample set was $G = [G_1, G_2, G_3, G_4, G_5, G_6]$. All samples were randomly sorted and added with slight noise in order to maintain natural conditions and increase the generalization of the overcomplete dictionary. G can be rewritten as $G = [g_1, g_2, g_3, \ldots, g_N]$.

The mathematical model of dictionary learning in D-CS-ECT is as follows:

$$\begin{cases} G = DX \\ G = [g_1, g_2, g_3, \ldots, g_N],\ X = [x_1, x_2, x_3, \ldots, x_N] \end{cases} \tag{16}$$

where $g_i \in R^{n*1}$ is the pixel vector, and $x_i \in R^{p*1}$ is the sparse coefficient column vector corresponding to g_i. $G \in R^{n*N}$ is the training sample set, and each of its columns represents an image. $X \in R^{p*N}$ is a matrix representing the set of sparse coefficients.

In 2006, Aharon et al. [38] proposed the K-SVD algorithm for dictionary learning. The K-SVD algorithm is a greedy algorithm that realizes signal approximation by alternately optimizing the dictionary and the sparse coefficients. In this paper, the K-SVD algorithm is used to learn the overcomplete dictionary, and its objective function is

$$\min ||G - DX||_F^2 \quad s.t\ ||x_i||_0 \le K \tag{17}$$

where x_i is a column vector in X and also the *K-sparse* sparse coefficient.

There are two stages used by the K-SVD algorithm in training the overcomplete dictionary, which are sparse coding and dictionary updating. In the sparse coding stage, in order to obtain the sparse matrix, the sparse coefficient vector corresponding to each sample is calculated [38–40]. In the dictionary updating stage, atoms in the overcomplete dictionary are updated according to the non-zero elements of the sparse matrix.

The pseudocode for the K-SVD algorithm is as follows:

```
Input: $G$, $\alpha$
Initialization: $D_0 = [g_1, g_2, \ldots, g_p]$;
for  $t = 1, 2, \ldots T$
    for  $u = 1, 2, \ldots p$
        SAMP: $X^{(t)} = \arg\min \|X^{(t)}\|_0 \quad s.t||G^{(t)} - D^{(t)}X^{(t)}|| \le \alpha$;
        $\boldsymbol{I} = \{On\ the\ u-th\ row\ of\ X,\ index\ columns\ where\ all\ non\text{-}zero\ elements\ are\}$;
        Clear the $u-th$ row of $X_I^{(u)}$;
        $E^{(u)} = G_I^{(t)} - D^{(t)}X_I^{(u)}$;
        $[U^{(u)}, \Delta^{(u)}, V^{(u)}] = SVD(E^{(u)})$;
        $X_I^{(u+1)} = \Delta_{(1,1)}^{(u)} \cdot (V_{1_{col}}^{(u)})^T$;
        $D_u^{(t)} = U_{1_{col}}^{(u)}$;
    end
end
Output: $D^{(T)}$, $X^{(T)}$
```

The above pseudocode can be explained by the following four steps:

(1) The training dataset $G(G \in R^{n\times N})$ is normalized, and the error parameter for the SAMP algorithm and the number of iterations are set to α and T, respectively.

(2) The number of atoms in the overcomplete dictionary $D(D \in R^{n\times p})$ is p and p column vectors are randomly selected from G to form the initial overcomplete dictionary, which is denoted as D_0.
(3) Sparse coding for G is achieved by using the SAMP algorithm to solve $X^{(t)}(X \in R^{p\times N})$.
(4) The dictionary is updated column by column after the sparse matrix is obtained. When updating an atom $D_u^{(t)}$, the error $E^{(u)}$ between $G_I^{(t)}$ and atoms other than $D_u^{(t)}$ is calculated, and is then decomposed with SVD to obtain $[U^{(u)}, \Delta^{(u)}, V^{(u)}]$. $D_u^{(t)}$ is updated by the first column in $U^{(u)}$, and $X_I^{(u)}$ by the product of $\Delta^{(u)}_{(1,1)}$ and $(V^{(u)}_{1_{col}})^T$.

In this study, the training sample set was large, so the time consumed in the sparse coding stage was much greater than that consumed in the dictionary update stage. Sparse coding was performed by the SAMP algorithm, which is fast in calculating the sparse coefficient vector of a single image and slow in calculating the training sample set. To solve this problem, a parallel computing method was adopted. Considering the computing power and running memory of the computer, the training sample set was evenly divided, and input to the SAMP algorithm was done in batches and in parallel. Sparse coefficient vectors were calculated simultaneously using the CPU and GPU to accelerate the iterations of the K-SVD algorithm.

4 Simulation and Evaluation

COMSOL Multiphysics® software was used to build the simulation model, and image reconstruction was realized in the MATLAB® environment. The experimental platform was a computer with an Intel® Core™ i7–6800k CPU @3.40 GHz, and an NVIDIA GeForce GTX 1080 Ti graphics card.

The measurement target was the two-phase flow in the pipeline, as shown in Fig. 7. R_1 and R_2 are the radius of the internal cross section and the thickness of the pipeline, respectively, L is the width of the electrode, θ_1 is the angle of the electrode attached to the outer wall, and θ_2 is the angle between the two adjacent electrodes. ε_1 and ε_2 are the relative permittivity values of the two mediums.

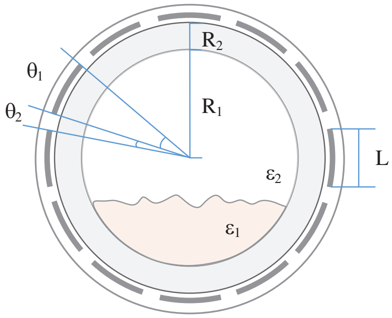

Figure 7: Parameters of the pipeline model with COMSOL Multiphysics®. $R_1 = 40$ mm, $R_2 = 5$ mm, L = 15 mm, $\theta_1 = 22.5°$, $\theta_2 = 7.5°$, $\varepsilon_1 = 1$, $\varepsilon_2 = 10$

The 66 × 1 capacitance vector and the 66 × 1281 sensitivity matrix were obtained from the simulation model. When solving for the 1281 × 1 pixel vector, the capacitance vector and the sensitivity matrix must be normalized. The overcomplete dictionary whose atomic number was set to 3000 based on experience converges after ten iterations of training with the K-SVD algorithm. For a better imaging effect, the overcomplete dictionary after 30 iterations were selected. The image reconstruction algorithms were OMP, GPSR, NS-Landweber, NS-Tikhonov, and NS-Newton-Raphson, and their parameters are shown in Table 1.

Table 1: Parameters of algorithms for different distributions

	OMP	GPSR	NS-Landweber	NS-Tikhonov	NS-Newton-Raphson
Central bubble	$K = 25$	$\beta = 5.01{*}10^{-6}$	$\theta = 1.14{*}10^{-7}$	$\mu = 2.23{*}10^{2}$	$\gamma = 9.55{*}10^{2}$
Eccentric bubble	$K = 13$	$\beta = 7.41{*}10^{-6}$	$\theta = 8.05{*}10^{-7}$	$\mu = 1.12{*}10^{3}$	$\gamma = 8.42{*}10^{7}$
Two bubbles	$K = 18$	$\beta = 9.25{*}10^{-3}$	$\theta = 8.13{*}10^{-6}$	$\mu = 2.86{*}10^{2}$	$\gamma = 4.15{*}10^{6}$
Three bubbles	$K = 22$	$\beta = 4.93{*}10^{-2}$	$\theta = 3.27{*}10^{-7}$	$\mu = 4.47{*}10^{2}$	$\gamma = 1.08{*}10^{7}$
Stratified	$K = 2$	$\beta = 6.12{*}10^{-1}$	$\theta = 5.11{*}10^{-6}$	$\mu = 5.84{*}10^{3}$	$\gamma = 1.09{*}10^{8}$
Annular	$K = 6$	$\beta = 1.00{*}10^{-2}$	$\theta = 1.02{*}10^{-6}$	$\mu = 9.51{*}10^{1}$	$\gamma = 4.78{*}10^{6}$

In order to study the noise resistance of different algorithms, 40 dB of noise was added to the capacitance vector. The imaging results are shown in Fig. 8. For the images reconstructed by the OMP algorithm, almost all distributions show many image artifacts: the bubbles are blurry, and their outlines diverge in multi-bubble distributions. With the GPSR algorithm, the image with the stratified distribution is clear, but target bubbles are deformed in the three-bubble distribution. The central bubble distribution by the NS–Landweber algorithm and the annular distribution by the NS–Tikhonov algorithm are different from their real distribution. Images obtained by the NS–Newton–Raphson algorithm have slight artifacts and slightly deformed bubbles, which enough to reflect the real distribution of the two-phase flow. A reasonable explanation for the poor images is the interference of noise and the soft field, and an incomplete training sample set that cannot cover the majority of the distributions in the two-phase flow.

Image error (IE) and a correlation coefficient (CC) were used to evaluate the quality of the reconstructed images. For ECT, the CC is given higher priority than the IE. IE and CC are given by

$$IE = \frac{||g' - g||}{||g||} \times 100\% \tag{18}$$

$$CC = \frac{\sum_{i=1}^{p} (g_i - \overline{g})(g_i' - \overline{g'})}{\sqrt{\sum_{i=1}^{p} (g_i - \overline{g})^2 \sum_{i=1}^{p} (g_i' - \overline{g'})^2}} \tag{19}$$

where g is the normalized pixel vector of the real image and g′ is the normalized pixel vector of the reconstructed image. $\bar{g}$ and $\bar{g}'$ are the average values of g and g′. The maximum value of CC is 1. A small IE and large CC indicate that the quality of image reconstruction is good. The results for IE and CC are shown in Tables 2 and 3.

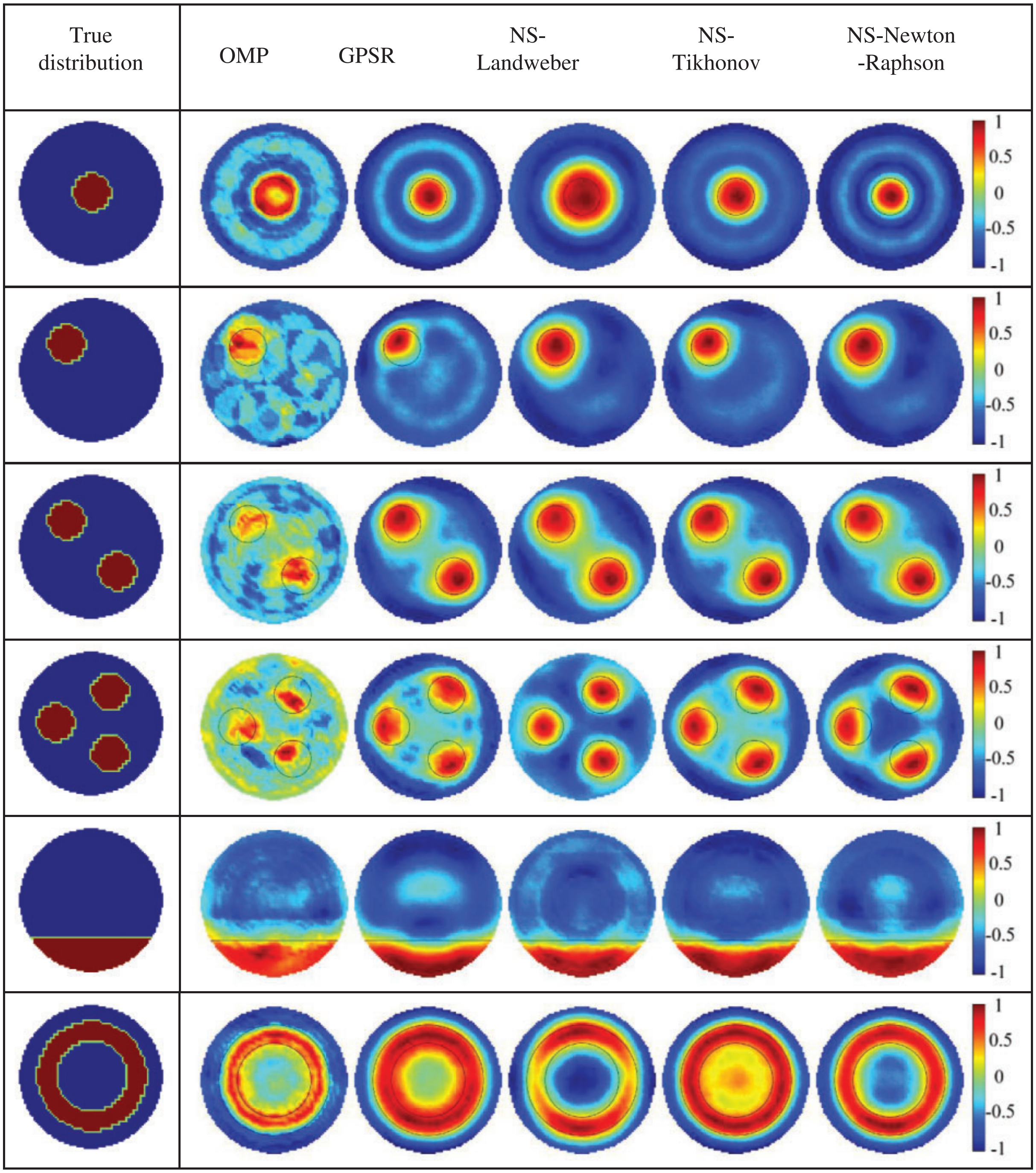

Figure 8: Reconstruction results based on simulation data of noise of SNR = 40 dB

IE is smallest and CC is largest on the whole for the stratified distribution, indicating that ECT is sensitive for imaging of stratified distribution. For most single-bubble distributions, the contrast between the single-bubble and the background is obvious. As the number of bubbles in multi-bubble distributions increases, the larger IE and the smaller CC are, the worse the imaging quality is. Sensitivity is non-linear in the imaging area, and the location and size of the bubbles are highly random, which increases the difficulty of imaging multi-bubble distributions. It is difficult to reconstruct an image for annular distribution because its IE and CC are the worst of all distributions, but the NS–Newton–Raphson algorithm that IE and CC have no obvious defects can be selected.

Table 2: Image error (IE) of reconstructed images

	OMP	GPSR	NS-Landweber	NS-Tikhonov	NS-Newton-Raphson
Center bubble	57.5931	41.4506	58.7963	40.7606	43.3536
Eccentric bubble	64.6041	47.329	44.8629	41.8379	34.6281
Two bubbles	73.8069	58.5772	63.5528	57.5421	59.7735
Three bubbles	91.0715	62.7431	59.2693	62.5968	63.0554
Stratified	53.9199	45.7729	47.0209	39.6289	47.3087
Annular	67.7863	73.5442	62.0886	75.2278	57.0617

Table 3: Correlation coefficient (CC) of reconstructed images

	OMP	GPSR	NS-Landweber	NS-Tikhonov	NS-Newton-Raphson
Center bubble	0.87988	0.90277	0.83647	0.927	0.89319
Eccentric bubble	0.8524	0.92237	0.89062	0.92095	0.91154
Two bubbles	0.82934	0.86045	0.83665	0.86518	0.8556
Three bubbles	0.64996	0.87236	0.92549	0.87906	0.84343
Stratified	0.93447	0.95555	0.98557	0.96981	0.95551
Annular	0.82293	0.85193	0.90564	0.85206	0.93776

In order to evaluate the reconstruction quality and stability of the five algorithms more intuitively, the mean and variance of IE and CC are given.

As shown in Fig. 9, The left picture in Fig. 9 is the average error value. The higher the value, the worse the imaging effect, the lower the value, the better the effect; the right picture is the average correlation coefficient value, the lower the coefficient, the worse the image quality, the higher the coefficient, the higher the image quality. The OMP algorithm has the highest mean for IE and the lowest mean of CC, indicating that the quality of the reconstructed images by the OMP algorithm is low. The mean values for the other four algorithms are similar, and the quality is better than that of the OMP. As shown in Fig. 10, The variance of each method, the larger the variance, the worse the imaging algorithm, the two large variances for the OMP algorithm reflect its poor stability. For the GPSR, NS–Landweber, and NS–Tikhonov algorithms, all the variances are relatively large because of the error between the three distributions (the three bubbles by GPSR, the center bubble by NS–Landweber, and the annular by NS–Tikhonov) and their true distributions are shown in Fig. 8. For the NS–Newton–Raphson algorithm, the variance of CC is small, and the algorithm is stable and not easily disturbed by noise.

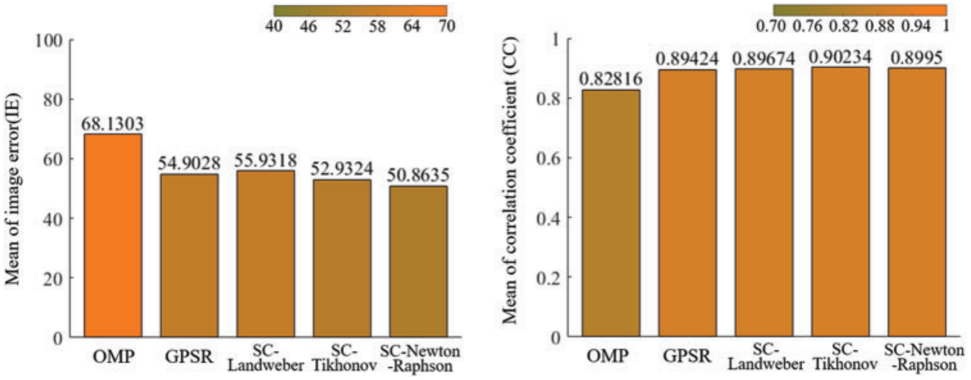

Figure 9: Mean of image error (IE) and correlation coefficient (CC) using different algorithms

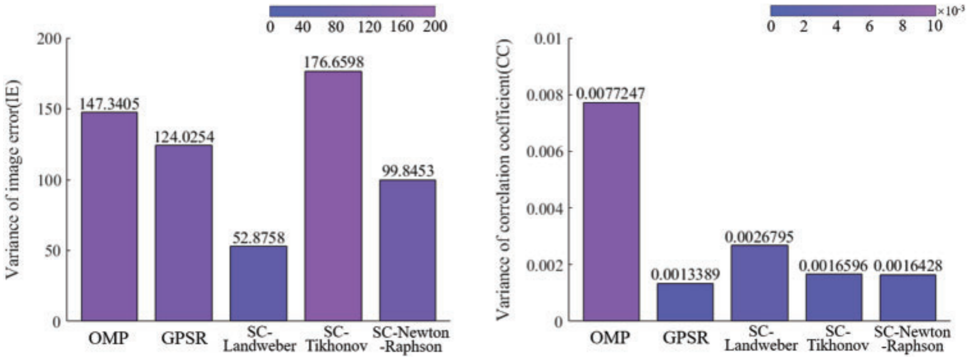

Figure 10: Variance of image error (IE) and correlation coefficient (CC) using different algorithms

5 Conclusion

In this paper, an image reconstruction method based on D-CS-ECT was discussed. Sparse representation of image signal was obtained by training an overcomplete dictionary with K-SVD, and the nonlinear relationship between observation capacitance and the approximate sparse coefficient was solved under the constraint of no sparsity. The two-phase flow in the pipeline was simulated in a noisy environment. Images were reconstructed by the NS–Landweber, NS–Tikhonov, and NS–Newton–Raphson algorithms and compared with the OMP and GPSR algorithms, which are classical sparse constraint algorithms. The NS–Landweber and NS–Tikhonov algorithms were able to reconstruct images clearly on the whole, but unstable reconstructions of the central bubble distribution and annular distribution indicated that the two-phase flow in the central region was not easy to image. The NS–Newton–Raphson algorithm was superior to the other four algorithms in overall image quality and stability, and its highly correlated reconstructed images were closer to the real two-phase flow distribution.

Acknowledgement: I would like to acknowledge Professor, Xuebin Qin, for inspiring my interest in the development of innovative technologies.

Funding Statement: This research was supported by the National Natural Science Foundation of China (No. 51704229), Outstanding Youth Science Fund of Xi'an University of Science and Technology (No. 2018YQ2-01).

Conflicts of Interest: The authors declare that they have no conflicts of interest to report regarding the present study.

References

1. Sharifi, M., Young, B. (2013). Electrical resistance tomography (ERT) applications to chemical engineering. *Chemical Engineering Research & Design, 91(9),* 1625–1645. DOI 10.1016/j.cherd.2013.05.026.
2. Cheney, M., Newell, I. (2011). Electrical impedance tomography. *Current Opinion in Critical Care, 18(1),* 35–41. DOI 10.1109/79.962276.
3. Yu, Z. Z., Peyton, A. T. (1993). Imaging system based on electromagnetic tomography (EMT). *Electronics Letters, 29(7),* 625–626. DOI 10.1049/el:19930418.
4. Xie, C. G., Plaskowski, A. (1989). 8-electrode capacitance system for two-component flow identification. Part 1: Tomographic flow imaging. *IEE Proceedings A (Physical Science Measurement and Instrumentation Management and Education), 136(4),* 173–183. DOI 10.1049/ip-a-2.1989.0031.
5. Li, Y., Yang, W., Xie, C. G., Huang, S., Wu, Z. et al. (2011). Gas/oil/water flow measurement by electrical capacitance tomography. *Measurement Science & Technology, 24(7),* 074001. DOI 10.1088/0957-0233/24/7/074001.
6. Gut, Z., Wolanski, P. (2010). Flame imaging using 3D electrical capacitance tomography. *Combustion Science and Technology, 182(10–12),* 1580–1585. DOI 10.1080/00102202.2010.497420.
7. Zhang, W., Cheng, Y., Wang, C., Yang, W., Wang, C. H. (2013). Investigation on hydrodynamics of triple-bed combined circulating fluidized bed using electrostatic sensor and electrical capacitance tomography. *Industrial & Engineering Chemistry Research, 52(32),* 11198–11207. DOI 10.1021/ie4009138.
8. Qiang, G., Meng, S., Wang, D., Zhao, Y., Liu, Z. (2017). Investigation of gas–solid bubbling fluidized beds using ect with a modified tikhonov regularization technique. *Aiche Journal, 64(1),* 29–41. DOI 10.1002/aic.15879.
9. Zheng, Q., Yang, M., Yang, J., Zhang, Q., Zhang, X. (2018). Improvement of generalization ability of deep cnn via implicit regularization in two-stage training process. *IEEE Access, 6,* 15844–15869. DOI 10.1109/ACCESS.2018.2810849.
10. Zheng, Q., Tian, X., Jiang, N., Yang, M. (2019). Layer-wise learning based stochastic gradient descent method for the optimization of deep convolutional neural network. *Journal of Intelligent and Fuzzy Systems, 37(3),* 1–14. DOI 10.3233/JIFS-190861.
11. Jang, J. D., Lee, S. H., Kim, K. Y., Choi, B. Y. (2006). Modified iterative landweber method in electrical capacitance tomography. *Measurement Science & Technology, 17(7),* 1909. DOI 10.1088/0957-0233/17/7/032.
12. Long, X., Mao, M., Lu, C., Li, R., Jia, F. (2021). Modeling of heterogeneous materials at high strain rates with machine learning algorithms trained by finite element simulations. *Journal of Micromechanics and Molecular Physics, 6(1),* 2150001. DOI 10.1142/S2424913021500016.
13. Liu, F., Wang, Z., Wang, Z., Qin, Z., Li, Z. et al. (2021). Evaluating yield strength of ni-based superalloys via high throughput experiment and machine learning. *Journal of Micromechanics and Molecular Physics, 5(4),* 2050015. DOI 10.1142/S2424913020500150.
14. Saxena, S., Animesh, S., Fullwood, M., Mu, Y. (2020). OnionMHC: A deep learning model for peptide—HLA-A*02:01 binding predictions using both structure and sequence feature sets. DOI 10.21203/rs.3.rs-124695/v1.
15. Chen, Y., Li, H. Y., Xia, Z. J. (2018). Electrical capacitance tomography image reconstruction algorithm based on modified implicit formula landweber method. *Computer Engineering, 44(1),* 268–273.

16. Tian, W., Ramli, M. F., Yang, W., Sun, J. (2017). Investigation of relaxation factor in landweber iterative algorithm for electrical capacitance tomography. *IEEE International Conference on Imaging Systems and Techniques*. IEEE. DOI 10.1109/IST.2017.8261455.
17. Donoho, D. L. (2006). Compressed sensing. *IEEE Transactions on Information Theory, 52(4),* 1289–1306. DOI 10.1109/TIT.2006.871582.
18. Lustig, M., Donoho, D., Pauly, J. M. (2007). Sparse mri: The application of compressed sensing for rapid mr imaging. *Magnetic Resonance in Medicine, 58(6),* 1182–1195. DOI 10.1002/(ISSN)1522-2594.
19. Candès, E. J. (2008). The restricted isometry property and its implications for compressed sensing. *Comptes Rendus Mathematique, 346(9–10),* 589–592. DOI 10.1016/j.crma.2008.03.014.
20. Jafarpour, S., Molina, R., Katsaggelos, A. K. (2008). Model-based compressive sensing. *IEEE International Symposium on Information Theory Proceeding*. DOI 10.1109/isit.2011.6034169.
21. Babacan, S. D., Molina, R., Katsaggelos, A. K. (2010). Bayesian compressive sensing using Laplace priors. *IEEE Transactions on Image Processing, 19*(*1*), 53–63. DOI 10.1109/TIP.2009.2032894.
22. Wang, H., Fedchenia, I., Shishkin, S., Finn, A., Colket, M. (2012). Electrical capacitance tomography: A compressive sensing approach. *IEEE International Conference on Imaging Systems & Techniques*.
23. Wu, X., Huang, G., Wang, J., Xu, C. (2013). Image reconstruction method of electrical capacitance tomography based on compressed sensing principle. *Measurement Science & Technology, 24(7),* 75–85.
24. Xin. J, W. U., Huang, G. X., Wang, J. W. (2013). Application of compressed sensing to flow pattern identification of ECT. *Optics and Precision Engineering*. DOI 10.3788/OPE.20132104.1062.
25. Zhang, L. F., Liu, Z. L., Tian, P. (2017). Image reconstruction algorithm for electrical capacitance tomography based on compressed sensing. *Tien Tzu Hsueh Pao/Acta Electronica Sinica, 45(2),* 353–358. DOI 10.3969/j.issn.0372-2112.2017.02.013.
26. Almurib, H., Kumar, N., Lombardi, F. (2018). Approximate DCT image compression using inexact computing. *IEEE Transactions on Computers, 67*(*2*), 149–159. DOI 10.1109/TC.2017.2731770.
27. Liu, Z., Yin, H., Fang, B., Chai, Y. (2015). A novel fusion scheme for visible and infrared images based on compressive sensing. *Optics Communications, 335,* 168–177. DOI 10.1016/j.optcom.2014.07.093.
28. You, Z., Raich, R., Fern, X., Kim, J. (2018). Weakly-supervised dictionary learning. *IEEE Transactions on Signal Processing,* 2527–2541. DOI 10.1109/TSP.2018.2807422.
29. Dou, P., Wu, Y., Shah, S. K., Kakadiaris, I. A. (2018). Monocular 3D facial shape reconstruction from a single 2d image with coupled-dictionary learning and sparse coding. *Pattern Recognition, 81,* 515–527. DOI 10.1016/j.patcog.2018.03.002.
30. Carrera, D., Boracchi, G., Foi, A., Wohlberg, B. (2018). Sparse overcomplete denoising: Aggregation versus global optimization. *IEEE Signal Processing Letters, 24*(*10*), 1468–1472. DOI 10.1109/LSP.2017.2734119.
31. Meribout, M., Saiedmran, M. (2017). Real-time two-dimensional imaging of solid contaminants in gas pipelines using an electrical capacitance tomography system. *IEEE Transactions on Industrial Electronics, 64(5),* 3989–3996. DOI 10.1109/TIE.2017.2652367.
32. Zhang, L., Yin, W. (2018). Image reconstruction method along electrical field centre lines using a modified mixed normalization model for electrical capacitance tomography. *Flow Measurement & Instrumentation, 62,* 37–43. DOI 10.1016/j.flowmeasinst.2018.05.011.
33. Guo, Z., Shao, F., Lv, D. (2009). New calculation method of sensitivity distribution for ETC. *Yi Qi Yi Biao Xue Bao/Chinese Journal of Scientific Instrument, 30(10),* 2023–2026. DOI 10.3321/j.issn:0254-3087.2009.10.003.
34. Candes, E. J., Eldar, Y. C., Needell, D. (2010). Compressed sensing with coherent and redundant dictionaries. *Applied and Computational Harmonic Analysis. 31(1),* 59–73. DOI 10.1016/j.acha.2010.10.002.
35. Parker, P. A., Bliss, D., Tarokh, V. (2015). CISS 2008. *The 42nd Annual Conference on Information Sciences and Systems.* IEEE Conference Publication.
36. Thong, T. D., Gan, L., Nguyen, N., Tran, T. D. (2010). Sparsity adaptive matching pursuit algorithm for practical compressed sensing. *Conference on Signals, Systems & Computers*. IEEE.
37. Figueiredo, M., Nowak, R. D., Wright, S. J. (2008). Gradient projection for sparse reconstruction: Application to compressed sensing and other inverse problems. *IEEE Journal of Selected Topics in Signal Processing, 1(4),* 586–597. DOI 10.1109/JSTSP.2007.910281.

38. Aharon, M., Elad, M., Bruckstein, A. (2006). K-SVD: An algorithm for designing overcomplete dictionaries for sparse representation. *IEEE Transactions on Signal Processing*, *54(11)*, 4311–4322. DOI 10.1109/TSP.2006.881199.
39. Long, X., Mao, M., Lu, C., Li, R., Jia, F. (2021). Modeling of heterogeneous materials at high strain rates with machine learning algorithms trained by finite element simulations. *Journal of Micromechanics and Molecular Physics, 6(1)*. DOI 10.1142/S2424913021500016.
40. Long, X. Mao, M. H., Lu, C. H., Lu, T. X., Jia, F. R. (2021). Prediction of dynamic compressive performance of concrete-like materials subjected to SHPB based on artificial neural network. *Journal of Nanjing University of Aeronautics & Astronautics, 53(5)*, 789–800. DOI 10.16356/j.1005-2615.2021.05.017.

Computer Modeling in
Engineering & Sciences

Tech Science Press

DOI: 10.32604/cmes.2022.019140

ARTICLE

A Novel Method for the Reconstruction of Road Profiles from Measured Vehicle Responses Based on the Kalman Filter Method

Jianghui Zhu[1,3], **Xiaotong Chang**[2], **Xueli Zhang**[2], **Yutai Su**[2] **and Xu Long**[2,*]

[1]School of Automation, Northwestern Polytechnical University, Xi'an, 710072, China

[2]School of Mechanics, Civil Engineering & Architecture, Northwestern Polytechnical University, Xi'an, 710072, China

[3]Chinese Flight Test Establishment, Xi'an, 710089, China

[*]Corresponding Author: Xu Long. Email: xulong@nwpu.edu.cn

Received: 05 September 2021 Accepted: 29 September 2021

ABSTRACT

The estimation of the disturbance input acting on a vehicle from its given responses is an inverse problem. To overcome some of the issues related to ill-posed inverse problems, this work proposes a method of reconstructing the road roughness based on the Kalman filter method. A half-car model that considers both the vehicle and equipment is established, and the joint input-state estimation method is used to identify the road profile. The capabilities of this methodology in the presence of noise are numerically demonstrated. Moreover, to reduce the influence of the driving speed on the estimation results, a method of choosing the calculation frequency is proposed. A road vibration test is conducted to benchmark the proposed method.

KEYWORDS

Road profile reconstruction; inverse problems; precise integration; Kalman filter; spatial resolution

1 Introduction

The road profile is considered an essential input that affects the vehicle dynamics; it may lead to the fatigue failure of the vehicle components or worsened riding comfort, especially for some special delivery vehicles. The understanding of vehicle responses is important for road quality evaluation, road roughness index calculation, vehicle dynamics analysis, suspension design, and control system development [1]. For technical and economic reasons, this information cannot be measured in standard vehicles, and must therefore be estimated using unique methods. The estimation of the excitation acting on a system from a given response is a typical inverse problem, which is usually ill-posed.

To ensure the normal usage, measurement, and maintenance of the road, a number of profilometers have been developed. Longitudinal profile analyzer (LPA) profilometers are tools and methods used to generate numerical sequences related to real road profiles [2,3]. However, the major drawback of these profilers is that they are not economical enough for application in common vehicles. There also exist some profile measurement methods based on visual inspections [4], but these are extremely expensive and may be impossible to apply in rainy weather. Some scholars have used neural networks to establish correlations between the vehicle response and road roughness, but they were revealed to be too complicated and time-consuming [5–7]. To deal with these problems, a method of control constraints was proposed by Burger [8]; however, this method is more suitable for nonlinear and complex models. An algebraic estimator designed for the estimation of the road profile excitation was investigated by Haddar et al. [9], and was validated on a quarter model with two degrees of freedom (DOFs).

While some methods based on model-based sliding mode observers were proposed in recent studies [4,10], the researchers considered a complex model, which is time-consuming. The final reconstruction result heavily relies on the quality of the model. Because this is an inverse problem in mechanics, relevant methods in this field can be referenced. In recent years, some deterministic-stochastic methods have been developed; these methods consider noise as a random process and assume that noise is involved not only in measurements, but also in state variables. Gillijns et al. [11] developed a recursive filter that uses system outputs to estimate system inputs and states. An augmented Kalman filter was proposed by Lourens et al. [12] for force recognition in structural dynamics; this filter includes the unknown force in the state vector and estimates it in combination with the state. Maes et al. [13,14] proposed a joint input-state estimation algorithm that can be used to identify the forces applied to structures, and can extrapolate the measured data to the unmeasured response quantity of interest. In addition, because it is constructed in a spatial state, it is ideal for combining information from different sensors available in the vehicle. Fauriat et al. [15] used an algorithm based on Kalman filtering theory to estimate the profiles of a road covered by a given vehicle.

The objective of the present research was to design, test, and apply an estimation algorithm to predict road roughness information from the measured response of a heavy special vehicle based on a half-car model. The remainder of this paper is organized as follows. First, road profile identification is defined as a typical inverse problem in mathematical physics based on a half-vehicle model in state space. Second, a method based on the principle of the selected algorithm, namely a joint input-response estimation method, is proposed to solve inverse problems within the stochastic framework. Then, a structural model of a heavy special vehicle at different speeds is considered as an example to verify the effectiveness of the proposed algorithm. Finally, several conclusions are drawn, and directions for future work are proposed.

2 Dynamic Equations of the Vehicle

When transporting certain equipment, the middle line of the vehicle can be placed along its longitudinal symmetric surface, and the sway vibration is generally smaller; thus, the model shown in Fig. 1 can be reduced to a two-dimensional plane model.

There are six DOFs in the model, which respectively represent the movement of the suspension, body, and equipment, and the coordinate system is constructed on the moving vehicle. The tire is linked with the road displacement $u(t)$, which involves the tire's stiffness k_t. The tire damping is assumed to be negligible. The truck has a rear two-axle suspension, but for the convenience of calculation, the parameters at each axis are combined. Then, the following 6-DOF differential equations of motion can be obtained.

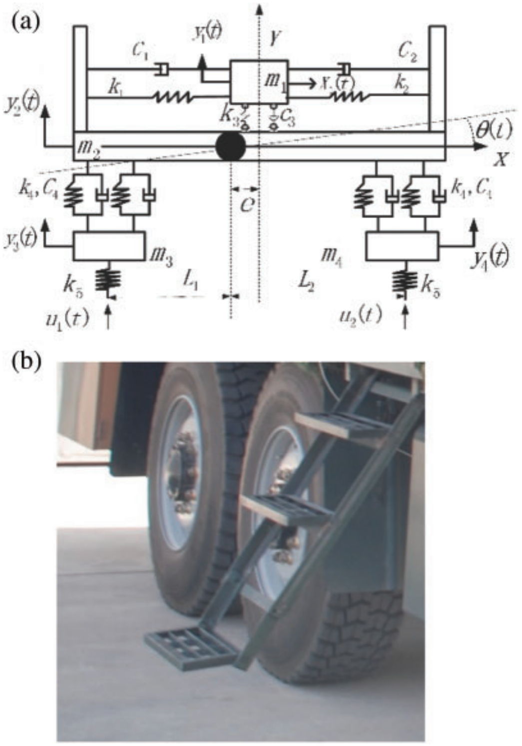

Figure 1: The equipment and transport vehicle model. (a) Vehicle model (b) Two-axle suspension

$$m_1\ddot{x}_1(t) + (c_1 + c_2)\dot{x}_1(t) + (k_1 + k_2)x_1(t) - \frac{(c_1L_1 + c_2L_2)}{2}\dot{\theta}^2(t) - \frac{(k_1L_1 + k_2L_2)}{2}\theta^2(t) = 0 \tag{1}$$

$$m_1\ddot{y}_1(t) + c_3\dot{y}_1(t) - c_3\dot{y}_2(t) - ec_3\dot{\theta}(t) + k_3y_1(t) - k_3y_2(t) - k_3e\theta(t) = 0 \tag{2}$$

$$\begin{aligned} &m_2\ddot{y}_2(t) - c_3\dot{y}_1(t) + (4c_4 + c_3)\dot{y}_2(t) - 2c_4\dot{y}_3(t) - 2c_4\dot{y}_4(t) + (ec_3 + 2c_4L_2 - 2c_4L_1)\dot{\theta}(t) - k_3y_1(t) + \\ &(k_3 + 4k_4)y_2(t) - 2k_4y_3(t) - 2k_4y_4(t) + (ek_3 - 2L_1k_4 + 2k_4L_2)\theta(t) = 0 \end{aligned} \tag{3}$$

$$m_3\ddot{y}_3(t) - 2c_4\dot{y}_2(t) + 2c_4\dot{y}_3(t) + 2c_4L_1\dot{\theta}(t) - 2k_4y_2(t) + (2k_4 + k_5)y_3(t) + 2k_4L_1\theta(t) = k_5u_1(t) \tag{4}$$

$$m_4\ddot{y}_4(t) - 2c_4\dot{y}_2(t) + 2c_4\dot{y}_4(t) - 2c_4L_2\dot{\theta}(t) - 2k_4y_2(t) + (2k_4 + k_5)y_4(t) - 2k_4L_2\theta(t) = k_5u_2(t) \tag{5}$$

$$\begin{aligned} &I\ddot{\theta}(t) - ec_3\dot{y}_1(t) + (2L_2c_4 + ec_3 - 2c_4L_1)\dot{y}_2(t) + 2c_4L_1\dot{y}_3(t) - 2c_4L_2\dot{y}_4(t) \\ &+ \left(2c_4L_1^2 + 2c_4L_2^2 + e^2c_3\right)\dot{\theta}(t) - ek_3y_1(t) + (ek_3 + 2k_4L_2 - 2k_4L_1)y_2(t) + 2k_4L_1y_3(t) \\ &-2k_4L_2y_4(t) + \left(2L_1^2k_4 + e^2k_3 + 2L_2^2k_4\right)\theta(t) = 0 \end{aligned} \tag{6}$$

Eqs. (1)–(6) constitute a 6-DOF nonlinear coupled dynamical differential equation system. Eq. (1) includes the nonlinear coupling terms $\theta^2(t)$ and $\dot{\theta}^2(t)$ in the body pitching angle θ. Because the length of the vehicle body was about 10 m, the pitch motion of the vehicle was much smaller than the vertical vibration of the body during the actual driving test; thus, the second-order traces $\theta^2(t)$ and $\dot{\theta}^2(t)$ can be ignored. Therefore, Eq. (1) is not coupled with Eqs. (2)–(6), so it can be solved separately. During the study of the vibration of vehicles and equipment, the solution and calculation of Eqs. (2)–(6) can be considered. The parameters and physical significance of the vehicle and equipment model are exhibited in Table 1.

Table 1: The model parameters

Parameter	Definition	Value	Unit
L_1	Distance from the center of gravity to the rear axle	3.19	m
L_2	Distance from the center of gravity to the front axle	6.19	m
e	Mass eccentricity	1.5	m
m_1	Weight of the equipment	1000	kg
m_2	Weight of the body	13000	kg
m_3,m_4	Weight of the tires	170	kg
I	Moment of inertia	124566	kg m^2
k_1,k_2	Horizontal stiffness	208000	N/m
k_3	Vertical stiffness	1000000	N/m
k_4	Suspension stiffness	2500000	N/m
k_5	Tire stiffness	1434000	N/m
c_1,c_2	Horizontal damping	142.88	N s/m
c_3	Vertical damping	0.79	N s/m
c_4	Suspension damping	0.0012	N s/m

Eqs. (2)–(6) can be written in matrix form as Eq. (7):

$$\mathbf{M}\ddot{\mathbf{Y}} + \mathbf{C}\dot{\mathbf{Y}} + \mathbf{K}\mathbf{Y} = \mathbf{S}_p\mathbf{F}\left(t\right), \tag{7}$$

where **M**, **C**, and **K** respectively denote the mass, damping, and stiffness matrices, and $\mathbf{S}_p$ denotes the input force influence matrix, each column of which provides the spatial distribution of the load time history in the corresponding element of the excitation vector $\mathbf{F}\left(t\right)$.

The following matrices are defined for the model:

$$\mathbf{M} = \begin{bmatrix} m_1 & 0 & 0 & 0 & 0 \\ 0 & m_2 & 0 & 0 & 0 \\ 0 & 0 & m_3 & 0 & 0 \\ 0 & 0 & 0 & m_4 & 0 \\ 0 & 0 & 0 & 0 & I \end{bmatrix},$$

$$\mathbf{C} = \begin{bmatrix} c_3 & -c_3 & 0 & 0 & -ec_3 \\ -c_3 & 4c_4 + c_3 & -2c_4 & -2c_4 & (ec_3 + 2c_4L_2 - 2c_4L_1) \\ 0 & -2c_4 & -2c_4 & 0 & 2L_1c_4 \\ 0 & -2c_4 & 0 & 2c_4 & -2L_2c_4 \\ -ec_3 & (ec_3 + 2c_4L_2 - 2c_4L_1) & 2L_1c_4 & -2L_2c_4 & \left(2c_4L_1^2 + 2c_4L_2^2 + e^2c_3\right) \end{bmatrix},$$

$$\mathbf{K} = \begin{bmatrix} k_3 & -k_3 & 0 & 0 & -ek_3 \\ -k_3 & (k_3 + 4k_4) & -2k_4 & -2k_4 & (ek_3 + 2L_2k_4 - 2L_1k_4) \\ 0 & -2k_4 & (2k_4 + k_5) & 0 & 2L_1k_4 \\ 0 & -2k_4 & 0 & (2k_4 + k_5) & -2L_2k_4 \\ -ek_3 & (ek_3 + 2L_2k_4 - 2L_1k_4) & 2L_1k_4 & -2L_2k_4 & \left(e^2k_3 + 2L_1^2k_4 + 2L_2^2k_4\right) \end{bmatrix},$$

$$\ddot{\mathbf{Y}} = \begin{Bmatrix} \ddot{y}_1 \\ \ddot{y}_2 \\ \ddot{y}_3 \\ \ddot{y}_4 \\ \ddot{\theta} \end{Bmatrix}; \quad \dot{\mathbf{Y}} = \begin{Bmatrix} \dot{y}_1 \\ \dot{y}_2 \\ \dot{y}_3 \\ \dot{y}_4 \\ \dot{\theta} \end{Bmatrix}; \quad \mathbf{Y} = \begin{Bmatrix} y_1 \\ y_2 \\ y_3 \\ y_4 \\ \theta \end{Bmatrix}, \ \mathbf{S}_p = \begin{bmatrix} 0 & 0 \\ 0 & 0 \\ 1 & 0 \\ 0 & 1 \\ 0 & 0 \end{bmatrix}, \text{ and } \mathbf{F} = \begin{bmatrix} k_5 u_1(t) \\ k_5 u_2(t) \end{bmatrix}$$

It is assumed that the front and rear wheels of the vehicle are driving in the same line; thus, the road excitations $u_1(t)$ and $u_2(t)$ are the same, but there is a time delay between them. The relationship between $u_1(t)$ and $u_2(t)$ in the time domain is given by the following equation:

$$u_1(t) = u_2(t - \Delta t), \quad \Delta t = \frac{L_1 + L_2}{v} \tag{8}$$

3 Mathematical Formulation

By introducing the state vector $\mathbf{X}(t) = \begin{bmatrix} \mathbf{Y}(t) \\ \dot{\mathbf{Y}}(t) \end{bmatrix}$, Eq. (7) can be written as

$$\dot{\mathbf{X}}(t) = \mathbf{AX}(t) + \mathbf{BF}(t), \tag{9}$$

where the system matrices $\mathbf{A}$ and $\mathbf{B}$ are defined as

$$\mathbf{A} = \begin{bmatrix} 0_{\mathrm{n\times n}} & \mathbf{I}_{\mathrm{n\times n}} \\ -\mathbf{M}^{-1}\mathrm{K} & -\mathbf{M}^{-1}\mathrm{C} \end{bmatrix}_{\mathrm{2n\times 2n}}, \quad \mathbf{B} = \begin{bmatrix} 0_{\mathrm{n\times n}} \\ \mathrm{M}^{-1}\mathrm{S}_{\mathrm{p}} \end{bmatrix}_{\mathrm{2n\times 1}}.$$

Consider the measurement data vector $\mathbf{Z}(t)$, which is expressed as a linear combination of the displacement, velocity, and acceleration vectors, as follows:

$$\mathbf{Z}(t) = \mathbf{S}_{\mathrm{a}}\ddot{\mathbf{Y}}(t) + \mathbf{S}_v\dot{\mathbf{Y}}(t) + \mathbf{S}_d\mathbf{Y}(t), \tag{10}$$

where $\mathbf{S}_{\mathrm{a}}$, $\mathbf{S}_v$, and $\mathbf{S}_d$ are selection matrices for acceleration, velocity, and displacement, respectively. Eq. (12) can be transformed into its state-space form:

$$\mathbf{Z}(t) = \mathbf{GX}(t) + \mathbf{JF}(t), \tag{11}$$

where the output influence matrix and direct transmission matrix are defined as

$$\mathbf{G} = \begin{bmatrix} \mathbf{S}_{\mathrm{d}} - \mathbf{S}_{\mathrm{a}}\mathbf{M}^{-1}\mathbf{K} & \mathbf{S}_{\mathrm{v}} - \mathbf{S}_{\mathrm{a}}\mathbf{M}^{-1}\mathbf{C} \end{bmatrix}, \ \mathbf{J} = \begin{bmatrix} \mathbf{S}_{\mathrm{a}}\mathbf{M}^{-1}\mathbf{S}_{\mathrm{p}} \end{bmatrix}.$$

The state-space model is derived starting from the classical discrete-time state equation with unknown noise vectors $\mathbf{w}_k$ and $\mathbf{v}_k$ which respectively represent the stochastic system and measurement noise.

$$\mathbf{X}_{k+1} = \mathbf{A}_c\mathbf{X}_k + \mathbf{B}_c\mathbf{F}_k + \mathbf{w}_k, \tag{12}$$

$$\mathbf{Z}_k = \mathbf{GX}_k + \mathbf{JF}_k + \mathbf{v}_k, \tag{13}$$

where $\mathbf{X}_k = \mathbf{X}(k\Delta t)$, $\mathbf{F}_k = \mathbf{F}(k\Delta t)$, $\mathbf{Z}_k = \mathbf{Z}(k\Delta t)$, $\mathrm{k} = 1, \ldots, \mathrm{N})$, $\mathbf{A}_c = \exp(\mathrm{A}\Delta \mathrm{t})$, and $\mathbf{B}_c = [\mathbf{A}_c - \mathbf{I}]\mathbf{A}^{-1}\mathbf{B}$. Moreover, and $\mathbf{w}_k$ and $\mathbf{v}_k$ are assumed to be mutually uncorrelated white noise signals with known covariance matrices $\mathbf{Q} = \mathbb{E}\left\{\mathbf{w}_k\mathbf{w}_l^T\right\} \geq 0$ and $\mathbf{R} = \mathbb{E}\left\{\mathbf{v}_k\mathbf{v}_l^T\right\} > 0$. To maintain the stability of the calculation, $\mathbf{A}_c$ can be solved by using the precise integration method [16].

A generic Kalman filter can be defined as a recursive linear state estimator designed to be optimal in a minimum-variance unbiased sense. A state estimate $\hat{\mathbf{X}}_{k|l}$ is defined as an estimate of $\mathbf{X}_k$ given $\{\mathbf{Z}_\mathrm{n}\}_{n=0}^{l}$ and its error covariance matrix $\mathbf{P}_{k|l}$ as $\mathbb{E}[(\mathbf{X}_k - \hat{\mathbf{X}}_{kl})(\mathbf{X}_k - \hat{\mathbf{X}}_{kl})^T]$.

In this context, the recursive prediction scheme can be applied to the measurement data $\mathbf{Z}_k$, from which the excitation is extracted. The initialized conditions $\hat{\mathbf{X}}_{0|-1}$ and $\tilde{\mathbf{F}}_{0|-1}$ are assumed to exist. The excitation and state estimates are then computed by following Steps (a) to (c).

(a) Input estimation

$$\widetilde{\mathbf{R}}_k = \mathbf{G}\mathbf{P}_{k|k-1}\mathbf{G}^T + \mathbf{R}$$

$$\mathbf{M}_k = \left(\mathbf{J}^T\widetilde{\mathbf{R}}_k^{-1}\mathbf{J}\right)^{-1}\mathbf{J}^T\widetilde{\mathbf{R}}_k^{-1}$$

$$\hat{\mathbf{F}}_{[k|k]} = \mathbf{M}_k\left(\mathbf{Z}_k - \mathbf{G}\hat{\mathbf{X}}_{[k|k-1]}\right)$$

$$\mathbf{P}_{\mathbf{F}[k|k]} = \left(\mathbf{J}^T\widetilde{\mathbf{R}}_k^{-1}\mathbf{J}\right)^{-1}$$

(b) Measurement update

$$\mathbf{L}_k = \mathbf{P}_{k|k-1}\mathbf{G}^T\widetilde{\mathbf{R}}_k^{-1}$$

$$\hat{\mathbf{X}}_{[k|k]} = \hat{\mathbf{X}}_{[k|k-1]} + \mathbf{L}_k\left(\mathbf{Z}_k - \mathbf{G}\hat{\mathbf{X}}_{[k|k-1]} - \mathbf{J}\hat{\mathbf{F}}_{[k|k]}\right)$$

$$\mathbf{P}_{k|k} = \mathbf{P}_{k|k-1} - \mathbf{L}_k\left(\widetilde{\mathbf{R}}_k - \mathbf{J}\mathbf{P}_{\mathbf{F}[k|k]}\mathbf{J}^T\right)\mathbf{L}_k^T$$

$$\mathbf{P}_{\mathbf{XF}[k|k]} = \mathbf{P}_{\mathbf{XF}[k|k]}^T = -\mathbf{L}_k\mathbf{J}\mathbf{P}_{\mathbf{F}[k|k]}$$

(c) Time update

$$\hat{\mathbf{X}}_{[k+1|k]} = \mathbf{A}_c\hat{\mathbf{X}}_{[k|k]} + \mathbf{B}_c\hat{\mathbf{F}}_{[k|k]}$$

$$\mathbf{P}_{k+1|k} = [\mathbf{A}_c\mathbf{B}_c]\begin{bmatrix}\mathbf{P}_{k|k} & \mathbf{P}_{\mathbf{XF}[k|k]}\\ \mathbf{P}_{\mathbf{XF}[k|k]} & \mathbf{P}_{\mathbf{F}[k|k]}\end{bmatrix}\begin{bmatrix}\mathbf{A}_c{}^T\\ \mathbf{B}_c{}^T\end{bmatrix} + \mathbf{Q}$$

In the present study, the state vector of the Kalman filter is $\mathrm{X} = [\dot{y}_1, \dot{y}_2, \dot{y}_3, \dot{y}_4, \dot{\theta}, y_1, y_2, y_3, y_4, \theta]^T$, and the measured vector is $\mathrm{Z} = [y_1, y_2, y_3, y_4, \theta]^T$. The model of the vehicle considered in this study is more complex than that which was considered in previous research [15], as the present model has more DOFs. This method is mainly used to estimate the input, but it can also be used to estimate the unmeasured response of the structure.

4 Simulation Results

In this section, the numerical results of the proposed estimator are presented. Two types of road profiles are considered, and the variation of the vehicle speed is taken into account to discuss the robustness of the estimators. Finally, the flowchart of the algorithm is provided.

4.1 Random Road Profile

A large amount of testing data indicates that road roughness is a stationary, Gaussian process with a zero mean and ergodic randomness, so a random input can reflect the actual road condition of the vehicle. Referring to the ISO8608 standard, the power spectral density (PSD) of pavement roughness can be fitted with the following formula:

$$G_q(n) = G_q(n_0)\left(\frac{n}{n_0}\right)^{-W}, \tag{14}$$

where n denotes the spatial frequency, which represents the number of cycles in which the wave is contained per meter, the unit of which is m^{-1}; $n_0 = 0.1\ \mathrm{m}^{-1}$ denotes the reference spatial frequency. Moreover, $G_q(n_0)$ denotes the PSD of the pavement roughness under the reference spatial frequency, which depends on the road level; it is also called the road roughness coefficient. $W = 2$ is the frequency index, which is the frequency of the oblique line in the double logarithmic coordinate; it determines the frequency structure of the roughness PSD. White noise can be used to simulate the road surface roughness, and its time-domain description is given by Eq. (15):

$$\dot{u}_r(t) = -2\pi n_1 v u_r(t) + 2\pi n_0\sqrt{G_q(n_0)\,v}\,\omega(t), \tag{15}$$

where $n_1 = 0.1\ \mathrm{m}^{-1}$ denotes the lower cut-off spatial frequency, $\omega(t)$ denotes zero-mean white noise, $u_r(t)$ denotes the vertical displacement excitation, and v denotes the speed of the transport vehicle. The road profile in the space domain is presented in Fig. 2 ($v = 10$ m/s).

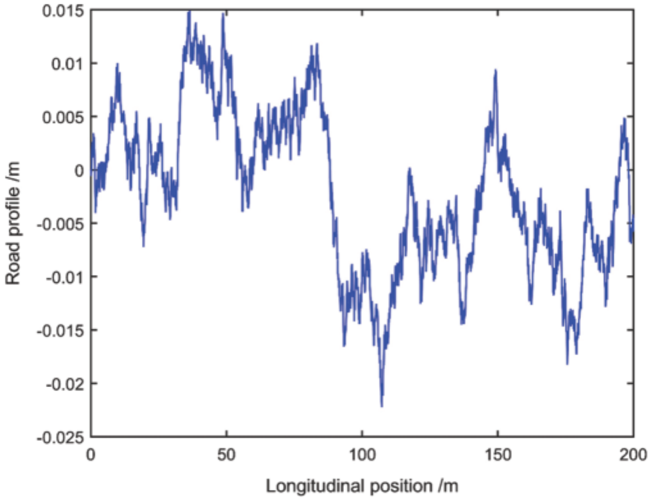

Figure 2: The road profile of ISO type E

The response of the vehicle was calculated in MATLAB by the precise Runge-Kutta integration method. The vertical acceleration responses of the vehicle body, front wheel, and rear wheel at $v = 10$ m/s are presented in Fig. 3, and the sampling frequency of the simulation was 200 Hz.

An important feature of the proposed method is the determination of its parameters, including the covariances and initial values. An empirical assessment of the magnitude of the parameters proposed in a previous study was adopted in the present work [15]. For a rough estimation of the parameters, the diagonal elements of the matrix Q were set as

[1e − 4 1e − 4 1e − 2 1e − 2 1e − 4 1e − 8 1e − 8 1e − 7 1e − 7 1e − 8], and the diagonal elements of the matrix R were set as [1e − 4 1e − 4 1e − 2 1e − 2 1e − 4]. The initial presumptions of the diagonal element of $P_{0|-1}$ were all set as 5×10^{-5}.

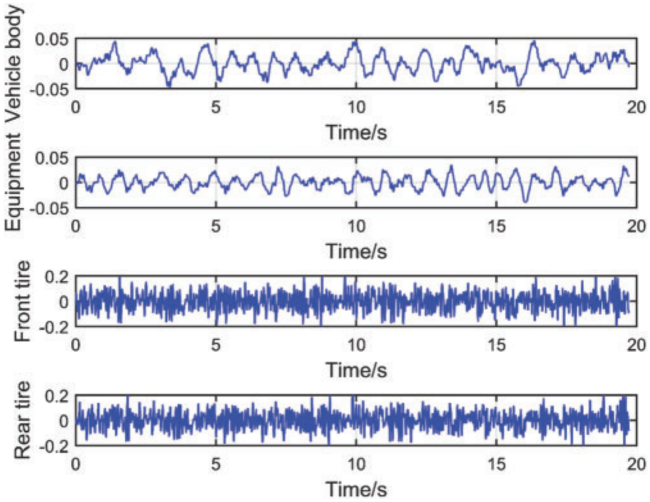

Figure 3: The responses of the vehicle

Once the parameters were determined, the proposed algorithm was used to estimate the road roughness, and the results are exhibited in Figs. 4 and 5. As can be seen from the figures, the road profile was identified comparatively accurately. It should be noted that the maximum standard spatial frequency was 10 m^{-1}. To recover the time-domain signal without distortion, the sampling frequency should not be less than twice the highest frequency in the analog signal spectrum. When analyzing the time-domain model, the maximum spatial frequency corresponding to the maximum time frequency was 10 m^{-1}, and only half of the maximum time frequency can be analyzed when analyzing the PSD of the signal (the corresponding spatial frequency was 5 m^{-1}).

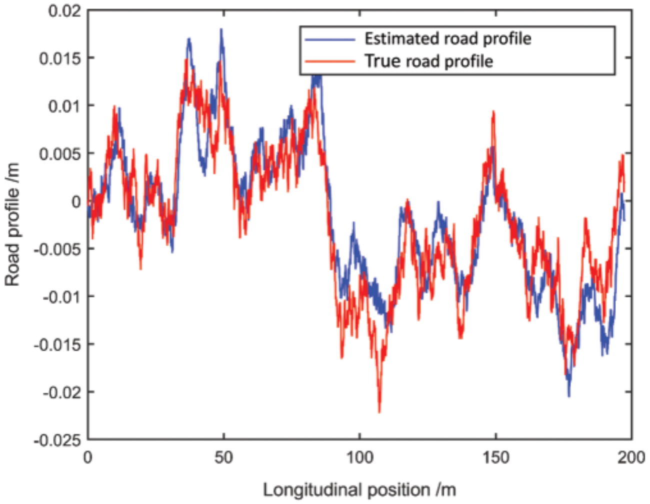

Figure 4: The comparison of the estimated and true road profiles

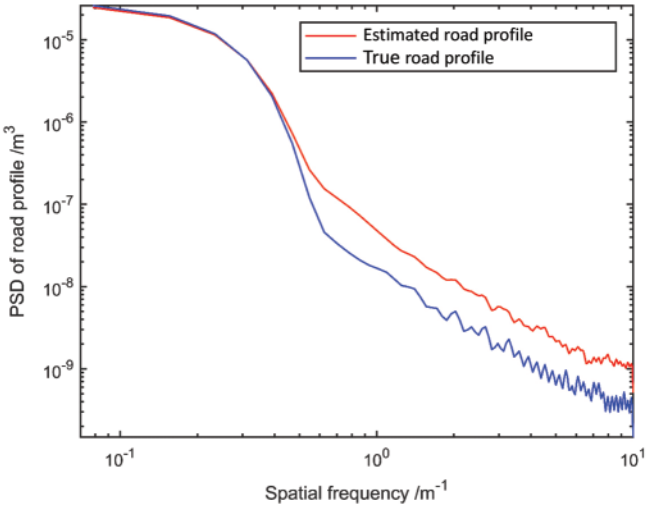

Figure 5: The comparison of the estimated and true road profiles in terms of the PSD

Because the model is random, the results of each run were different. Table 2 presents the root-mean-square errors (RMSEs) between the true road profile and the estimated results of five algorithm runs.

Table 2: The RMSEs of the true road profile and the estimated results (%)

	1st time	2nd time	3rd time	4th time	5th time	Average
RMSE	8.84	10.34	7.61	7.47	7.39	8.33

4.2 Uneven Road Surface

When a vehicle passes on an uneven road surface, the road will have an impact on the equipment and the vehicle system through the tires, which can seriously threaten the safety of the equipment.

Considering an uneven road surface, such as a ditch, the rectangular pulse function is used to simulate the pavement. Supposing that the car rises at time t_0, A denotes the height of the obstacle, and d denotes the length of the obstacle, the impact of the road surface is expressed as follows:

$$u_r(t) = \begin{cases} A & t_0 \le t \le t_0 + d/v \\ 0 & 0 < t < t_0, \mathrm{t} > \mathrm{t}_0 + \mathrm{d/v} \end{cases} \tag{16}$$

The road profile was estimated using the proposed method ($A = 0.2$ m, $d = 0.8$ m, $t_0 = 0.8$ s, $v = 10$ m/s), and the result is presented in Fig. 6. From the figure, it is evident that the wave peak was more accurate, but the null part was partially disturbed. The estimation over a discrete obstacle was also considered, and the result is exhibited in Fig. 7. It can be seen that the results may be improved if the parameters are set more reasonably.

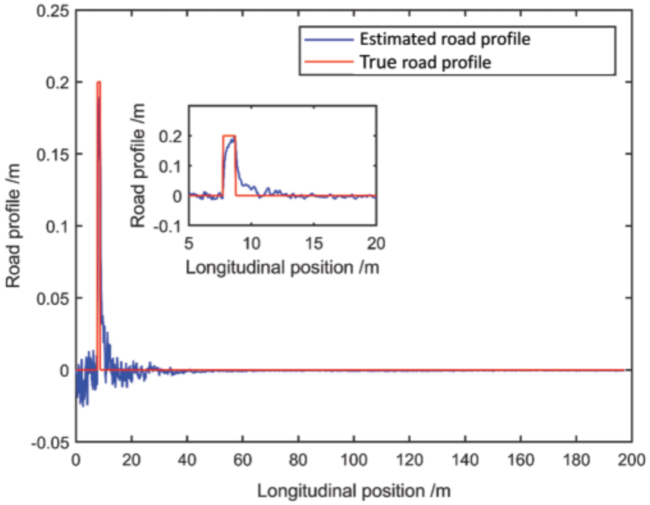

Figure 6: The estimated and true road profiles (impact)

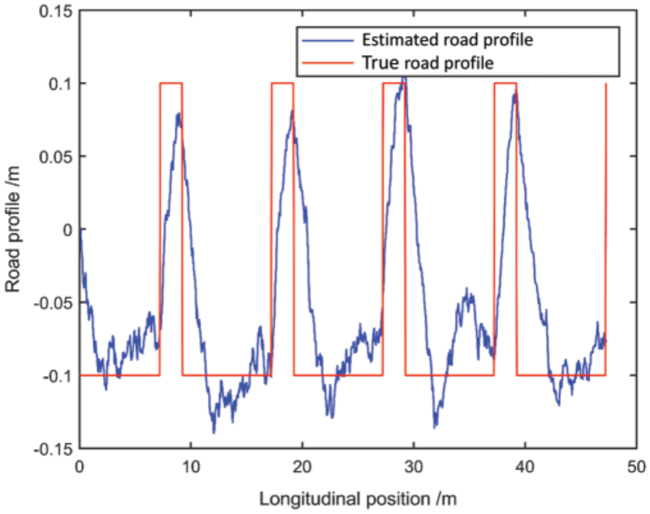

Figure 7: Estimation in the presence of discrete obstacles

4.3 The Influence of the Vehicle Speed

It was pointed out in a previous study [15] that depending on the speed of the vehicle, a portion of the spatial frequency content of the road profile may be underestimated, and the estimation results of a vehicle at high speeds and low speeds are quite different.

However, via many numerical experiments, it was found that when keeping the other parameters unchanged, the calculation frequency of the Kalman filter can be adjusted appropriately, and similar estimated results can be obtained at different speeds. The approach is to keep the total computation time of the filter algorithm similar, i.e., to keep the spatial resolution constant. In this study, the sampling frequency was set to $1/20v$ (to ensure the maximum spatial frequency of the pavement spectrum), and the calculation time was set to L/v. For example, when the speed was set to 10 m/s, the frequency was set to 200 Hz; when the speed was set to 20 m/s, the frequency was set to 400 Hz (the total distance remained the same). The sampling frequency of the sensor is invariable in practical applications; thus, the resampling frequency of the algorithm must be changed according to the speed. Figs. 8 and 9 present the road profiles estimated at different speeds.

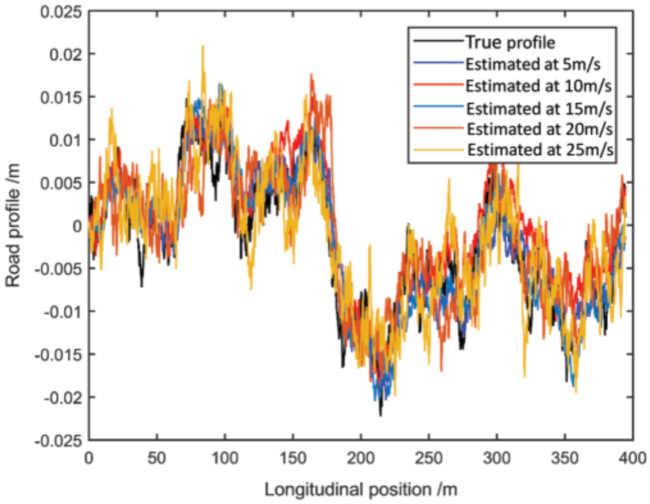

Figure 8: The road profiles estimated at different speeds

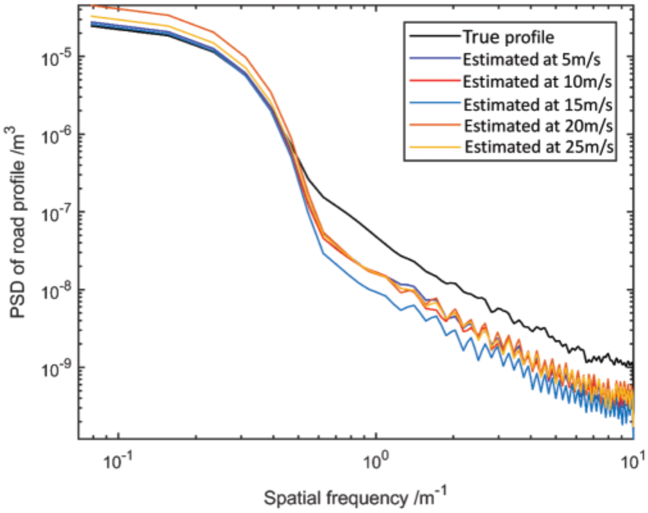

Figure 9: The road profiles estimated at different speeds in terms of the PSD

After adjusting the speed algorithm, the proposed method can be summarized as a self-explanatory flowchart, as presented in Fig. 10.

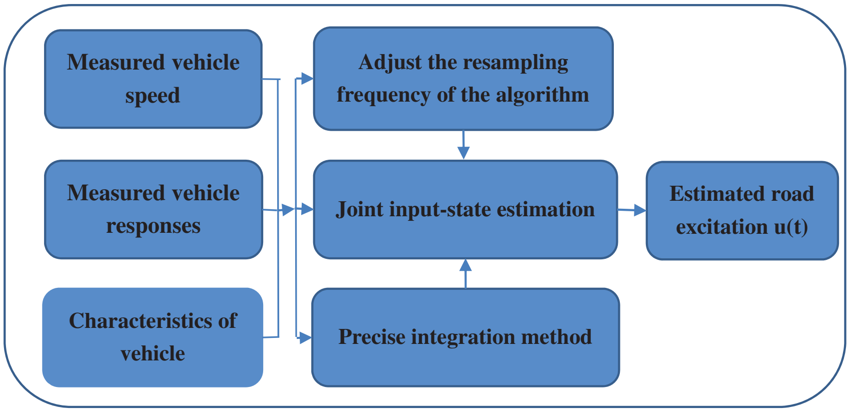

Figure 10: The flowchart of the proposed method

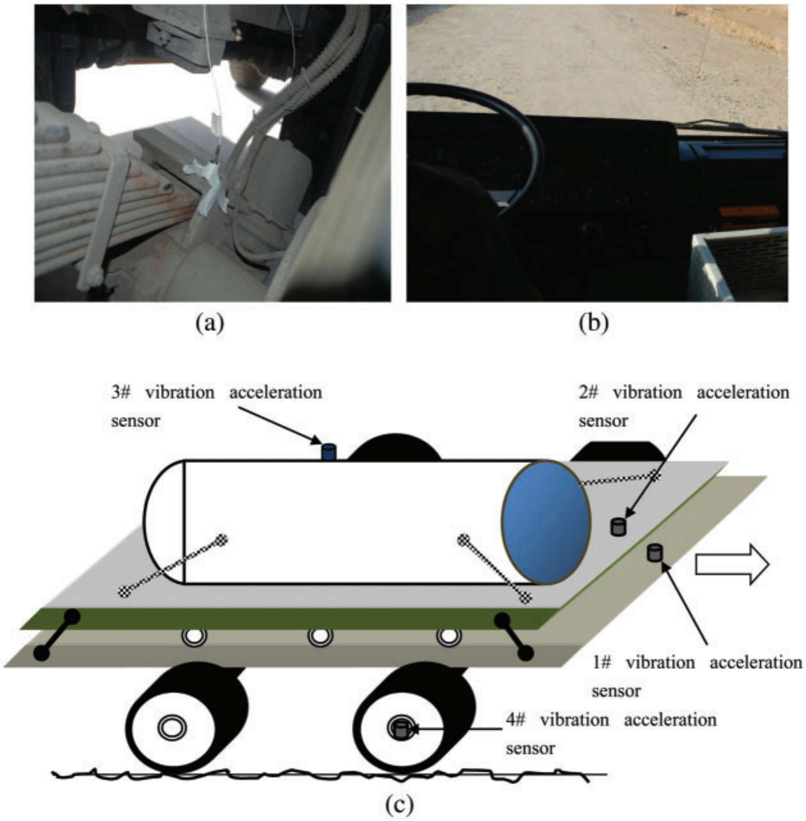

Figure 11: The schematic diagram and photos of the vehicle driving vibration test. (a) Acceleration sensor (b) Test site (c) Sensor installation diagram

5 Experimental Study and Numerical Benchmark via Road Testing

A real vibration measurement test was carried out on a road with known parameters and various actual road conditions at different speeds. The results not only have important practical reference value, but can also provide an important benchmark for theoretical research.

To clearly present the test state, Fig. 11 illustrates the schematic diagram of the structure of the test vehicle and the sensor installation. There was a sliding support plate between the carrier and the carriage. A DHDAS dynamic signal acquisition and analysis system was used to record the vertical acceleration at four locations, as obtained by PCB 393B04 uniaxial accelerometers (with a measurement range of ±49 m/s^2).

Two cases were considered, namely those at the speeds of 13.89 m/s (Case 1) and 9.72 m/s (Case 2). The sampling frequency was 5000 Hz, and each sampling period was 1 min. Because it was difficult to maintain a stable speed, only the time periods in which the speed was relatively stable were used for calculation. The acceleration responses of the four sensors in the two cases are respectively exhibited in Figs. 12 and 13.

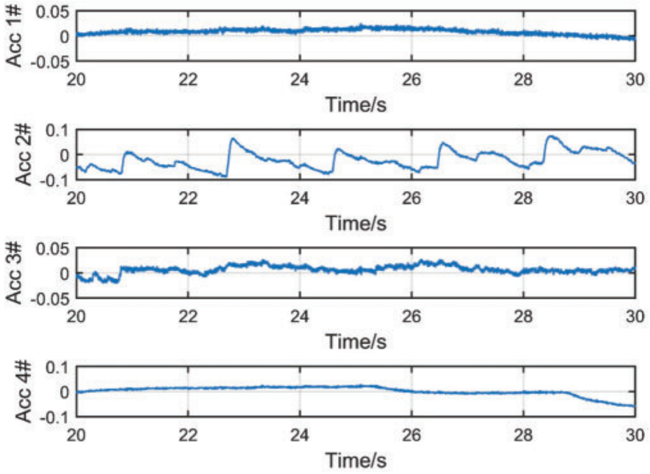

Figure 12: The acceleration responses of the vehicle in Case 1 (unit: m/s^2)

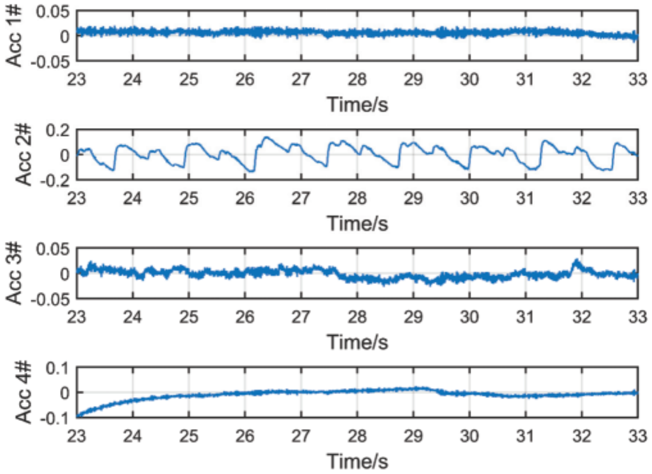

Figure 13: The acceleration response of the vehicle in Case 2 (unit: m/s^2)

The proposed method was then used to identify the pavement. It should be noted that the test data contained high levels of noise, which was filtered by the singular spectrum analysis (SSA) method proposed by Hossein et al. [17]. Figs. 14–17 present the estimation results of the two cases, and the RMSEs were 15.99% and 21.17%, respectively.

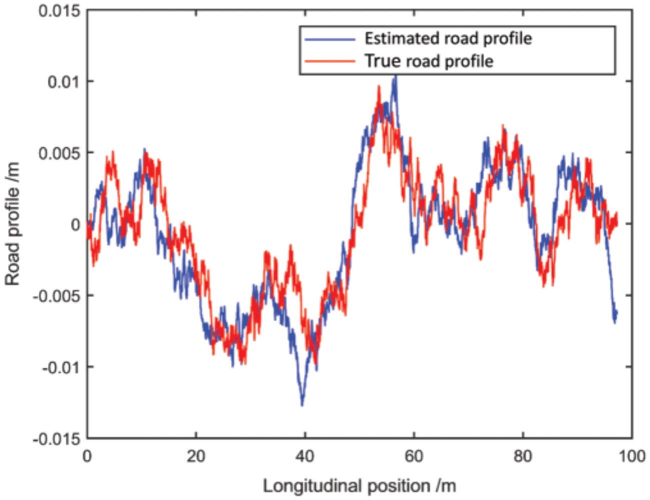

Figure 14: The estimated and true road profiles (Case 1)

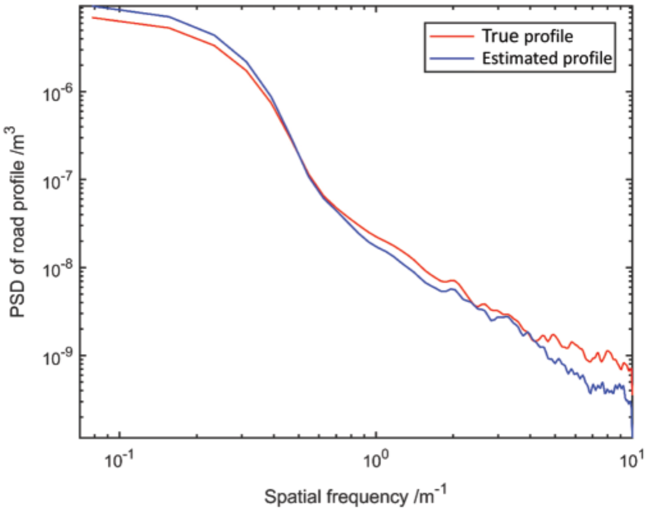

Figure 15: The estimated and true road profiles in terms of the PSD (Case 1)

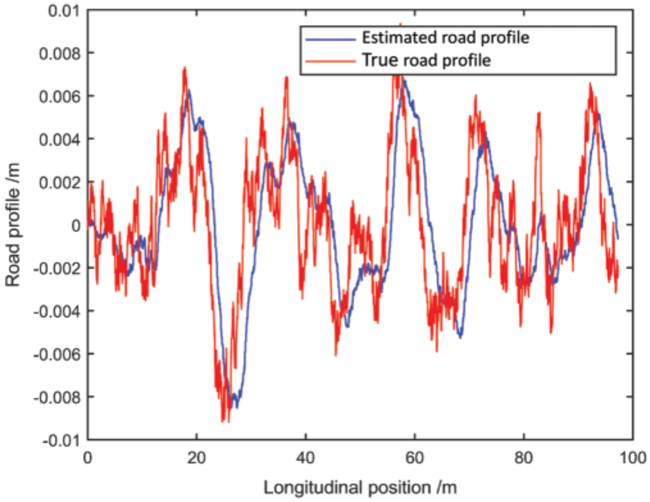

Figure 16: The estimated and true road profiles (Case 2)

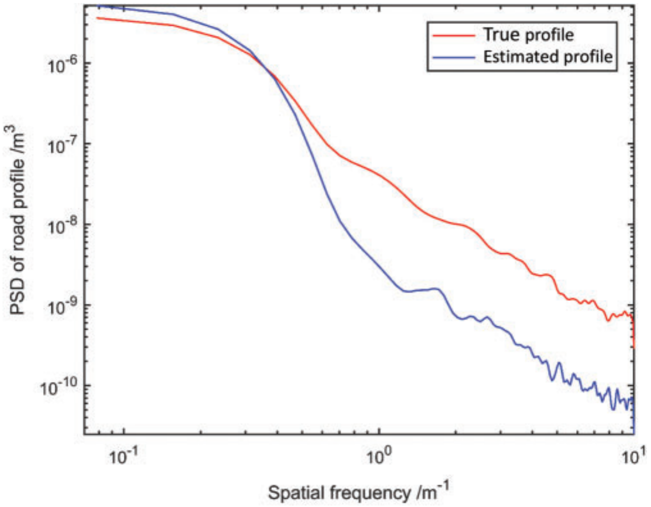

Figure 17: The estimated and true road profiles in terms of the PSD (Case 2)

6 Conclusions

In this paper, a road profile estimation method based on the joint-input method was proposed. The obtained estimates may be used to predict load variability and calculate the vehicle responses, especially in the early stages of vehicle design. Moreover, to reduce the influence of the driving speed on the estimation results, a method of choosing the calculation frequency was proposed. To improve the stability of the algorithm, the precise integration method is used to calculate the algorithm parameters. The simulation results reveal that the RMSE of road roughness recognition was less than 10%, and the maximum error of discrete obstacle recognition was less than 15%. The effectiveness of the proposed method was also verified by experimental data.

In the future, the adaptive algorithm will be used to estimate corresponding parameters. The proposed method will also be applied in different driving situations (e.g., cornering, steering, accelerating, braking). It will also be applied to a nonlinear model, particularly a coupled car and road model.

Funding Statement: This work was supported by the Natural Science Foundation of Shaanxi Province (Grant No. 2021KW-25), the Astronautics Supporting Technology Foundation of China (Grant No. 2019-HT-XG), and the Fundamental Research Funds for the Central Universities (Grant No. 3102018ZY015).

Conflicts of Interest: The authors declare that they have no conflicts of interest to report regarding the present study.

References

1. Poussot-Vassal, C., Sename, O., Dugard, L. (2008). Attitude and handling improvements based on optimal skyhook and feedforward strategy with semi-active suspensions. *International Journal of Vehicle Autonomous Systems, Special Issue on Modeling and Simulation of Complex Mechatronic Systems, 6(3–4),* 308–329. DOI 10.1504/IJVAS.2008.023589.
2. Piasco, J. M., Legeay, V. (1997). Estimation de l'uni longitudinal deschaussees par filtrage du signal del'analyseur de profil en long. *Traitement du Signal, 14(4),* 359–372. DOI hdl.handle.net/2042/2007.
3. Imine, H., Delanne, Y., M'sirdi, N. K. (2005). Road profile inputs for evaluation of the loads on the wheels. *Vehicle System Dynamics, 43(sup1),* 359–369. DOI 10.1080/00423110500108945.
4. Kim, H. J., Yang, H. S., Park, Y. P. (2010). Improving the vehicle performance with active suspension using road-sensing algorithm. *Computers and Structures, 80(18–19),* 1569–1577. DOI 10.1016/S0045-7949(02)00110-4.
5. Yousefzadeh, M., Azadi, S., Soltani, A. (2010). Road profile estimation using neural network algorithm. *Journal of Mechanical Science and Technology, 24(3),* 743–754. DOI 10.1007/s12206-010-0113-1.
6. Solhmirzaei, A., Azadi, S., Kazemi, R. (2012). Road profile estimation using wavelet neural network and 7-DOF vehicle dynamic systems. *Journal of Mechanical Science and Technology, 26(10),* 3029–3036. DOI 10.1007/s12206-012-0812-x.
7. Ngwangwa, H. M., Heyns, P. S., Labuschagne, F. J. J., Kululanga, G. K. (2010). Reconstruction of road defects and road roughness classification using vehicle responses with artificial neural networks simulation. *Journal of Terramechanics, 47(2),* 97–111. DOI 10.1016/j.jterra.2009.08.007.
8. Burger, M. (2013). Calculating road input data for vehicle simulation. *Multibody System Dynamics, 31(1),* 93–110. DOI 10.1007/s11044-013-9380-9.
9. Haddar, M., Baslamisli, S. C., Chaari, R., Chaari, F., Haddar, M. (2019). Road profile identification with an algebraic estimator. *Journal of Mechanical Engineering Science, 233(4),* 1139–1155. DOI 10.1177/0954406218767470.
10. Imine, H., Delanne, Y., M'sirdi, N. (2006). Road profile input estimation in vehicle dynamics simulation. *Vehicle System Dynamics, 44(4),* 285–303. DOI 10.1080/00423110500333840.
11. Gillijns, S., de Moor, B. (2007). Unbiased minimum-variance input and state estimation for linear discrete-time systems with direct feedthrough. *Automatica, 43(5),* 934–937. DOI 10.1016/j.automatica.2006.11.016.
12. Lourens, E., Reynders, E., de Roeck, G., Degrande, G., Lombaert, G. (2012). An augmented Kalman filter for force identification in structural dynamics. *Mechanical Systems and Signal Processing, 27(3),* 446–460. DOI 10.1016/j.ymssp.2011.09.025.
13. Maes, K., Smyth, A. W., de Roeck, G., Lombaert, G. (2016). Joint input-state estimation in structural dynamics. *Mechanical Systems and Signal Processing, 70–71,* 445–466. DOI 10.1016/j.ymssp.2015.07.025.
14. Lourens, E., Papadimitriou, C., Gillijns, S., Reynders, E., de Roeck, G. et al. (2012). Joint input-response estimation for structural systems based on reduced-order models and vibration data from a limited number of sensors. *Mechanical Systems and Signal Processing, 29(4),* 310–327. DOI 10.1016/j.ymssp.2012.01.011.

15. Fauriat, W., Mattrand, C., Gayton, N., Beakou, A., Cembrzynski, T. (2016). Estimation of road profile variability from measured vehicle responses. *Vehicle System Dynamics, 54(5),* 585–605. DOI 10.1080/00423114.2016.1145243.
16. Zhang, S., Deng, Z., Li, W. (2007). A precise Runge-Kutta integration and its application for solving nonlinear dynamical systems. *Applied Mathematics and Computation, 184(2),* 496–502. DOI 10.1016/j.amc.2006.06.054.
17. Hassani, H., Soofi, A. S., Zhigljavsky, A. A. (2010). Predicting daily exchange rate with singular spectrum analysis. *Nonlinear Analysis: Real World Applications, 11(3),* 2023–2034. DOI 10.1016/j.nonrwa.2009.05.008.

Computer Modeling in
Engineering & Sciences

Tech Science Press

DOI: 10.32604/cmes.2022.018965

ARTICLE

Visualization Detection of Solid–Liquid Two-Phase Flow in Filling Pipeline by Electrical Capacitance Tomography Technology

Ningbo Jing[1], **Mingqiao Li**[1], **Lang Liu**[2,*], **Yutong Shen**[1], **Peijiao Yang**[1] **and Xuebin Qin**[1]

[1]College of Electrical and Control Engineering, Xi'an University of Science and Technology, Xi'an, 710054, China

[2]College of Energy Engineering, Xi'an University of Science and Technology, Xi'an, 710054, China

[*]Corresponding Author: Lang Liu. Email: liulang@xust.edu.cn

Received: 26 August 2021 Accepted: 15 October 2021

ABSTRACT

During mine filling, the caking in the pipeline and the waste rock in the filling slurry may cause serious safety accidents such as pipe blocking or explosion. Therefore, the visualization of the inner mine filling of the solid–liquid two-phase flow in the pipeline is important. This paper proposes a method based on capacitance tomography for the visualization of the solid–liquid distribution on the section of a filling pipe. A feedback network is used for electrical capacitance tomography reconstruction. This reconstruction method uses radial basis function neural network fitting to determine the relationship between the capacitance vector and medium distribution error. In the reconstruction process, the error in the linear back projection is removed; thus, the reconstruction problem becomes an accurate linear problem. The simulation results show that the reconstruction accuracy of this algorithm is better than that of many traditional algorithms; furthermore, the reconstructed image artifacts are fewer, and the phase distribution boundary is clearer. This method can help determine the location and size of the caking and waste rock in the cross section of the pipeline more accurately and has great application prospects in the visualization of filling pipelines in mines.

KEYWORDS

Electrical capacitance tomography; mine backfilling; visualization detection; image reconstruction; radial basis function neural network

1 Introduction

In the process of mining, cemented tailing filling technology is often adopted to reduce environmental pollution and solve problems such as surface subsidence [1]. The slurry of the mine filling body is a solid–liquid two-phase flow that contains tailings, waste rock, cementing material, water, and other components, which flows in a complex manner in the filling pipeline [2]. During transportation, owing to pressure change, pipe distribution position, and other factors, problems such as internal deposition, scaling, and blockage of pipelines can easily occur, which can affect the safety of the filling pipeline and the mine filling process. To avoid the blockage of the filling pipeline and reduce the detection cost, the visual detection of the pipeline has attracted increasing attention [3]. Liu et al. [4] proposed the use of electrical resistance tomography technology to detect the filling pipeline, but there was no considerable imaging effect. Electrical capacitance tomography (ECT) technology can help visualize the phase distribution in a pipeline cross-section and obtain reliable and intuitive results for pipeline detection.

ECT, a nondestructive testing method, is an effective means to monitor multiphase flow. As the permittivity of the medium in the measured pipeline may vary, ECT can calculate the permittivity distribution from the measured capacitance through the reconstruction algorithm, which can reflect the corresponding phase distribution [5]. Based on the different computing principles of reconstruction, reconstruction algorithms can be classified as non-iterative and iterative algorithms. Linear back projection (LBP) [6] and Tikhonov regularization [7] are examples of non-iterative algorithms, whereas the Newton-Raphson algorithm [8] and the algebraic reconstruction technique (ART) [9] are iterative algorithms. Non-iterative algorithms are fast but have poor accuracy. Although iterative algorithms have high accuracy, their effect is still not ideal. Owing to the soft field effect of the reconstruction problem, there is a nonlinear relationship between the measured capacitance and the distribution of the dielectric constant. However, all of the above algorithms are linear reconstruction algorithms, which perform calculations based on the linear relationship. Therefore, linearization errors are introduced in the reconstruction, which results in a decrease in accuracy [10–12]. In recent years, many researchers have applied the fitting and prediction capabilities of neural networks to reconstruction algorithms. Li et al. [13] proposed a reconstruction algorithm based on a radial basis function neural network (RBFNN). The reconstruction speed is high, the effect is satisfactory, and it has a certain practical value. Tian et al. [14] established an image reconstruction framework using the radial basis function and the sparsity of the phase distribution. Zhu et al. [15] developed a deep convolutional neural network and adopted a mixed training strategy to map the capacitance to the permittivity distribution. Zheng et al. [16] developed a self-encoder neural network using a fully connected network to solve the image reconstruction problem of ECT. Yang et al. [17] further optimized the reconstructed image based on the U-Net framework. Wang et al. [18] inputted the results of Landweber iterative reconstruction into a two-channel convolutional neural network, which improved the feature extraction capability of the network and the reconstruction effect of the image details.

In this study, an ECT reconstruction feedback network based on an RBFNN was established, and the center selection of the RBFNN was realized using the orthogonal least squares (OLS) algorithm. There are major errors in the calculation results of linear reconstruction algorithms. Using a feedback reconstruction network, the errors were removed, and accurate imaging results were obtained.

In Section 2, the system model and mathematical principle of capacitance tomography are introduced. Section 3 describes the proposed ECT feedback network reconstruction method, the RBFNN, and the training dataset. In Section 4, the corresponding experiments and results are presented. Section 5 presents a summary and prospects for future research.

2 Principle

In this study, an ECT system was investigated and verified through simulation experiments. The ECT system is illustrated in Fig. 1. This system consists of a 12-electrode ECT sensor, a capacitance measurement circuit, and an upper computer (PC).

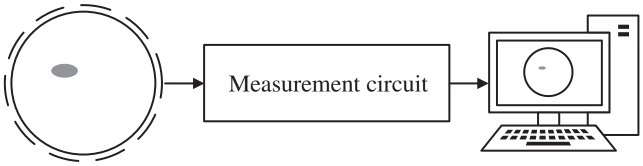

Figure 1: ECT system

The 12-electrode ECT system was studied, and there were 66 independent measured capacitance values. Fig. 1 shows the ECT sensor. In the two-dimensional ECT model shown in Fig. 2, 12 electrodes are distributed on the outside of the pipe and close to the pipe wall; furthermore, a shield is used to reduce interference from the outside of the system, and there are two different media in the pipe under test.

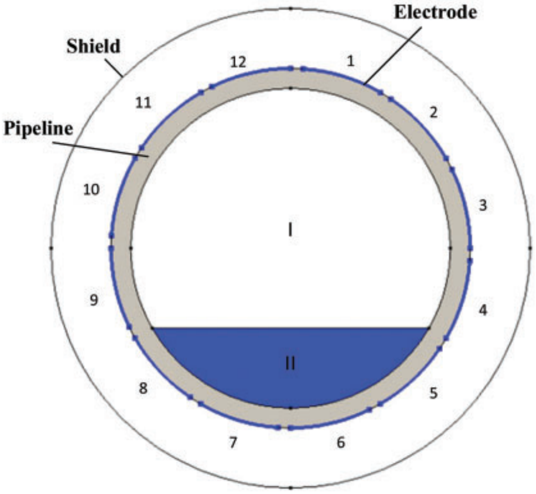

Figure 2: ECT sensor model

In the capacitance tomography system, there is a nonlinear relationship between the capacitance C between the plates and the dielectric constant ε:

$$C = -\frac{1}{V}\iint_{\Gamma} \varepsilon(x, y)\nabla\phi(x, y)d\Gamma \tag{1}$$

where V is the potential difference between the corresponding plates, $\varepsilon(x, y)$ is the measurement region, $\phi(x, y)$ is the dielectric constant at the corresponding position within the measurement region, and $\phi(x, y)$ is the potential at the corresponding position. Eq. (1) can be expressed by a sensitivity-based linear model [19] as follows:

$$\lambda = Sg \tag{2}$$

where λ represents the normalized capacitance vector, S is the sensitivity matrix, and g is the normalized dielectric constant matrix. S represents the sensitivity of the capacitance vector to the permittivity distribution. The changing trend of the dielectric constant vector can be reflected by the pixel distribution; that is, g can also be represented as a pixel vector.

Because the number of pixels required for imaging is much larger than the number of measured capacitance values, the dimension of g is much larger than that of C. The number of calculations required for sensitivity S will increase with an increase in the precision of the sensitive field partition. Because the condition number of S is large, the disturbance with a small measured capacitance value will cause a large change in the dielectric constant [20]. Therefore, the solution to the inverse problem based on Eq. (2) is inconclusive.

To address these problems, this paper proposes the use of an RBFNN to establish the nonlinear relationship between capacitance and dielectric constant values and to select the center of the RBFNN using the OLS method.

3 Reconstruction Algorithm and Training Samples

In this study, the LBP reconstruction algorithm was used to solve the ECT inverse problem, and an RBFNN was used to realize the nonlinear mapping between the approximation measurement capacitance and LBP reconstruction error. An OLS was used to optimize the RBFNN. Thus, the ECT feedback network was implemented. This section introduces the overall framework of the ECT feedback network based on the RBFNN, the principle of OLS-RBF, and the generation of the training set.

3.1 Feedback Network

In the LBP algorithm, the solution of the dielectric constant value is expressed as follows:

$$g = S^T \lambda \tag{3}$$

where S^T represents the transpose of the sensitivity matrix. Because the LBP algorithm is a linear reconstruction algorithm and there is a nonlinear relationship between the measured capacitance and dielectric constant distribution in the ECT reconstruction problem, the reconstructed image is not accurate, and severe distortion and artifacts may occur. The image error (IE) of the LBP reconstruction is expressed as follows:

$$e_g = g - g_{LBP} \tag{4}$$

Hypothesis $f(\cdot)$ represents the nonlinear relationship between the measured capacitance and the reconstruction error. Therefore, we have

$$e_g = f(\lambda) \tag{5}$$

which can be obtained through Eq. (4) as follows:

$$g = g_{LBP} + f(\lambda) \tag{6}$$

If the nonlinear relationship between the measured capacitance and the reconstruction error is known, the error generated by Eq. (3) can be reduced using Eq. (6) to improve the reconstruction accuracy.

An RBFNN based on the OLS algorithm was established to realize the nonlinear mapping between the measured capacitance and the reconstruction error. The feedback ECT reconstruction method based on the RBFNN proposed in this paper is shown in Fig. 3, where C represents the capacitance vector, G represents the original image in the training set, G_{LBP} represents the image obtained by the LBP algorithm, and e_G represents the difference between G and G_{LBP}. In the reconstruction process, g_{LBP} represents the image obtained by the LBP algorithm, e_g represents the image difference predicted by the trained RBFNN, and g represents the final reconstructed image.

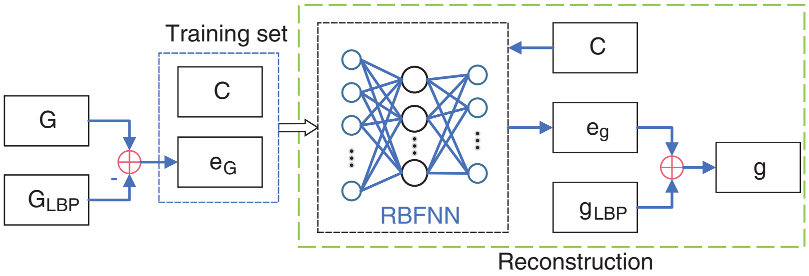

Figure 3: Structure of ECT feedback network

3.2 RBF Neural Network

An RBFNN has a feedforward structure with a single hidden layer, and the application of its kernel function can map low-dimensional linearly indivisible data to high-dimensional space, making it linearly separable in a high-dimensional space [21]. Owing to its local approximation ability and nonlinear characteristics, it can approximate the continuous function of arbitrary accuracy. Owing to the inaccuracy of the inverse problem of ECT and the nonlinearity of the distribution of capacitance as well as the media constant, the reconstruction of the LBP algorithm will result in major errors. The proposed reconstruction algorithm uses the trained RBFNN to predict such errors and eliminate them in the reconstruction process in order to realize an accurate calculation of the media distribution. The structure of the RBFNN is shown in Fig. 4. The input of the network is the capacitance vector, and the output is the predicted IE.

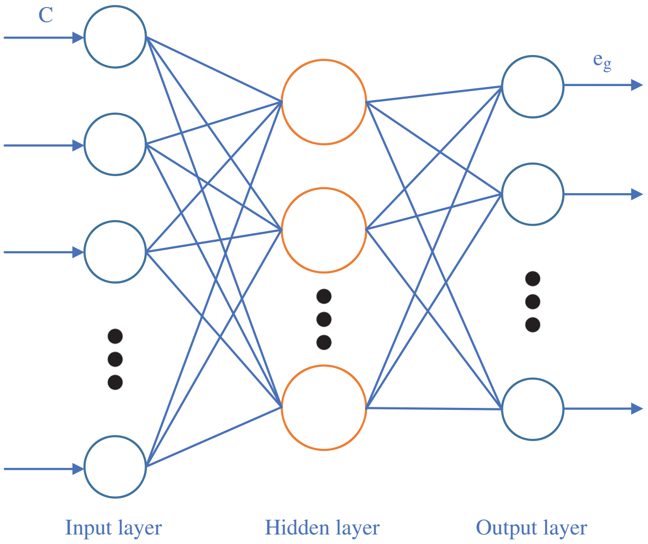

Figure 4: Structure of RBF network

The RBFNN takes neurons as nodes and the radial basis function as the excitation function. The activation function of the hidden layer node responds locally to the input. When the input is close to the central range of the base function, the hidden layer node will produce a large output; when the input is far from the central point, the output decays exponentially. The hidden layer neurons obtain the output layer by linear addition.

RBFs are non-negative real-valued functions whose values depend on the input distance from the central point and are radially symmetric. The Gaussian function is expressed as follows:

$$\phi(||x - c_i||) = e^{(\frac{||x-\mu_i||^2}{2\sigma^2})} \tag{7}$$

where x is the input, c_i is the center point of the ith node of the hidden layer, σ_i is the width variance of the ith node, and $||\cdot||$ is the Euclidean norm. Let y be the output of the network-output layer node,

$$y = \sum_{i=1}^{M} \omega_i \phi(||x - c_i||) \tag{8}$$

ω_i is the weight of the ith hidden layer connected to the output node, which is determined by the linear OLS method through input x and the corresponding expected output. The hidden layer is composed of M nodes. The input data are inputted to the network, and the response of the hidden layer is calculated; subsequently, the output of the network is calculated using the initial weight. In the training process, the weight is constantly adjusted to minimize the error between the network output and the expected output. The RBFNN is also called the local response function [22] because it only trains some weights that have a significant influence on the output.

When using an RBFNN, the most important factor is selecting the center point. In this study, the OLS algorithm was used to select the center and construct the RBFNN. RBF network can be viewed as the following regression model:

$$Y = P\theta + E \tag{9}$$

where, $Y = [\mathrm{y}_1,\mathrm{y}_2,\ldots,\mathrm{y}_n]^T$, $P = [p_1, p_2, \ldots, p_M]$, $\theta = [\theta_1, \theta_2, \ldots, \theta_M]^T$, $E = [\varepsilon_1,\varepsilon_2,\ldots,\varepsilon_n]^T$, ε is the error.

OLS transforms the P set into orthogonal basis vectors, and then obtains the effect of each basis vector on the output,

$$P = WA \tag{10}$$

where, A is an upper triangular matrix in M dimension with diagonal 1, W is an N × M matrix, and

$$W^T W = H \tag{11}$$

where H is a diagonal matrix whose diagonal element is h_i,

$$h_i = w_i^T w_i \tag{12}$$

w_i is an orthonormal basis vector. And Eq. (9) can be transformed into

$$Y = Wg + E \tag{13}$$

where, g in OLS algorithm is represented as

$$g = H^{-1} W^T Y \tag{14}$$

θ in Eq. (9) can be solved by the following formula:

$$A\theta = g \tag{15}$$

The gram-Schmidt method can be used to obtain the value of the least squares estimate θ.

Center selection OLS algorithm

---

1. Set the number of hidden layer nodes M and initial RBF center c_i in advance ($1 \leq i \leq M$);
2. Calculate the regression matrix P according to the input data X;
3. Select the regression operator by OLS algorithm: W_k represents the kth column of the regression operator matrix. k = 1, let the columns of P be the first columns of W, calculate error, The regression operator with large error is selected as the first column of W; k≥2, The remaining n-k columns in P are the kth columns of W, use Gram-Schmidt method to orthogonalize it to the kth columns and calculate the error, the regression operator with large errors is regarded as the kth column of W.

3.3 Training Samples

COMSOL Multiphysics finite element software was used to establish four distributions of ECT models: single-core, two-core, three-core, and stratified. When modeling different samples in COMSOL, different parameters were used to describe their characteristics. Figs. 5a–5c show the core distribution, and the parameters describing the sample are the center position and radius. Fig. 5d shows the stratified distribution, and its parameters are the height of the stratified distribution interface and the inclination angle between the normal line of the interface and the horizontal line. Different samples can be created by generating random parameters.

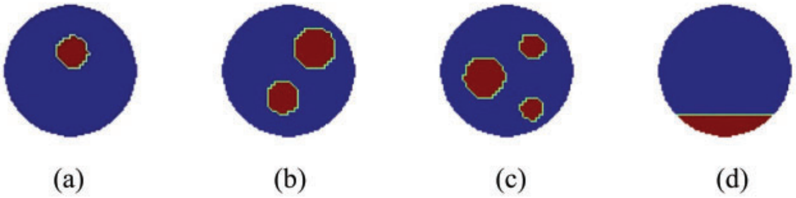

Figure 5: Training samples (a) Single-core (b) Two-core (c) Three-core (d) Stratified

Each distribution sample was simulated by COMSOL to obtain 5,000 datasets, with a total of 20,000 data sets. Each dataset consists of a measured capacitance vector C and a dielectric constant value vector g. C and g are the input and expected output of the network, respectively. To accelerate the convergence speed of the network training, before using the data set to train the network, each group of measured capacitance values needs to be normalized. The normalization formula for C is as follows:

$$\lambda_{ij} = \frac{1/C_{ij}^{m} - 1/C_{ij}^{l}}{1/C_{ij}^{h} - 1/C_{ij}^{l}} \tag{16}$$

where λ_{ij}, C_{ij}^{m}, C_{ij}^{h} and C_{ij}^{l} respectively represent the normalized capacitance between the i-j electrode pair, the measured capacitance, the capacitance when the measured area is filled with a medium with a high relative permittivity and a medium with a low relative permittivity.

4 Simulations Experiments

To verify the effectiveness of the proposed reconstruction method, two criteria of correlation coefficient (CC) and image error (IE) are used to quantitatively evaluate the reconstruction accuracy:

$$CC = \frac{\sum_{i=1}^{N} (g_i - \bar{g})(G_i - \bar{G})}{\sqrt{\sum_{i=1}^{N} (g_i - \bar{g})^2 \sum_{i=1}^{N} (G_i - \bar{G})^2}} \tag{17}$$

$$IE = \frac{\mathrm{g} - G}{G} \tag{18}$$

where G represents the distribution of the dielectric constant of the original image, G represents the distribution of the dielectric constant of the reconstructed image, $\bar{G}$ is the average value of G, and $\bar{g}$ is the average value of G.

Fig. 6 shows the reconstruction results of noiseless data calculated by the proposed algorithms, ART algorithm, Tikhonov algorithm, and Landweber iterative method. Table 1 shows the IE and CC, corresponding to the results in Fig. 6. For the reconstruction results, our algorithm had a lower IE, higher CC, and better imaging effect. The reconstruction results show that the proposed algorithm can significantly reduce artifacts in the reconstruction results in all cases and more accurately display the position where the phase distribution changes; it also achieves high reconstruction accuracy. The ART algorithm has a good reconstruction effect for the core flow, but it cannot obtain the exact reconstruction results for the laminar flow distribution. The Tikhonov and Landweber algorithms perform better on laminar flow than ART, but they cannot eliminate artifacts in the core flow reconstruction results. Because the nonlinearity of the ECT inverse problem is removed in the reconstruction process, the reconstruction results are closer to the real permittivity distribution, and there are fewer artifacts.

To further study the anti-noise performance of the algorithm, the capacitance data are added to the noise and then inputted to the feedback reconstruction network for calculation. The signal-to-noise ratio (SNR) is expressed as follows:

$$SNR = \frac{P_{signal}}{P_{noise}} \tag{19}$$

where, P_{signal} represents the measurement signal and P_{noise} represents the noise signal.

Noise was added to the capacitor vector, as shown in Fig. 7. First, the capacitance matrix was expanded, and then Gaussian noise with a preset SNR ($\mathrm{SNR} = 50$) was added to each row of the expanded matrix. Any column of the expanded matrix can be used as a result of the added noise. Gaussian noise with a preset SNR ($\mathrm{SNR} = 50$) was added to each row.

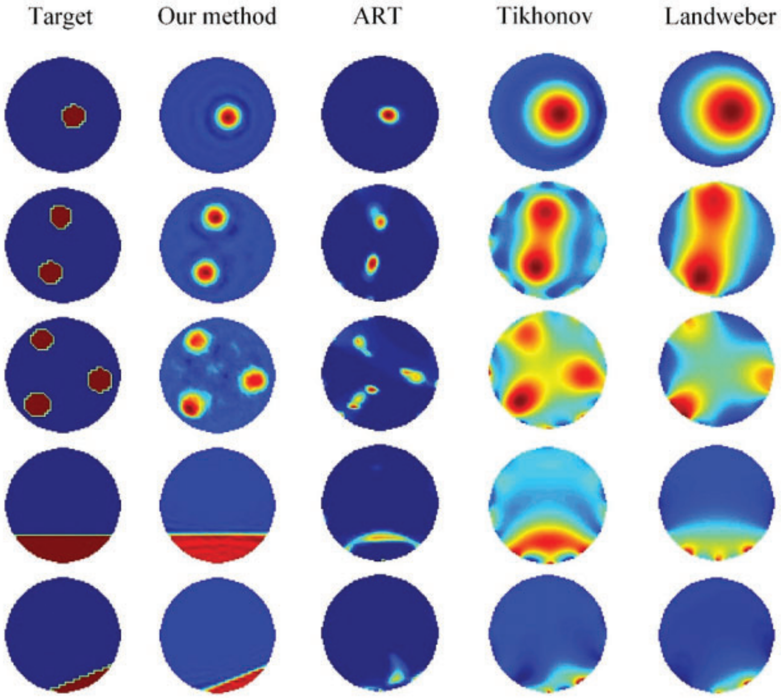

Figure 6: Comparison of simulation experiments

Table 1: Evaluation of simulation experiment result

	Our method		ART		Tikhonov		Landweber	
	IE (%)	CC	IE (%)	CC	IE (%)	CC	IE (%)	CC
1	3.46	0.9956	1.30	0.9887	14.19	0.9431	22.52	0.8861
2	2.71	0.9908	4.59	0.9623	21.46	0.9264	26.64	0.8600
3	4.38	0.9871	6.81	0.9315	24.36	0.9387	28.87	0.7773
4	3.12	0.9957	8.24	0.8917	12.13	0.9347	2.08	0.9463
5	2.06	0.9987	4.25	0.9725	5.09	0.9822	2.78	0.9837

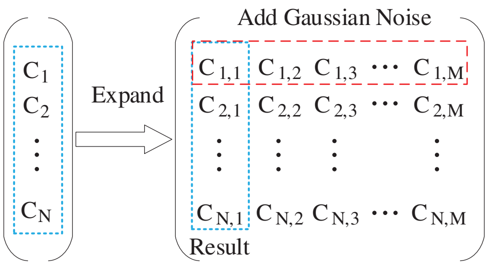

Figure 7: Processes of noise-contaminated capacitance generation

Fig. 8 shows the reconstruction results for the noisy data. The proposed algorithm still has a good imaging effect when the capacitance data are polluted by noise. Thus, the proposed reconstruction method has strong noise resistance and good generalization ability; furthermore, the reconstruction effect is satisfactory. The proposed method can be used for the visualization of filling pipelines based on ECT technology.

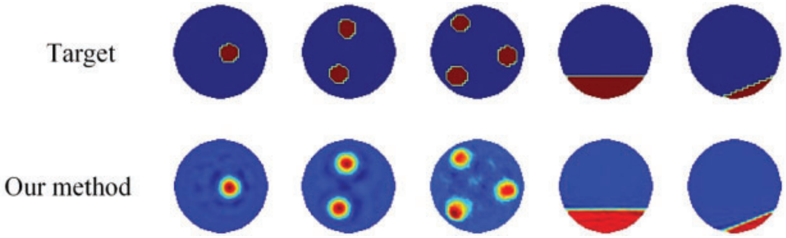

Figure 8: Reconstruction results based on noise-contaminated simulation data

5 Conclusions

A feedback reconstruction network based on an RBFNN was proposed for mine filling pipeline visualization and to reduce the error caused by nonlinearity in the ECT reconstruction process. After the calculation error caused by the linear algorithm is removed from the model, the ECT reconstruction problem is transformed from nonlinear to linear inverse. In this study, typical two-phase flow data samples were used to train the RBFNN for predicting the reconstruction error, and the LBP algorithm was used to complete the image reconstruction. In the simulation results, for the data without noise and the data interfered by noise, the proposed reconstruction method has a high reconstruction accuracy, fewer imaging artifacts, and a clear phase distribution boundary. It can effectively judge the caking and blockage in the pipeline, which has an important application prospect. The feedback reconstruction network greatly reduces the error of the linear model of ECT. It can be combined with a more complex reconstruction algorithm to further improve the accuracy of the reconstruction algorithm, providing a theoretical basis for the visual detection of mine filling pipelines.

Acknowledgement: I would like to acknowledge Professor, Ningbo Jing, for inspiring my interest in the development of innovative technologies.

Funding Statement: This research was supported by the National Natural Science Foundation of China (No. 51704229), Outstanding Youth Science Fund of Xi'an University of Science and Technology (No. 2018YQ2-01).

Conflicts of Interest: We declare that we have no financial and personal relationships with other people or organizations that can inappropriately influence our work, there is no professional or other personal interest of any nature or kind in any product, service and/or company that could be construed as influencing the position presented in, or the review of, the manuscript entitled, “Visualization Detection of Solid–Liquid Two-phase Flow in Filling Pipeline by Electrical Capacitance Tomography Technology”.

References

1. Qi, C. C., Chen, Q. S., Fourie, A. (2018). Pressure drop in pipe flow of cemented paste backfill: Experimental and modeling study. *Powder Technology, 333,* 9–18. DOI 10.1016/j.powtec.2018.03.070.
2. Chen, Q. S., Zhang, Q. L., Andy, F., Chen, X., Qi, C. C. (2017). Experimental investigation on the strength characteristics of cement paste backfill in a similar stope model and its mechanism. *Construction and Building Materials, 154(1),* 34–43. DOI 10.1016/j.conbuildmat.2017.07.142.
3. Fedi, Z., Emilia, B., Moez, L. (2019). Internal pipe area reconstruction as a tool for blockage detection. *Journal of Hydraulic Engineering, 145(6),* 1–12. DOI 10.1061/(ASCE)HY.1943-7900.0001602.
4. Liu, L., Fang, Z. Y., Wu, Y. P. (2018). Experimental investigation of solid–liquid two-phase flow in cemented rock-tailings backfill using electrical resistance tomography. *Construction and Building Materials, 175(1),* 267–276. DOI 10.1016/j.conbuildmat.2018.04.139.
5. Romanowski, A. (2019). Big data-driven contextual processing methods for electrical capacitance tomography. *IEEE Transactions on Industrial Informatics, 15(3),* 1609–1618. DOI 10.1109/TII.9424.
6. Guo, Q., Li, X., Hou, B., Mariethoz, G., Ye, M., Yang, W. et al. (2020). A novel image reconstruction strategy for ECT: Combining two algorithms with a graph cut method. *IEEE Transactions on Instrumentation and Measurement, 69(3),* 804–814. DOI 10.1109/TIM.19.
7. Li, L., Zhang, Y., Song, L. (2014). An image fusion algorithm for ECT based on Tikhonov algorithm and wavelet transform. *International Journal of Signal Processing Image Processing, 2(7),* 51–60. DOI 10.14257/ijsip.
8. Hu, H., Liu, X., Wang, X. (2016). A self-adapting Landweber algorithm for the inverse problem of electrical capacitance tomography (ECT). *IEEE International Instrumentation and Measurement Technology Conference Proceedings*, pp. 1–6. China.
9. Xie, H., Wang, H., Wang, L. (2019). Comparative studies of total-variation-regularized sparse reconstruction algorithms in projection tomography. *AIP Advances, 9(8),* 1–11. DOI 10.1063/1.5116246.
10. Xie, H. J., Xia, T., Tian, Z. N. (2021). A least squares support vector regression coupled linear reconstruction algorithm for ECT. *Flow Measurement and Instrumentation, 77,* 4879–4890. DOI 10.1016/j.flowmeasinst.2020.101874.
11. Zheng, J., Peng, L. (2020). A deep learning compensated back projection for image reconstruction of electrical capacitance tomography. *IEEE Sensors Journal, 20(9),* 4879–4890. DOI 10.1109/JSEN.7361.
12. Ye, J., Yang, W., Wang, C. (2020). Low-rank matrix recovery for electrical capacitance tomography. *IEEE International Instrumentation and Measurement Technology Conference*, pp. 1–5. New Zealand.
13. Li, J., Yang, X., Wang, Y. (2012). An image reconstruction algorithm based on RBF neural network for electrical capacitance tomography. *Sixth International Conference on Electromagnetic Field Problems and Applications*, pp. 1–4. China.
14. Tian, W., Suo, P., Liu, D. (2021). Simultaneous shape and permittivity reconstruction in ECT with sparse representation: Two-phase distribution imaging. *IEEE Transactions on Instrumentation and Measurement, 70(1),* 1–14. DOI 10.1109/TIM.2020.3007908.
15. Zhu, H., Sun, J., Long, J. (2020). Deep image refinement method by hybrid training with images of varied quality in electrical capacitance tomography. *IEEE Sensors Journal, 21(5),* 6342–6355. DOI 10.1109/JSEN.7361.
16. Zheng, J., Peng, L. (2018). An autoencoder based image reconstruction for electrical capacitance tomography. *IEEE Sensors Journal, 18(13),* 5464–5474. DOI 10.1109/JSEN.2018.2836337.
17. Yang, X., Zhao, C., Chen, B. (2020). Big data driven U-Net based electrical capacitance image reconstruction algorithm. *IEEE International Conference on Imaging Systems and Techniques*, pp. 1–6. United Arab Emirates.
18. Wang, L., Liu, X., Chen, D. (2020). ECT image reconstruction algorithm based on multiscale dual-channel convolutional neural network. *Complexity, 8,* 1–12. DOI 10.1155/2020/4918058.
19. Hu, H., Xiao, L., Wang, X. (2016). A self-adapting Landweber algorithm for the inverse problem of electrical capacitance tomography (ECT). *IEEE International Instrumentation and Measurement Technology Conference Proceedings*, pp. 1–6. China.

20. Cui, Z. Q., Wang, Q., Xue, Q. (2016). A review on image reconstruction algorithms for electrical capacitance/resistance tomography. *Sensor Review, 36(4),* 429–445. DOI 10.1108/SR-01-2016-0027.
21. Dong, J., Zhao, Y., Liu, C. (2019). Orthogonal least squares based center selection for fault-tolerant RBF networks. *Neurocomputing, 2(2),* 302–309. DOI 10.1016/j.neucom.2019.02.039.
22. Sun, Q., Shi, T. M. (2009). Sensors structure optimization of ECT based on RBF neural network and PSO. *Control and Instruments in Chemical Industry,* 169–176.

Computer Modeling in
Engineering & Sciences

Tech Science Press

DOI: 10.32604/cmes.2022.020388

ARTICLE

A Frost Heaving Prediction Approach for Ground Uplift Simulation Due to Freeze-Sealing Pipe Roof Method

Shengjun Deng[1,2,3], **Haolin Chen**[1], **Xiaonan Gong**[2], **Jiajin Zhou**[2], **Xiangdong Hu**[4] **and Gang Jiang**[1,*]

[1]Institute of Geotechnical Engineering, Nanjing Tech University, Nanjing, 210009, China

[2]Research Center of Coastal and Urban Geotechnical Engineering, Zhejiang University, Hangzhou, 310058, China

[3]Department of Civil and Environmental Engineering, Princeton University, Princeton, NJ, 08544, USA

[4]Key Laboratory of Geotechnical and Engineering of Ministry of Education, Department of Geotechnical Engineering, Tongji University, Shanghai, 200092, China

*Corresponding Author: Gang Jiang. Email: g.jiang@njtech.edu.cn

Received: 20 November 2021 Accepted: 27 December 2021

ABSTRACT

Freeze-sealing pipe roof method is applied in the Gongbei tunnel, which causes the ground surface uplift induced by frost heave. A frost heaving prediction approach based on the coefficient of cold expansion is proposed to simulate the ground deformation of the Gongbei tunnel. The coefficient of cold expansion in the model and the frost heaving rate from the frost heave test under the hydration condition can achieve a good correspondence making the calculation result closer to the actual engineering. The ground surface uplift along the lateral and longitudinal direction are respectively analyzed and compared with the field measured data to validate the model. The results show that a good agreement between the frost heaving prediction model and the field measured data verifies the rationality and applicability of the proposed model. The maximum uplift of the Gongbei tunnel appears at the center of the model, gradually decreasing along with the lateral and longitudinal directions. The curve in the lateral direction presents a normal distribution due to the influence of the constraint of two sides, while the one along the lateral direction shapes like a parabola with the opening downward due to the temperature field distribution. The model provides a reference for frost heaving engineering calculation.

KEYWORDS

Freeze-sealing pipe roof method; artificial ground freezing method; tunnel construction; frost heave; temperature field

1 Introduction

Freeze-sealing pipe roof (FSPR) method as an innovative pre-supporting method in tunnel engineering is applied in the Gongbei tunnel of Hongkong-Zhuhai-Macau Bridge, which is the first application in the world. Engineering applications using FSPR method has been appeared in recent years with the rapid development of underground space technology. FSPR method combines pipe-roofing method and artificial ground freezing method. The definition of FSPR method is that jacking pipes with large diameter are laid out in a circle along the cross section of tunnel in advance, then the artificial ground freezing method is adopted to freeze soil between jacking pipes to prevent water from entering into tunnel during excavation. The pipe jacking mainly plays a role of load bearing, while ground freezing mainly plays a role of water sealing [1–3]. However, ground surface uplift occurs during tunnel construction due to the ground freezing. The ground uplift is mainly caused by frost heave of frozen soil between steel pipes. Particular emphasis is placed on the ground surface deformation, therefore a rational method to predict the deformation of frost heave is required. Generally, the available frost heave model can be classified into three categories: the theoretical model, semi-empirical formula model and numerical model [4,5]. The theoretical model focuses on describing the physical changes in matter during the soil freezing process. The early proposal of this model was presented by Miller, who caught the attention of physicists and engineers by rigid ice model [6]. Subsequently, the model was further developed [7]. The semi-empirical formula model is not only used to explain the frost heaving phenomenon, but also to the frost heave calculation [8,9]. Typical models include segregation potential model proposed by Konrad [10–13], the rigid-ice model proposed by Miller and developed by O'Neill et al. [14], the coupled heat-fluid model proposed by Harlan [15], the thermal mechanical model proposed by Fromend et al. [16]. The numerical model is proposed based on combined thermal-hydraulic-mechanical field [17,18], elastic foundation beam theory [19] and other similar methods [20–22]. Also, numerous scholars have devoted their efforts to calculation methods for frost heave force, such as elastoplastic calculation model for surrounding rock proposed by Feng et al. [23], a mathematical mechanical model for tunnel in cold region proposed by Lai et al. [24], a coupled analytical approach for underground excavation problems proposed by Yang et al. [25]. A practical method was proposed by combining the advantages of laboratory testing or numerical simulation to simulate and predict the ground surface deformation during the AGF construction process [26,27]. From the perspective of engineering application, a major limitation in model analysis of frost heave is that model parameters have no practical physical meaning, and even if it is, it is difficult to measure. The accuracy of the model depends on the accuracy of the test parameters. There are some studies about the buried pipeline in frozen ground involving the test parameters [28,29], but lack a practical frost heaving calculation model [30]. Accordingly, a new model is proposed to predict the frost heave deformation. The model proposes the coefficient of cold expansion related with frost heaving rate from test as calculation parameter, which makes the model parameters correspond to the actual engineering. The ground surface uplift distribution of the Gongbei tunnel is analyzed based the proposed model. Meanwhile, the simulation result is verified by comparing with the field monitoring data.

2 The Proposed Frost Heaving Prediction Approach

ABAQUS as a three-dimensional finite element program is employed currently to carry out the numerical study. It is well known that temperature variation can lead to heat-induced expansion in frozen soil. Here we ignore the effect of temperature on strain ratio because it is small enough compared to frost heave. We propose the coefficient of cold expansion to simulate the expansion process, which is related to temperature. The basic framework of the model is as follows.

2.1 Equation of Thermal Equilibrium

For the isotropic homogeneous material, equation of thermal equilibrium is expressed as Eq. (1).

$$\rho c\frac{\partial T}{\partial t} = \lambda \times \nabla^2 T + q_{\mathrm{v}} \tag{1}$$

where ρ is mass density, c is specific heat, λ is thermal conductivity, t is the time, T is the temperature, q_v is internal heat source.

2.2 *A New Approach for Frost Heaving Prediction*

(1) One-dimensional model

For transient heat conduction without internal heat source in semi-infinite domain, the equation can be expressed as Eq. (2).

$$\frac{\partial T}{\partial t} = a \cdot \nabla^2 T = a \cdot \frac{\partial^2 T}{\partial x^2} \tag{2}$$

where $a = \lambda/\rho c$

Fig. 1 is the temperature distribution at a special time in semi-infinite domain. Assume that T_0 is the initial temperature for the whole domain, $T_f (T_f < T_0)$ is the given boundary temperature at $x = 0$ when freezing begins, the thermophysical parameters are constant.

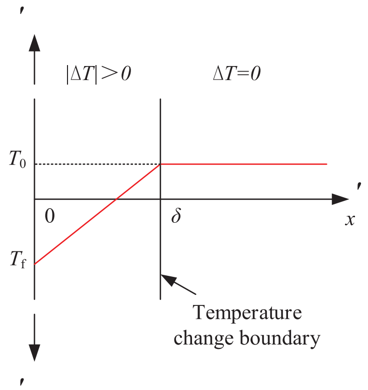

Figure 1: Temperature distribution at a special time t in semi-infinite domain

The equation of initial condition can be represented as Eq. (3).

$$T = T_0, 0 \le x \le +\infty, t = 0 \tag{3}$$

The equation of boundary conditions can be represented as Eq. (4).

$$\begin{cases} T = T_f, x = 0, t > 0 \\ T = T_0, x = +\infty, t > 0 \end{cases} \tag{4}$$

On the basis of $\theta = T - T_f$, the following Eq. (5) can be obtained by the Laplace transformed and Eqs. (2)–(4).

$$\frac{\theta}{\theta_0} = \frac{T - T_f}{T_0 - T_f} = erf(\frac{x}{2\sqrt{at}}) = erf(\varphi) \tag{5}$$

where Gaussian error function $erf(\varphi)$ can be expressed as Eq. (6).

$$erf(\varphi) = \frac{2}{\sqrt{\pi}} \int_0^{\varphi} e^{-z^2} dz \tag{6}$$

When $\frac{x}{2\sqrt{at}} = 2$, $\frac{T-T_f}{T_0-T_f} \approx 1$, $T = T_0$, that is $x = \delta = 4\sqrt{at_\delta}$, the temperature at this point has not changed exactly at the time t_δ, which is the critical point of temperature change. Accordingly, the semi-infinite domain can be divided into two zones by the $x = \delta$, shown in Fig. 1. One is the left zone between $x = 0$ and $x = \delta$, where temperature changes. The other one is the right zone start from $x = \delta$ to $x = \infty$, For the temperature distribution at this time, it can be described by Eq. (7).

$$\nabla^2 T = \frac{\partial^2 T}{\partial x^2} = 0 \tag{7}$$

The boundary conditions are as shown in Eq. (8).

$$\begin{cases} T = T_f, x = 0 \\ T = T_0, x = \delta \end{cases} \tag{8}$$

The Eq. (8) is substituted into Eq. (7), then the formula of temperature distribution is as follows:

$$T = T_f + \frac{x}{\delta}\left(T_0 - T_f\right) \quad (0 \le x \le \delta) \tag{9}$$

$\delta = 4\sqrt{at_\delta}$ is substituted into Eq. (9), which is equivalent to

$$T = T_f + \frac{x}{4\sqrt{at_\delta}}\left(T_0 - T_f\right) \quad (0 \le x \le \delta) \tag{10}$$

Hereafter, the formula of temperature change can be expressed as

$$\Delta T = T - T_0 = \left(T_0 - T_f\right) \cdot \left(\frac{x}{4\sqrt{at_\delta}} - 1\right) (0 \le x \le \delta) \tag{11}$$

According to the following statements, a new frost heaving prediction model is established. (1) The pore water in the soil becomes ice, causing the volume of the soil to expand. The moisture migration causing the frost heaving phenomenon is the main factor. The findings above are discovered by Taber and Beskow through the soil frost heaving test [31,32]. (2) The moisture migration is subject to the temperature gradient [33,34]. In this model, temperature gradient appears in the left zone between $x = 0$ and $x = \delta$ of Fig. 1 where we assume that the frost heave occurs.

Therefore, the linear frost heaving rate can be calculated as follows:

$$\alpha = \eta \cdot \int_0^{+\infty} |\Delta T| dx = \eta \cdot \int_0^{\delta} |\Delta T| dx \tag{12}$$

In which, α is linear frost heaving rate, η represents the relative change of frost heave generated per unit temperature reduction in the x direction. The Eq. (13) can be further derived through substituting Eq. (11) into Eq. (12).

$$\alpha = \eta \cdot \frac{\delta}{2}\left(T_0 - T_f\right) = \eta \cdot 2\sqrt{at_\delta}\left(T_0 - T_f\right) \tag{13}$$

Based on the assumptions above, the maximum frost heaving rate can be expressed as Eq. (14).

$$\alpha_f = \eta \cdot \Delta T_f = \eta \cdot \left(T_0 - T_f\right) \tag{14}$$

where α_f is the maximum linear frost heaving rate.

Based on the frost heaving test of saturated soil under hydration conditions, α_f of different soil samples can be measured. Moreover, the coefficient η of different soil samples corresponding to different soil layers can be calculated at a special initial temperature T_0 and given boundary temperature T_f. According to the Eq. (14), the coefficient of cold expansion η corresponding to different soil layers can be expressed as follows:

$$\eta = \alpha_f/(T_0 - T_f) \tag{15}$$

where we name the coefficient $\eta(\eta > 0)$ as the coefficient of cold expansion.

(2) Two-dimensional model

For two-dimensional model, assume that $(T_f - T_0)$ is the temperature change at the surface of pipe $(r = r_0)$ when freezing begins. Position $r = \delta$ is the temperature change boundary, where the temperature change is zero. Accordingly, the two-dimensional temperature change distribution can be divided into two zones by the annulus $r = \delta$, shown in Fig. 2. One is the internal zone between $r = r_0$ and $r = \delta$, where temperature changes. The other one is the external zone start from $r = \delta$ to ∞, where there is no change in temperature.

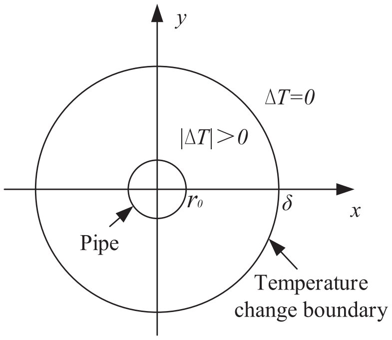

Figure 2: Temperature change distribution based on single pipe in two dimensions

According to the above, the equation of boundary conditions can be represented as

$$\begin{cases} \Delta T = T_f - T_0, r = r_0, t > 0 \\ \Delta T = 0, r = \delta, t > 0 \end{cases} \tag{16}$$

In Eq. (16), ΔT can be expressed as

$$\Delta T = (T_f - T_0) \cdot \frac{\ln \frac{\delta}{r}}{\ln \frac{\delta}{r_0}} \tag{17}$$

In which, δ is the diameter of the temperature change boundary annulus, r is the diameter of the annulus, r_0 is the diameter of pipe.

Therefore, the surface frost heaving rate can be calculated as follows:

$$\beta = \eta \cdot \iint |\Delta T| \, dxdy = \eta \cdot \int_0^{2\pi} d\theta \int_{r_0}^{\delta} |\Delta T| r dr \tag{18}$$

where β represents the surface frost heaving rate, θ represents the angle in polar coordinates, r represents the diameter in polar coordinates. The formula can be further derived through substituting Eq. (17) into Eq. (18).

$$\beta = \eta \cdot (T_0 - T_f) \cdot \frac{2\pi}{\ln \frac{\delta}{r_0}} \left[\frac{1}{2} {r_0}^2 \ln \frac{r_0}{\delta} + \frac{1}{4} (\delta^2 - {r_0}^2) \right] \tag{19}$$

where the coefficient of cold expansion η as the basic characteristics of material can be obtained according to Eq. (15).

(3) Three-dimensional model

The three-dimensional model is composed of multiple two-dimensional models along the longitudinal direction. The numerical simulation of frost heave is based on the model above.

(4) Finite element calculation

Since the elastic modulus varies with temperature, the frost heave strain includes the elastic strain and the temperature strain.

$$\Delta\varepsilon_n = \Delta\varepsilon_n^e + \Delta\varepsilon_n^T \tag{20}$$

where $\Delta\varepsilon_n$ represents the frost heave strain, $\Delta\varepsilon_n^e$ represents the elastic strain increment, $\Delta\varepsilon_n^T$ represents the temperature strain increment.

The elastic strain increment can be calculated by Hooke's law as follows:

$$\Delta\varepsilon_n^e = \frac{1}{E_e} Q\Delta\sigma_n \tag{21}$$

$$Q = \begin{bmatrix} 1 & -\mu_s & -\mu_s & 0 & 0 & 0 \\ -\mu_s & 1 & -\mu_s & 0 & 0 & 0 \\ -\mu_s & -\mu_s & 1 & 0 & 0 & 0 \\ 0 & 0 & 0 & 2(1+\mu_s) & 0 & 0 \\ 0 & 0 & 0 & 0 & 2(1+\mu_s) & 0 \\ 0 & 0 & 0 & 0 & 0 & 2(1+\mu_s) \end{bmatrix} \tag{22}$$

where E_e is the modulus, μ_s is the poisson's ratio.

Based on the obtained temperature field and the concept of linear expansion coefficient, temperature strain increment can be calculated. The results are as follows:

$$\Delta\varepsilon_n^T = \{\alpha\Delta T_n, \alpha\Delta T_n, \alpha\Delta T_n, 0, 0, 0\}^T \tag{23}$$

where α is the coefficient of cold expansion that is the expansion in ABAQUS software. ΔT_n is the temperature change of the node.

At any period Δt, based on the basic assumption of elastic theory, the physical equation (stress-strain relationship) can be expressed as the following equation:

$$\Delta\sigma_n = (\bar{D}_n)(\Delta\varepsilon_n - \Delta\varepsilon_n^T) \tag{24}$$

$$\bar{D}_n = E_n Q^{-1} \tag{25}$$

The node force of the element

$$\Delta F^e = \iiint B^T \Delta\sigma \, dxdydz \tag{26}$$

The stiffness matrix of the element

$$k^e = \iiint B^T \bar{D}_n dxdydz \tag{27}$$

Thus, the whole equilibrium equation is as follows:

$$K\Delta\delta_n = \Delta P_n^L + \Delta P_n^T \tag{28}$$

In which, K is the global stiffness matrix, ΔP_n^L is the incremental node load caused by external load, ΔP_n^T is the incremental node load caused by temperature.

The displacement increment $\Delta\delta_n$ of each node can be obtained by the Eq. (28), and then substituted into the Eq. (24), the stress increment ΔQ_n of each node can be obtained.

3 Validation of the Frost Heaving Prediction Model: Gongbei Tunnel Case

3.1 Engineering Description

To verify the validity and feasibility of the proposed frost heaving prediction model, numerical results of the ground uplift due to freeze-sealing pipe roof method is compared with the field measured data. The freeze-sealing pipe roof (FSPR) method combining pipe roofing method and artificial ground freezing method is firstly applied in the Gongbei tunnel with the length of 255 m, which is a critical link of Hongkong-Zhuhai-Macau Bridge. Fig. 3 shows the FSPR structure, which consists of frozen soil and 36 pieces of 1620 mm diameter roofing pipes around the circumference of excavation. The spacing between the pipe edges ranges between 355 to 358 mm. In the normal direction of the tunnel circumference, the odd number roof pipes are shifted by 30 cm to the tunnel direction with respect to the even diameter pipes. The excavation cross-sectional area is approximately 345 m^2 with 18.8 m in width and 20.6 m in height, which is the largest single tunnel excavation in China. The tunnel is buried within soft sandy and silty clay about 4.5 m below the ground surface. The purpose of ground freezing is preventing groundwater from entering the tunnel. A freezing process will last for 50 days before excavation. However, the ground surface uplift occurs due to the frost heave. And the amount of frost heave is simulated by the frost heaving prediction model. The correspondingly outcomes are employed to validate the proposed model.

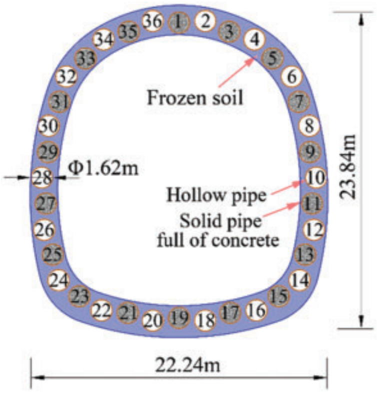

Figure 3: The cross section of FSPR structure

3.2 Geometric Modeling

3.2.1 Geometric Model and Material

The ground deformation due to frost heave is simulated using the finite element software ABAQUS. It is assumed that the soil layers are horizontally distributed, isotropic and homogeneous, while roofing pipes and concrete are isotropic homogeneous elastic materials. Refer to the detailed investigation survey data of the Gongbei tunnel, the adjacent soil layers are combined into one layer for calculation. There are five soil layers in the model. The geometry of the model (255 m × 150 m × 60 m in length × width × height) and its cross section are respectively shown in Figs. 4 and 5. The upper surface of the model is ground surface, which is freely constrained. The bottom surface is fully constrained, and the two sides parallel to the tunnel axis are bounded by the normal direction in the x direction. The two sides perpendicular to the tunnel axis are the working well edges constrained by both y and z directions. Tie constraint is adopted between the roofing pipes and surrounding soil. According to the temperature of Zhuhai City in June 2016, the initial temperature of the model is set as 28°C. Since the positive temperature does not cause frost heaving, the value of the initial temperature has little effect on the frost heave calculation. During the freezing phase, the outer surface temperature of roofing pipe is set as -15°C. The soil along the coastal areas expresses elastoplastic properties and can be considered as homogeneous materials. According to the Subsection 2.2 Eq. (15), the coefficient of cold expansion η is obtained by the maximum frost heaving rate α_f of the freezing test for each soil layer under the hydration condition when the initial temperature $T_0 = 28$°C and given boundary temperature $T_f = -15$°C. Thus, the mechanical and thermophysical parameters of the model can be respectively found in Tables 1 and 2.

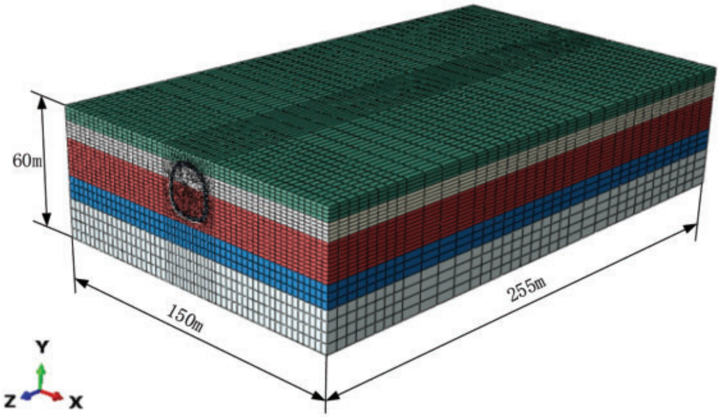

Figure 4: Geometry of the Gongbei tunnel model

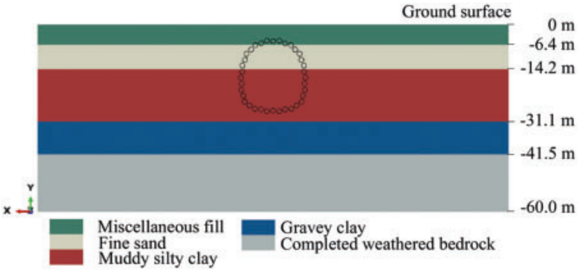

Figure 5: Layout of the roofing pipes in layered soil

In which, the maximum frost heaving rate is obtained from a model calibration based on soil frost heave test under hydration conditions for each soil layer in laboratory. And the coefficient of cold expansion is calculated according to Eq. (15).

Table 1: Mechanical parameters of the material

Category	Thickness (m)	Friction angle φ (°)	Cohesion c (MPa)	Elastic modulus E(Pa)	Poisson's ratio μ
Miscellaneous fill	6.4	13.9	39.9	4.6	0.3
Fine sand	7.8	9.2	13	14.4	0.3
Muddy silty clay	16.9	26.4	14.3	20.1	0.3
Gravel clay	10.4	25.3	12.5	6.5	0.3
Completely weathered bedrock	18.5	19.2	22.8	4.2	0.3
Roofing pipe	——	——	——	3.0e + 4	0.3
Concrete	——	——	——	2.06e + 5	0.2

Table 2: Thermophysical parameters of the material

Category	Density ρ (kg/m^3)	Thermal conductivity λ (W·m^{-1}·K^{-1})	Specific heat capacity c (J·kg^{-1}·K^{-1})	Maximum frost heaving rate α_f (%)	Coefficient of cold expansion η
Miscellaneous fill	1950	1.69	2558	1.1	0.00026
Fine sand	1960	1.758	2680	1.08	0.00025
Muddy silty clay	1980	1.893	2933	3.4	0.00079
Gravel clay	1820	1.79	2778	3.3	0.00077
Completely weathered bedrock	1780	1.887	2815	1.18	0.00027
Roofing pipe	7850	45	460	——	——
Concrete	2400	1.28	970	——	——

3.2.2 Feature Sections

In order to facilitate the analysis of ground surface uplift law, the feature sections are selected, including lateral direction and longitudinal direction. All sections are symmetrically distributed. There are 24 lateral monitoring sections (YK + 390∼YK + 630) along the longitudinal direction, where YK + 400 is the first monitoring section, 10 m from the boundary. Meanwhile, the monitoring data on the corresponding section (YK + 400, YK + 430, YK + 440) is obtained separately, shown in Fig. 6.

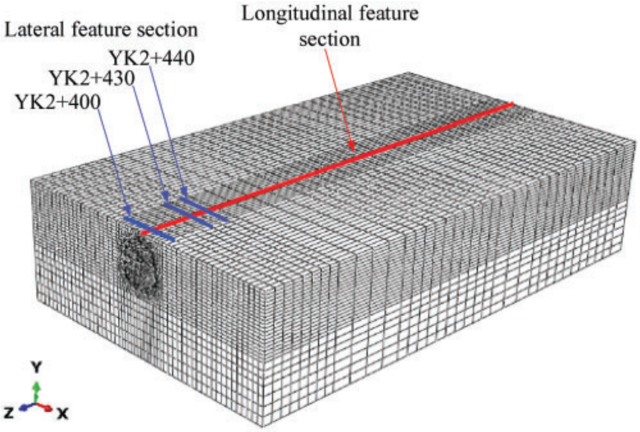

Figure 6: Feature sections

3.3 *Finite Element Model*

The finite element model consists of soil part, pipe-roofing part, concrete part, and lining part, with a total of approximately 489016 elements, including C3D8T elements and C3D6T elements, shown in Fig. 7. The soil in the coastal area exhibits elastoplastic properties and is considered as a homogeneous material. The Mohr-Coulomb model is used for soil. The pipe roofing, concrete and lining are simulated by an isotropic elastic model. Considering the influence of temperature and frost heave, the coupled temperature-displacement element is chosen and the implementation of frost heave depends on the coefficient of thermal expansion in the ABAQUS software.

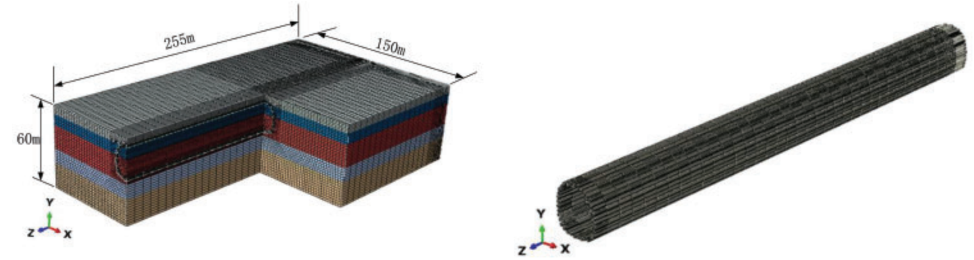

(a) Model profile

(b) Pipe roofing

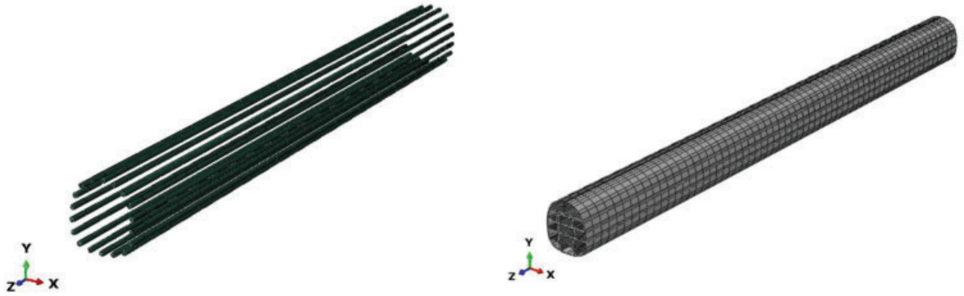

(c) Concrete

(d) Lining

Figure 7: Finite element model

There are 5 steps throughout the whole construction process, containing initial ground stress balance, pipe jacking, backfilling pipe with concrete, soil freezing, tunnel excavation. The ground stress is first released 40% during excavation, and then fully released after support. The main calculation process in Fig. 8 is as follows:

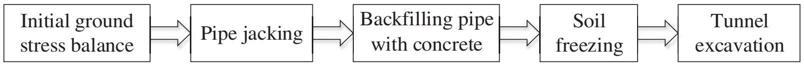

Figure 8: Simulation process

3.4 Model Validation

3.4.1 Temperature Field

Temperature is one of the factors affecting the frost heave effect, which indirectly affects the soil deformation, therefore the temperature field is the basis for calculating the soil deformation. The initial temperature of the model is 28°C, and the positive temperature does not cause frost heaving. Thus, the value of the initial temperature has little effect on the frost heave calculation. After freezing process of 50 days, the thickness of the frozen soil reaches the required width of 2 m. The temperature distribution is shown in Fig. 9.

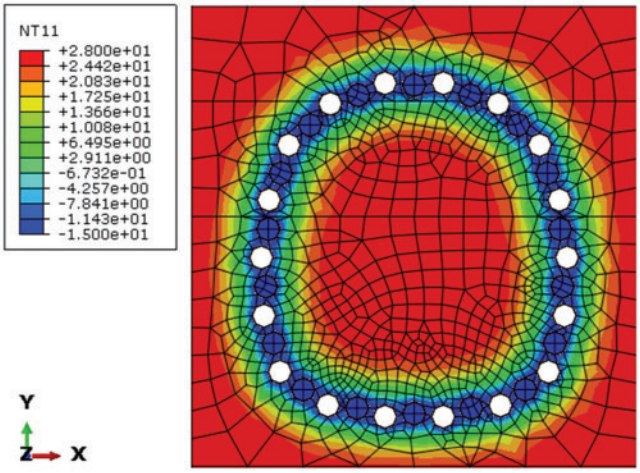

Figure 9: Temperature distribution when freezing for 50 days

3.4.2 Ground Surface Uplift

The ground equilibrium is achieved by ABAQUS when the surface is horizontal. Then the frost heaving model is applied to predict the vertical uplift of ground surface due to frost heave. Fig. 10 shows the deformation of ground surface uplift after 50 days of freezing. The maximum uplift appears at the center of the model with the value of 285.6 mm, gradually decreasing along the longitudinal and lateral directions. The results along the longitudinal direction are mainly affected by the constraints of the two sides, while the one along the lateral direction is caused by the temperature field distribution.

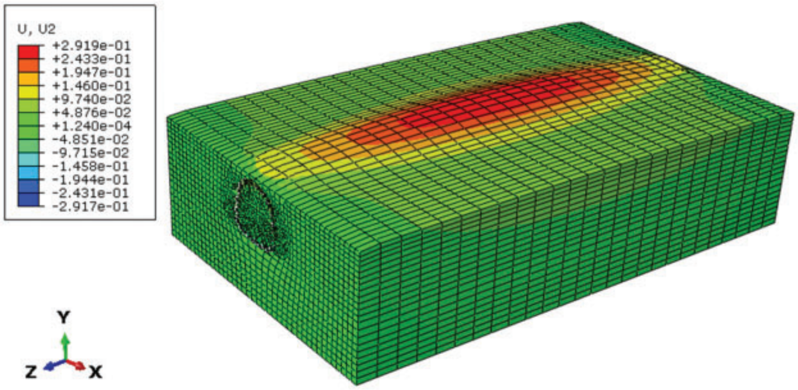

Figure 10: Deformation drawing of ground surface uplift (Zoom in 20 times)

Fig. 11 illustrates the comparison between the results obtained by the model prediction and the field monitoring data at cross section YK2 + 400, YK2 + 430, YK2 + 440 after 50 days of freezing. Both the model simulation results and field monitoring data show that the maximum value of ground surface uplift appears at the symmetry axis of the tunnel section, and the amount of frost heaving on both sides gradually becomes smaller. The curve is shaped like normal distribution. The maximum values of the prediction model curve and the field measured curve at section YK2 + 400 are 75.0 and 72.7 mm, the values of YK2 + 430 are 180.0 and 168.2 mm, and the values at YK2 + 440 are 195.8 and 178.5 mm, respectively. Therefore, the two curves match well in terms of data and shape. Due to the different freezing scheme during different construction period, the curve of the field measurement and model simulation is asymmetric.

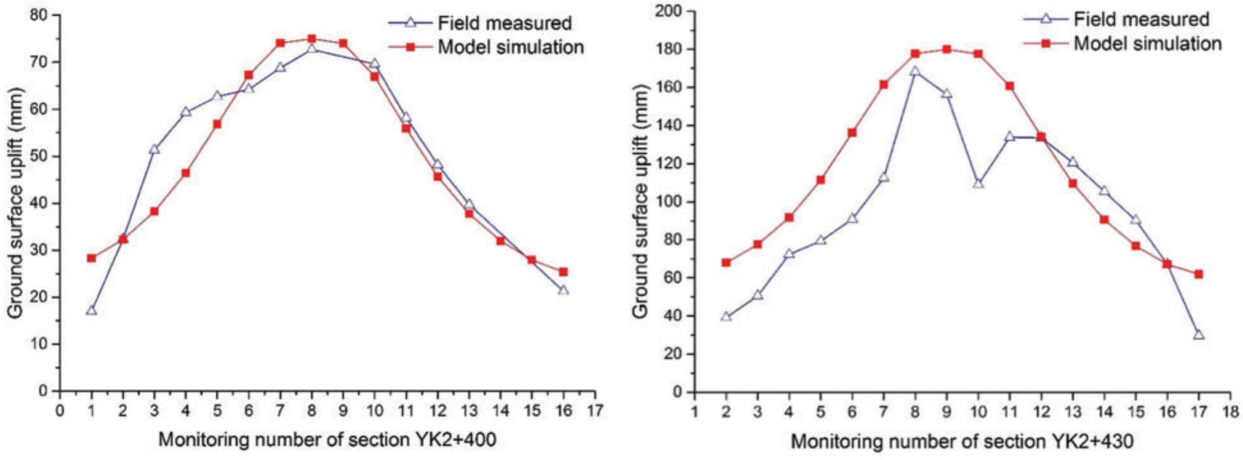

(a) Section YK2+400 (b) Section YK2+430

Figure 11: (Continued)

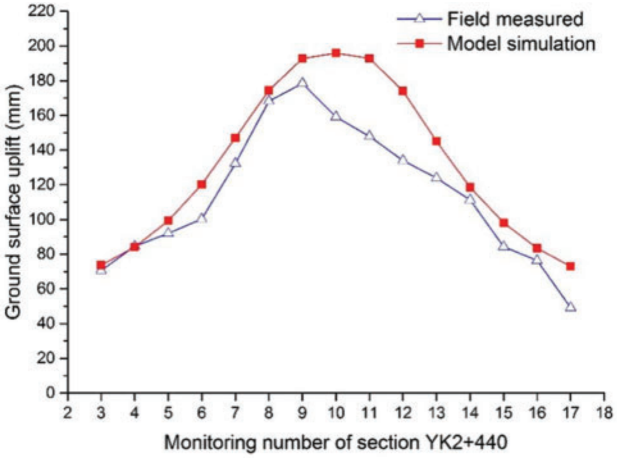

(c) Section YK2+440

Figure 11: Comparison of model prediction and field monitoring along the cross section

The vertical uplift of ground surface after 50 days of freezing due to frost heave along the longitudinal direction of the tunnel is also analyzed, shown in Fig. 12. The shape of the curve is similar to the parabola with the opening downward. The vertical uplift in the middle span of the tunnel is larger, and the amount of ground uplift near the working wells at both ends is gradually reduced because of the restraining effect from the two sides. Due to the different excavation progress, when the excavation speed is slow, the freezing intensity is relatively high, and the frost heave is relatively large, and vice versa. Therefore, there is a big difference between the field measurement and numerical simulation at 100 and 200 m in the longitudinal direction of the tunnel.

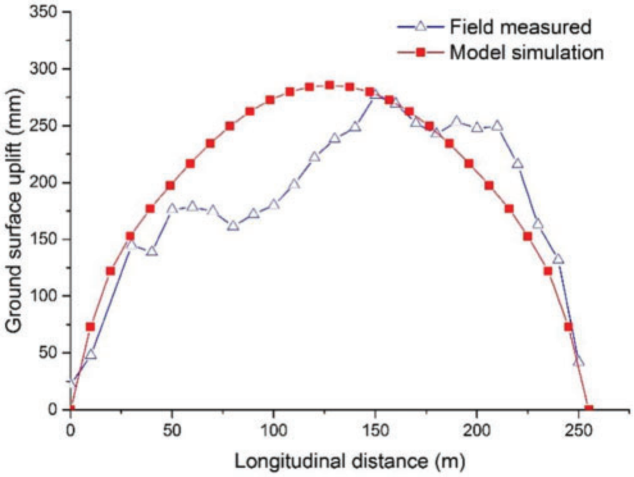

Figure 12: Comparison of model prediction and field monitoring along the longitudinal

A good agreement is discovered between the model prediction and field measured data, except for some misfits that are due to inhomogeneous soil and local grouting that affecting heat transfer and groundwater seepage. In addition, the weight and dynamic load of the surface buildings make the monitoring data slightly smaller than the model result in some local location. The favorable agreement indicates that the proposed frost heaving prediction model can well predict the ground surface uplift due to frost heave.

4 Conclusions

The ground deformation due to FSPR method involves a complicated hydrothermal coupling process, which is difficult to accurately simulate. According to that, a frost heaving prediction approach is proposed to simulate ground deformation of the Gongbei tunnel. The proposed model deals with the frost heave calculation by combining the coefficient of cold expansion based on the calculation equation and the frost heaving test under hydration conditions. From the result analysis of prediction model and field monitoring, some conclusions are drawn:

(1) The coefficient of cold expansion in model and the frost heaving rate from the test under the hydration condition can achieve a good correspondence that makes the calculation result closer to the actual engineering.

(2) The numerical simulation and monitoring data of the Gongbei tunnel are employed to validate the proposed model, and a good agreement between the frost heaving prediction model and the field measured data verifies the rationality and applicability of the proposed model to predict the ground deformation.

(3) The maximum uplift of the Gongbei tunnel appears at the center of the model, gradually decreasing along the lateral and longitudinal directions. The result in the lateral direction represents a normal distribution due to the influence of the constraint of two sides, while the one along the lateral direction shapes like a parabola with the opening downward due to the temperature field distribution.

It should be noted that the application of the proposed frost heaving prediction model to the Gongbei tunnel will be a reference for similar cases.

Acknowledgement: The author wishes to thank the high-performance computing cluster of Computer Science Department at Princeton University and the editor Dr. Lynn Wang for the careful format review.

Funding Statement: This work is supported by the financial support from National Natural Science Foundation of China (No. 51478340), Natural Science Foundation of Jiangsu Province (No. BK20200707), The Natural Science Foundation of the Jiangsu Higher Education Institutions of China (No. 20KJB560029), China Postdoctoral Science Foundation (No. 2020M671670), Key Laboratory of Soft Soils and Geoenvironmental Engineering (Zhejiang University), Ministry of Education (No. 2020P04), the support above is gratefully acknowledged.

Conflicts of Interest: The authors declare that they have no conflicts of interest to report regarding the present study.

References

1. Hu, X., Deng, S., Ren, H. (2017). In situ test study on freezing scheme of freeze-sealing pipe roof applied to the gongbei tunnel in the Hong Kong-Zhuhai-Macau Bridge. *Applied Sciences, 7(1),* 27. DOI 10.3390/app7010027.

2. Hu, X., Deng, S., Wang, Y. (2018). Analytical solution to steady-state temperature field with typical freezing tube layout employed in freeze-sealing pipe roof method. *Tunnelling and Underground Space Technology, 79,* 336–345. DOI 10.1016/j.tust.2018.06.014.
3. Hong, Z., Hu, X., Fang, T. (2020). Analytical solution to steady-state temperature field of freeze-sealing pipe roof applied to gongbei tunnel considering operation of limiting tubes. *Tunnelling and Underground Space Technology, 105,* 571. DOI 10.1016/j.tust.2020.103571.
4. Bronfenbrener, L., Bronfenbrener, R. (2010). Modeling frost heave in freezing soils. *Cold Regions Science and Technology, 61,* 43–64. DOI 10.1016/j.coldregions.2009.12.007.
5. Xia, C., Lv, Z., Wang, Y. (2020). Advance and review on frost heaving force calculation methods in cold region tunnels. *China Journal of Highway and Transport, 33,* 35–43. DOI 10.3969/j.issn.1001-7372.2020.05.003.
6. Miller, R. (1978). Frost heaving in non-colloidal soils. *Proceedings of 3rd International Conference on Permafrost*, pp. 708–713. Ottawa, Canada.
7. O'Neill, K., Miller, R. (1980). Numerical solutions for a rigid-ice model of secondary frost heave. *2nd International Symposium on Ground Freezing*, pp. 656–669. Trondheim, Norway.
8. Rajaei, P., Baladi, G. (2015). Frost heave: A semi-empirical model based on field data. *16th International Conference on Cold Regions Engineering*, pp. 382–393. Salt Lake City, Utah.
9. Lai, Y., Pei, W., Zhang, M., Zhou, J. (2014). Study on theory model of hydro-thermal-mechanical interaction process in saturated freezing silty soil. *International Journal of Heat and Mass Transfer, 78,* 805–819. DOI 10.1016/j.ijheatmasstransfer.2014.07.035.
10. Konrad, J., Morgenstern, N. (1981). The segregation potential of a freezing soil. *Canadian Geotechnical Journal, 18,* 482–491. DOI 10.1139/t81-059.
11. Konrad, J., Morgenstern, N. (1982). Effects of applied pressure on freezing soils. *Canadian Geotechnical Journal, 19,* 494–505. DOI 10.1139/t82-053.
12. Konrad, J. (1993). Frost heave in soil: Concepts and engineering. *Canadian Geotechnical Journal, 31,* 223–245. DOI 10.1139/t94-028.
13. Konrad, J. (2005). Estimation of segregation potential of finegrained soils using the frost heave response of two reference soils. *Canadian Geotechnical Journal, 42,* 38–50. DOI 10.1139/t04-080.
14. O'Neill, K., Miller, R. (1985). Exploration of a rigid ice model of frost heave. *Water Resources Research, 21,* 281–296. DOI 10.1029/WR021i003p00281.
15. Harlan, R. (1973). Analysis of coupled heat-fluid transport in partially frozen soil. *Water Resources Research, 9,* 1314–1323. DOI 10.1029/WR009i005p01314.
16. Fromend, M., Mikkola, M. (1991). Thermomechanical modeling of freezing soil. *Proceeding of 6rd Inernational Symposium on Ground Freezing*, pp. 17–24. Beijing, China.
17. Zheng, H., Kanie, S. (2015). Combined thermal-hydraulic-mechanical frost heave model based on Takashi's equation. *Journal of Cold Regions Engineering, 29(4),* 1–19. DOI 10.1061/(ASCE)CR.1943-5495.0000089.
18. Wu, Y., Zhai, E., Zhang, X., Wang, G., Lu, Y. (2021). A study on frost heave and thaw settlement of soil subjected to cyclic freeze-thaw conditions based on hydro-thermal-mechanical coupling analysis. *Cold Regions Science and Technology, 188,* 1–10. DOI 10.1016/j.coldregions.2021.103296.
19. Li, Z., Yao, X., Zhang, R., Shao, H., Wang, Z. (2020). Frost heave mechanical model of concrete lining trapezoidal canal considering nonuniform frost heave of foundation soil based on elastic foundation beam theory. *Nongye Gongcheng Xuebao/Transactions of the Chinese Society of Agricultural Engineering, 36(21),* 114–121. DOI 10.11975/j.issn.1002-6819.2019.15.015.
20. Lv, Z., Xia, C., Li, Q., Si, Z. (2019). Empirical frost heave model for saturated rock under uniform and unidirectional freezing conditions. *Rock Mechanics and Rock Engineering, 52(3),* 955–963. DOI 10.1007/s00603-018-1666-z.

21. Zheng, L., Gao, Y., Zhou, Y., Tian, S. (2020). Research on surface frost heave and thaw settlement law and optimization of frozen wall thickness in shallow tunnel using freezing method. *Yantu Lixue/Rock and Soil Mechanics, 41(6),* 2110–2121. DOI 10.16285/j.rsm.2019.1102.
22. Tang, L., Yang, L., Wang, X., Yang, G., Ren, X. et al. (2021). Numerical analysis of frost heave and thawing settlement of the pilesoil system in degraded permafrost region. *Environmental Earth Sciences, 80(20),* 1–19. DOI 10.1007/s12665-021-09999-4.
23. Feng, Q., Jiang, B. S., Zhang, Q., Wang, L. P. (2014). Analytical elasto-plastic solution for stress and deformation of surrounding rock in cold region tunnels. *Cold Regions Science and Technology, 108,* 59–68. DOI 10.1016/j.coldregions.2014.08.001.
24. Lai, Y., Wu, Z., Zhu, Y., Zhu, L. (2000). Elastic visco-plastic analysis for earthquake response of tunnels in cold regions. *Cold Regions Science and Technology, 31,* 175–188. DOI 10.1016/S0165-232X(00)00011-2.
25. Yang, P., Ke, J., Wang, J., Chow, Y., Zhu, F. (2006). Numerical simulation of frost heave with coupled water freezing, temperature and stress fields in tunnel excavation. *Computers and Geotechnics, 33,* 330–340. DOI 10.1016/j.compgeo.2006.07.006.
26. Zheng, L., Gao, Y., Zhou, Y., Liu, T., Tian, S. (2021). A practical method for predicting ground surface deformation induced by the artificial ground freezing method. *Computers and Geotechnics, 130,* 1–16. DOI 10.1016/j.compgeo.2020.103925.
27. Zhou, J., Zhao, W., Tang, Y. (2021). Practical prediction method on frost heave of soft clay in artificial ground freezing with field experiment. *Tunnelling and Underground Space Technology, 107,* 1–17. DOI 10.1016/j.tust.2020.103647.
28. Wen, Z., Sheng, Y., Jin, H. (2010). Thermal elasto-plastic computation model for a buried oil pipeline in frozen ground. *Cold Regions Science and Technology, 64,* 248–255. DOI 10.1016/j.coldregions.2010.01.009.
29. Na, S., Kebria, M., Roy, K. (2020). A coupled thermo-hydro-mechanical model for capturing frost heave under chilled gas pipelines. *13th International Pipeline Conference, IPC, Virtual, American Society of Mechanical Engineers (ASME)*, pp. 1–6. Calgary, AB, Canada.
30. Hawlader, B., Morgan, V., Clark, J. (2006). Modelling of pipeline under differential frost heave considering post-peak reduction of uplift resistance in frozen soil. *Canadian Geotechnical Journal, 43,* 282–293. DOI 10.1139/t06-003.
31. Taber, S. (1930). The mechanics of frost heaving. *Journal of Geology, 38,* 303–317. DOI 10.1086/623720.
32. Beskow, G. (1935). *Soil freezing and frost heaving with special application to roads and railroads.* The Swedish Geological Society Year Book No. 3. Chicago: Northwestern University.
33. Philip, J., DeVries, D. (1957). Moisture movement in porous material under temperature gradients. *Transaction of American Geophysical Union, 38,* 222–232. DOI 10.1029/TR038i002p00222.
34. Milly, C. (1982). Moisture and heat transport in hysteretic, in homogeneous porous medias: A matrix head-based formulation and a numerical model. *Water Resources Research, 18,* 489–498. DOI 10.1029/WR018i003p00489.

Computer Modeling in
Engineering & Sciences

Tech Science Press

DOI: 10.32604/cmes.2022.020386

ARTICLE

A Hybrid Regional Model for Predicting Ground Deformation Induced by Large-Section Tunnel Excavation

Shengjun Deng[1,2,3,*], **Yang He**[1], **Xiaonan Gong**[2], **Jiajin Zhou**[2] **and Xiangdong Hu**[4]

[1]Institute of Geotechnical Engineering, Nanjing Tech University, Nanjing, 210009, China

[2]Research Center of Coastal and Urban Geotechnical Engineering, Zhejiang University, Hangzhou, 310058, China

[3]Department of Civil and Environmental Engineering, Princeton University, Princeton, 08544, USA

[4]Key Laboratory of Geotechnical and Engineering of Ministry of Education, Department of Geotechnical Engineering, Tongji University, Shanghai, 200092, China

*Corresponding Author: Shengjun Deng. Email: sjdeng@njtech.edu.cn

Received: 20 November 2021 Accepted: 17 February 2022

ABSTRACT

Due to the large number of finite element mesh generated, it is difficult to use full-scale model to simulate large-section underground engineering, especially considering the coupling effect. A regional model is attempted to achieve this simulation. A variable boundary condition method for hybrid regional model is proposed to realize the numerical simulation of large-section tunnel construction. Accordingly, the balance of initial ground stress under asymmetric boundary conditions achieves by applying boundary conditions step by step with secondary development of Dynaflow scripts, which is the key issue of variable boundary condition method implementation. In this paper, Gongbei tunnel based on hybrid regional model involving multi-field coupling is simulated. Meanwhile, the variable boundary condition method for regional model is verified against model initialization and the ground deformation due to tunnel excavation is predicted via the proposed hybrid regional model. Compared with the monitoring data of actual engineering, the results indicated that the hybrid regional model has a good prediction effect.

KEYWORDS

Freeze-sealing pipe roof method; frozen soil; tunnel; regional model; dynaflow

1 Introduction

The ground surface deformation due to construction is one of the most concerning issues in shallow-buried underground excavation [1–4]. Finite element method is an effective method to explore the law. However, for large-section engineering, especially complex ones related to coupled moisture, heat and stress field, the computational efficiency is very low and the computational effort is large [5,6]. Due to the large size and complexity of the model, the mesh division is rough, thus the local details of the model may not be considered. It is difficult to ensure the precision of the concerned region. In consideration of computational effort and calculation precision for such large-scale model, a variable boundary condition method for hybrid regional model of underground engineering is proposed. As the size of the model is greatly reduced, the calculation efficiency and precision can be greatly improved, which makes some complex numerical simulation possible.

For the large-scale structure, there are two methods to deal with local regions. One is to refine the mesh of local region in the whole model, but only for the case where the whole model adopts the solid element and the shell element [7–9]. The other one is to extract the regional model in the overall model. In other words, the local finite element model is established separately and the meshing is refined. Then the corresponding boundary conditions and loads are applied to the truncated boundary of the whole model, and the finite element analysis is performed [10].

But for underground engineering, the model becomes more complicated because it involves the balance of initial ground stress [11]. This type of problem is achieved through large-scale model tests [12,13]. Therefore, there are few cases where underground engineering problems are solved through regional model. The difference between full-scale model and regional model is whether the boundary condition changes. Obviously, the boundary condition of regional model will change after the step of ground stress equilibration, which is the key issue. In this paper, Gongbei tunnel is taken as an example to simulate the regional model based on the script of a standard finite element package Dynaflow™ [14].

This paper presents hybrid regional model to realize the numerical simulation of such large-section tunnel construction, which is the first attempt in underground engineering. Two input files are written through secondary development of Dynaflow script to implement the calculation of hybrid regional model. The proposed hybrid regional model can realize the balance of ground stress under asymmetry boundary condition. The verification of the model is made by initialization and comparing the computational results of the model with the monitoring data. The computing realization of hybrid regional model can serve as a reference for similar large-section underground engineering.

2 Concept of Hybrid Regional Model

2.1 Hybrid Regional Model

Due to the ground stress equilibration involved, the core issue of using regional model to simulate an underground engineering case is the processing of boundary conditions. The simulation process is divided into two major stages, the balance of initial ground stress and the construction. As shown in Fig. 1, considering the symmetry of the model, the left half of the model is taken as a regional model. The model contains two parts of covering soil and the crown of the tunnel, where the crown part will be removed during excavation stage. In the stage of ground stress equilibration, the boundary conditions on the left and right sides are symmetrically distributed as shown in Fig. 1A. Once entering the construction stage, the boundary conditions on the left side will change, forming an asymmetrical state. Since the left side face is less constrained in vertical direction near the ground surface, other parts are restricted by more the surrounding soil, which can be approximated as complete constraints. Therefore, vertical constraint is added to the left boundary to simulate the constraints of the lateral soil, shown in Fig. 1B.

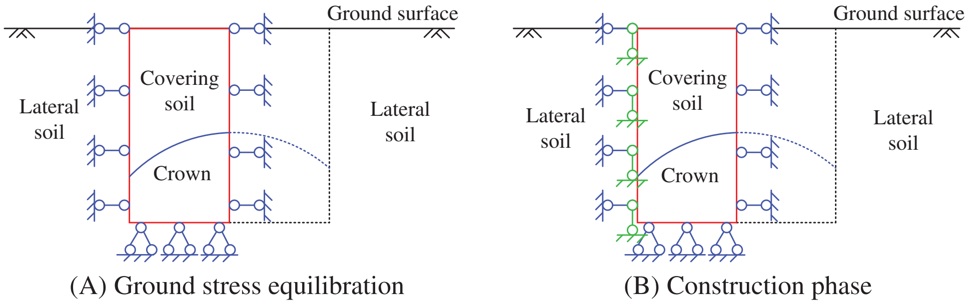

(A) Ground stress equilibration (B) Construction phase

Figure 1: Boundary conditions of hybrid regional model at different phases

2.2 *Model Strategy for Tunneling Simulation*

Considering that the ground stress equilibration can only be carried out under symmetric boundary condition, in order to set up the boundary conditions under asymmetric condition, the process needs to be divided into two steps, corresponding to two input files, file A and file B.

The simulation is performed by the script of Dynaflow™, which is a finite element software. The preprocessing of hybrid regional model depends on Gmesh [15], which is a three-dimensional finite element grid generator with a build-in CAD engine and post-processor. Its design goal is to provide a fast, light and user-friendly meshing tool with parametric input and advanced visualization capabilities, while the post processing depends on FemGV [16], which is a general purpose pre-and post-processor for Finite Element Analysis (FEA) software. The calculation flow is shown in Fig. 2. As described above, the implementation of boundary condition is divided into two steps. Input file A is responsible for the calculation of the ground stress equilibration stage. The ground stress result of input file A is called by input file B as initial ground stress state of construction stage, which is not affected by the asymmetric boundary condition applied later. The above introduction is the main framework of regional model simulation. Finally, the implementation and verification of the hybrid regional model script will be reflected in the Gongbei tunnel case.

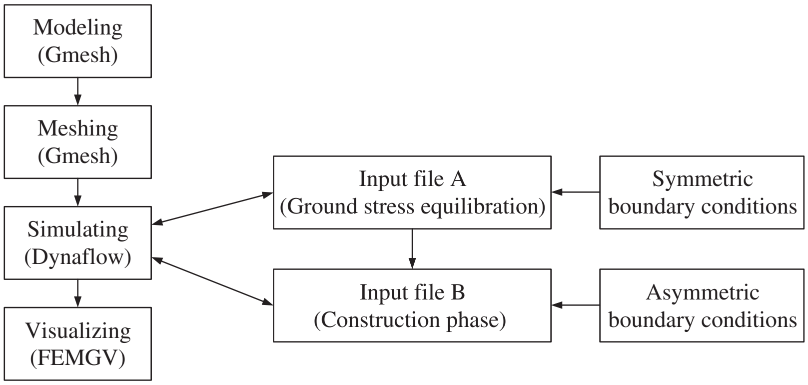

Figure 2: Calculation procedure

3 Application of Hybrid Regional Model in 3D Tunneling Simulation

3.1 Brief Description of Gongbei Tunnel

The Freeze-Sealing Pipe Roof (FSPR) method is applied to Gongbei tunnel that is a critical link of Hongkong-Zhuhai-Macau Bridge. Meanwhile, it is the first application in the world. The definition of FSPR method is that large diameter steel pipes are laid out in a circle around the cross section of tunnel in advance, and then the artificial ground freezing method is adopted to freeze soil between pipe roof to form waterproof curtain [17,18]. The freezing tubes that circulates low temperature brine installed inside the roofing pipes [19]. Fig. 3 shows the original design of the pipe roofing, which consists of 36 pieces of 1620 mm diameter roofing pipes around the circumference of excavation. The spacing between the pipe edges ranges between 35.5 and 35.8 cm. In the normal direction of the tunnel circumference, the odd number roof pipes are shifted by 30 cm to the tunnel direction with respect to the even diameter pipes. The excavation cross-sectional area is approximately 345 m^2 with 18.8 m in width and 20.6 m in height, which is the largest single tunnel excavation in China. The tunnel is buried within soft sandy about 4.5 m below the ground surface at the Gongbei customer port.

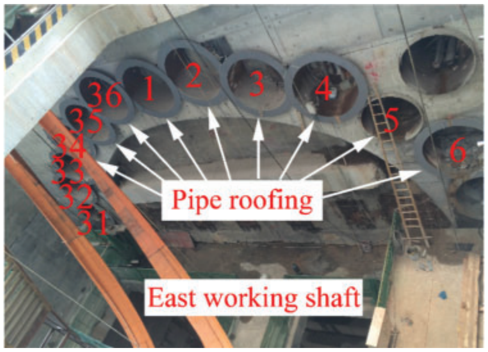

Figure 3: Layout of the pipe-roofing

Some scholars did research about the mechanical mechanism of steel pipes-frozen soil composite structure through laboratory test. A preliminary model test study of simplified composite structure with two pipes and three pipes was conducted, respectively [20–23]. Few scholars did research about combined pipe roof and frozen soil structure, especially with finite element method. The reason is that the model is too large and complex so that the computational efficiency is extremely low and the computational effort is large, which is also the issue to be solved in this paper.

There're three stages before excavation, pipe jacking, concrete filling and ground freezing. The roofing pipes are designed to be jacked section by section with a sectional length of 4 m from the construction shaft at one end of the tunnel alignment and received in the construction shaft at the other end of the tunnel alignment. To control the ground movement during pipe jacking, small tunnel boring machines (TBMs) are applied to tunnel through the ground, followed by the jacking of the pipe sections [24,25]. And then concrete will be filled into the odd pipes, which is good for heat conduction. After that, ground freezing will last 50 days before tunnel excavation and the thickness of frozen soil should be in control of 2∼2.6 m during construction. Supports and lining will be used during and after excavation. Concrete backfilling of even pipes and thawing process will be carried out after the completion of excavation.

3.2 Geometry Model

In consideration of mesh scale effect and computational capability, the local part of the composite structure was chosen to simulate. Fig. 4A shows that local symmetry model is located at the top of the FSPR composite structure, including one hollow steel pipe and half of concrete-filled steel pipe. The geometry of hybrid regional model is shown in Fig. 4B. The distance between the top point of concrete-filled steel pipe and ground surface is 4.5 m. The diameter of the steel pipe is 1.62 m with 0.02 m thickness. The space between two pipes is 0.355 m.

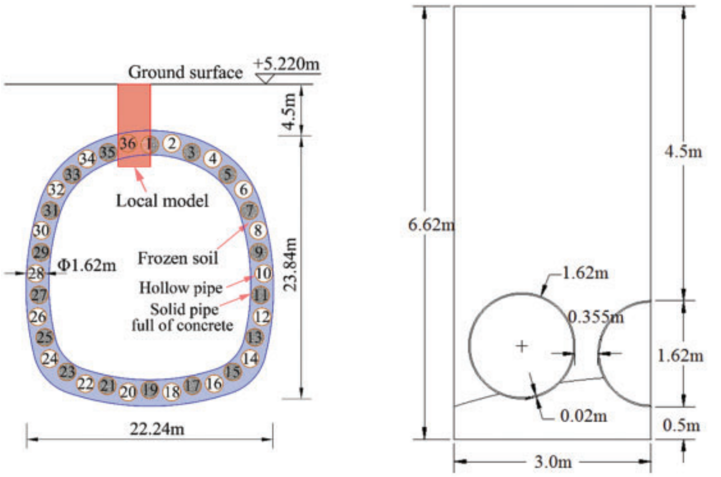

(A) Position of regional model (B) Geometry of local symmetry model

Figure 4: Local simulation model

3.3 3D Finite Element Model

According to the simplified model above, Fig. 5 is 3D mesh model of the hybrid regional model with 0.8 m thickness, which is the maximum excavation length for each step. 3D model can reflect the longitudinal force characteristics more than 2D, which is closer to the real working condition. There are 6 parts in the model, which is made up of soil, steel pipes, concrete. There are 5134 nodes and 31505 elements in total.

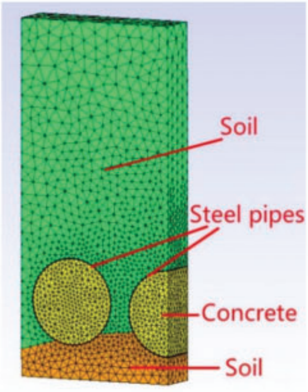

Figure 5: 3D mesh model

3.4 Boundary Conditions

In actual construction, tunnel excavation starts from the top of the crown where the deformation is the largest. Fig. 6 shows the region of the hybrid regional model under the observation of inside view of the tunnel. It shows the soil excavation section and the lower half part of the steel pipe only. The upper half part of the model extending to the surface is hidden in the soil.

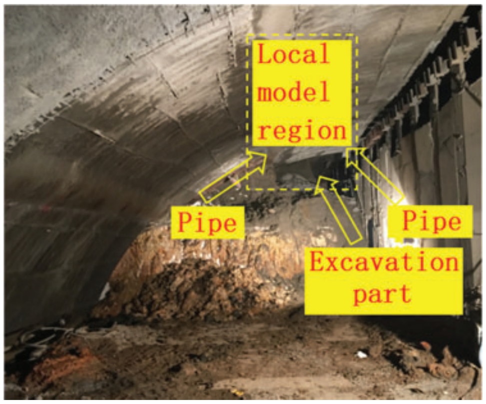

Figure 6: Hybrid regional model region of actual construction

The constraints of each face of actual project are shown in Fig. 7A. The upper surface y_b perpendicular to the y-axis is free, the lower surface y_0 is constrained by the vertical y direction; the right-side surface x_0 perpendicular to the x-axis is the symmetry axis surface, constrained by the horizontal x direction, while the left of left-side surface x_a is soil, subject to horizontal x constraints and incomplete constraints in the vertical y direction. The faces z_0 and z_c perpendicular to the z-axis are constrained by the constraints of horizontal z direction and incomplete constraints of vertical y direction. In actual construction, the constraining force along the faces z_0 and z_c of tunnel excavation direction (z-axis) are different. The lower part of steel pipe of the face z_c is restrained by the y direction support, the upper part is incompletely constrained by the surrounding soil, while the face z_0 is affected by the surrounding soil too, which is incompletely constrained.

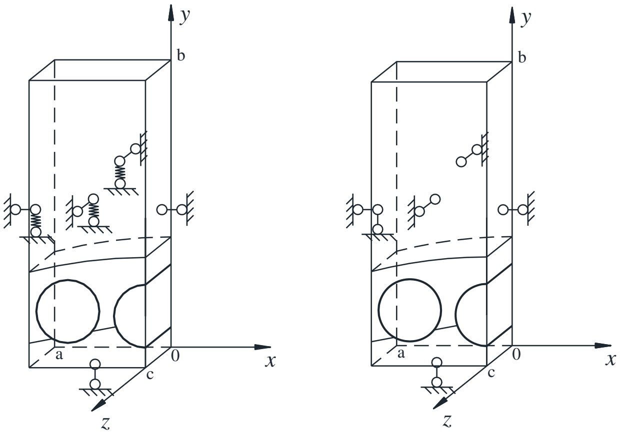

(A) Actual project model (B) Simplified model

Figure 7: Boundary condition of hybrid regional model

The incomplete constrain mentioned above is related to the displacement and restraint capability of the face itself. The constraining force on the faces are different and the situation is more complicated. In Fig. 7A, the constraint is represented by a spring. Due to tunnel length of 255 m, the cross-sectional size and shape do not change along the tunnel excavation direction (z-axis). The force of the tunnel is perpendicular to the excavation direction, and there is no change along the excavation direction. And the thickness of model is only 0.8 m, which is very small relative to the full length of the tunnel. According to that, it can be seen as a plane strain problem, thus the faces z_0 and z_c perpendicular to z-axis can be simplified as z direction constraints, shown in Fig. 7B. Since the left side face is less constrained in the y direction near the ground surface, other parts are restricted by more the surrounding soil, which can be approximated as complete constraints. Therefore, the incomplete constraint of the left side face x_a in the y direction can be simplified to full constraint, and the node constraint at the surface can be released to approach the actual engineering situation. The simplified model is shown in Fig. 7B. Due to the complexity of the actual constraints, the node constraints on the same boundary face are different, and it is difficult to precisely simulate. Thus, the actual model and the simplified model have a little differences, but it does not affect the qualitative guidance for the project. This paper aims to achieve a preliminary simulation of the hybrid regional model and provides a new idea for the calculation of complex models of underground engineering. The processing of boundary conditions needs to be gradually improved through new methods.

The balance of initial ground stress under asymmetric boundary conditions is the key to the implementation of hybrid regional model. Unlike full-scale model, the boundary condition of hybrid regional model will change after ground stress equilibration. In order to realize such process, the boundary condition of different direction should be added step by step. Thus, the process is divided into two steps. Fig. 8 is the front view of local symmetry model along the excavation direction. Fig. 8A represents the boundary condition when ground stress balances. There is only one direction boundary condition on the left face. The Fig. 8B represents the actual working condition. There are two directions boundary condition on the left face. The difference between two steps is the vertical constraint of the left boundary.

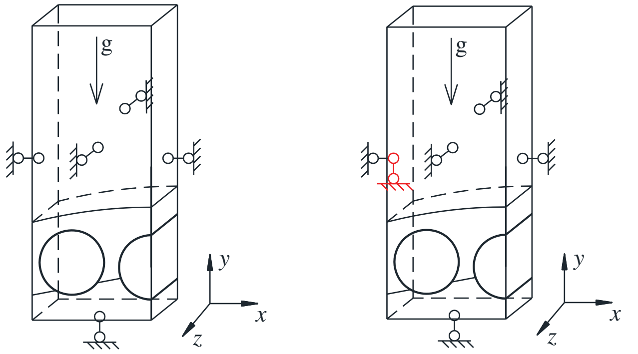

(A) The first step (origin) (B) The second step (restart)

Figure 8: Two steps of boundary conditions for hybrid regional model

As the calculation flow described in Section 2, the first step and second step are respectively implemented by input file A and input file B. In file A, the result of ground stress equilibration is recorded and inputted to file B as initial step. In file B, boundary condition shown in Fig. 8B works after initialization.

There are gravity, water pressure and temperature in simulation. The initial soil temperature is 28°C. The water pressure is distributed evenly and the initial water pressure of ground surface is 0.

3.5 Governing Equation

The simulation of this model considers the stress field [26–28], temperature field [29] and hydraulic field [30]. Each part satisfies the following equations. The constitutive model of Mohr-Coulomb is adopted in soil material [31].

(1) Solid equation can be expressed as Eq. (1)

$$\nabla \cdot (\underset{\sim}{\sigma} - \underset{\sim}{\beta}\theta\underset{\sim}{\delta}) + \rho\underset{\sim}{b} = 0 \tag{1}$$

where $\underset{\sim}{\sigma}$ represents soil stress, $\underset{\sim}{b}$ represents body force (per unit mass), ρ represents mass density, θ represents temperature, $\underset{\sim}{\beta}$ represents thermal moduli, $\underset{\sim}{\beta} = \frac{E}{1-2\mu}\underset{\sim}{\alpha}$, $\underset{\sim}{\alpha}$ represents thermal expansion moduli.

For saturated porous media applications, it can be expressed as Eq. (2).

$$\underset{\sim}{\sigma} = \underset{\sim}{\sigma}'^{S} - bp^{w}\underset{\sim}{\delta} \tag{2}$$

where $\underset{\sim}{\sigma}'^{S}$ represents solid effective stress, p^{w} represents pore fluid pressure, $b = 1 - C_s/C_m$; C_s represents solid grains compressibility, C_m represents solid matrix compressibility; total mass density $\rho = \rho^{s} + \rho^{w}$, solid mass density $\rho^{s} = (1-\varphi)\rho_s$, fluid mass density $\rho^{w} = \varphi\rho_w$, ρ_s represents solid mass density, ρ_w represents fluid mass density, φ represents porosity.

(2) Heat equation can be expressed as Eq. (3)

$$\rho c\frac{d\theta}{dt} - \nabla \cdot [k \cdot \nabla\theta] = \rho h \tag{3}$$

where θ represents temperature, $\underset{\sim}{k}$ represents thermal conductivity, ρ represents mass density, c represents specific heat, h represents heat source.

(3) Darcy flow equation can be expressed as Eq. (4)

$$\nabla \cdot \left[\frac{\underset{\sim}{k}}{\mu} \cdot (\nabla p - \rho\underset{\sim}{b})\right] = 0 \tag{4}$$

where $\underset{\sim}{k}$ represents hydraulic conductivity, μ represents fluid viscosity, p represents fluid pressure, ρ represents fluid mass density, $\underset{\sim}{b}$ represents body force (per unit mass).

(4) Mohr-coulomb model

The yield function is of the following type:

$$f = \sqrt{\frac{3}{2}tr\underset{\sim}{s}^{2}} + \frac{6\sin\varphi}{3-\sin\varphi}(p-a)g(\theta) \tag{5}$$

In which: $a = c/\tan\varphi$, c represents cohesion, φ represents friction angle, $\underset{\sim}{s} = \underset{\sim}{\sigma} - p \underset{\sim}{\rightarrow} \delta'$, $p = \frac{1}{3}tr\underset{\sim}{\sigma}$

Among Eq. (5), $g(\theta)$ can be expressed as Eq. (6).

$$g(\theta) = \frac{2M_k}{(1 + M_k) - (1 - M_k)\sin 3\theta} \tag{6}$$

In which: $\sin 3\theta = -\sqrt{6}\bar{J}_3/\bar{J}_2^{3/2}$, $\bar{J}_2 = tr\underset{\sim}{s}^2$, $\bar{J}_3 = tr\underset{\sim}{s}^3$, $M_k = \frac{3-\sin\theta}{3+\sin\theta}$

According to the governing equation above, the relationship between each one is associated through common parameters. Fig. 9 shows the coupling process of hydro-thermal-mechanical field, which is implemented in Dynaflow. The relationship between elastic module and temperature is in Eq. (7).

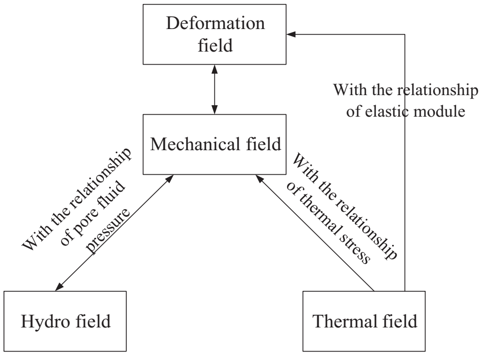

Figure 9: Schematic of the hydro-thermal-mechanical coupling process

3.6 Material Property

Soil material is simulated by Mohr-Coulomb yield criteria. Roofing pipes and concrete materials are set up on the basis of elastic theory. Due to the diversity of soil layers based on Chinese standard of JTG D63–2007, it is considered as homogeneous soil here for the convenience of analysis [32]. Table 1 shows different material parameters of this model [33]. Table 2 shows the mechanical, hydraulic and thermal properties of soil [34].

Table 1: Parameters of general properties

Classifications	Density(kg/m^3)	Poisson ratio	Elastic modulus(Pa)
Soil	1950	0.29	2.0e+7
Roofing pipe	7850	0.3	2.06e+11
Concrete	2400	0.2	3.0e+10

According to the test of laboratory, we know that the temperature have effect on the material parameters. The relationship of material parameters and temperature of frozen soil lists below, shown in Table 3. Thus, the functional relationships between elastic module and temperature is written into the finite element program by script.

Table 2: The general mechanical, hydraulic and thermal properties of soil

Classifications	Parameters	Value
Mechanical parameters	Fluid mass density(kg/m^3)	1.0e+3
	Fluid bulk modulus(Pa)	2.0e+9
	Porosity	0.2
	Cohesion(Pa)	100
	Internal friction angle	27
	Calculate mobilized friction angle(Pa)	6.2e+6
Hydraulic parameters	Fluid compressibility(Pa^{-1})	4.5e-10
	Grains compressibility(Pa^{-1})	1.0e-7
	Mobility(m/s)	1.0e-10
Thermal parameters	Specific heat capacity of soil matrix(J/(kg°C))	1450
	Specific heat capacity of fluid(J/(kg°C))	4200
	Specific heat capacity of roofing pipe(J/(kg°C))	450
	Thermal expansion of soil(°C^{-1})	12.e-6
	Thermal expansion of pipe(°C^{-1})	18.e-6
	Thermal conductivity(w/(m k))	1.8

Table 3: Elastic modulus with temperature

Temperature(°C)	-5	-10	-15
Elastic modulus(Pa)	4.7e+7	8.3e+7	12.2e+7

Note: where the parameter determination of frozen soil is carried out in a low temperature condition.

The fitting formula of elastic modulus is as follows, which represents the effect of temperature field on stress field.

$$E(T) = -4143T^3 + 191773T^2 - (2.e + 6)T + (3.e + 7) \tag{7}$$

where T satisfies the following range: $-15^\circ\mathrm{C} \le T \le 28^\circ\mathrm{C}$.

3.7 Simulation Procedure

To make the step time of construction simulation as real as possible, time dependence should be taken into account. There are 227 steps of the numerical simulation, which contains the process of initialization, pipe jacking, soil digging, backfilling pipe with concrete, freezing, tunnel excavation. The time for each construction step is simulated and the arrangement of each step shows in Table 4.

The thermo-hydro-mechanical coupling model is divided into 9 zones, including 23 groups. It is illustrated by the following Table 5, which corresponds to script.

Table 4: Table of stage arrangement

Phases	Stagger	Pressure	Stress	Temperature	Duration	Steps	Time
Initialization						step0	0
	stagger1, 2, 3	pressure0	stress0	temperature0	0.235 d		
Pipe inserted						step1	t1
	stagger4, 5	consolidation1		temperature1	0.235 d		
Soil digging						step2	t2
	stagger6, 7	consolidation2		temperature2	0.235 d		
Fill concrete						step3	t3
	stagger8, 9	consolidation3		temperature3	0.235 d		
Freezing process						step4	t4
	stagger10, 11	consolidation4		temperature4	51.759 d		
Excavation						step224	t5
	stagger12, 13	consolidation5		temperature5	0.7 d		
End					53.4 d	step227	t6

Note: where d = day, dt = 0.235 day, t1 = “dt” = 0.235 day, t2 = “2∗dt” = 0.471 day, t3 = “3∗dt” = 0.706 day, t4 = “4∗dt”= 0.941 day, t5 = “224∗dt”= 52.7 days, t6 = “227∗dt”= 53.4 days, consolidation means the coupled of water pressure and stress.

Table 5: Grouping table

Regions	Solid	Moi	Heat
zone1(upper soil)	S1(GROUP1)	D1(GROUP2)	H1(GROUP3)
zone2(lower soil)	S2(GROUP4)	D2(GROUP5)	H2(GROUP6)
zone3(digging soil)	S3(GROUP7)	D3(GROUP8)	H3(GROUP9)
zone4(digging soil)	S4(GROUP10)	D4(GROUP11)	H4(GROUP12)
zone5(left soil)	S5(GROUP13)	D5(GROUP14)	H5(GROUP15)
zone6(right soil)	S6(GROUP16)	D6(GROUP17)	H6(GROUP18)
zone7(left pipe)	S7(GROUP19)		H7(GROUP20)
zone8(right pipe)	S8(GROUP21)		H8(GROUP22)
zone9(concrete)	S9(GROUP23)		

Note: where “left soil” means the soil at the original position of left pipe. Similarly, the “right soil” means the soil at the original position of right pipe. “Lower soil” means the excavation part. “Digging soil” means soil inside the pipes.

Partition sketch of each phase is shown in Fig. 10. The model of initialization contains zone1(S1,D1,H1), zone2(S2,D2,H2), zone3(S3,D3,H3), zone4(S4,D4,H4), zone5(S5,D5,H5), zone6 (S6,D6,H6), shown in Fig. 10A. The pipe inserted phase contains zone1(S1,D1,H1), zone2(S2,D2,H2), zone3(S3,H3), zone4(S4,H4), zone7(S7,H7), zone8(S8,H8), shown in Fig. 10B, which indicates that the soil of zone5, zone6 in original area was replaced by the pipe of zone7, zone8. The soil digging phase contains zone1(S1,D1,H1), zone2(S2,D2,H2), zone7(S7,H7), zone8(S8,H8), which means the soil of zone3, zone4 was removed, shown in Fig. 10C. The phases of fill concrete and freezing process contains zone1(S1,D1,H1), zone2(S2,D2,H2), zone7(S7,H7), zone8(S8,H8), zone9(S9), which means the concrete element of zone9 was activated, respectively shown in Figs. 10D and 10E. The excavation phase contains zone1(S1,D1,H1), zone7(S7,H7), zone8(S8,H8), zone9(S9), which means the lower soil of zone2 was removed, shown in Fig. 10F.

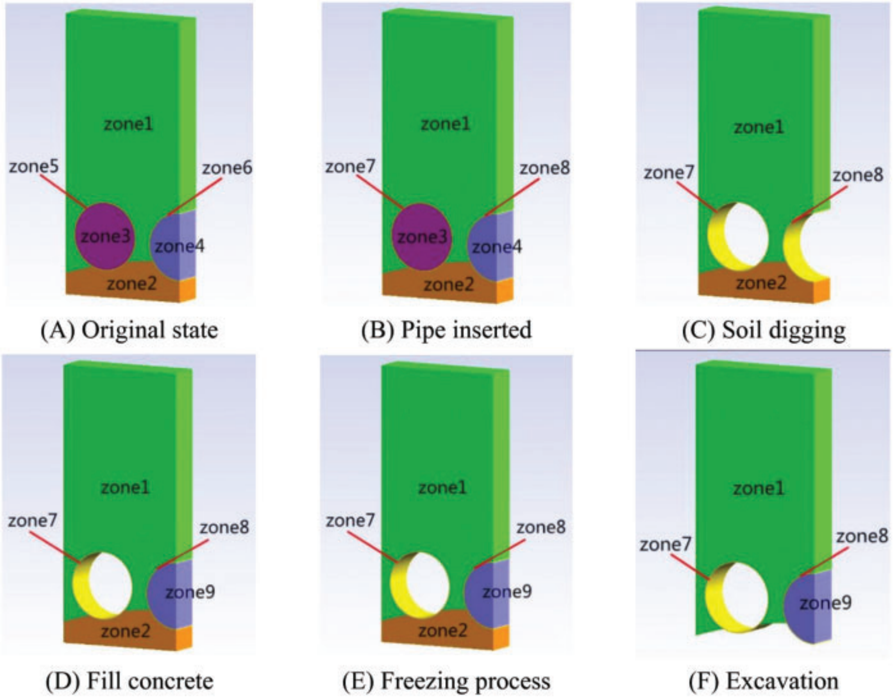

(A) Original state (B) Pipe inserted (C) Soil digging

(D) Fill concrete (E) Freezing process (F) Excavation

Figure 10: Partition sketch of each phase

4 Results and Discussion

4.1 Verification against Model Initialization

In order to assess the applicability of the proposed hybrid regional model, the construction simulation of Gongbei tunnel is performed. The first step is to verify the initialization of the model.

The duration of initialization is 0.22 day, which means enough time for distribute initial water pressure, temperature and ground stress. The initial vertical stress is assumed to be lithostatic. The experiments in laboratory were conducted to get the basic physical-mechanical parameters, which was directly relevant to simulated precision. The initialization is the key step to ensure the accuracy of model. The model of initialization contains zone1(S1,D1,H1), zone2(S2,D2,H2), zone3(S3,D3,H3), zone4(S4,D4,H4), zone5(S5,D5,H5), zone6(S6,D6,H6). Initial temperature is 28°C, shown in Fig. 11A. The temperature distribution is reasonable. Initial pore water pressure and ground stress have rational distribution, respectively shown in Figs. 11B and 11C. The initial pore water pressure is assumed to be hydrostatic pressure and the value gradually increases with depth. That is to say, the initial ground stress has a similar pattern to initial water pressure. As shown below, the initialization of temperature-water pressure-stress was successfully implemented, which verified the correctness of hybrid regional model.

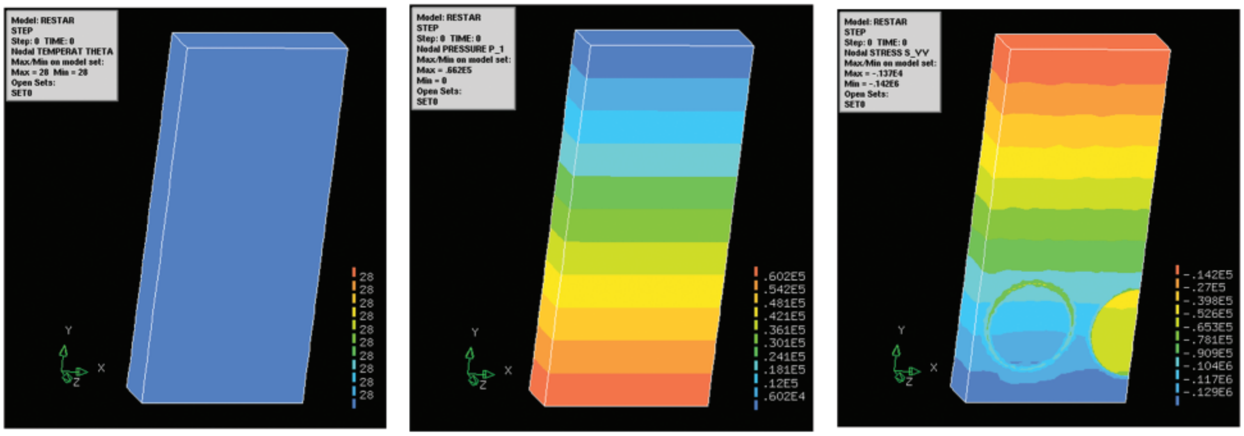

(A) Initial temperature (28°C) (B) Initial pore water pressure (C) Initial stress S_YY

Figure 11: Initialization of temperature-water pressure-stress

4.2 Simulation Results

4.2.1 Feature Points of the Model

In order to facilitate the analysis, typical feature points are set to describe the results. There are four feature points in the model, which are shown in Fig. 12. P1 is located in the ground surface. P2 is located in the top of the right steel pipe. P3 is located in the bottom of the right steel pipes. And P4 is located between two pipes. The temperature, water pressure and displacement are respectively analyzed.

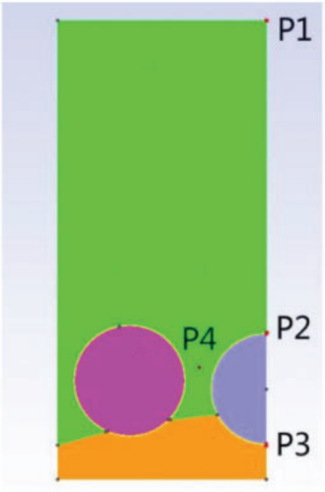

Figure 12: Feature points of the model

4.2.2 Thermal Behavior

The artificial ground freezing technique is the key to the project. So temperature changes should be paid more attention. The initial temperature is 28°C, shown in Fig. 13A. After backfilling steel pipe with concrete, freezing process begin. The surface temperature of steel pipe is −10°C and spread all around, shown in Fig. 13B. According to Fig. 13C below, frozen curtain of over 2 m thickness is formed and maintained in 50 days. Thus the time for freezing is reasonable. And the thickness of frozen soil meet the requirements of 2 m.

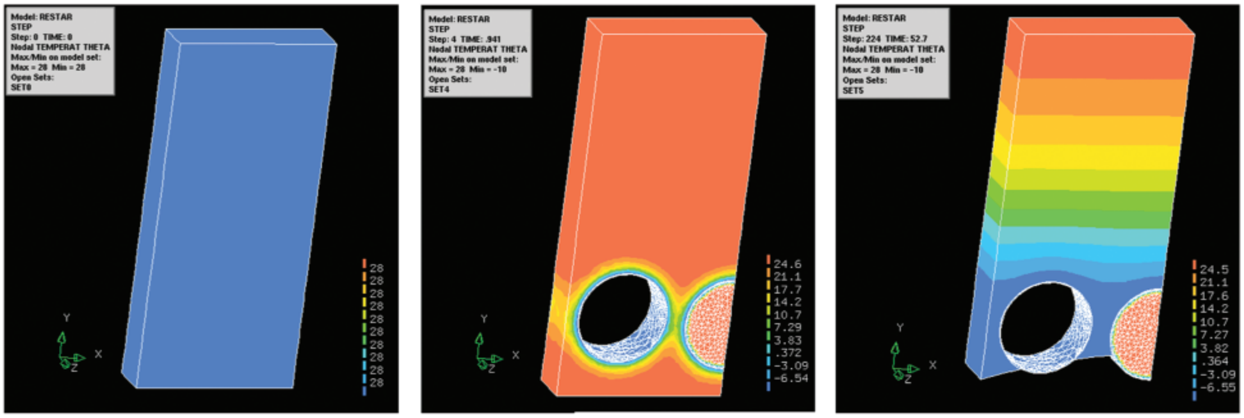

(A) Initialization (B) Freezing process (C) Excavation

Figure 13: Temperature of each phase

Feature point P1 of ground surface is far away from cold source, and the cold amount is difficult to diffuse to ground surface in 50 days, so the temperature is always 28°C, shown in Fig. 14A. Feature point P2 and P3 was respectively located at the top and bottom of the right steel pipe. At first, the temperature is 28°C. Then the temperature suddenly drops to −10°C when freezing process begin, shown in Figs. 14B and 14C. P4 represents the soil temperature between steel pipes. The temperature gradually varies from 28°C to −8°C within 40 days during the freezing phase, shown in Fig. 14D. The temperature of feature points indicates that temperature change goes well and duration of freezing is reasonable.

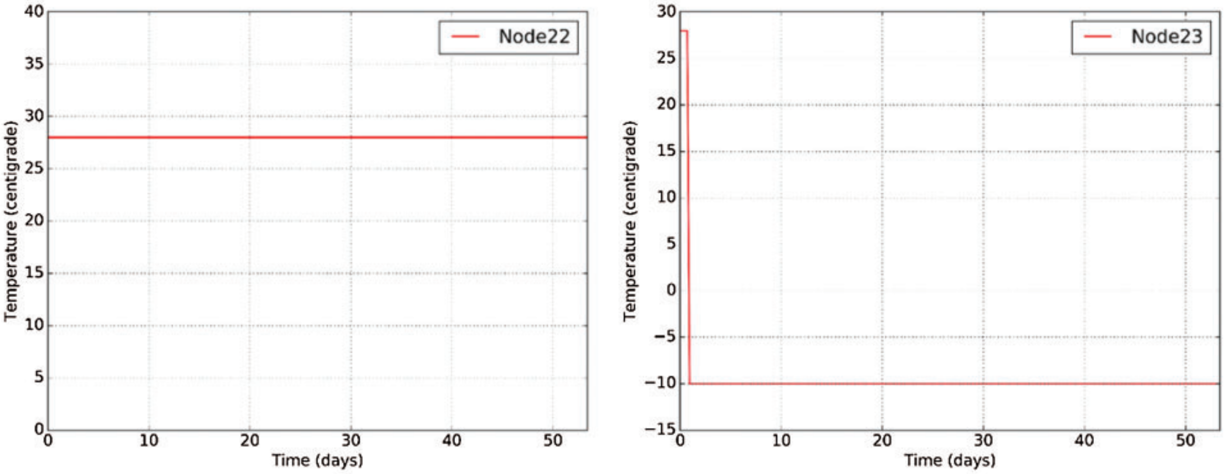

(A) P1 (B) P2

Figure 14: (Continued)

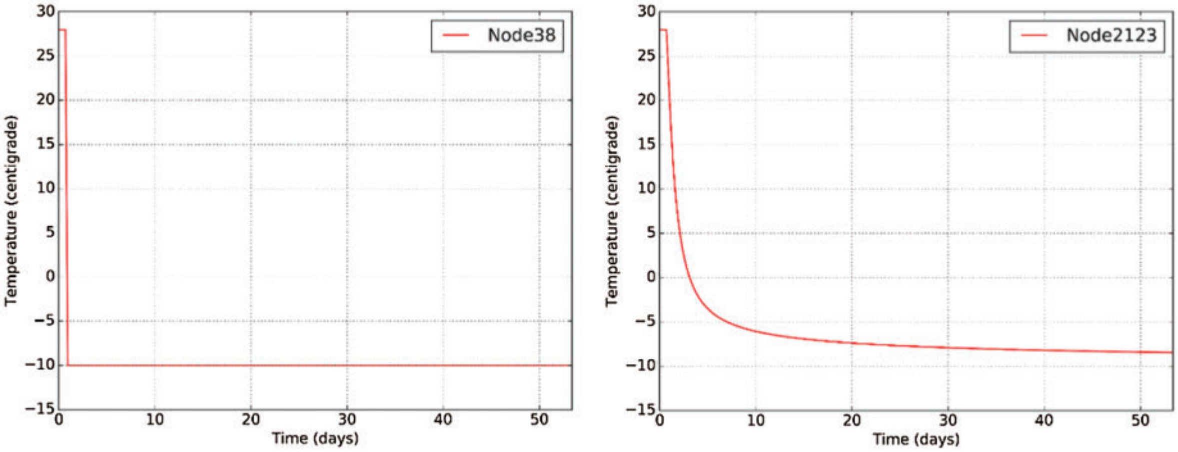

(C) P3 (D) P4

Figure 14: Temperature of feature point

4.2.3 Hydraulic Behavior

Groundwater is one of the most important factors to influence the safety of tunnel construction. The distribution of water pressure ran uniformly in this project. The construction steps had only a little effect on it, and could be redistributed in short time. The value of ground surface point P1 is always 0 in Fig. 15A, because the construction had little effect on the position far away. Feature points P2 and P4 had the same law curve, which was respectively shown in Figs. 15B and 15D. The maximum water pressure reached 0.0465 MPa after backfilling the concrete. In the freezing process, the water pressure decreased with the time until smooth. When excavation, a sudden increase occurred and restored for redistribution in one or two days. There was a sudden drop in the water pressure about P3 when excavation, shown in Fig. 15C, because water pressure redistributed with the removing of bottom part. Thus, excavation step should be paid more attention to prevent leakage, which is a potential hazards in this project.

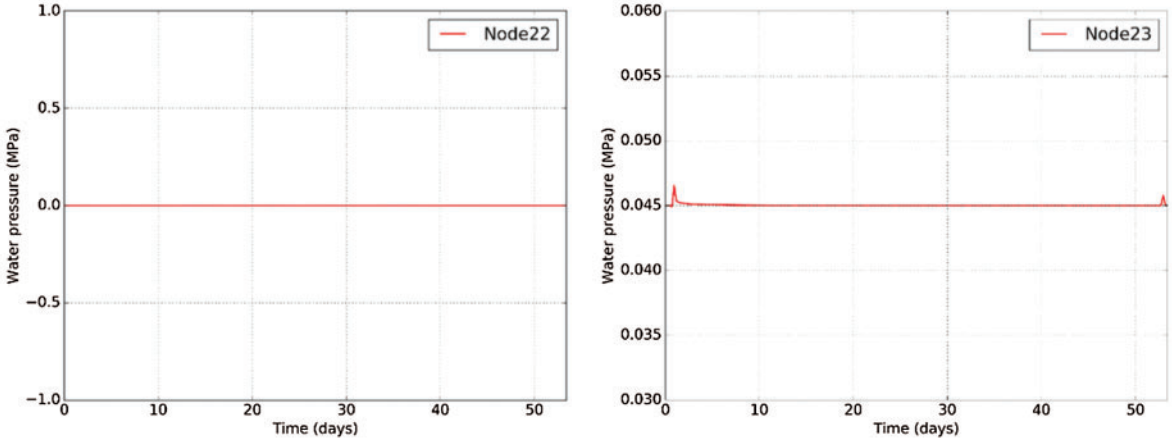

(A) P1 (B) P2

Figure 15: (Continued)

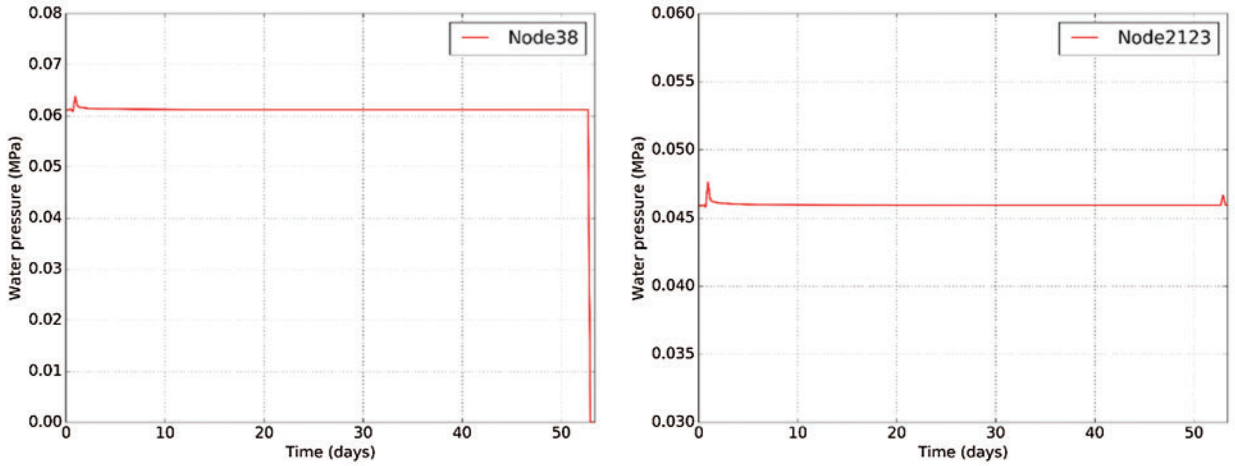

(C) P3 (D) P4

Figure 15: Water pressure of feature point

4.2.4 *Mechanical Behavior*

The deformation as an intuitive index varies with each step. To visualize the deformation of each construction step, vector diagram is used to display, shown in Fig. 16. Deformation changes at each step. The maximum deformation occurs during excavation phase. The deformation of ground surface increases from left to right.

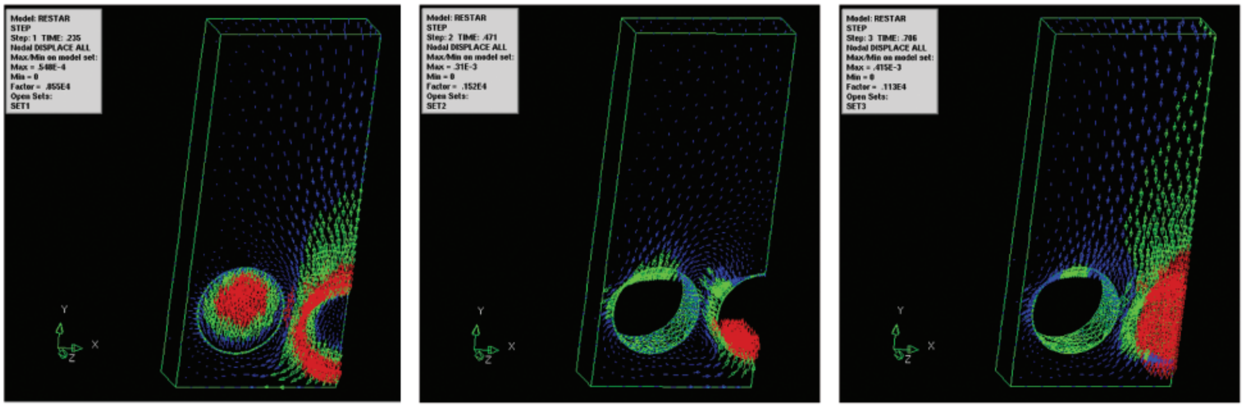

(A) Pipe inserted (B) Soil digging (C) Fill concrete

Figure 16: (Continued)

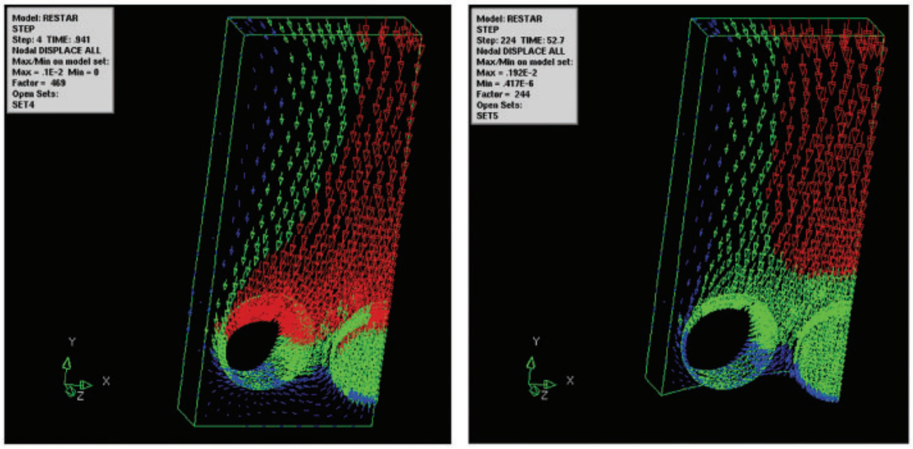

(D) Freezing process (E) Excavation

Figure 16: Vector diagram of each phase

The feature point P1 of ground surface decreases with the freezing process and rapidly decreases when excavation, shown in Fig. 17A. The maximum settlement of P1 is 3.01 mm. The vertical displacement of feature point P2 at the top of right steel pipe decreases with the temperature reducing and rapidly decreases when excavation, shown in Fig. 17B. The maximum vertical displacement of P2 is 4.26 mm, which is the maximum displacement among feature points. Meanwhile, the value is in an acceptable range of the project. The vertical displacement of feature point P3 at the bottom of right steel pipe decreases with the freezing process and rapidly decreases when excavation, shown in Fig. 17C. The maximum vertical displacement of P3 is 3.80 mm. The vertical displacement of feature point P4 between two steel pipes decreases with the freezing process and rapidly decreases when excavation, shown in Fig. 17D. The maximum vertical displacement of P4 is 1.82 mm.

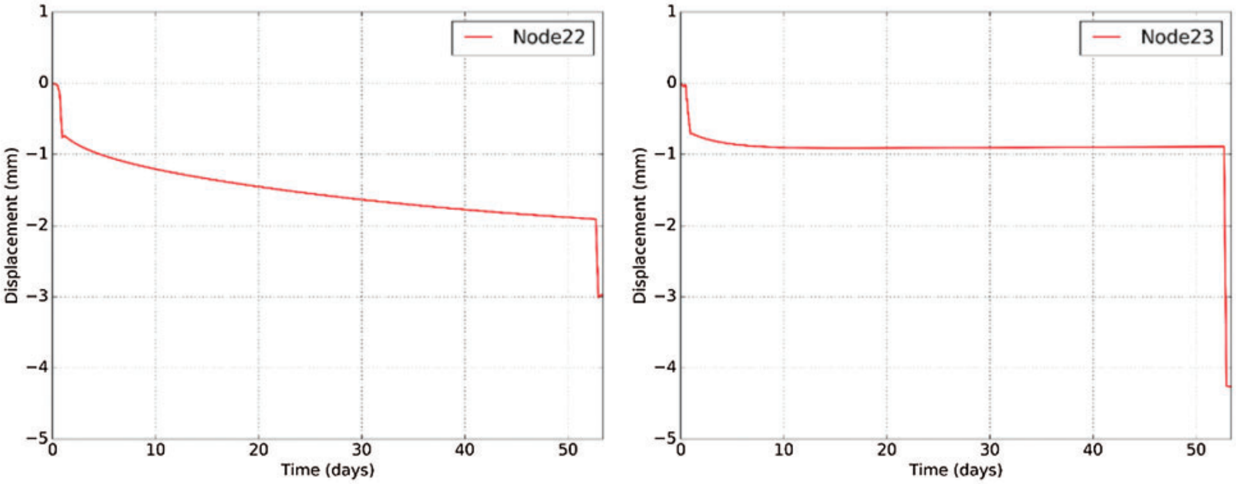

(A) P1 (B) P2

Figure 17: (Continued)

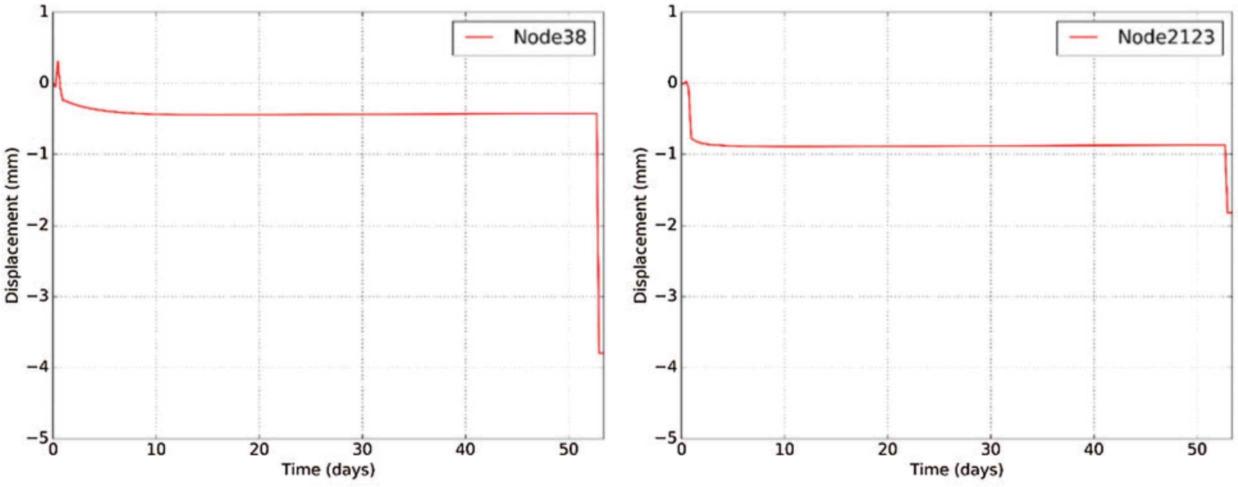

(C) P3 (D) P4

Figure 17: Vertical displacement of feature points

The maximum vertical displacement of each step was shown in Fig. 18. The maximum vertical displacement appeared at the top of right steel pipe with the value of 0.0548 mm when steel pipe was inserted. The maximum vertical displacement appeared at the bottom of right pipe with the value of 0.31 mm vertical up when the soil was removed. The maximum vertical displacement appeared at the top of right steel pipe with the value of 0.415 mm when the right steel pipe was filled with concrete. As the steel pipe has good rigidity, there is little displacement. At the beginning of freezing process, the vertical displacement changes to 1 mm with the effect of temperature and water pressure, which appeared at the center of ground surface. After excavation, the maximum vertical displacement appeared at the top of right steel pipe with the value of 4.26 mm.

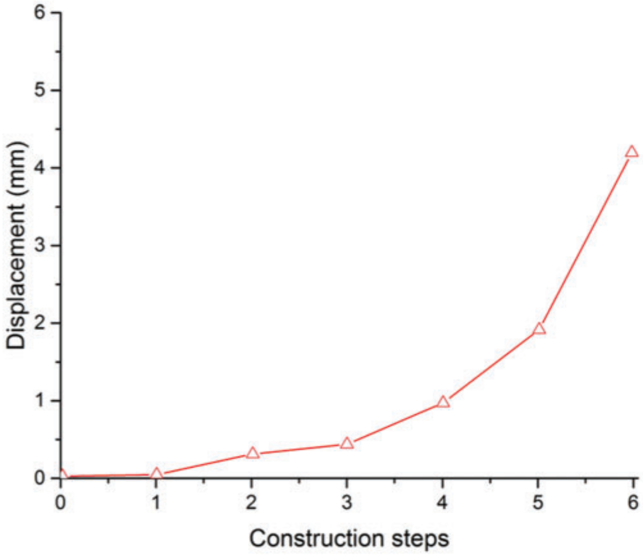

Figure 18: Maximum vertical displacement of each step

The deformation of ground surface was also an important index to reflect the safety of the project. Considering the symmetry of the model, the settlement curve presents the form of normal distribution. The maximum displacement of ground surface appeared at the point P1 with the value of −2.98 mm. In order to further verify the accuracy of the proposed hybrid regional model, the results calculated by the present method are compared with the monitoring data of actual project. As shown in Fig. 19, both two curves have a reasonable agreement. In addition, the large deviation of individual monitoring values is due to construction factors such as local grouting and frost heaving. Therefore, the result of the hybrid regional model is in a reasonable and acceptable range of this project.

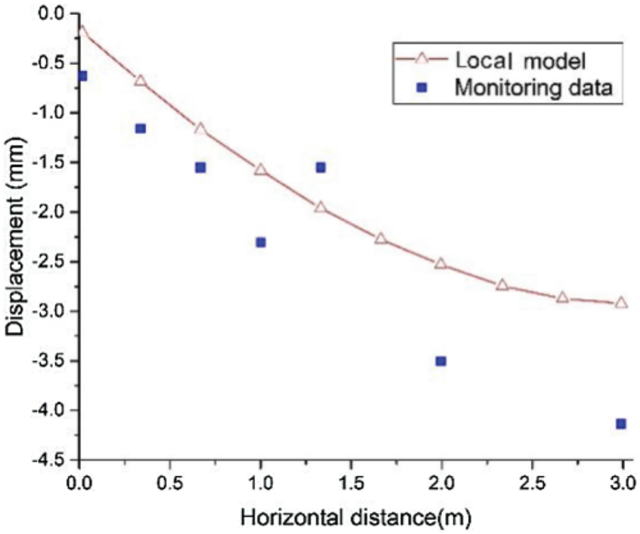

Figure 19: Displacement of ground surface after excavation

5 Conclusions

In this paper, a variable boundary condition method for hybrid regional model considering the thermal-hydro-mechanical coupling was used to simulate large-scale tunnel construction induced by excavation, and the model was validated against the initialization and deformation of Gongbei tunnel. Finally, it was compared with the monitoring data of ground surface deformation, and the following conclusions were drawn:

(1) The balance of initial ground stress under asymmetric boundary conditions was successfully implemented and verified through secondary development of DTNAFLOW script, which divided the application of boundary conditions into two phases.

(2) The accuracy of the proposed hybrid regional model was verified by comparing with the ground surface deformation of monitoring data, and the result indicated that regional model has good prediction effect.

(3) Based on regional model, the surface settlement curve of Gongbei tunnel presents the form of normal distribution. The maximum displacement of ground surface appeared above the top of concrete-filled steel pipe (point P1) with the value of −2.98 mm.

(4) According to the water pressure and deformation of Gongbei tunnel, the maximum vertical displacement occurred at the bottom of the right pipe after excavation. The value will reach to 4.26 mm without any support. Therefore, the phase of excavation had higher risk and should

be paid more attention to. The time control for each construction step should be arranged properly, especially in the freezing and excavation steps. Besides, it might be more effective to set the temporary support at the bottom of the right pipe.

However, there are still have some shortcomings. For instance, the boundary conditions between hybrid regional model and actual engineering are not exactly the same and need further study. It should be noted that the application of the proposed hybrid regional model to Gongbei tunnel related cases will be a reference for similar large-scale underground engineering construction.

Acknowledgement: The authors wish to special thank Prof. Jean H. Prevost for the careful guidance as my supervisor during the studying period at Princeton University as VSRC scholar. Also thanks to the high-performance computing cluster of Computer Science Department at Princeton University and the editor Dr. Aubrey Dou for her careful format review.

Funding Statement: This work is supported by the financial support from National Natural Science Foundation of China (No. 51478340), Natural Science Foundation of Jiangsu Province (No. BK20200707), Natural Science Foundation of the Jiangsu Higher Education Institutions of China (No. 20KJB560029), China Postdoctoral Science Foundation (No. 2020M671670), Key Laboratory of Soft Soils and Geoenvironmental Engineering (Zhejiang University), Ministry of Education (No. 2020P04). The support above is gratefully acknowledged.

Conflicts of Interest: The authors declare that they have no conflicts of interest to report regarding the present study.

References

1. Zheng, L., Gao, Y., Zhou, Y., Liu, T., Tian, S. (2021). A practical method for predicting ground surface deformation induced by the artificial ground freezing method. *Computers and Geotechnics, 130,* 1–16. DOI 10.1016/j.compgeo.2020.103925.
2. Li, F., Chen, G. (2020). Study on deformation characteristics of ground surface settlement during shield tunnel construction of river floodplain in Nanjing. *Journal of the China Railway Society, 42(7),* 155–160. DOI 10.3969/j.issn.1001-8360.2020.07.020.
3. Ruan, H., Wang, Y., Wan, Y., Yu, X., Zeng, C. et al. (2021). Three-dimensional numerical modeling of ground deformation during shield tunneling considering principal stress rotation. *International Journal of Geomechanics, 21(7),* 04021095. DOI 10.1061/(ASCE)GM.1943-5622.0002048.
4. Zhang, T., Ge, L., Zheng, G. (2019). Deformation of surface and subsurface ground due to tunnel excavation in sand. *Tianjin Daxue Xuebao/Journal of Tianjin University Science and Technology, 52,* 113–119. DOI 10.11784/tdxbz201902030.
5. Wang, W., Kosakowski, G., Kolditz, O. (2009). A parallel finite element scheme for thermo-hydro-mechanical (THM) coupled problems in porous media. *Computers & Geosciences, 35(8),* 1631–1641. DOI 10.1016/j.cageo.2008.07.007.
6. Arson, C., Gatmiri, B. (2012). Thermo-hydro-mechanical modeling of damage in unsaturated porous media: Theoretical framework and numerical study of the EDZ. *International Journal for Numerical and Analytical Methods in Geomechanics, 36(3),* 272–306. DOI 10.1002/nag.1005.
7. Rucker, C., Gunther, T., Spitzer, K. (2006). Three-dimensional 3D modelling and inversion of DC resistivity data incorporating topography-I. *Geophysical Journal International, 166(2),* 495–505. DOI 10.1111/j.1365-246X.2006.03010.x.

8. Liu, Z. J., Zheng, H., Dong, W., Ge, X., Sun, G. (2017). Local mesh refinement in numerical manifold method based on refined physical patches. *Rock and Soil Mechanics, 38(4),* 1211–1217. DOI 10.16285/j.rsm.2017.04.036.
9. Ye, L., Li, Y., Liu, Y., Li, G., Yang, H. (2016). 3D finite element modeling of marine controlled-source electromagnetic fields using locally refined unstructured meshes. *Chinese Journal of Geophysics, 59(12),* 4747–4758. DOI 10.6038/cjg20161233.
10. Chen, L. (2016). *Analysis of mechanical behavior of whole bridge and key parts for a long-span railway continuous steel truss girder bridge* (*Master Thesis*). Central South University, China.
11. Loganathan, N., Poulos, H. G. (1998). Analytical prediction for tunneling-induced ground movements in clays. *Journal of Geotechnical and Geoenvironmental Engineering, 124(9),* 846–856. DOI 10.1061/(ASCE)1090-0241(1998)124:9(846).
12. Yang, S., Tao, Y., Xu, P. (2019). Large-scale model experiment and numerical simulation on convergence deformation of tunnel excavating in composite strata. *Tunnelling and Underground Space Technology, 94,* 103–133. DOI 10.1016/j.tust.2019.103133.
13. Yue, J., Li, W., Gao, P., Zhang, S. (2021). Development and application of large-scale model test system for underwater shield tunnels. *Proceedings of the Institution of Civil Engineers-Structures and Buildings, 174(12),* 981–991.
14. Prevost, J. H. (1983). *Dynaflow (version 02 release 10.A)*. USA: Princeton University.
15. Geuzaine, C., Remacle, J. F. (2009). Gmsh: A three-dimensional finite element mesh generator with built-in pre- and post-processing facilities. *International Journal for Numerical Methods in Engineering, 79(11),* 1309–1331. DOI 10.1002/nme.2579.
16. Arno, W., Jonna, M. (2010). *FemGV user's manual release 7.2 release notes*. TNO Diana BV, the Netherlands.
17. Liu, J. G., Ma, B. S., Cheng, Y. (2018). Design of the Gongbei tunnel using a very large cross-section pipe-roof and soil freezing method. *Tunnelling and Underground Space Technology, 72,* 28–40. DOI 10.1016/j.tust.2017.11.012.
18. Pan, J., Gao, H., Shi, P. (2015). A study of combined pipe-roof scheme optimization for the bored section of the Gongbei tunnel. *Modern Tunnelling Technology, 52(3),* 55–62. DOI 10.13807/j.cnki.mtt.2015.03.008.
19. Hu, X., Deng, S., Ren, H. (2017). *In situ* test study on freezing scheme of freeze-sealing pipe roof applied to the Gongbei tunnel in the Hong Kong-Zhuhai-Macau Bridge. *Applied Sciences, 7(1),* 27. DOI 10.3390/app7010027.
20. Hu, X., Deng, S., Wang, Y. (2018). Test investigation on mechanical behavior of steel pipe-frozen soil composite structure based on freeze-sealing pipe roof applied to Gongbei tunnel. *Tunnelling and Underground Space Technology, 79,* 346–355. DOI 10.1016/j.tust.2018.06.033.
21. Hu, X., Deng, S., Wang, Y. (2018). Mechanical tests on bearing capacity of steel pipe-frozen soil composite structure applied in Gongbei tunnel. *Chinese Journal of Geotechnical Engineering, 40(8),* 1–10. DOI 10.11779/CJGE201808014.
22. Wang, Y. (2013). *Mechanical property analysis of steel pipe-frozen soil composite structure in freeze-sealing pipe roof method* (*Master Thesis*). Tongji University, China.
23. Zhang, W. (2016). *Experimental study on mechanical behavior of steel pipe-frozen soil composite structure in freeze-sealing pipe roof method* (*Master Thesis*). Tongji University, China.
24. Zhang, P., Ma, B., Zeng, C., Xie, H., Li, X. et al. (2016). Key techniques for the largest curved pipe jacking roof to date: A case study of Gongbei tunnel. *Tunnelling and Underground Space Technology, 59,* 134–145. DOI 10.1016/j.tust.2016.07.001.
25. Zhang, P., Behbahani, S. S., Ma, B. S. (2018). A jacking force study of curved steel pipe roof in Gongbei tunnel: Calculation review and monitoring data analysis. *Tunnelling and Underground Space Technology, 72,* 305–322. DOI 10.1016/j.tust.2017.12.016.

26. Prevost, J., Tao, D. (1983). Finite element analysis of dynamic coupled thermoelastic problems with relaxation times. *Journal of Applied Mechanics, 50,* 817–822. DOI 10.1115/1.3167151.
27. Tao, D., Prevost, J. (1984). Relaxation effects on generalized thermoelastic waves. *Journal of Thermal Stresses, 7,* 79–89. DOI 10.1080/01495738408942197.
28. Tao, D. (1984). *Finite element analysis of thermo elasticity problems* (*Ph.D. Thesis*). Princeton University, USA.
29. Prevost, J. (1982). Nonlinear transient phenomena in saturated porous media. *Computer Methods in Applied Mechanics and Engineering, 30(1),* 3–18. DOI 10.1016/0045-7825(82)90052-4.
30. Masud, A., Hughes, T. (2002). A stabilized mixed finite element method for darcy flow. *Computer Methods in Applied Mechanics and Engineering, 191,* 4341–4370. DOI 10.1016/S0045-7825(02)00371-7.
31. Prevost, J. (1978). Plasticity theory for soil stress-strain behavior. *Journal of Engineering Mechanics, 104(5),* 1177–1194. DOI 10.1061/JMCEA3.0002411.
32. Ministry of Transport (2019). *Code for design of ground base and foundation of highway bridges and culverts (JTG 3363—2019)*. China: People's Communications Press.
33. Ministry of Construction (1999). *Standard for soil test method (GB/T 50123-1999)*. China: China Planning Press.
34. State Administration of Work Safety (2011). *Artificial frozen soil physics mechanics performance test (MT/T 593–2011)0*. China: Coal Industry Standard of the People's Republic of China.

Computer Modeling in
Engineering & Sciences

Tech Science Press

DOI: 10.32604/cmes.2022.020853

ARTICLE

Dynamic Mechanical Behavior and Numerical Simulation of an Ancient Underground Rock Mass under Impact Loading

Baoping Zou*, **Zhiping Liu, Weifeng Jin, Haonan Ding and Zhanyou Luo**

School of Civil Engineering and Architecture, Zhejiang University of Science and Technology, Hangzhou, 310023, China

*Corresponding Author: Baoping Zou. Email: zoubp@zust.edu.cn

Received: 16 December 2021 Accepted: 18 February 2022

ABSTRACT

To study the dynamic mechanical properties of tuff under different environmental conditions, the tuff from an ancient quarry in Shepan Island was prepared. The impact damage to the rock was tested using a triaxial dynamic impact mechanical testing system (TDIMTS) with different ground stresses, temperatures, and groundwater pressures. The time-strain relationship, dynamic stress-strain relationship, energy dissipation law, energy-peak strain relationship, and the impact damage pattern of the tuff specimens under impact air pressures were investigated. The TDIMTS experiment on ancient underground rock mass under impact loading was also simulated using the finite element analysis software LS-DYNA based on the Holmquist-Johnson-Cook (HJC) material model. The dynamic failure process, failure pattern and peak stress of tuff specimen were calculated. The simulation results obtained using the above methods were in good agreement with the experimental results. The results of the dynamic experiment show that with the same local stress, groundwater pressure, and temperature, the damage to the tuff specimens caused by blasting and quarrying disturbances gradually increases as the impact pressure increases. Under the same local stress, groundwater pressure, and temperature, the energy required to rupture the tuffs in ancient underground caverns is relatively small if the impact pressure is low accordingly, but as the impact pressure increases, the damage to the tuff caused by quarrying disturbance gradually increases. The damage gradually increases and the degree of damage to the tuff and the strain energy exhibit asymptotic growth when the tuff specimens are subjected to the greater strain energy, increasing the degree of rupturing of the tuff. In addition, the average crushing size decreases with increasing strain energy. By comparing the simulation results with the experimental results, it was found that the HJC model reflected the dynamic impact performance of tuff specimen, and the simulation results showed an evident strain rate effect. These results of this study can offer some guidance and theoretical support for the stability evaluation, protection, and safe operation of the ancient underground caverns in future.

KEYWORDS

Ancient underground caverns; numerical simulation; thermal-hydraulic-mechanical coupling; dynamic impact; tuff; stability of surrounding rock

1 Introduction

Ancient underground engineering cave chambers are a class of immovable cultural relics [1], and they are the best physical evidence of the prosperity of the quarrying industry and the high mining techniques in ancient Chinese society. The distribution of caverns in ancient underground engineering is shown in Table 1 (This is also an ancient underground project that China has developed). The above ancient underground cavern groups have common characteristics. They are all artificially excavated, which belong to shallow and ultra-shallow underground engineering and have special cavern structure. The stability of the rock surrounding these caverns is not only directly related to the operation and safety of ancient underground cave chamber, but it also determines the development and conservation of the entire ancient underground cave chamber. To date, studies of ancient underground cavern chambers have mainly focused on the hydrological engineering geological conditions, stability evaluation [2–4], geological hazard prevention, and long-term protection [5,6]. Studies have also been conducted on the damage mechanical properties of rock masses. However, most of these studies have focused on static mechanical properties. Zhang et al. [7] analyzed the characteristics of the particle size distribution, the disintegration resistance index, and the swelling discriminatory characteristics of dry disintegrates in ancient underground cave chambers. Gao et al. [8] studied the mechanism of vault fracture development in ancient underground cave chambers in Longyou using a multi-factor approach. Gao et al. [9] studied the mechanism and pattern of fracture development in the roof of Cave 3 in the Longyou Grotto.

Table 1: Distribution of caverns in ancient underground engineering of China

No.	Name	Province
1	Shanghuashan ancient quarry	Zhejiang
2	Wushan grottoes	Zhejiang
3	Shepandao ancient quarry	Zhejiang
4	Feifengyan ancient quarry	Zhejiang
5	Changyu ancient quarry	Zhejiang
6	Heidong ancient quarry	Zhejiang
7	Suichang gold	Zhejiang
8	Longyou grottoes	Zhejiang
9	Huashan grottoes	An’hui

In fact, all of the ancient underground chambers discovered so far have been quarried (blasted and excavated) to different degrees or on different scales in recent modern times and are a partially water-filled or water-filled [1]. The influences of the complex geological environment (seepage, temperature, and stress fields) and engineering disturbances on the long-term stability of underground caverns cannot be ignored. For example, Yang et al. [10] studied the stress wave propagation characteristics, dynamic stress-strain relationship, and energy dissipation law of a laminated composite rock body composed of a combination of red sandstone and grey sandstone. Zou et al. [11] studied the dynamic stress-strain characteristics and the correlation between the dynamic deformation modulus and the loading rate, as well as the dependence of the peak stress/strain on the loading rate, the axial and confining pressures, the hydraulic pressure, the temperature and the absorption energy. Xu et al. [12] investigated the dynamic compressive mechanical properties of concrete under true triaxial confinement. Selyutina et al. [13] explored the fracture properties of saturated concrete and rock under dynamic loading. Wang et al. [14] explored the dynamic compressive damage properties of rock unloading. Long et al. [15,16] investigated the dynamic constitutive behaviour for different strain rates using the split-Hopkinson pressure bar with the applied gas gun pressure. Liu et al. [17] studied the drop impact and thermal cycling of electronic packaging structures. However, the ancient underground cavern chambers were all excavated artificially, and they all have self-stabilization times of hundreds or even thousands of years, while the engineering geological and hydrogeological conditions of the surrounding rock, the environmental conditions, and the long-term strength of the rock material have changed. The existing research results can hardly meet the development needs of the ancient underground cavern chambers. It is necessary to carry out experimental studies on the dynamic impact mechanical properties of ancient underground cavern rock masses under coupled ground stress, temperature, and groundwater conditions.

Therefore, in this study, tuff samples from Shepandao in Zhejiang Province were taken as an example, and the dynamic rupture characteristics of the tuff were analyzed by testing the dynamic impact force characteristics of the tuff under different coupled ground stress, temperature, and groundwater pressure conditions using a self-developed triaxial dynamic impact mechanics testing system. The results of this study provide a theoretical basis for the long-term stability evaluation, protection, and safe operation of ancient underground caverns.

2 Experimental Research

2.1 Specimen Preparation

The tests were carried out on tuff collected from the ancient underground quarry in Shepang Island, Zhejiang Province. The ancient underground caverns are shown in Fig. 1. Sample processing preparation is shown in Fig. 2. The tests were conducted in accordance with the Standard for Test Methods of Engineering Rock (GBT50266-2013) and the recommendations of the International Society of Rock Mechanics (ISRM) [18]. A φ 96 mm × 48 mm disc specimen was used for the dynamic compression deformation test, a φ 50 mm × 100 mm cylindrical specimen was used for the static uniaxial compressive strength test, and a φ 50 mm × 25 mm cylindrical specimen was used for the static splitting tensile strength test. The uniaxial compressive strength and tensile strength tests were carried out using φ 50 mm × 25 mm cylindrical specimens, and the loading rate for both the uniaxial compressive strength and tensile strength tests was 0.5 MPa/s. No fewer than three specimens were used for each group of rocks in each type of test. The test results obtained were processed, and the average values were used. The physical and mechanical parameters of the rocks are presented in Table 2. After testing, the static stress of the sample is 91.245 Mpa. During the processing, the rocks were processed into parallel laminated surfaces according to the original rock layer of the tuff. The two ends of the rock samples were polished using a self-developed rock and soil cutting and grinding machine (Fig. 3) to control the non-parallelism and non-verticality of the ends of the rock samples to within ±0.02 mm. The main advantage of cutting and grinding machine is that the cutter can move freely to achieve any height and width of the rock cutting and grinding. Rock cutting sizes range from 20 to 300 mm.

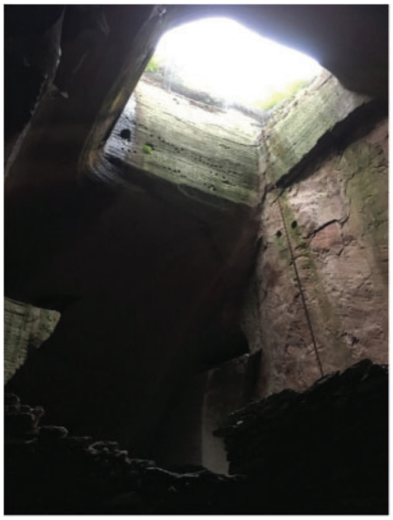

Figure 1: Ancient underground caverns

Figure 2: Sample processing preparation

Table 2: Physical and mechanical parameters of the rock specimens

Rock name	Density (g . cm^{-3})	Compressive strength (MPa)	Tensile strength (MPa)	Poisson's ratio
Tuff	2.47	79.34	5.2	0.15

Figure 3: Self-developed rock and soil cutting and grinding machine

2.2 *Basic Assumptions*

According to one-dimensional wave theory, the engineering stress, strain, and strain rate of the specimen can be described as Eqs. (1)–(3) [11,19].

$$\sigma(t) = \frac{E_t A_t}{2A_s}[\varepsilon_r(t) + \varepsilon_f(t) + \varepsilon_t(t)] \tag{1}$$

$$\varepsilon(t) = \frac{C_t}{L_s}\int_0^t [\varepsilon_r(t) - \varepsilon_f(t) - \varepsilon_t(t)]\mathrm{d}t \tag{2}$$

$$\dot{\varepsilon}(t) = \frac{C_t}{L_s}[\varepsilon_r(t) - \varepsilon_f(t) - \varepsilon_t(t)] \tag{3}$$

where $\sigma(t)$, $\varepsilon(t)$ and $\dot{\varepsilon}(t)$, are the dynamic stress, strain, strain rate. A_t and A_s, are the cross sectional area of elastic rod and sample. $\varepsilon_r(t)$, $\varepsilon_f(t)$ and $\varepsilon_t(t)$, are the strain values of incident, reflected and transmitted waves.

When these assumptions are satisfied, stress, strain, and strain rate can also be described as Eqs. (4)–(6) [19].

$$\sigma(t) = \frac{E_t A_t}{A_s}\varepsilon_T(t) \tag{4}$$

$$\varepsilon(t) = -2\frac{C_t}{L_s}\int_0^t \varepsilon_F(t)\mathrm{d}t \tag{5}$$

$$\dot{\varepsilon}(t) = -2\frac{C_t}{L_s}\varepsilon_F(t) \tag{6}$$

2.3 Testing Equipment

The tests were carried out on a triaxial dynamic impact mechanics testing system designed independently by the Zhejiang University of Science and Technology (Fig. 4). The testing system is mainly composed of a triaxial thermal-hydraulic coupling system (Figs. 5 and 6), a firing system, an incidence rod, a transmission rod, a data acquisition device, and a test analysis system. Among them, the bullet, incidence rod, and transmission rod are all cylindrical steel rods with a diameter of 100 mm and lengths of 600, 5000, and 4000 mm, respectively. The main pressure valve of the triaxial and perimeter pressure power loading system is 0–60 MPa, the main pressure valve of the permeation hydrodynamic loading system is 0–45 MPa, and the main pressure valve of the temperature power loading system is −100°C to 100°C. The main function of the testing system is to simulate the dynamic compression and deformation characteristics of a geotechnical body under the coupling of multiple fields, such as ground stress, infiltration water pressure, and high and low temperatures in different deposition environments.

Figure 4: TDIMTS

The triaxial dynamic impact mechanics testing system includes five parts: loading drive system, pressure bar system, energy absorption system, signal acquisition system, and signal processing system. When the sample is correctly installed in the Thermal-hydraulic-mechanical triaxial coupling system, it is affected by axial pressure, confining pressure, osmotic water pressure and temperature. Since the axial pressure, confining pressure, osmotic water pressure and temperature are all static loads, the incident bar and transmission bar are essentially affected by one-dimensional stress and subject to one-dimensional stress wave theory.

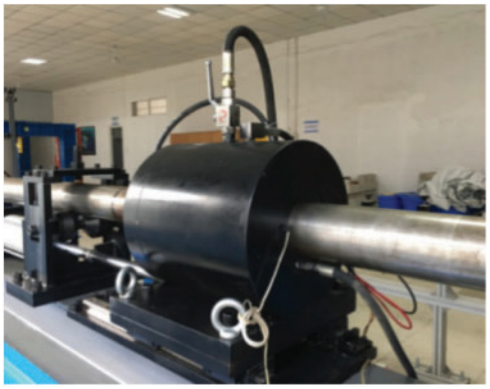

Figure 5: Thermal-hydraulic-mechanical triaxial coupling system

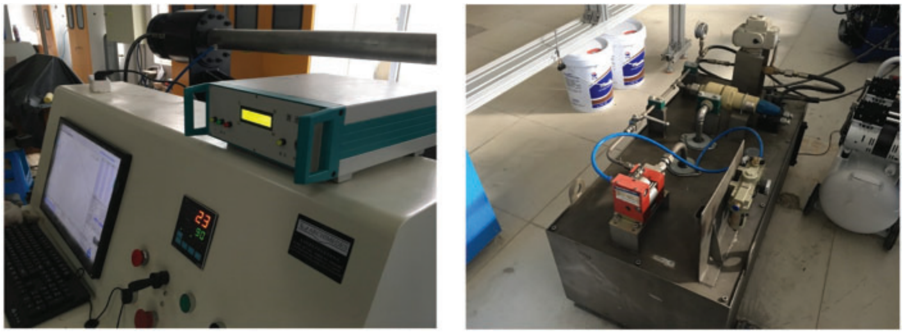

(a) Operational control system

(b) Seepage control system

(c) Temperature control system

(d) Dynamic impact control system

Figure 6: Key systems of the triaxial dynamic impact mechanics testing system

2.4 Test Program

The entire test was divided into 5 steps. Step 1 is the application of axial pressure, step 2 is the application of circumferential pressure, step 3 is the application of water pressure, step 4 is the application of warm pressure, and step 5 is the dynamic compression test. To reduce the effect of the friction between the specimen and the incidence and projection rods, grease was applied evenly to both ends of the specimen. The specimen was placed between the incidence and transmission rods, and the impact incidence energy was varied by adjusting the magnitude of the air pressure inside the storage chamber and the position of the bullet in the firing chamber. Li et al. [1] found that ancient underground cavern chambers are disturbed by blasting and quarrying to different degrees and at different scales in modern times, and Dai et al. [20] suggested that the destructive damage characteristics of blasting stress waves on rocks can be tested using the Split Hopkinson pressure bar (SHPB) method. Therefore, the impact incidence energy of this test was used to simulate blasting and quarrying disturbances.

Since the maximum thickness of the overlying strata of the ancient underground cavern in Shepandao is 30 m, the vertical principal stress was selected to calculate the *in situ* stress $б_v$ is 0.025Z according to the B-C-Haimson in-situ stress calculation method [21], where Z is the depth in meters. After the calculation, the vertical principal stress was 0.75 MPa. In order to facilitate the test operation, the ground stress was set to 1 MPa during the test. According to the depth-low temperature relationship curve of He et al. [22], the groundwater temperature was selected as normal temperature for the experimental design.

When exploring the effects of blasting quarry disturbance on the ancient underground cave chamber tuff, the number of serpentine rock samples collected was limited by the fact that Shepandao is a national geological mine park and the local tourism management department is concerned with the ecological protection of the ancient underground quarry. Thus, in order to control the number of specimens, a typical test protocol was selected for the study. Eight sets of tuff specimens were selected for the test, with a size of φ 96 mm × 48 mm (Table 3).

Table 3: Selected typical testing scheme

Typical experimental program	Earth stress (MPa)	Groundwater pressure (MPa)	Temperature (°C)	Quarry disturbance (MPa)
1	1	1	25	0.8
2	1	1	25	0.9
3	1	1	25	1.0
4	1	1	25	1.1
5	1	1	25	1.2
6	1	1	25	1.3
7	1	1	25	1.4
8	1	1	25	1.5

During the test, a strain signal was generated during the propagation of the impact stress wave through the incident and transmission rods, and a pair of strain gauges were attached to the middle of the incident and transmission rods immediately adjacent to the triaxial thermal-hydraulic coupling system. The data were collected using an ultra-dynamic strain-gathering instrument.

2.5 *Experimental Results*

2.5.1 Time-Dynamic Stress Relationship

The time-dynamic stress curves of the tuff specimens under different impact air pressures are shown in Fig. 7.

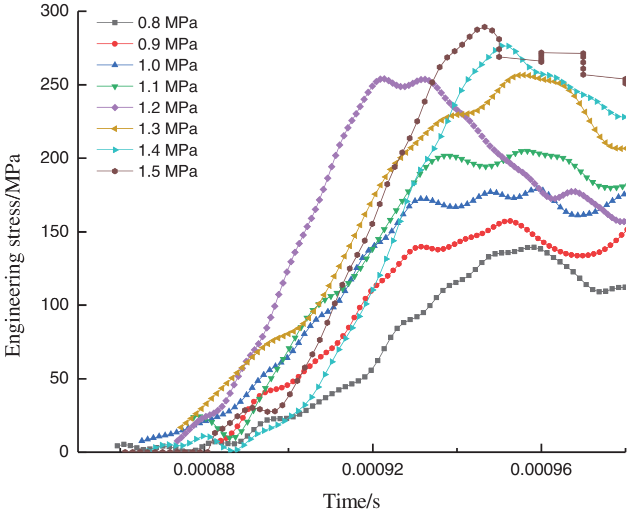

Figure 7: Time-stress curves for tuff under different impact pressures

As can be seen from Fig. 7, when the tuff specimen began to generate stress, the stress increased with increasing impact air pressure. The tuff stress in scenario 1 was the smallest, the stress in scenario 8 was the largest, and the stress in scenario 8 was 1.97 times that in scenario 1. The time it took to generate the stress was 0.00086 s, and the stress started to decrease at 0.00095 s. Then, it tended to level off.

2.5.2 Time-Strain Relationship

The time-strain curves of the tuff specimens under different impact air pressures are shown in Fig. 8.

As can be seen from Fig. 8, the strain range of the tuff specimens increased linearly from 0 to 0.04 with increasing time from 0.000855 to 0.0011 s. At impact air pressures of less than 1.1 MPa, the strain range was 0.04 to 0.05, totaling 50%. The strain growth of the tuff tended to slow down after 0.0011 s.

It can also be seen from Fig. 8 that the peak strain was greatest when the tuff was subjected to an impact air pressure of 1.1 MPa, indicating that the tuff was already damaged. As the tuff complies with Hooke's law, since the peak stress in the tuff was around 285 MPa, σ was constant, and the Poisson's ratio of the tuff was constant, which indicates that the dynamic modulus of the elasticity of the tuff changed during the dynamic test.

2.5.3 Dynamic Stress-Strain Relationship

The stress-strain curves of the tuff specimens under different impact air pressures are shown in Fig. 9.

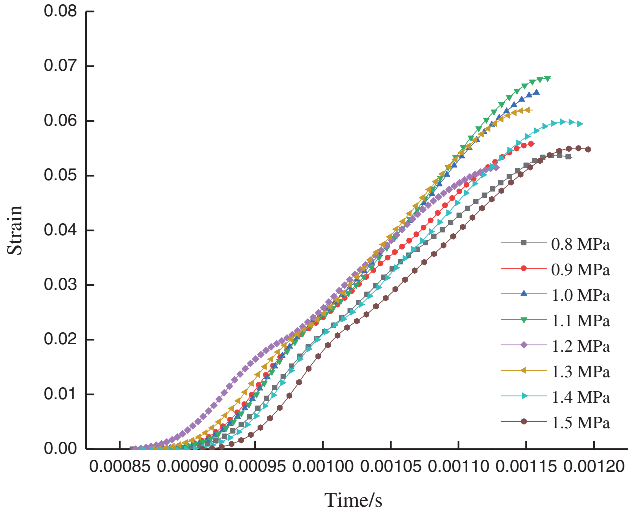

Figure 8: Time-strain curves for tuff under different impact pressures

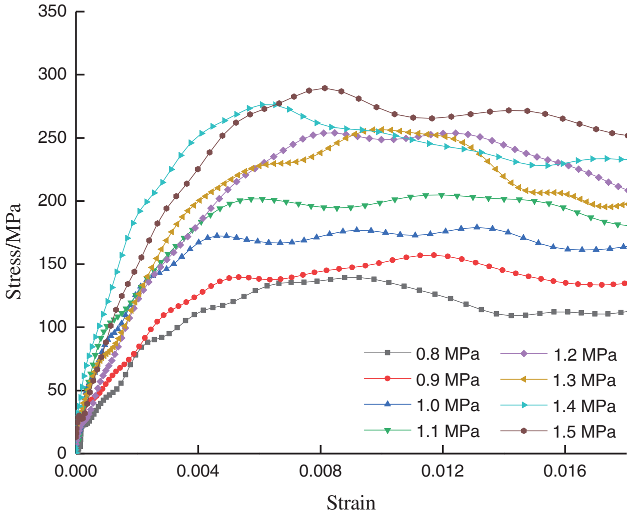

Figure 9: Stress-strain curves for tuff under different impact pressures

As can be seen from Fig. 9, the peak stress and peak strain of the tuff specimens increased with increasing impact air pressure. When the axial and circumferential pressures were 1 MPa, the permeated water pressure was 1 MPa, the temperature was 25°C, and the impact air pressure reached 1.5 MPa, the peak stress in scenario 8 was the largest (275.07 MPa), and the peak strain was 0.0081. When the axial and circumferential pressures were 1 MPa, the permeated water pressure was 1 MPa, the temperature was 25°C, and the impact air pressure reached 0.8 MPa, the peak stress in scenario 1 was the smallest (139.08 MPa). When the axial and circumferential pressures were 1 MPa, the permeated water pressure was 1 MPa, the temperature was 25°, and the impact air pressure reached 0.8 MPa, the peak stress in scenario 1 was the smallest (139.44 MPa), and the peak strain was 0.0056. The peak stress and peak strain in scenario 8 were 1.97 and 1.45 times those in scenario 1, respectively. This indicates that the impact compression damage process of the tuff at different impact air pressures has obvious stages, and the dynamic stress-strain curve of the rock can be roughly divided into three stages: a non-linear compression-density stage, an elastic deformation stage, and an unloading stage. The tuff exhibited the characteristics of the non-linear compression-density stage in the early stage of loading, followed by the elastic deformation stage with linear growth, and it gradually exhibited the characteristics of the plastic deformation stage in the middle stage of loading. The peak stress and peak strain of the tuff increased as the impulsive air pressure increased, and when the peak strength was reached, the stress decreased, exhibiting an unloading phase.

During the non-linear compression phase, the stress-strain curve curved upwards. The microcracks and pores in the rock were squeezed, the pores and holes shrank, and the cracks closed, resulting in the tuff being squeezed tighter and tighter. The stress-strain in the elastic deformation phase was proportional, with stress concentrations or shear deformations occurring at microdefects in the rock, resulting in further crack development. The peak stress in the tuff specimen in the unloading phase decreased rapidly, and the large number of microcracks in the rock expanded and caused damage.

2.5.4 Energy Dissipation Analysis

The time-strain energy relationship of the tuff specimens under different impact air pressures is shown in Fig. 10. Strain energy of tuff under different impact pressure is shown in Fig. 11.

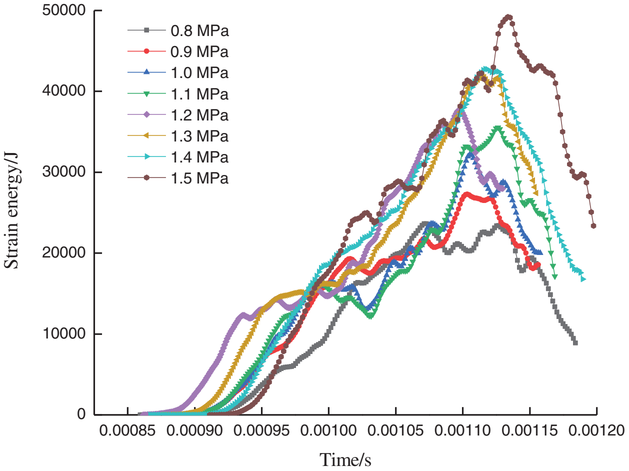

Figure 10: Time-strain energy curves for tuff under different impact pressures

As can be seen from Fig. 10, the strain energy of the tuff gradually increased as the impact air pressure increased. When the axial and circumferential pressures were 1 MPa, the permeated water pressure was 1 MPa, the temperature was 25°C, and the impact air pressure reached 1.5 MPa, the corresponding strain energy was the largest at 0.001135 s in scenario 8, i.e., 49210.74 J. When the axial and circumferential pressures were 1 MPa, the permeated water pressure was 1 MPa, the temperature was 25°C, and the impact air pressure reached 0.8 MPa, the corresponding strain energy in scenario 1 was the maximum at 0.001071 s, i.e., 23,641.14 J. The strain energy in scenario 8 was 2.08 times that in scenario 1.

It can also be seen from Fig. 10 that the energy required to rupture the tuff in the ancient underground cavern was small when the local stress, groundwater pressure, temperature, and quarrying disturbance were all small; however, as the quarrying disturbance increased, the degree of damage to the tuff specimen increased, resulting in the energy required to rupture the tuff also increasing, indicating that more energy input and higher stress levels will inevitably result in the tuff specimen breaking more fully, which is largely consistent with the findings of Yang et al. [10] (The results show that the dynamic mechanical properties and energy dissipation laws of composite rock mass have obvious strain rate effect). Therefore, the development and conservation of ancient underground cave chambers should pay sufficient attention to the unloading effect because tourism development, which drains the groundwater in ancient underground caves, causes the overall balance of the groundwater level and seepage patterns in the original chambers and the surrounding strata to be broken, resulting in stress redistribution in order to release energy.

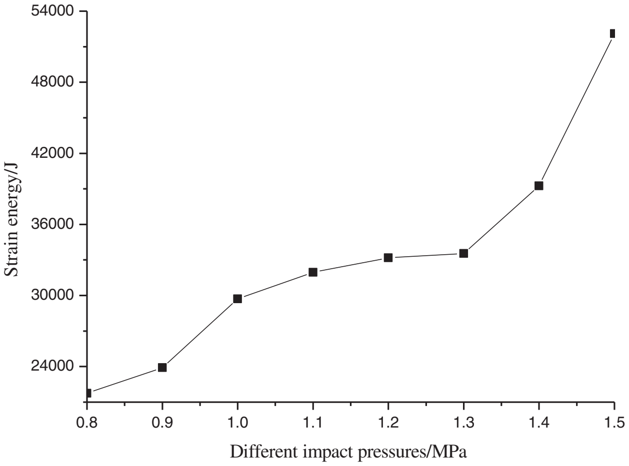

Figure 11: Strain energy of tuff under different impact pressure

As can be seen from Fig. 11, since the bullet impact direction is the same as the horizontal lamination direction of the tuff, the degree of damage to the tuff specimens increased with increasing strain energy. Compared to the strain energy of the tuff specimens under an impacting air pressure of 0.8 MPa, the average strain energies under stresses of 0.9, 1.0, 1.1, 1.2, 1.3, 1.4, and 1.5 MPa were 9.91%, 36.58%, 46.92%, 52.52%, 54.19%, 80.49%, and 139.53% higher, respectively. The tuff specimen in scenario 1 (Impact pressure 0.8 MPa) was only slightly damaged, with an obvious crack generated in the middle of the specimen's surface, and the strain energy was smaller. The tuff specimen in scenario 3 (Impact pressure 1.0 MPa) generated a more obvious shear surface at 45° on the right side of the surface, at which time the strain energy increased accordingly. The tuff specimen in scenario 8 (Impact pressure 1.5 MPa) experienced the greatest degree of damage and exhibited a core-retention type block fragmentation. The strain energy increased significantly, transferring the energy formed by the impact of the compression bar to the tuff specimen, resulting in the formation and development of microcracks within the specimen, which led to its rupture. This is because the horizontal laminated tuff specimens were loaded parallel to the laminae, and the microcracks and pores within the specimen were less likely to expand along the laminae when stressed. Therefore, the degree of damage to the tuff specimens exhibited an asymptotic growth pattern with increasing strain energy, which is generally consistent with the findings of Ping et al. [23] (The results show that the proportion of absorbed energy and incident energy is relatively constant, and absorbed energy increases with the incident energy growing). This indicates that as the strain energy to which the tuff specimens was subjected increased, the degree of tuff fracturing became more intense, and the average fragmentation size decreased with increasing strain energy.

2.5.5 Absorption Energy vs. Peak Strain

Under the action of different impact air pressures, the deformation of the tuff specimens was related to the transfer of energy, and the curve of the absorbed energy versus the peak strain and the fitted curve are shown in Fig. 12.

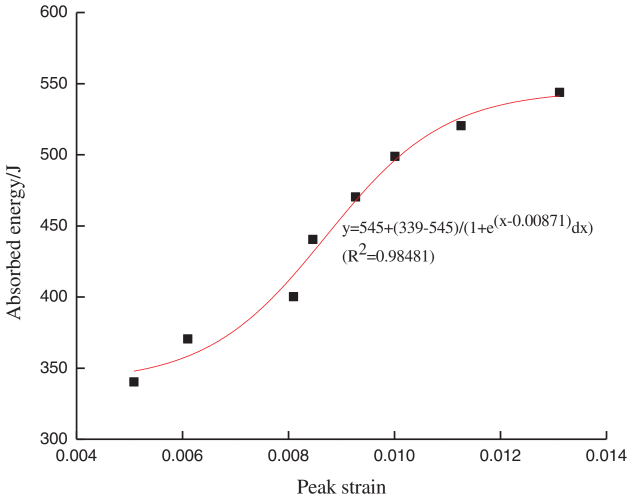

Figure 12: Peak strain-absorbed energy for tuff under different impact pressures

As can be seen from Fig. 12, as the peak strain increased, the energy absorbed by the tuff specimen exhibited a growth trend. The absorbed energy in the peak strain range of 0.008–0.012 accounted for 62.5%. When the peak strain is greater than 0.012, the growth of the energy absorbed by the tuff specimen tended to slow down, indicating that the tuff specimen was close to destruction. The higher the peak strain of the tuff was, the more cracks it contained, and the required absorbed energy was higher.

3 Numerical Simulation

3.1 HJC Model

The material model for TDIMTS numerical simulation is virtually associated with the dynamic behavior of rocks under impact loading. The dynamic mechanical behavior of brittle materials such as concrete and rocks, in most case, could be described by the HJC model, Riedel-Hiermaier-Thoma (RHT) model, Taylor-Chen-Kuszmaul (TCK) model, continuous smooth cap (CSC) model and the Karagozian-Case (K-C) model [24,25]. Moreover, Cardu et al. [24,26] utilized the Blast Damage Index (BDI) criterion to evaluate the stability of a rock slope under blasting. For LS-DYNA 3D, the HJC model is considered to be applicable to rock and concrete materials under large deformation and high strain rate [24–28]. In this work, the HJC model as the damage model of impact loading is employed to describe the dynamic behavior of rock masses. The damage model HJC focuses more on interactions and heterogeneity than the traditional elastic and fracture models [24,29]. It can well interpret the dynamic responses of rocks under impact loading and the results obtained using the HJC model agreed well with that of laboratory investigations [24,29]. For HJC model, the evolution of stress *vs.* strain can be described as Eq. (7). The yield surface is illustrated in Fig. 13a [24,28].

$$\sigma^* = \left[A(1-D) + BP^{*N}\right](1 + C\ln\dot{\varepsilon}^*) \tag{7}$$

where $\sigma^* = \sigma/f_c$, σ represents the stress, f_c is the uniaxial compressive strength under static loading, A denotes the normalized cohesion strength, D is the damage factor, B indicates the dimensionless pressure hardening coefficient, dimensionless pressure $P^* = P/f_c$, P represents the actual pressure, C denotes the strain rate coefficient, N refers to the pressure hardening index, the dimensionless strain rate $\dot{\varepsilon}^* = \dot{\varepsilon}/\dot{\varepsilon}_0$, $\dot{\varepsilon}$ is the actual strain rate and $\dot{\varepsilon}_0$ is the reference strain rate.

The damage factor $D(0 \leq D \leq 1)$ is defined as the sum of the equivalent plastic strain and plastic volumetric strain, as shown in Eq. (8) and Fig. 13b [24].

$$D = \sum \frac{\Delta\varepsilon_p + \Delta\mu_p}{\varepsilon_p^f + \mu_p^f} \tag{8}$$

where $\Delta\varepsilon_p$ is the increment of equivalent plastic strain, $\Delta\mu_p$ denotes the increment of plastic volumetric strain, $\varepsilon_p^f + \mu_p^f = D_1(P^* + T^*)^{D_2} = f(P) \geq EF_{MIN}$ which represents the plastic strain when the material is finally fractured at constant pressure P. The parameter EF_{MIN} is the amount of plastic strain before fracture. D_1 and D_2 are the damage constants, respectively.

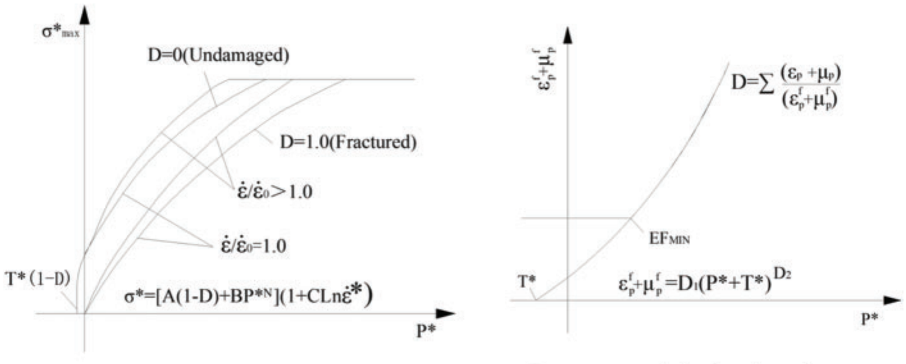

(a) Equation of the yield surface (b) Damage model of rock and concrete

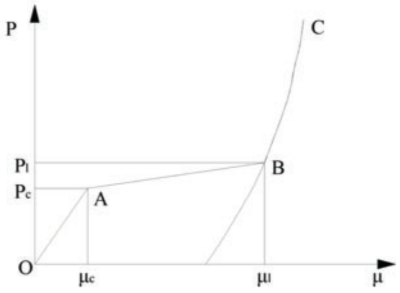

(c) Hydrostatic pressure and volumetric strain curve of rock and concrete

Figure 13: Original HJC model [24,28]

The relationship between the hydrostatic pressure and the volumetric strain of the rock and concrete is expressed by the segmental state equation shown in Fig. 13c [24]. Stage OA describes the linear elastic stage when $p < p_c$, and both the loading section and unloading section can be described as Eq. (9) [24].

$$p = K_e\mu \tag{9}$$

where K_e is the bulk modulus, p_c and μ_c are the crushing pressure and crushing volumetric strain in the uniaxial compressive experiment, respectively.

Stage AB is a plastic transition stage during which $p_c \le p < p_l$, and plastic deformation occurs as the voids of concrete are compressed [24].

Loading section can be described as Eq. (10).

$$p = p_l + \frac{(p_l - p_c)(\mu - \mu_l)}{\mu_l - \mu_c} \tag{10}$$

where p_l is the locking pressure, and μ_l is the locking volumetric strain.

Unloading section can be described as Eqs. (11) and (12).

$$p - p_{\max} = [(1 - F)K_e + FK_l]\,(\mu - \mu_{\max}) \tag{11}$$

$$F = \frac{\mu_{\max} - \mu_c}{\mu_l - \mu_c} \tag{12}$$

where K_l is the plastic volumetric modulus, $p_{\max}$ and $\mu_{\max}$ are the maximum volumetric pressure and volumetric strain before unloading in which the holes of the concrete and rock are expelled and damage occurs accompanied by cracks.

Stage BC is a fully compacted stage during which $p > p_l$, when the pressure reaches p_l, the holes are crushed completely. The relationship between p and μ is represented by a cubic polynomial [24].

Loading section can be described as Eqs. (13) and (14).

$$p = K_1\bar{\mu} + K_2\bar{\mu}^2 + K_3\bar{\mu}^3 \tag{13}$$

$$\bar{\mu} = \frac{\mu - \mu_L}{1 + \mu_L} \tag{14}$$

where $\bar{\mu}$ is the amended volumetric strain, and K_1, K_2 and K_3 are constants.

Unloading section can be described as Eq. (15).

$$p - p_{\max} = K_l(\bar{\mu} - \bar{\mu}_{\max}) \tag{15}$$

The material parameters for the HJC model are determined on the basis of previous research [24–29] and site geology for the studied ancient underground rock mass. Table 4 presents the properties of the rock masses.

Table 4: Properties of rock masses for the HJC model

Density (g/cm^3)	N	FS	D1	A	B	C
2.47	0.76	1.34	0.04	1.05	1.65	0.007

3.2 Finite Element Modeling

3.2.1 Modeling and Meshing

Three-dimensional solid element of SOLID 164 was selected for the modeling unit in ANSYS/LS-DYNA software. In order to simulate the actual test situation, a full model is adopted for modeling. The finite element model components included sample, incident bar, and transmission bar (see Fig. 14). The sample length was 50 mm, the incident bar length was 5000 mm, the transmission bar length was 4000 mm, and all the diameters were 100 mm. The bullet is simulated by the actual loaded dynamic pressure. The incident bar and the transmission bar used the same elastic material, which had an elastic modulus of 210 GPa, a density of 7.8 g/cm^3, and a compressional wave velocity of 5100 m/s.

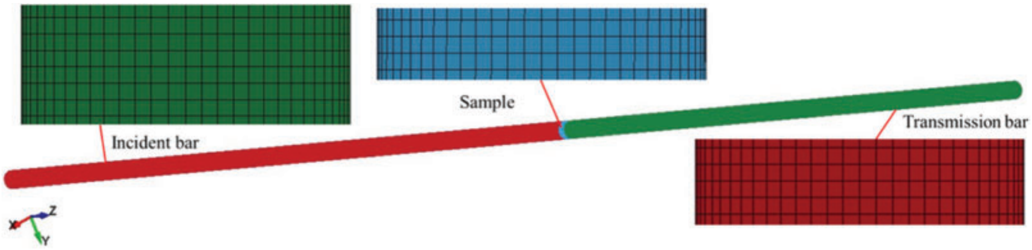

Figure 14: Finite element modeling

Considering the model accuracy and computational efficiency, the proposed model adopts the mapping grid partitioning method. The unstructured grids are generated using the HYPERMESH software. The cell size depends on the element size and related density. Mesh smoothing is performed by an auto-mesh smoothing algorithm [24]. The mesh size was 5 mm for incident bar, the transmission bar and the sample. The incident bar is divided into 380,000 units. The transmission bar is divided into 303,200 units. The rock sample is divided into 3790 units.

3.2.2 Contact Select

Contact type of ∗ CONTACT_AUTOMATIC_SURFACE_TO_SURFACE in LS-DYNA is used for the contact between the incident bar, transmission bar and the sample. It is very important to select the main and secondary surfaces of rock samples, incident and transmission rods. The friction between the sample and the pressure bar is ignored. The setting of the contact surface is shown in Fig. 15.

3.2.3 Load Application

In order to simulate the dynamic impact of bullet, the measured incident stress pulse is directly applied to the end of the incident bar (see Fig. 16). The load applied to simulate bullet impact force is mainly realized in HYPERMESH software. It is completed by using PRESSURE function in module ANALYSIS. Earth stress, groundwater pressure, temperature are realized by applying pressure and temperature field around the rock sample, respectively (see Fig. 17). These loads are assigned by PRESSURE and TEMPERATURES function in module ANALYSIS, which are applied to the outer surface of the sample.

3.2.4 Erosion Algorithm

As the fracturing of rocks differs from that of the joints, the erosion algorithm which allows several fracture criteria to be predefined in the modeling is employed to determine the fracturing processes of different materials [24–29]. It is difficult to track the crack propagation process in dynamic impact test. In this investigation, the failure criterion of maximum principal strain is utilized with the Erosion algorithm. The whole process of dynamic fracture is tracked by the numerical simulation algorithm. During numerical simulation, the element will be invalid and thus be killed by the code of LS-DYNA3D if the calculated stress or strain state of the element meets the failure criterion predefined by the Erosion algorithm [24].

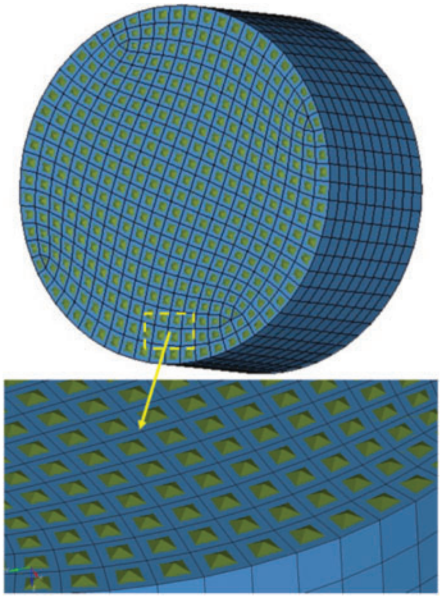

Figure 15: Setting of contact surface

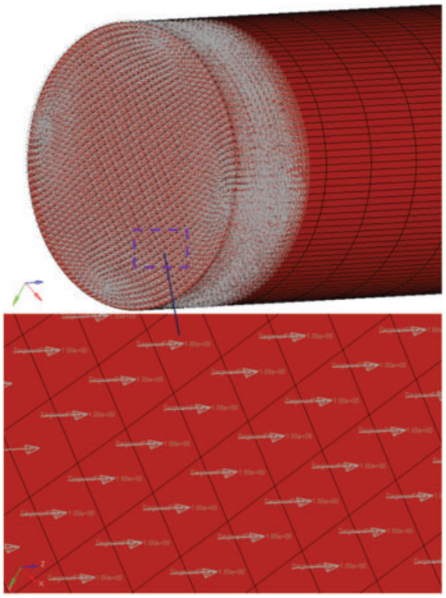

Figure 16: Impact pressure load of the incident bar

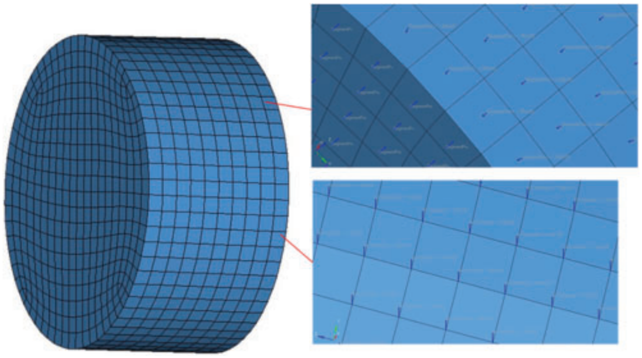

Figure 17: Earth stress, groundwater pressure and temperature load on sample

3.3 Dynamic Failure Process of Sample

The evolution process of peak stress of samples under different impact pressures is shown in Fig. 18. The comparison between the numerical simulation results and the experimental results of peak stress is shown in Fig. 19. As shown in Figs. 18 and 19, the peak stress value of numerical simulation is in good agreement with the results of dynamic impact test. It shows that the numerical model established in this study can be used to simulate the dynamic mechanical properties of different rocks under higher impact pressures.

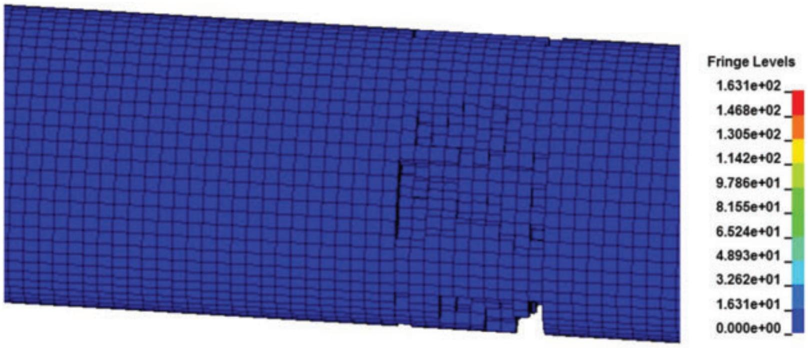

(a) Impact pressure 0.8

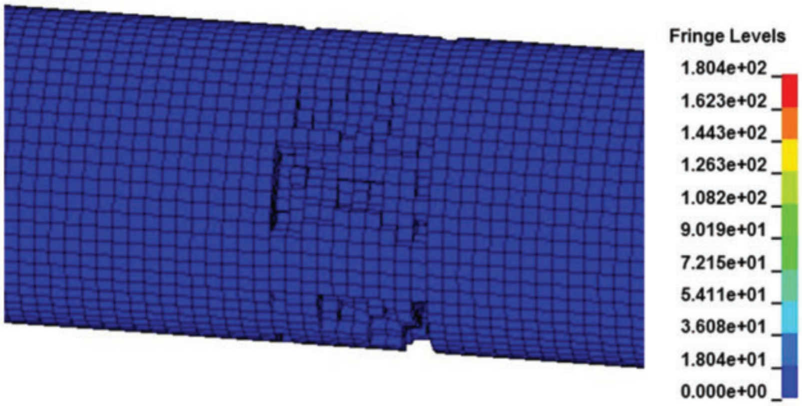

(b) Impact pressure 0.9

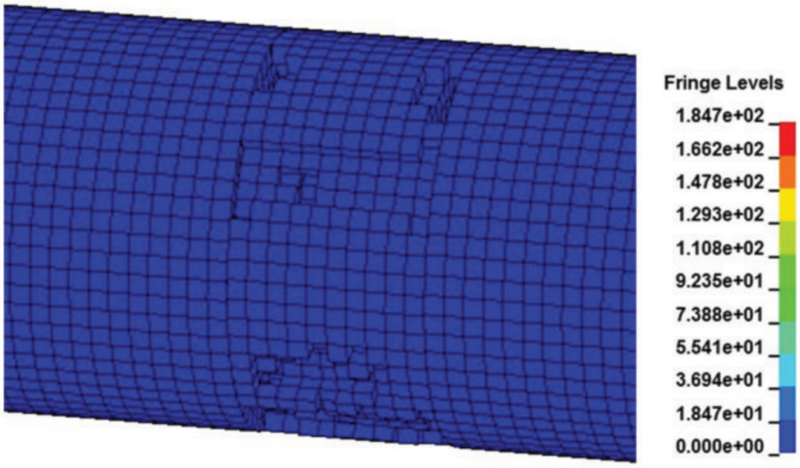

(c) Impact pressure 1.0

Figure 18: (Continued)

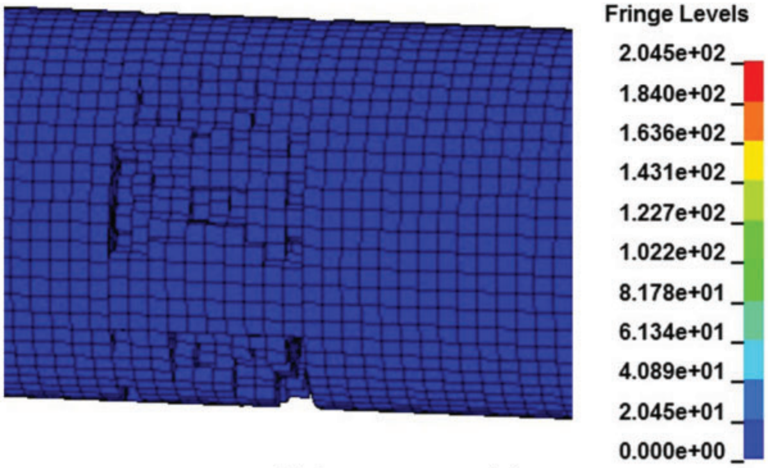

(d) Impact pressure 1.1

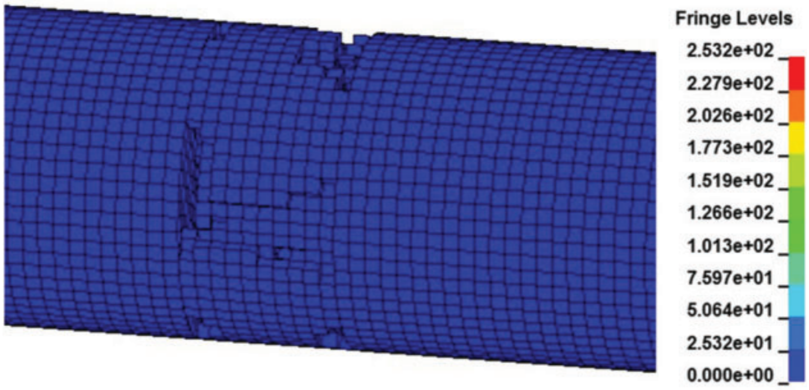

(e) Impact pressure 1.2

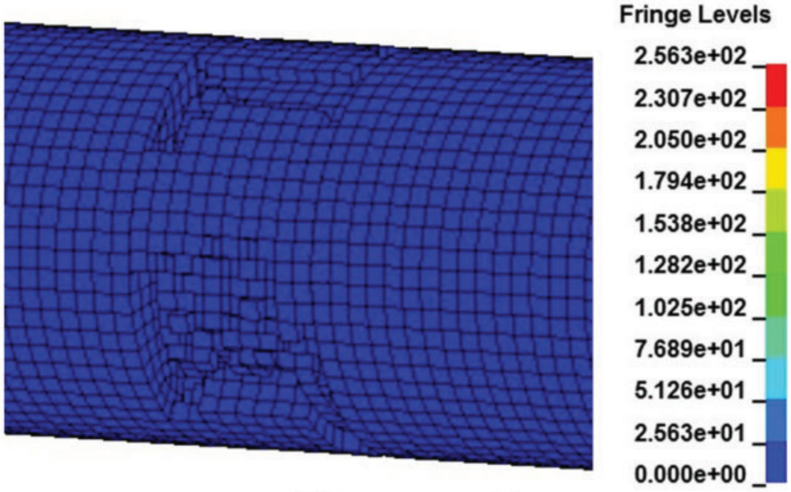

(f) Impact pressure 1.3

Figure 18: (Continued)

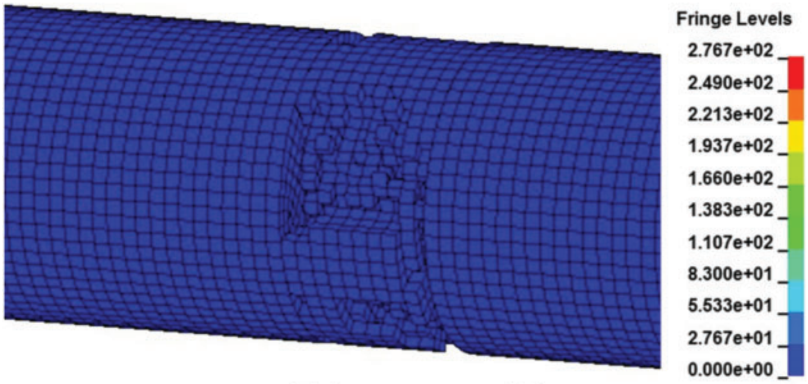

(g) Impact pressure 1.4

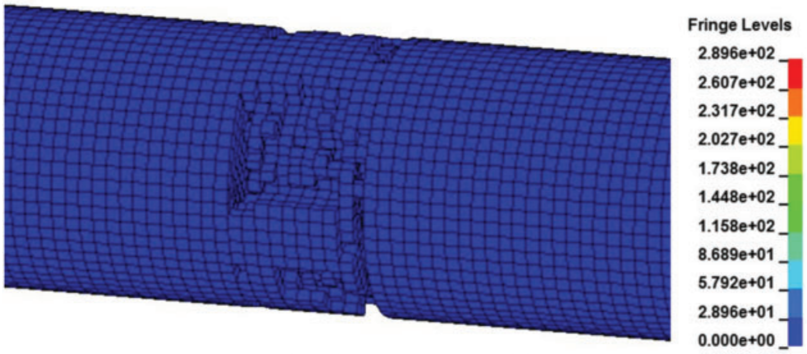

(h) Impact pressure 1.5

Figure 18: Evolution process of stress of samples under different impact pressures

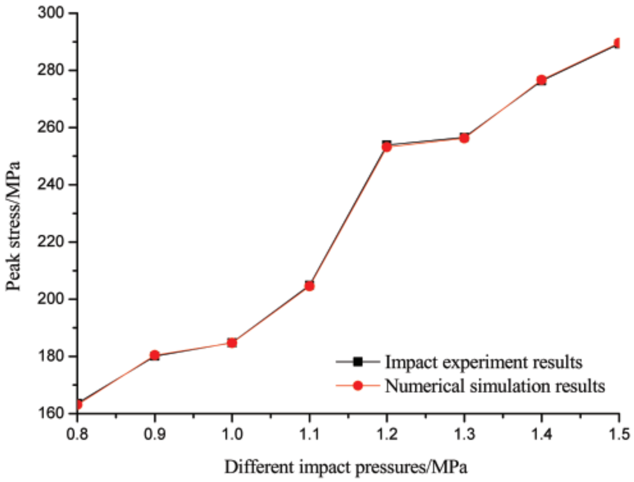

Figure 19: Comparison between the numerical simulation results and the experimental results of peak stress

3.4 Failure Pattern of Sample

Comparison of failure patterns of samples under different impact pressures is shown in Fig. 20. As shown in Fig. 20, the transformation mode of sample failure pattern has a high similarity with the test results. According to the comparison of failure patterns of rock mass, the failure degree of samples increases with the increase of strain rate.

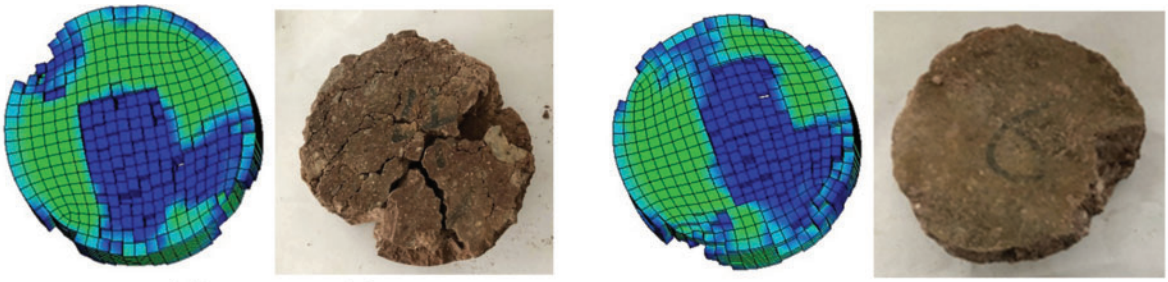
(a) Impact pressure 0.8 (b) Impact pressure 0.9

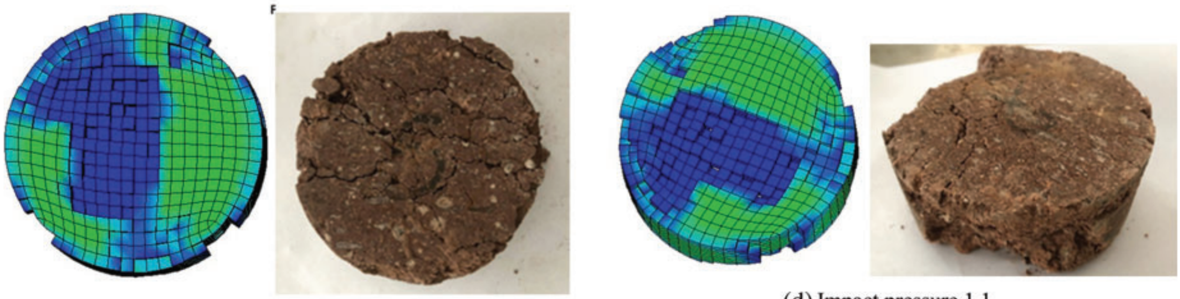
(c) Impact pressure 1.0 (d) Impact pressure 1.1

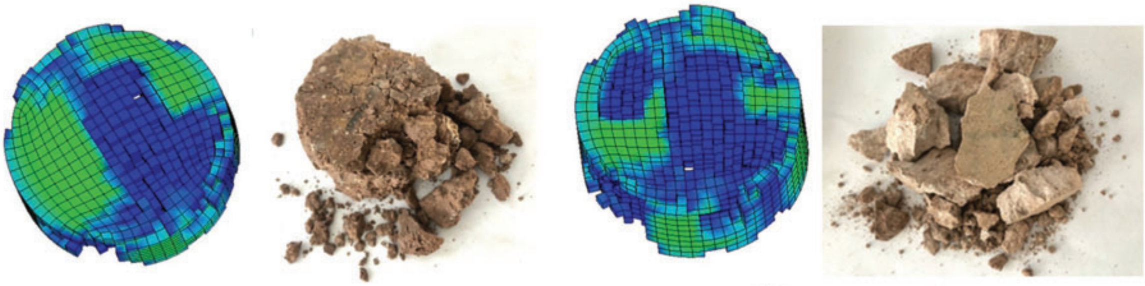
(e) Impact pressure 1.2 (f) Impact pressure 1.3

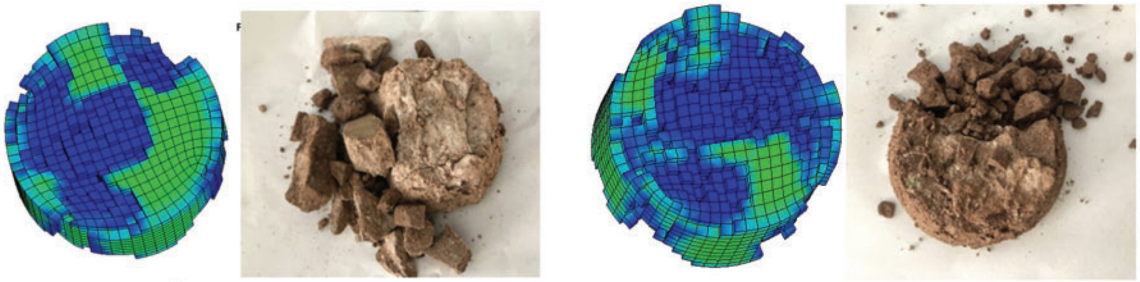
(g) Impact pressure 1.4 (h) Impact pressure 1.5

Figure 20: Comparison of failure patterns of samples under different impact pressures

4 Conclusions

The dynamic characteristics of the tuff collected from an ancient quarry in Shepan Island, Zhejiang Province, were studied using a TDIMTS, and the main conclusions are as follows:

(1) Under the same local stress, groundwater pressure, and temperature, the damage to the tuff specimen caused by blasting and quarrying disturbances gradually increased with increasing impact air pressure.

(2) Under the same local stress, groundwater pressure, and temperature, the energy required to rupture the tuff from the ancient underground chamber was small when the impact air pressure was relatively low; however, the damage to the tuff specimens from the quarrying disturbance gradually increased with increasing of the impact air pressure.

(3) Finally, the degree of damage to the tuff specimen and the strain energy exhibited asymptotic growth. When under high strain energy, the degree of rupturing of the tuff was much more serious than that under low strain energy, and the average crushing size decreased with increasing of the strain energy.

(4) The TDIMTS experiment on tuff specimen under thermal-hydraulic-mechanical coupling was simulated using the HJC model and LS-DYNA software. The dynamic failure process, failure pattern and peak stress of tuff specimen were calculated, and the simulation results were proven to be reliable. By comparing the simulation results with the experimental results, it was found that the HJC model reflected the dynamic impact performance of tuff specimen, and the simulation results showed an evident strain rate effect.

Funding Statement: The financial supports for this research project by the National Natural Science Foundation of China (No. 41602308). This research was supported by Zhejiang Provincial Natural Science Foundation of China under Grant No. LY20E080005.

Conflicts of Interest: The authors declare that they have no conflicts of interest to report regarding the present study.

References

1. Li, L., Yang, Z., Yue, Z. (2018). Scientific researches of large ancient rock underground openings in zhejiang province and their inspirations. *Journal of Engineering Geology, 26(1),* 73–84. DOI 10.13544/j.cnki.jeg.2018.01.008.
2. Yang, Z., Qu, J., Li, L., He, W., Luo, Q. et al. (2017). Quarrying technique and its adaptability to engineering geological conditions in Changyudongtian ancient underground quarry: A case study of shuiyun cavern complex. *Journal of Engineering Geology, 25(4),* 1113–1122. DOI 10.13544/j.cnki.jeg.2017.04.026.
3. Jaffé, R., Prous, X., Calux, A., Gastauer, M., Nicacio, G. et al. (2018). Conserving relics from ancient underground worlds: Assessing the influence of cave and landscape features on obligate iron cave dwellers from the eastern Amazon. *PeerJ, 6(3),* 1–18. DOI 10.7717/peerj.4531.
4. Marinos, V., Vazaios, I., Papathanassiou, G., Kaklis, T., Goula, E. (2019). 3D modelling of the ancient underground quarries of the famous parian marble in the aegean sea, Greece and assessment of their stability using LiDAR scanning. *Quarterly Journal of Engineering Geology and Hydrogeology, 52(1),* 61–73. DOI 10.1144/qjegh2017-145.
5. Zhang, Z., Li, L., Xu, W., Fu, Y., Feng, J. (2015). Flat-plate roof collapse of shallow caverns and protective measures: A case study of longyou ancient siltstone caverns. *Natural Hazards, 76(1),* 191–213. DOI 10.1007/s11069-014-1481-0.

6. Wei, X., Zhai, Y., Hu, R., Yang, Z., Fu, Y. (2019). Thinking for the rockfall in longyou cavern and its prevention method. *Geotechnical Investigation and Surveying, 10,* 1–6 (in Chinese). DOI CNKI:SUN:GCKC.0.2019-10-001.
7. Zhang, W., Shang, Y., Qu, Y., Sun, Y., Lin, D. et al. (2013). Grain size distribution of collapsed scraps of argillaceous rock and its relationship with expansibility: An experimental study. *Rock and Soil Mechanics, 34(1),* 66–73 (in Chinese). DOI 10.16285/j.rsm.2013.01.013.
8. Gao, B., Zhang, H., Yang, Z., Fu, Y. (2019). The development mechanism and control technology visualization of the vault cracks in the ancient underground cavern of longyou. *Episodes, 42(4),* 287–299. DOI 10.18814/epiiugs/2019/019023.
9. Gao, B., Zhang, H., Yang, Z. (2019). Crack development mechanism and reinforcement support of the rock roof of No. 3 cavern in longyou grottoes. *Journal of Engineering Geology, 28(3),* 565–573 (in Chinese). DOI 10.13544/j.cnki.jeg.2019-258.
10. Yang, R., Li, W., Fang, S., Zhu, Y., Li, Y. (2019). Experimental study on impact dynamic characteristics of layered composite rocks. *Chinese Journal of Rock Mechanics and Engineering, 38(9),* 1747–1757 (in Chinese). DOI 10.13722/j.cnki.jrme.2019.0021.
11. Zou, B., Luo, Z., Xu, F., Ding, H., Tao, Z. et al. (2020). Experimental study on impact dynamic characteristics of deep sandstone under thermal-hydraulic-mechanical coupling conditions. *Chinese Journal of Rock Mechanics and Engineering, 39(9),* 1750–1761 (in Chinese). DOI 10.13722/j.cnki.jrme.2020.0205.
12. Xu, S., Shan, J., Zhang, L., Zhou, L., Gao, G. et al. (2020). Dynamic compression behaviors of concrete under true triaxial confinement: An experimental technique. *Mechanics of Materials, 140,* 1–18. DOI 10.1016/j.mechmat.2019.103220.
13. Selyutina, N., Petrov, Y. (2020). Fracture of saturated concrete and rocks under dynamic loading. *Engineering Fracture Mechanics, 225,* 1–18. DOI 10.1016/j.engfracmech.2018.11.052.
14. Wang, H., Dyskin, A., Dight, P., Pasternak, E., Hsieh, A. (2020). Review of unloading tests of dynamic rock failure in compression. *Engineering Fracture Mechanics, 225,* 1–17. DOI 10.1016/j.engfracmech.2018.12.022.
15. Long, X., Mao, M., Lu, C., Li, R., Jia, F. (2021). Modeling of heterogeneous materials at high strain rates with machine learning algorithms trained by finite element simulations. *Journal of Micromechanics and Molecular Physics, 6(1),* 1–24. DOI 10.1142/S2424913021500016.
16. Long, X., Xu, J., Wang, S., Tang, W., Chang, C. (2020). Understanding the impact response of lead-free solder at high strain rates. *International Journal of Mechanical Sciences, 172,* 1–10. DOI 10.1016/j.ijmecsci.2020.105416.
17. Liu, Y., Long, X., Wang, H., Lu, J., Sun, R. et al. (2021). Sequential analysis of drop impact and thermal cycling of electronic packaging structures. *Proceedings of the 22th International Conference on Electronic Packaging Technology of the IEEE*, Xiamen, China.
18. Dai, F., Huang, S., Xia, H., Tan, Z. (2010). Some fundamental issues in dynamic compression and tension tests of rocks using split Hopkinson pressure bar. *Rock Mechanics and Rock Engineering, 43(6),* 657–666. DOI 10.1007/s00603-010-0091-8.
19. Zhou, Z., Li, X., Ye, Z., Liu, K. (2010). Obtaining constitutive relationship for rate-dependent rock in SHPB tests. *Rock Mechanics and Rock Engineering, 43,* 697–706. DOI 10.1007/s00603-010-0096-3.
20. Dai, R., Guo, X., Gong, Q., Pu, C. J., Zhang, Z. (2011). SHPB test on blasting damage protection of tunnel surrounding rock. *Rock and Soil Mechanics, 32(1),* 77–83 (in Chinese). DOI 10.16285/j.rsm.2011.01.031.
21. Song, Y., Bian, J., Jia, G. (2009). Deep initial ground stress features and prediction method. *Design of Water Resources and Hydroelectric Engineering, 28(4),* 42–45 (in Chinese). DOI 10.3969/j.issn.1007-6980.2009.04.016.
22. He, M., Guo, P. (2013). Deep rock mass thermodynamic effect and temperature control measures. *Chinese Journal of Rock Mechanics and Engineering, 32(12),* 2377–2393 (in Chinese). DOI 10.3969/j.issn.1000-6915.2013.12.001.

23. Ping, Q., Luo, X., Ma, Q., Yuan, P. (2015). Broken energy dissipation characteristics of sandstone specimens under impact loads. *Chinese Journal of Rock Mechanics and Engineering, 34(2),* 4197–4203 (in Chinese). DOI 10.13722/j.cnki.jrme.2015.0585.
24. Zou, B., Xu, Z., Wang, J., Luo, Z., Hu, L. (2020). Numerical investigation on influential factors for quality of smooth blasting in rock tunnels. *Advances in Civil Engineering, 2020,* 1–17. DOI 10.1155/2020/9854313.
25. Wang, C., Song, R., Wang, G., Zhang, S., Cao, X. et al. (2020). Modifications of the HJC (Holmquist-Johnson-Cook) model for an improved numerical simulation of roller compacted concrete (RCC) structures subjected to impact loadings. *Materials, 13(6),* 1–19. DOI 10.3390/ma13061361.
26. Cardu, M., Mancini, R., Oggeri, C. (2004). Ground vibration problems in the excavation of tunnels under small rock cover. *Proceedings of the Symposium on Environmental Issues and Waste Management in Energy and Mineral Production*, pp. 353–356. Antalya, Turkey.
27. Holmquist, T., Johnson, G. (1993). A computational constitutive model for glass subjected to large strains, high strain rates and high pressures. *Proceedings of the 14th International Symposium on Ballistics of the IEEE Press*, pp. 591–600. Quebec, Canada.
28. Tai, Y., Chu, T., Hu, H., Wu, J. (2011). Dynamic response of a reinforced concrete slab subjected to air blast load. *Theoretical and Applied Fracture Mechanics, 56(3),* 140–147. DOI 10.1016/j.tafmec.2011.11.002.
29. Jiang, N., Zhou, C. (2012). Blasting vibration safety criterion for a tunnel liner structure. *Tunnelling and Underground Space Technology, 32,* 52–57. DOI 10.1016/j.tust.2012.04.016.

Computer Modeling in
Engineering & Sciences

Tech Science Press

DOI: 10.32604/cmes.2022.021164

ARTICLE

Monitoring Study of Long-Term Land Subsidence during Subway Operation in High-Density Urban Areas Based on DInSAR-GPS-GIS Technology and Numerical Simulation

Yu Song[1], Xuejun Chen[1], Baoping Zou[2,*], Jundong Mu[3], Rusheng Hu[4], Siqi Cheng[5] and Shengli Zhao[3]

[1]College of Civil and Architecture Engineering, Guilin University of Technology, Guilin, 541004, China

[2]School of Civil Engineering and Architecture, Zhejiang University of Science and Technology, Hangzhou, 310023, China

[3]Hangzhou Metro Group Co., Ltd., Hangzhou, 310003, China

[4]China Railway Tunnel Bureau Group Co., Ltd., Guangzhou, 511458, China

[5]General Supervision Station of Construction Engineering Quality and Safety of Hangzhou, Hangzhou, 310005, China

*Corresponding Author: Baoping Zou. Email: zoubp@zust.edu.cn

Received: 30 December 2021 Accepted: 18 March 2022

ABSTRACT

During subway operation, various factors will cause long-term land subsidence, such as the vibration subsidence of foundation soil caused by train vibration load, incomplete consolidation deformation of foundation soil during tunnel construction, dense buildings and structures in the vicinity of the tunnel, and changes in water level in the stratum where the tunnel is located. The monitoring of long-term land subsidence during subway operation in high-density urban areas differs from that in low-density urban construction areas. The former is the gathering point of the entire urban population. There are many complex buildings around the project, busy road traffic, high pedestrian flow, and less vegetation cover. Several existing items require monitoring. However, monitoring distance is long, and providing early warning is difficult. This study uses the 2.8 km operation line between Wulin Square station and Ding'an Road station of Hangzhou Subway Line 1 as an example to propose the integrated method of DInSAR-GPS-GIS technology and the key algorithm for long-term land subsidence deformation. Then, it selects multiscene image data to analyze long-term land subsidence of high-density urban areas during subway operation. Results show that long-term land subsidence caused by the operation of Wulin Square station to Ding'an Road station of Hangzhou Subway Line 1 is small, with maximum subsidence of 30.64 mm, and minimum subsidence of 11.45 mm, and average subsidence ranging from 19.27 to 21.33 mm. And FLAC3D software was used to verify the monitoring situation, using the geological conditions of the soil in the study area and the tunnel profile to simulate the settlement under vehicle load, and the simulation results tended to be consistent with the monitoring situation.

KEYWORDS

Long-term land subsidence; subway operation; DInSAR-GPS-GIS technology; high-density urban areas; urban subway; numerical simulation

1 Introduction

Subways constructed in soft soil areas, such as Shanghai and Hangzhou in China, are currently in operation. By the end of 2020, 45 cities in mainland China have opened subway lines with a total length of 7978.19 km [1]. The urban distribution of subway operation indicates that nearly 90% of the operating mileage is concentrated in the high-density urban areas of Beijing–Tianjin–Hebei, Yangtze River Delta, and Pearl River Delta city clusters. After a certain period of subway operation, some factors will cause long-term land subsidence, such as the vibration subsidence of foundation soil caused by train vibration load, incomplete consolidation deformation of foundation soil during tunnel construction, dense buildings (structures) in the vicinity of the tunnel, and changes in water level in the stratum where the tunnel is located [2]. For example, the long-term subsidence increment of Shanghai Dapu Road Cross River Tunnel after 16 years of operation reaches 120 mm, and the subsidence caused by the construction of the Grimsby tunnel took 10 years to reach equilibrium [3]. Therefore, the occurrence of long-term land subsidence is a relatively slow process, but the accumulation of subsidence over a long period will have an adverse impact on the normal operation and safe usage of a subway, such as causing tunnel leakage, tunnel cracking, and damage, and endangering adjacent buildings (structures), pile foundations, and underground pipelines. Moreover, it will seriously affect the smoothness of a track, increase the interaction force of the wheel-rail system, increase the vibration of the tunnel structure, affect the vibration and noise of buildings close to the subway tunnel or above it, and affect the ride comfort of passengers [4].

Long-term land subsidence monitoring in high-density urban areas during subway operation differs from those in low-density urban construction areas, urban suburbs, and other areas. A high-density urban area is a commercial, financial and trade, entertainment, and cultural center of a city. It is also the gathering point of the urban population. Many existing items require monitoring, including the main structure of a foundation pit, and buildings and structures along with subways, pipelines, and bridges [2]. However, the characteristics of the linear distribution of a subway exhibit a long monitoring distance and difficulty in providing early warning. If traditional urban land subsidence monitoring methods, such as GPS, precise leveling observation, and underground fine observation methods (bedrock marks, and layering marks) are adopted, then a considerable amount of time, labor, material, and financial resources will be consumed; observation points will be sparsely distributed; the operation cycle will be long, and labor intensity will be high. These traditional methods cannot be used for all-weather observation. Simultaneously, they will have difficulty in accurately determining the deformation influence range of regional land subsidence. However, existing early warning systems for land subsidence during subway operation exhibit limitations, such as considering only cumulative subsidence and subsidence rate when characterizing subsidence, which cannot reflect the three-dimensional distribution of long-term land subsidence. Moreover, a clear long-term land subsidence classification and early warning index system are lacking in the relevant norms of China's subway industry, which causes certain difficulties in the prevention and control of land subsidence disasters in high-density urban areas. Therefore, a scientific, efficient, and comprehensive high-tech monitoring method is urgently required to conduct a long-term land subsidence study during subway operation; to provide decision-making information for the prevention, control, and early warning of long-term land subsidence disasters in high-density urban areas during subway operation; and to effectively prevent and control long-term land subsidence disasters in cities.

Given the limitation in the period, most current domestic and foreign studies on long-term land subsidence during subway operation have focused on body subsidence and dynamic response caused by train vibration and the prediction of long-term land subsidence. In terms of body subsidence and dynamic response, Leclerc et al. [5] explored the use of submarine coral reefs as a record of long-term coastal vertical motion to determine the deformation rate and discuss its origins. Chen et al. [6] studied the long-term deformation in lava fields emplaced between 1998 and 2007 at Piton de la Fournaise, and conducted an in-depth investigation over the influence of post-emplacement lava subsidence processes on the instability of the Eastern Flank. Tang et al. [7] systematically studied the dynamic response of soft soils in high-speed rail foundations. Shi et al. [8] analyzed the evolution law of cumulative plastic dynamic strain and established the prediction model of cumulative plastic strain based on the dynamic triaxial tests of intensely and moderately weathered argillaceous siltstone. Di et al. [9] analyzed the settlement differences of five subways in the Yangtze River Delta region on soft deposits and proposed measures to reduce settlement differences. Qiu et al. [10] used finite element software to simulate the consolidation behavior of loess and found that the long-term settlement results obtained from the simulation matched the results of field monitoring. Huang et al. [11] used finite element simulation software, through the soil-water full coupling dynamic finite element method, to analyze the settlement of saturated clay soil under trainload. Tan et al. [12] conducted a monitoring study on the deformation of subway tunnels and found that there is variability in the amount of settlement in different areas. Di et al. [13] conducted a study on the long-term settlement of Nanjing Metro Line 10 and found that the maximum settlement of Metro Line 10 was 240 mm within 5.75 years of completion. However, the a forementioned studies rarely involved long-term land subsidence problems caused by train reciprocating vibrations in tunnels, monitoring methods, and early warning systems for long-term land subsidence in high-density urban areas during subway operation remain lacking.

In recent years, interferometric synthetic aperture radar (InSAR) technology has been increasingly applied to the topographic survey. This technology exhibits the following characteristics: noncontact survey, unnecessary monitoring of control network setting, sub-millimeter accuracy, high efficiency, low cost, wide-coverage, no weather influence, and high spatial resolution. Therefore, InSAR has also been applied to the monitoring of land subsidence during subway operations. Fadhillah et al. [14] used the InSAR technique to generate deformation time series maps using the Stamfs method to investigate subsidence in four areas. Shi et al. [15] used the SBAS-InSAR technique to analyze subsidence in Xi'an and to predict land subsidence. Hu et al. [16] used the SBAS-InSAR technique to analyze the subsidence in the Fuzhou area and found that the SBAS-InSAR technique is a more effective monitoring tool in the construction and maintenance of the city. Given that InSAR technology exhibits the characteristics of all-weather observation and high spatial resolution, its satellite archived data can be used to monitor the historical long-term land subsidence characteristics of high-density urban areas during subway operation, monitor ground deformation at any time in the present and in the future, and overcome the inability of the traditional level setting and GPS monitoring network to obtain long-term land subsidence historical deformation information. However, this technology is highly sensitive to atmospheric errors, remote sensing satellite orbit errors, surface conditions, and temporal irrelevance. In addition, InSAR images lack natural surface features, which causes difficulty in their application. By contrast, GPS technology belongs to point positioning. It has a high time resolution and can perform the continuous observation. Therefore, the two technologies, InSAR and GPS, are complementary. GIS technology can collect, manage, operate, analyze, simulate, and display spatial data. It can be used to interpret and analyze the results of InSAR-GPS comprehensively and spatially. Therefore, the integration of InSAR-GPS-GIS technology to monitor long-term land subsidence in high-density urban areas during subway operation can overcome the limitations of a single technology application, quantitatively study long-term land subsidence, and monitor land subsidence changes at the sub-millimeter level in real-time during subway operation.

In this study, the 2.8 km operating line from Wulin Square station to Ding'an Road station of Hangzhou Metro Line 1 is used as an example to analyze the long-term subsidence in high-density urban areas during metro operation by InSAR-GPS-GIS technology.

2 DInSAR-GPS-GIS Integrated Method

2.1 Sentinel-1A Satellite Data

With a total length of 2.8 km, the region from Wulin Square station to Ding'an Road station of Hangzhou Subway Line 1 is selected as the research area, including Wulin Square station, Fengqi Road station, Longxiangqiao station, and Ding'an Road station. The study area is the largest commercial street in Hangzhou. Yan'an Road connects the three largest business circles of Hangzhou (Wulin, Hubin, and Wushan Business Circles) in series, and the population of the study area is large. Many important buildings, such as Hangzhou Tower, Yintai Wulin Department Store, and Hangzhou Department Store, are distributed on both sides of the road. A total of 20 scenes Sentinel-1A satellite data are downloaded for processing in the research area. For InSAR techniques, the atmospheric delay benefit is one of the most significant error sources and cannot be completely eliminated, so various researchers find ways to reduce the errors. This study uses GPS technology for precise coordinates and multi-scene image data for error reduction.

2.2 Digital Elevation Model (DEM) Data

The DEM data used in this study are obtained from Shuttle Radar Topography Mission (SRTM) 90 m data. The converted DEM data in standard format are shown in Fig. 1.

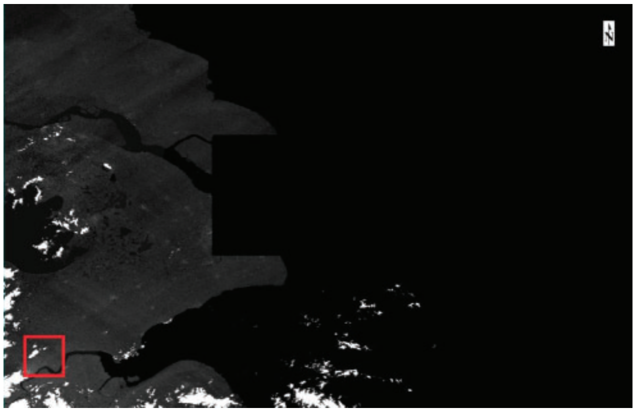

Figure 1: DEM data of the study area

2.3 Satellite Precision Orbit Data (POD)

POD Precise Orbit Ephemerides data are adopted to remove systematic errors caused by orbital errors. Sentinel-1 satellite POD are imaged into time format file S1A_OPER_AUX_POEORB_OPOD _20170628T121621_V20170607T225942_20170609T005942. The empirical orthogonal function (EOF) indicates that the imaging satellite is S1A, the release date of POD is June 28, 2017, and the data imaging date is June 08, 2017.

2.4 GPS Control Point in Research Area

Combined with the research area, the key coordinates of the region from Wulin Square station to Ding'an Road station are located, and the coordinates of the key points are obtained, as shown in Fig. 2 and Table 1. The soil type of the study area mainly includes clayey silt, mucky clay, very soft silty clay, and silty clay. The surface water in the project area has a great influence on the construction of adjacent stations and tunnels.

Figure 2: Locations of key points in the research area

Table 1: GPS coordinates of key points in the research area

Serial number	GPS point	Longitude	Latitude	Note
1	Point 1	120.170928	30.278203	Wulin Square station
2	Point 2	120.170353	30.268285	Fengqi Road station
3	Point 3	120.170496	30.260612	Longxiangqiao station
4	Point 4	120.171287	30.254123	Jianhengli
5	Point 5	120.174305	30.251814	Ding’an Road station
6	Point 6	120.16101	30.278702	Tianmu Mountain Road and Huancheng West Road Intersection
7	Point 7	120.163022	30.266351	Shengtangguan Pavilion
8	Point 8	120.168915	30.256868	West Lake Lotus Area
9	Point 9	120.178617	30.270406	North Zhonghe Road station
10	Point 10	120.181132	30.25431	Qinghua Hotel

2.5 Data Processing Based on ArcGIS

The ArcMap component of ArcGIS Desktop is used for data processing to import experimental data and display them inline chart form through ArcMap software to illustrate the law of long-term land subsidence changing with time.

2.6 DInSAR-GPS-GIS Integrated Method

The DInSAR-GPS-GIS integrated method is primarily based on the multi-view integration platform, as shown in Fig. 3.

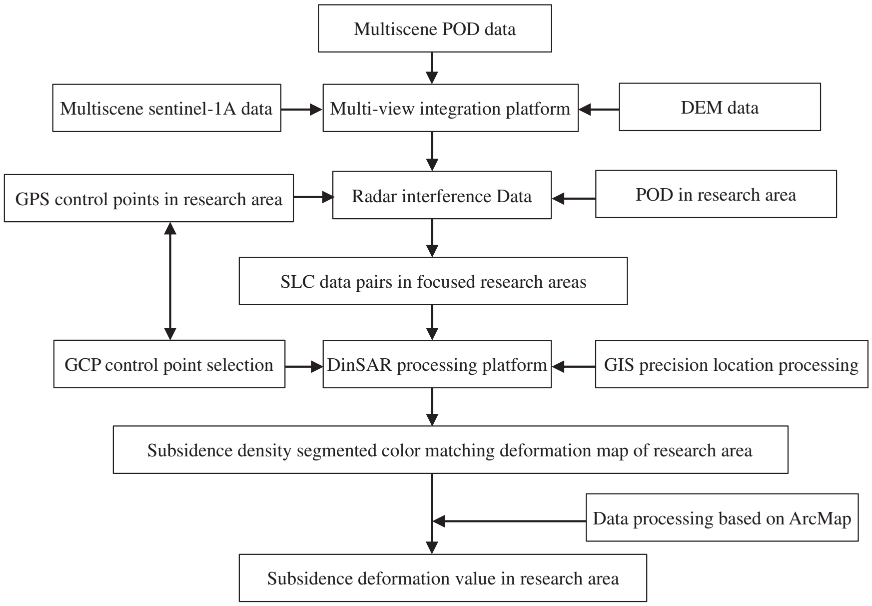

Figure 3: DInSAR-GPS-GIS integrated process

3 Key Algorithm of DInSAR Deformation

3.1 DInSAR Deformation Processing Flow

The flowchart of DInSAR deformation processing is shown in Fig. 4.

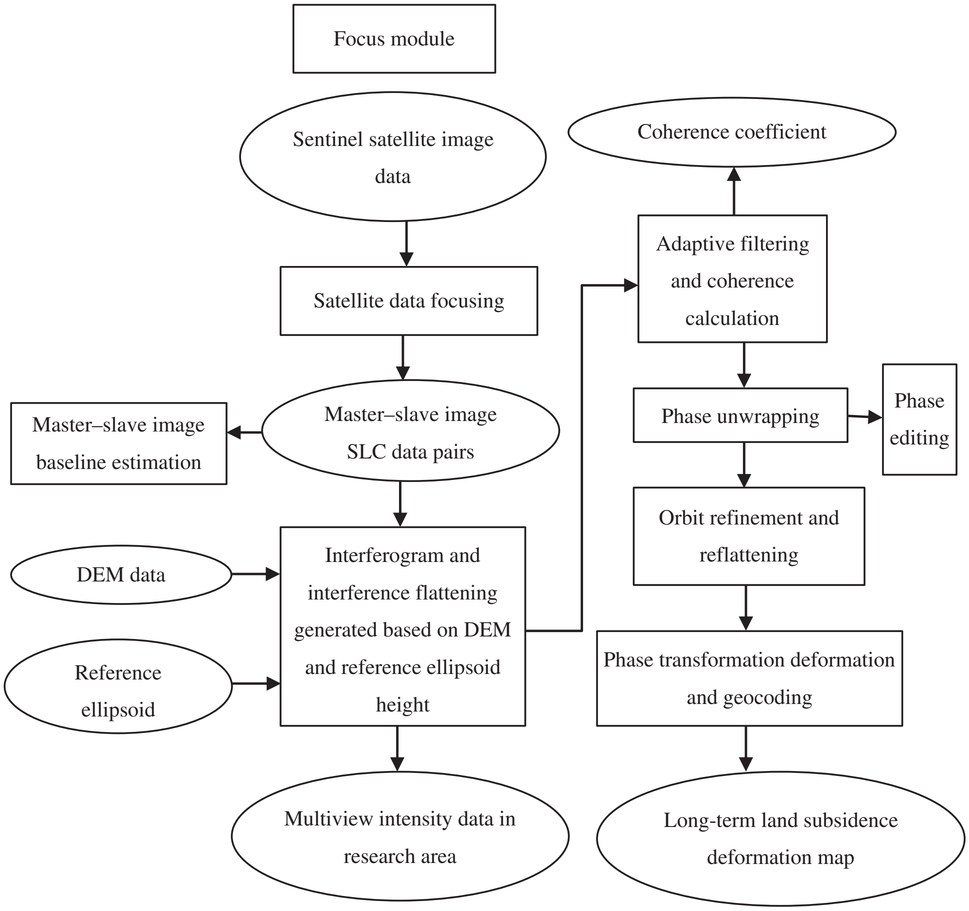

Figure 4: Flowchart of DInSAR deformation processing

3.2 Intensity Data of the Entire Scene Image

The obtained satellite data of Sentinel-1A for two scenes are used as an example, namely 20160601 and 20161128. 20160601 satellite data are selected as master images, whereas 20161128 satellite data are selected as slave images. The intensity map of the entire scene image in the research area is presented in Fig. 5.

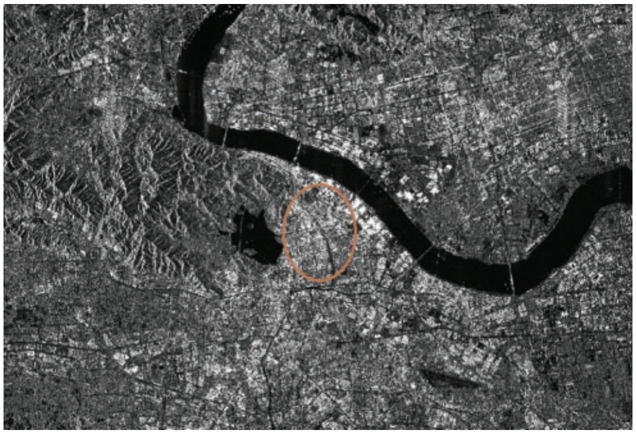

Figure 5: Intensity map of the entire scene image in the research area

3.3 Baseline Estimation Analysis

The theoretical height and theoretical deformation accuracy of baseline estimation in the research area are shown in Figs. 6 and 7, respectively.

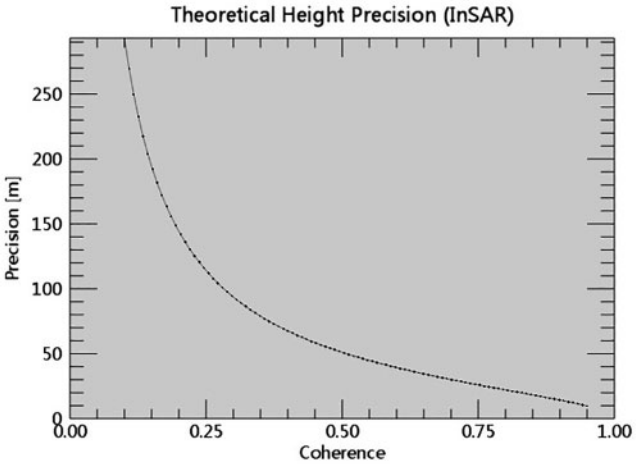

Figure 6: Theoretical height accuracy

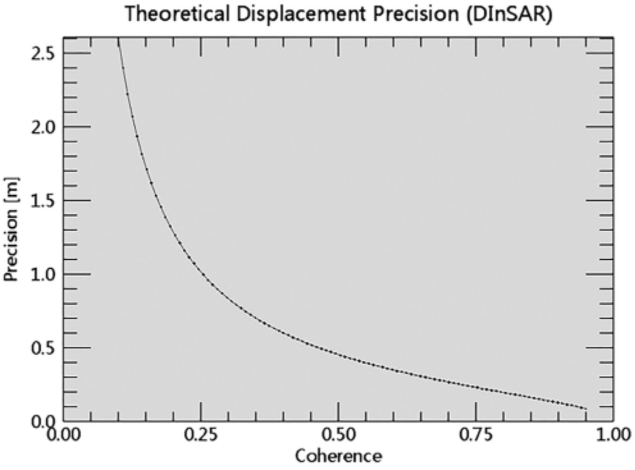

Figure 7: Theoretical deformation accuracy

The baseline estimation results in the research area are as follows:

Normal Baseline (m) = 59.401, Critical Baseline min-max (m) = [−6452.217]−[6452.217], Range Shift (pixels) = 2.734, Azimuth Shift (pixels) = −8.031, Slant Range Distance (m) = 879019.561, Absolute Time Baseline (Days) = 180, Doppler Centroid diff. (Hz) = −31.079, Critical min-max (Hz) = [−486.486]−[486.486], 2π Ambiguity height (InSAR) (m) = 261.718, 2π Ambiguity displacement (DInSAR) (m) = 0.028, 1 Pixel Shift Ambiguity height (Stereo Radargrammetry) (m) = 21984.307, 1 Pixel Shift Ambiguity displacement (Amplitude Tracking) (m) = 2.330, Master Incidence Angle = 39.623, Absolute Incidence Angle difference = 0.004.

The baseline estimation results indicate that the spatial baseline of the two-scene master-slave satellite data is 59.401 m, which is considerably less than the critical baseline of 6452.217 m. It satisfies the accuracy condition. The time baseline is 180 days. The surface deformation represented by a phase change period during DInSAR processing is 0.028 m.

3.4 Interferogram Generation

Image alignment is the first step that needs to be performed in InSAR data processing. This process requires that the same pair of pixel points of the two images correspond to the same pixel cell on the ground according to the coordinate mapping relationship between the corresponding points of the two images, and the complex values corresponding to the corresponding image elements in the two images are multiplied by the complex values, and the result of the two-phase conjugate multiplication is the interferogram. The selected polarization mode is VV, Range Looks is 5, Azimuth Looks is 1, Grid Size for Suggested Looks is 20, and Coregistration with DEM is True. The Global parameter sets Make TIFF True. The obtained interferogram after flattening in the research area is shown in Fig. 8 (One color cycle in the interferogram represents a 2π change in phase: red-yellow-blue-green is a complete 2π change cycle), and the master image intensity map is shown in Fig. 9.

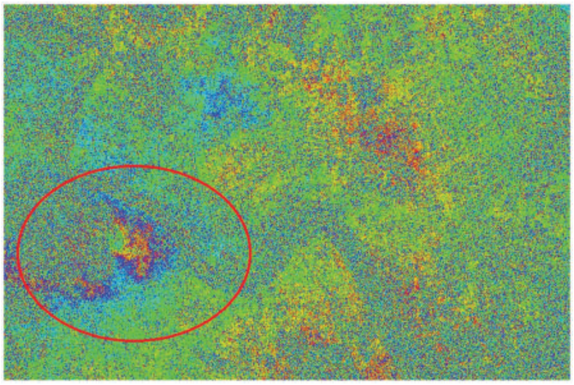

Figure 8: Interferogram after flattening in the research area

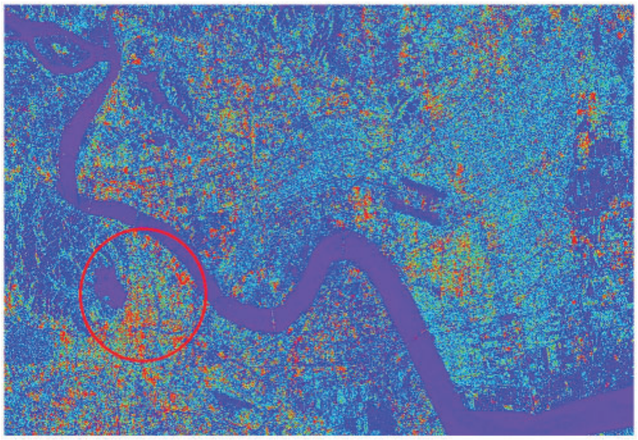

Figure 9: Master image intensity map after flattening in the research area

3.5 Filtering and Coherence Calculation

Three filtering methods, namely, adaptive, boxcar, and Goldstein, are available. Considering that the adaptive method is suitable for high-resolution data, the boxcar method uses the frequency of local interference fringes to optimize the filter and maintain small interference fringes as much as possible. Despite the variability of the filter in the Goldstein method, it improves the definition of interference fringes in the research area and reduces the decorrelation noise caused by spatial or temporal baselines. Therefore, the Goldstein method is selected to process the filtering of the research area, and the interferogram INTERF_out _fint (as shown in Fig. 10) and the coherence coefficient map INTERF_out _cc (as shown in Fig. 11) after filtering in the research area.

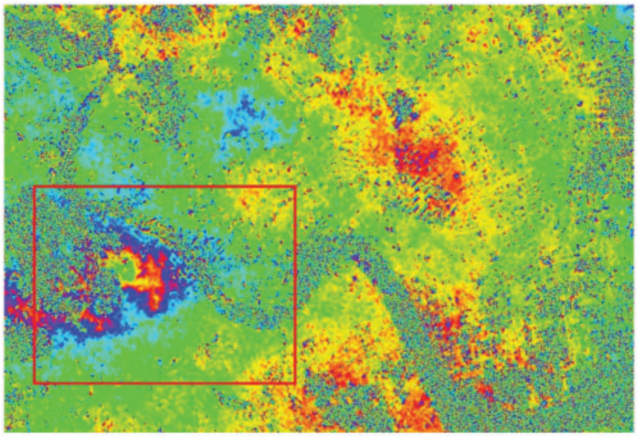

Figure 10: Interferogram after filtering in the research area

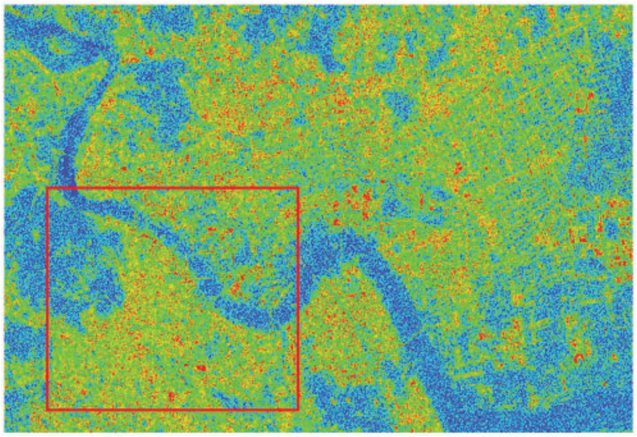

Figure 11: Coherence coefficient map in the research area

3.6 Phase Unwrapping

Phase change takes 2π as its period. As long as the phase change exceeds 2π, the phase will start and the cycle will begin again. Therefore, phase unwrapping involves unwrapping the phase after flattening and filtering, such that it corresponds to the linearly changing terrain information, and solving the 2π ambiguity problem. Three types of unwrapping methods, namely, region growing, minimum cost flow (MCF), and Delaunay MCF, are available. The region growing method does not set an extremely high coherence threshold to leave adequate free growth space. The phase mutation part exists as an unwrapped island on the unwrapped image. This method reduces the errors caused by phase mutation. The MCF method can achieve better results than the region growing method when unwrapping is difficult due to a large area of low coherence or other factors that restrict growth. This method uses a square grid, considers all the pixels in the image, and masks the pixels whose coherence is less than the threshold. The Delaunay MCF method is different from the MCF method because it does not consider all the pixels in an image but only those whose coherence is greater than the threshold value. Moreover, it uses Droney triangular grids instead of square grids. Therefore, the MCF method is selected as the unwrapping method, 1.0 is selected for the unwrapping decomposition level, and 0.2 is selected for the unwrapping coherence threshold. The phase unwrapping results in INTERF_out_upha are shown in Fig. 12.

3.7 Selection of Ground Control Points (GCPs)

GCPs should be selected away from the deformation area, phase jump area with unwrapping errors, and residual terrain phase. When dealing with surface deformation caused by DInSAR, a GCP can be selected at a position far from the deformation area in the absence of orbital errors. If orbital errors occur, then multiple GCPs should be considered as stable reference points from which the error phase can be calculated and removed by the program. The selection of GCPs is shown in Fig. 13.

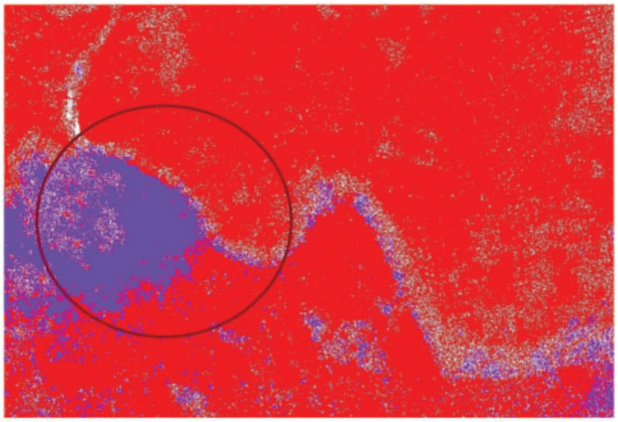

Figure 12: Phase unwrapping results

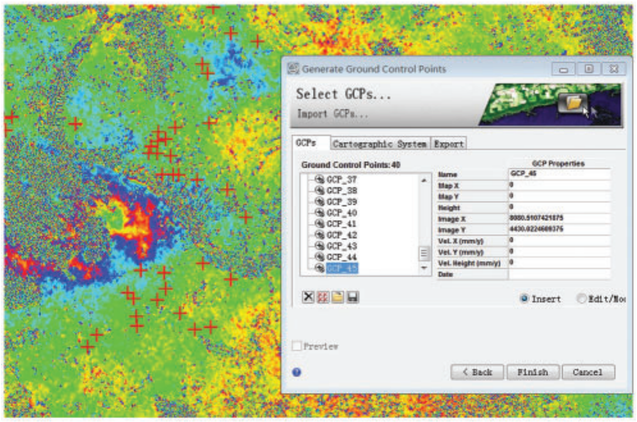

Ground Control Points: 40

GCP Properties	
Name	GCP_45
Map X	0
Map Y	0
Height	0
Image X	8080.5107421875
Image Y	4430.0224609375
Vel. X (mm/y)	0
Vel. Y (mm/y)	0
Vel. Height (mm/y)	0
Date	

● Insert

Figure 13: Selection of GCPs

3.8 Refinement and Reflattening

Refinement and reflattening involve the calculation of orbit refinement and phase shift, the elimination of possible slope phase, and the correction of satellite orbit and phase shift. Polynomial refinement is selected as the refinement method. The algorithm is robust and can be used even when the baseline is small. The Refinement Res Phase Poly Degree selects 3, which is the number of polynomials used to estimate the phase slope in the deflattening process. If the number of control point inputs is small, then the number of times will automatically decrease. The number 3 indicates that the phase slope with a constant phase shift in the range and azimuth directions will be corrected.

After the refinement and reflattening process, the optimized results are as follows:

ESTIMATE A RESIDUAL RAMP

Points selected by the user = 40, Valid points found = 40, Extra constrains = 2, Polynomial Degree choose = 3, Polynomial Type: $= k0 + k1 * rg + k2 * az$, Polynomial Coefficients (radians): $k0 = 24.7173808990$, $k1 = 0.0006048432$, $k2 = -0.0046972519$, Root Mean Square error (m) = 63.2093312825, Mean difference after Remove Residual refinement (rad) = −0.1101105943, Standard Deviation after Remove Residual refinement (rad) = 1.5099697025.

The interferogram INTERF_out_reflat_fint after reflattening is shown in Fig. 14, and the unwrapping results in INTERF_out_reflat_upha after reflattening are presented in Fig. 15.

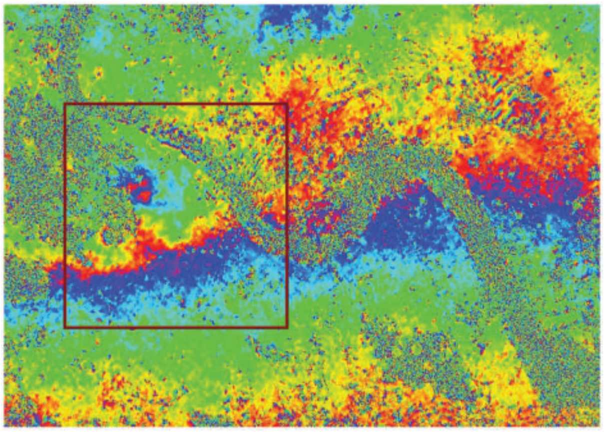

Figure 14: Interferogram after reflattening in the research area

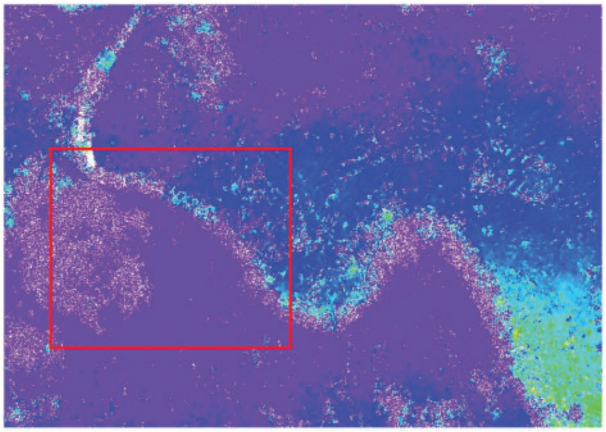

Figure 15: Unwrapping results after reflattening in the research area

3.9 Phase-to-Displacement Conversion and Geocoding

Phase-to-displacement conversion and geocoding combine the absolutely calibrated and unwrapped phases with the composite phase and convert them into deformation data and geocode them into a mapping coordinate system. By default, the system obtains deformation in the LOS direction. The product coherence threshold is 0.2, and the phase whose coherence is greater than this value is changed to the deformed value. Vertical displacement selects False, and the deformation in the vertical direction is not calculated. Slope displacement selects False, and the deformation in the slope direction is not calculated. Displacement custom direction selects False. Azimuth angle selects 0. The inclination angle selects 0. X dimension (m) selects 20. Y dimension (m) selects 20. Dummy removal selects True to mask the areas outside the image.

The deformation in the LOS direction is shown in Fig. 16. The coherency coefficient map of geocoding _slc_out_disp_cc_geo is shown in Fig. 17.

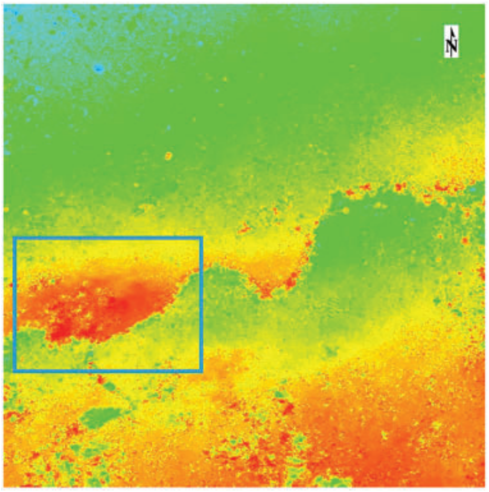

Figure 16: Deformation in the LOS direction in the research area

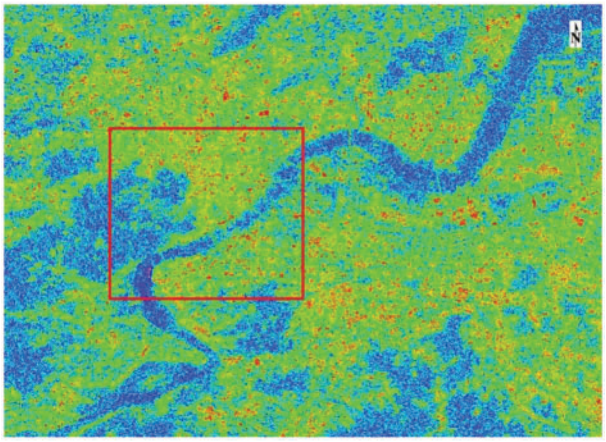

Figure 17: Coherency coefficient map of geocoding in the research area

4 Dynamic Analysis of Long-Term Land Subsidence during Subway Operation

20160601 Satellite Data Analysis

The deformation in the LOS direction _slc_out_disp is shown in Fig. 18.

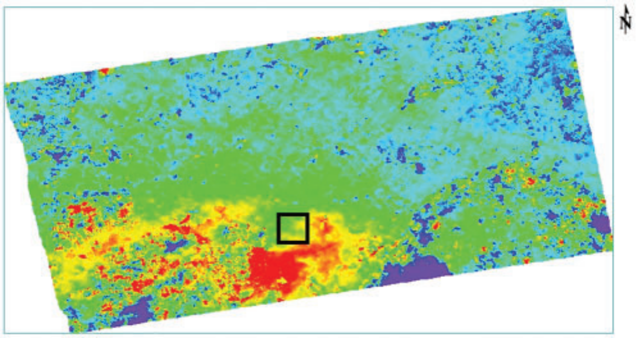

Figure 18: Deformation in the LOS direction in the research area

The comparison between satellite DEM and deformation area in the research area is presented in Fig. 19, and the deformation value in the research area is provided in Fig. 20. The satellite image data on June 01, 2016 indicate that the maximum subsidence is 27.76 mm, the minimum subsidence is 14.71 mm, and the average subsidence is 21.33 mm in the research area from Wulin Square station to Ding'an Road station of Hangzhou Subway Line 1.

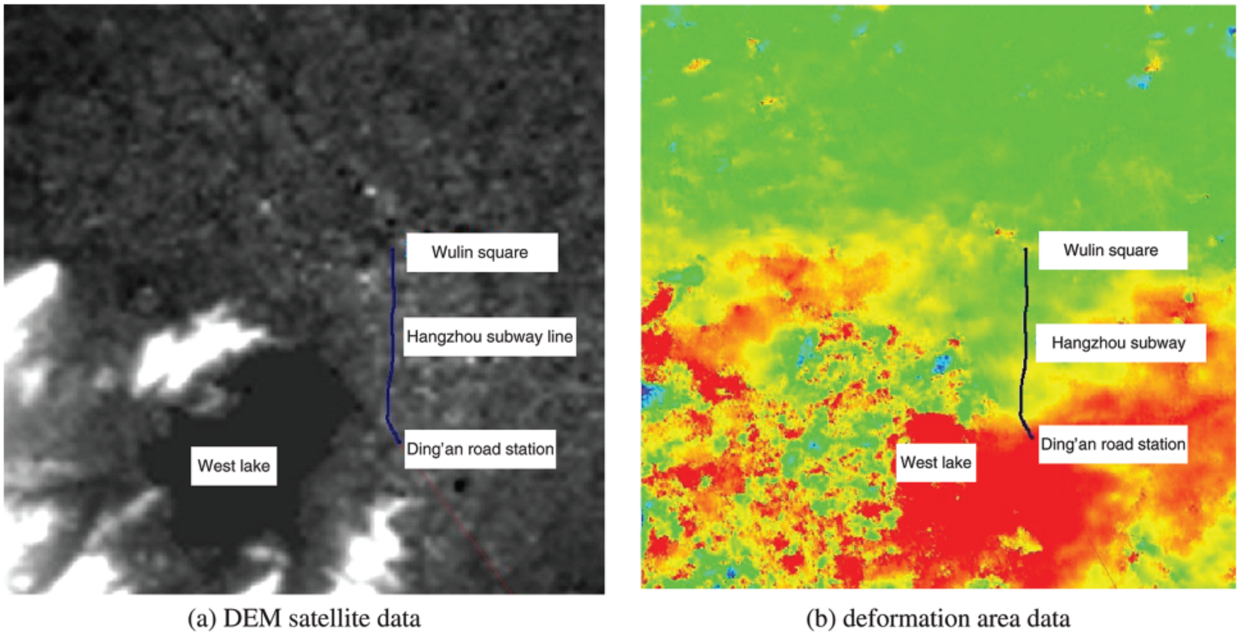

(a) DEM satellite data (b) deformation area data

Figure 19: Comparison between DEM satellite data and deformation area data in the research area

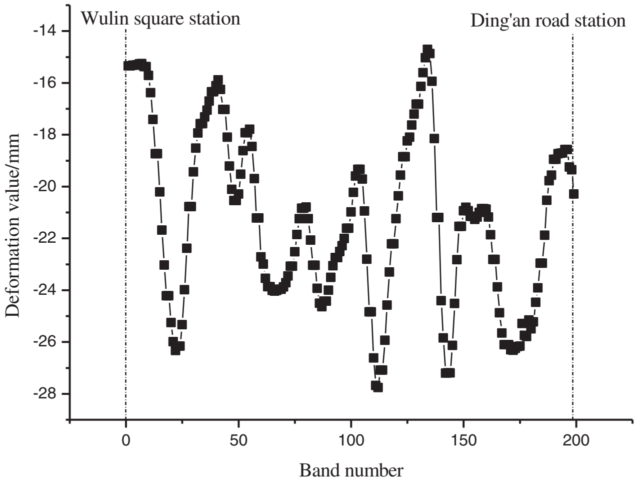

Figure 20: Deformation value in the research area

5 Numerical Simulation and Analysis of Results

5.1 Numerical Model Setup

According to the location of Hangzhou Subway Line 1 and the surrounding location of the soil geological conditions, as shown in Table 2; using rhino software to construct the tunnel-soil 3D geological generalization model of Hangzhou Subway Line 1; and imported into FLAC3D software, as shown in Fig. 21. The model size is 100 m in horizontal length, 60 m in height and 60 m in width, and the complex soil layer is simplified into a five-layer soil structure to facilitate the calculation. The Moore-Coulomb soil ontology model is used, the soil layers include fill layer, powder clay layer, silt clay layer, powder clay layer, powder clay sand layer; the diameter of the tunnel is 6 m, and double tunnels are used, 12 m apart, located 15 m below the surface edge and 6 m from the centerline of the surface.

Table 2: Basic physical and mechanical parameters of each layer of soil and tunnel

Number	Name of material	Thickness	Young's modulus	Poisson's ratio	Weight density	Angle of internal friction	Cohesion
1	Fill	3	20	0.3	19.9	12	25.3
2	Powdery clay	6	17	0.3	19.3	10	27.2
3	Silty clay	7.5	13.5	0.3	18.8	8	17.5
4	Powdery clay	5	15	0.3	18.9	11	26
5	Chalky soil with chalky sand	38.5	40	0.3	19.6	30	11.6
6	Tunnel lining	/	35000	0.2	28	/	/
7	Tunnel bed	/	20000	0.2	21	/	/

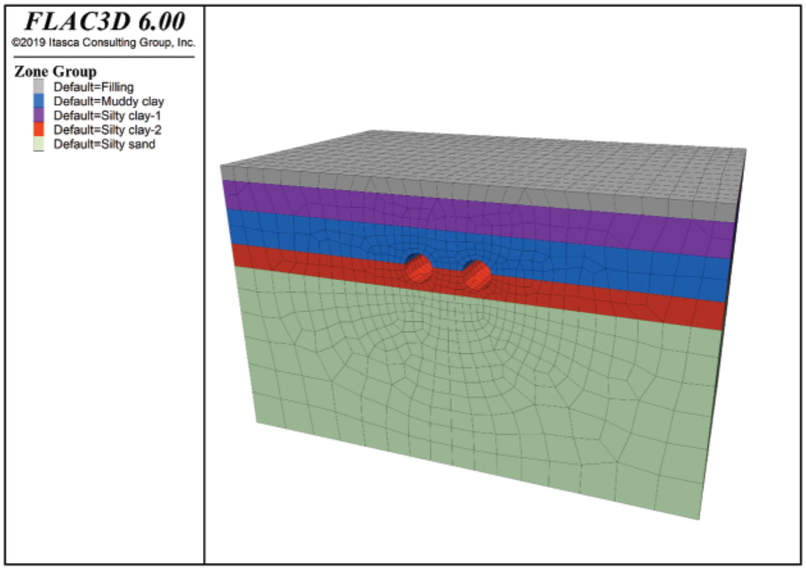

Figure 21: Tunnel-soil 3D model

5.2 *Analysis of Numerical Simulation Results*

The train dynamic load is the key to subway environmental vibration response analysis. Considering the limitation of the test conditions of the subway train dynamic load real measurement method and the limitation of the empirical formula method, the train one-track model is established using the US five-level track upset spectrum to obtain the train dynamic load; through a series of steps such as modeling, grid calculation cell division, parameter setting, constraint boundary conditions, establishing force field, calculating yield criterion establishment, etc., the vertical stress, maximum principal stress and displacement clouds of the tunnel-soil 3D finite element model are obtained and the results are analyzed, respectively.

(1) Analysis of vertical stress and maximum principal stress results

The train will be subject to vertical force and horizontal force at the same time during operation, and the horizontal force usually dominates during high-speed travel.

From Figs. 22 and 23, it can be seen that the horizontal stress is numerically greater than the vertical stress during the high-speed operation of the train, and in the soil layer in the area below the excavated tunnel, it can be clearly seen that its horizontal stress is greater than the vertical stress, which is more consistent with the actual situation.

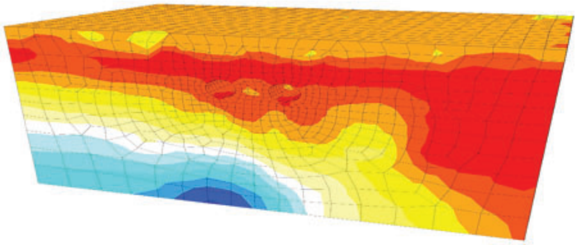

Figure 22: Vertical stress images

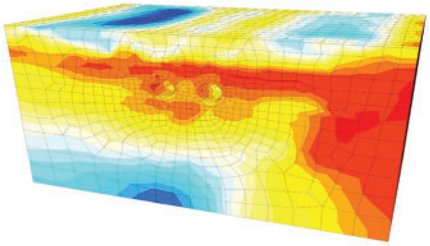

Figure 23: Horizontal stress of images

The main stress is positively correlated with the tunnel depth and soil depth, and the maximum main stress is usually at the bottom, but due to the excavation of the tunnel, the stress concentration phenomenon is generated on the surrounding soil, resulting in a rapid increase in stress, and with the completion of excavation, the stress concentration phenomenon gradually disappears, and the stress near the tunnel only increases to a certain extent compared to the distal end, and the overall trend of stress distribution becomes larger with the increase of depth, and the maximum main stress also appears at The maximum principal stresses also appear at the bottom of the soil, and the results presented in the model calculation clouds agree with the basic theory to a large extent. The maximum principal stress diagram is shown in Fig. 24.

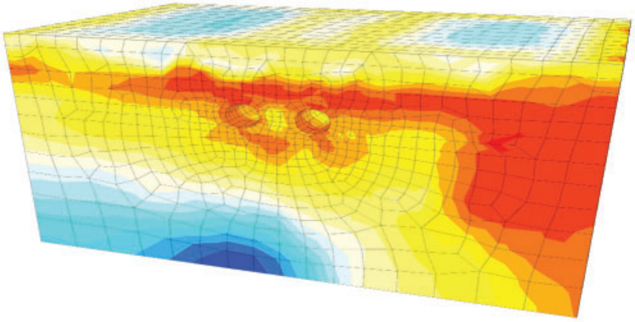

Figure 24: The maximum principal stress diagram

(2) Displacement results analysis

The train vibration load will cause deformation, and the ground surface will collapse under long-term train vibration load, uneven settlement, and other geohazard problems.

From Fig. 25, it can be concluded that the soil layer beneath the tunnel has a large deformation under the joint action of vibration load and stress concentration of the train, and the displacement deformation gradually decreases along the direction of the buried thickness of the soil layer, which is caused by the additional stress effect generated by the vibration load, and the long-term settlement maximum value of the ground surface has a tendency to increase first and then gradually decrease under the action of long-term vibration load. Overall, the deformation trends shown by the numerical simulation displacement cloud results are basically consistent with the DInSAR-GPS-GIS Integrated Method.

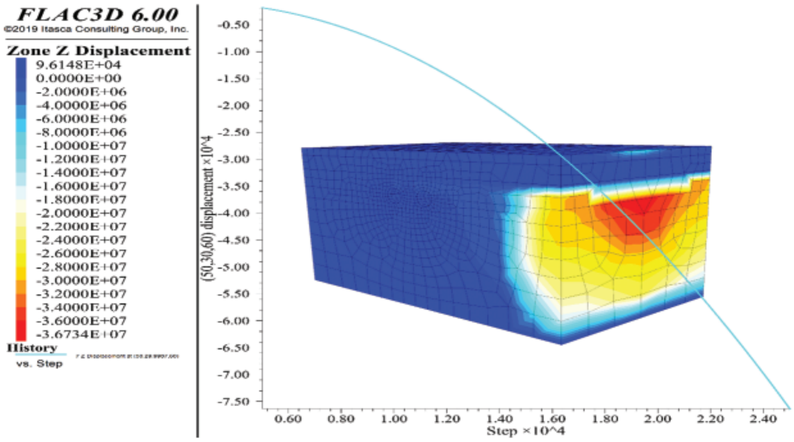

Figure 25: Vertical displacement diagram

6 Conclusions

Using the 2.8 km operation line between Wulin Square station and Ding'an Road station of Hangzhou Subway Line 1 as an example, this study proposes the integrated method of DInSAR-GPS-GIS technology, including Sentinel-1A satellite data, satellite POD, DEM data, GPS control points, and ArcGIS processing methods. This study presents the key algorithm for long-term land subsidence deformation during subway operation, including DInSAR deformation processing flow, baseline estimation, master-slave image file polarization mode selection, interferogram generation, filtering and coherence calculation, phase unwrapping, control point selection, orbit refinement and reflattening, phase transformation deformation, and geocoding. Multiscene image data, such as 20160601, 20161128, 20170608, and 20170912 satellite data, are selected to analyze long-term subsidence in high-density urban areas during subway operation. The long-term subsidence caused by the operation of Hangzhou Metro Line 1 from Wulin Square station to Ding'an Road station was found to be smaller in the study section compared to the long-term maximum subsidence of 240 mm in Nanjing Metro Line 10, China. The maximum subsidence is 30.64 mm, the minimum subsidence is 11.45 mm, and the average subsidence ranges from 19.27 to 21.33 mm. Based on the basic data of the study area, FLAC3D software was used to simulate the settlement of the study area subjected to vehicle loading, and it was found that the simulation results tended to be consistent with the monitoring by DInSAR-GPS-GIS technology, thus proving the reasonableness and accuracy of the algorithm.

Funding Statement: The financial supports for this research project by the National Natural Science Foundation of China (Nos. 41602308, 41967037). This research was supported by Zhejiang Provincial

Natural Science Foundation of China under Grant No. LY20E080005. This research was funded by National Key Research and Development Projects of China (No. 2019YFC507502) and Guangxi Science and Technology Plan Project (No. RZ2100000161).

Conflicts of Interest: The authors declare that they have no conflicts of interest to report regarding the present study.

References

1. China Business Information Network (2021). List of Subway Lines in Operation in Chinese Cities in 2020 (in Chinese). https://top.askci.com/news/20210303/1630341373357.shtml.
2. Zou, B. P., Sun, D., Mu, J. D., Xu, Z. P. (2021). Comprehensive risk evaluation in the long-term operation of urban subway based on multiple indices. *Mathematical Problems in Engineering, 2021,* 1–13. DOI 10.1155/2021/5521630.
3. Zhang, D. M., Huang, H. W., Yang, J. (2005). Influence of partial drainage of linings on long-term surface settlement over tunnels in soft soils. *Chinese Journal of Geotechnical Engineering, 27(12),* 1430–1436 (in Chinese). DOI 10.3321/j.issn:1000-4548.2005.12.012.
4. Zou, B. P., Wang, J. X., Tian, Q., Guo, W., Yang, J. H. et al. (2015). Numerical analysis of the soil deformation caused by tunneling under vehicle loads in the coastal reclamation area. *Mathematical Problems in Engineering, 2015,* 1–11. DOI 10.1155/2015/937245.
5. Leclerc, F., Feuillet, N. (2019). Quaternary coral reef complexes as powerful markers of long-term subsidence related to deep processes at subduction zones: Insights from Les Saintes (Guadeloupe French West Indies). *Geosphere, 15(4),* 983–1007. DOI 10.1130/GES02069.1.
6. Chen, Y., Zhang, K. F., Froger, J., Tan, K., Remy, D. et al. (2018). Long-term subsidence in lava fields at piton de la Fournaise volcano measured by InSAR: New insights for interpretation of the Eastern Flank motion. *Remote Sensing, 10(4),* 597. DOI 10.3390/rs10040597.
7. Tang, Y. Q., Yang, Q., Ren, X. W., Xiao, S. Q. (2019). Dynamic response of soft soils in high-speed rail foundation: *In situ* measurements and time domain finite element method model. *Canadian Geotechnical Journal, 56(12),* 1832–1848. DOI 10.1139/cgj-2018-0555.
8. Shi, Y. F., Cao, C. W., Chen, X. S., Zhang, L. C., Huang, Y. et al. (2021). Dynamic distortion and long-term settlement of weathered argillaceous siltstone under subway tunnel base in Nanchang, China. *Journal of Performance of Constructed Facilities, 35(6),* 1–9. DOI 10.1061/(ASCE)CF.1943-5509.0001659.
9. Di, H. G., Zhou, S. H., Guo, P. J., He, C., Zhang, X. H. et al. (2020). Observed long-term differential settlement of metro structures built on soft deposits in the Yangtze River Delta region of China. *Canadian Geotechnical Journal, 57(6),* 840–850. DOI 10.1139/cgj-2018-0524.
10. Qiu, J. L., Liu, H. Q., Lai, J. X., Lai, H. P., Chen, J. X. et al. (2018). Investigating the long-term settlement of a tunnel built over improved loessial foundation soil using jet grouting technique. *Journal of Performance of Constructed Facilities, 32(5),* 04018066. DOI 10.1061/(ASCE)CF.1943-5509.0001155.
11. Huang, Q., Huang, H. W., Ye, B., Zhang, D. M., Gu, L. L. et al. (2017). Dynamic response and long-term settlement of a metro tunnel in saturated clay due to moving train load. *Soils and Foundations, 57(6),* 1059–1075. DOI 10.1016/j.sandf.2017.08.031.
12. Tan, J., Cui, Z. D., Yuan, L. (2016). Study on the long-term settlement of subway tunnel in soft soil area. *Marine Georesources and Geotechnology, 34(5),* 486–492. DOI 10.1080/1064119X.2015.1030806.
13. Di, H. G., Zhou, S. H., Xiao, J. H., Gong, Q. M., Luo, Z. (2016). Investigation of the long-term settlement of a cut-and-cover metro tunnel in a soft deposit. *Engineering Geology, 204,* 33–40. DOI 10.1016/j.enggeo.2016.01.016.

14. Fadhillah, M., Achmad, A., Lee, C. (2020). Integration of InSAR time-series data and GIS to assess land subsidence along subway lines in the Seoul Metropolitan Area, South Korea. *Remote Sensing, 12(21),* 1–25. DOI 10.3390/rs12213505.
15. Shi, W., Chen, G., Meng, X. M., Jiang, W. Y., Chong, Y. et al. (2020). Spatial-temporal evolution of land subsidence and rebound over Xi'an in Western China revealed by SBAS-InSAR analysis. *Remote Sensing, 12(22),* 1–21. DOI 10.3390/rs12223756.
16. Hu, B., Yang, B., Zhang, X. F., Chen, X. L., Wu, Y. (2019). Time-series displacement of land subsidence in Fuzhou downtown, monitored by SBAS-InSAR technique. *Journal of Sensors, 2019,* 1–12. DOI 10.1155/2019/3162652.

Computer Modeling in
Engineering & Sciences

Tech Science Press

DOI: 10.32604/cmes.2023.022475

ARTICLE

Computational Modeling of Intergranular Crack Propagation in an Intermetallic Compound Layer

Tong An[1,2,*], **Rui Zhou**[1,2], **Fei Qin**[1,2,*], **Pei Chen**[1,2], **Yanwei Dai**[1,2] **and Yanpeng Gong**[1,2]

[1]Institute of Electronics Packaging Technology and Reliability, Faculty of Materials and Manufacturing, Beijing University of Technology, Beijing, 100124, China

[2]Beijing Key Laboratory of Advanced Manufacturing Technology, Beijing University of Technology, Beijing, 100124, China

*Corresponding Authors: Tong An. Email: antong@bjut.edu.cn; Fei Qin. Email: qfei@bjut.edu.cn

Received: 11 March 2022 Accepted: 22 June 2022

ABSTRACT

A micromechanical model is presented to study the initiation and propagation of microcracks of intermetallic compounds (IMCs) in solder joints. The effects of the grain aggregate morphology, the grain boundary defects and the sensitivity of the various cohesive zone parameters in predicting the overall mechanical response are investigated. The overall strength is predominantly determined by the weak grain interfaces; both the grain aggregate morphology and the weak grain interfaces control the crack configuration; the different normal and tangential strengths of grain interfaces result in different intergranular cracking behaviors and play a critical role in determining the macroscopic mechanical response of the system.

KEYWORDS

Cohesive zone element; intergranular cracking; polycrystalline material; intermetallic compound (IMC)

Nomenclature

a_i	the coordinates of the nuclei
A	the area of the IMC layer
A_{el}	the area of the cohesive interface element
b_i	the coordinates of the nuclei
$\mathbf{D}_{loc}$	the cohesive constitutive tangent stiffness matrix
E	the Young's modulus
$\mathbf{F}^{el}$	the nodal force vector of the interface element
G^c	the critical energy release rate
$\mathbf{H}$	the matrix of the shape function
$\mathbf{J}$	the Jacobian matrix
k_n	the unloading/reloading stiffness in the normal direction
k_t	the unloading/reloading stiffness in the tangential direction
$\mathbf{K}^{el}$	the tangential stiffness of the interface element
K_I	the stress intensity factor

L	the width of the IMC layer
N	the shape function
p_i	a nucleus
P	a set of n nucleus in a plane
q	the coupling parameter
r	the coupling parameter
t_{m}	the average thickness of the IMC layer
$\mathbf{T}$	the traction vector
ΔT_{n}	the increment of the normal traction
T_{n}	the normal traction component
$T_{\mathrm{n,max}}$	the maximum normal traction
ΔT_{t}	the increment of the tangential traction
T_{t}	the tangential traction component
$T_{\mathrm{t,max}}$	the maximum tangential traction
$\mathbf{T}_{\mathrm{loc}}$	the local traction vector
$\mathbf{u}_I$	the nodal displacement vector
$\mathbf{u}_I^{\mathrm{bottom}}$	the nodal displacements of the bottom nodes
$\mathbf{u}_I^{\mathrm{top}}$	the nodal displacements of the top nodes
$\boldsymbol{\Delta}\mathbf{u}_I$	the relative displacements between each pair of the nodes
$\boldsymbol{\Delta}\mathbf{u}_{\mathrm{loc}}$	the local separating displacement vector
W	the width of the cohesive interface element
x_i	the center points of each regular hexagon
$\mathbf{X}_I$	the initial coordinates of the nodes on the mid-line
$\mathbf{x}_I^{\mathrm{R}}$	the coordinates of the nodes on the mid-line after deformation
y_i	the center points of each regular hexagon
κ	the Weibull parameter
ν	the Poisson's ratio
$\boldsymbol{\Theta}$	the transformation matrix
α	the contact stiffness
$\boldsymbol{\delta}$	the separating displacement vector
$\delta_{\mathrm{cr,n}}$	the critical normal separating displacement
δ_{n}	the normal separating displacement
$\Delta\delta_{\mathrm{n}}$	the increment of the normal separating displacement
$\delta_{\mathrm{cr,t}}$	the critical tangential separating displacement
δ_{t}	the tangential separating displacement
$\Delta\delta_{\mathrm{t}}$	the increment of the tangential separating displacement
δ_{n}^{*}	the value of δ_{n} after complete shear separation
δ_{tol}	the specific penetration tolerance
λ	the Weibull parameter
ϕ_{n}	the cohesive energy under the pure mode-I (opening)
ϕ_{t}	the cohesive energy under the pure mode-II (shearing)
ξ	the local element coordinate
IMC	intermetallic compounds
UEL	user subroutine to define an element in the finite element code ABAQUS
VCFEM	Voronoi cell finite element model

1 Introduction

Solder joint is a key factor affecting the electrical, thermal, and mechanical performance of electronic packages. At the solder joint-Cu pad interface, the intermetallic compound (IMC) is crucial for forming a functional metallurgical bonding. However, excessive growth of IMC layer is considered to be an initiation site for microcracks, which will degrade the mechanical strength of the solder joint [1]. To achieve improved performance, effective modeling for understanding the failure mechanism of the IMC layer in the solder joint is indispensable for the reliable design of electronic packages.

As a polycrystalline quasi-brittle material, the morphological characteristics of the IMC microstructure, such as the grain shape, size and defects, have a great influence on the failure mechanism of the IMC. However, most of the previous research [2,3] focused on the macroscopic failure behavior, not the microstructural damage evolution of the IMC. These works cannot account for the microstructure characteristics of the IMC and the grain boundary defects with random distribution in the IMC layer. As a result, finite element (FE) analysis results are not consistent with the experimental results. Therefore, a model accounting for the microstructure-based mechanism of IMC failure is important for understanding the micromechanical behavior of the IMC layer that controls the macroscopic response.

Some efforts have been made to develop an effective numerical procedure to describe material intergranular cracking in polycrystalline brittle material using the FE analysis [4,5]. With such models, the explicit discrete nature of the polycrystalline microstructure was retained, and the interface elements were applied to simulate the intergranular cracking behavior. The material failure in these models was not limited by specific fracture criteria; therefore, the initiation and propagation of microcracks were a natural outcome of the material response, the boundary constraints and the applied loading.

The three essential factors of the method are the geometric characterization of microstructure of polycrystalline materials, the description of the grain boundary defects and the numerical simulation of the grain interface behavior.

Geometric representation of grain microstructure. Typically, regular or irregular microstructures are generated in numerical modeling to reflect the geometry of polycrystalline structures on the microscopic scale. For example, Onck et al. [6] used regular hexagonal grains to study intergranular creep cracking of polycrystalline materials. In addition, a voronoi cell finite element model (VCFEM) which can be used to simulate the arbitrary microstructure of a multiphase material was proposed by Ghosh et al. [7]. Two-dimensional voronoi tessellations were applied to generate a micromechanical model for describing the brittle compressive fracture of polycrystalline ice [8,9]. Furthermore, the voronoi tessellation-based simulation was extended to three-dimensional modeling, which was employed to study the cracking process of brittle ceramics [10] and to account for the heterogeneity of polycrystalline materials [11,12]. Both regular and irregular microstructures have been extensively used in computational materials science [13–16]. In this analysis, regular hexahedral grains and irregular polygonal grains are established and applied to study the influence of the grain aggregate morphology on the crack configuration and the overall response.

Grain boundary defects. It has been realized that the existence of pre-existing flaws at grain boundaries have great influence on the mechanical properties of polycrystalline materials [17,18]. Therefore, grain boundary defects should be considered in the model [4,14]. In this analysis, the grain interface properties are described by a Weibull distribution to account for the grain boundary defects, and their influence on the crack configuration and the overall response is discussed.

Numerical modeling of grain interface behavior. The constitutive description of the grain interface should account for the relevant physical mechanisms, such as grain boundary sliding, separation, and microcracking by coalescence. The cohesive zone model has been considered a feasible tool for describing the debonding behavior of material interfaces. The concept of the cohesive zone model was originally proposed by Barenblatt [19] and Dugdale [20]. Needleman [21] used the traction-separation relationship specified by the cohesive zone law to investigate void nucleation and fracture growth at particle-matrix interfaces. In this analysis, the cohesive interface element is applied, and the behavior of the element is governed by the cohesive zone law.

The parameters of the cohesive zone law play a crucial role in determining the macroscopic mechanical response of materials. The magnitudes of the parameters vary widely, ranging from MPa to GPa for traction, J to kJ for energy, and nm to mm for separating displacement. The effect of various parameters in the cohesive zone law on the macroscopic failure of materials has been examined in the literature [22–25]. It is commonly believed that the failure behavior is dominated primarily by the energy that controls separation; thus, cohesive energy is the most important parameter. The question raised here is as follows: Can changing the maximum traction applied at the grain interfaces change the micro and macro mechanical response of a polycrystalline material, even if the cohesive energy is the same? To answer the question, we compared the predictions of the models with different maximum tractions applied in the normal and tangential directions of grain interfaces.

In this paper, a micromechanical model of an IMC layer is constructed. The polycrystalline microstructure is represented by the polygonal grains generated by voronoi tessellation. The cohesive zone elements, which are carried out by using a user-defined subroutine (UEL) in ABAQUS, are embedded along the grain interfaces to simulate the microcrack cracking process. The influence of the grain aggregate morphology, stochastically distributed grain boundary defects, and various cohesive zone parameters on the overall mechanical response and failure behavior are considered and discussed.

2 Grain-Level Micromechanical Model of the IMC Layer

2.1 Microstructure of the IMC

Fig. 1 presents a schematic diagram of the cross-section of a solder joint. The Cu_6Sn_5 η-phase and Cu_3Sn ε-phase are the two phases formed between the Cu substrate and the Sn-based solder during the soldering and aging process. Before aging, only a layer of Cu_6Sn_5 was observed, and the Cu_3Sn was too thin to be observed (Fig. 2a). The solder/IMC interface showed scallop shape and was extremely rough. After isothermal aging, an IMC layer consisting of both the Cu_6Sn_5 and Cu_3Sn layers can be observed. Both layers became thicker and the solder/IMC interface became more planar (Fig. 2b) [26]. Figs. 2c and 2d show the SEM micrographs of the Cu_6Sn_5 grains. Before aging, the Cu_6Sn_5 grains appeared to be round-like, and typical polygonal Cu_6Sn_5 grains can be observed after isothermal aging. According to experimental observations, delamination and cleavage of the IMC mainly occur in the layer of Cu_6Sn_5 grains, and the Cu_3Sn grains remain mostly intact [27]. This suggests that we should pay more attention to the Cu_6Sn_5 layer rather than the Cu_3Sn layer when modeling the solder joint.

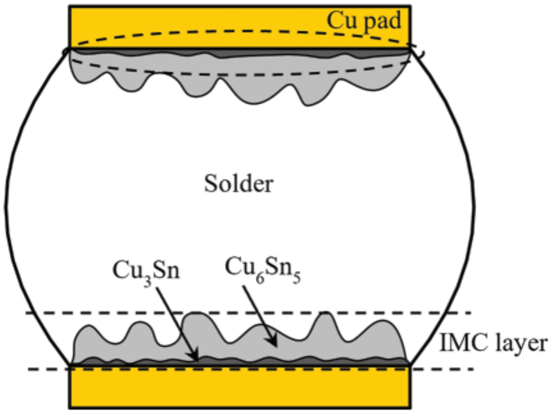

Figure 1: Schematic diagram of solder joint section

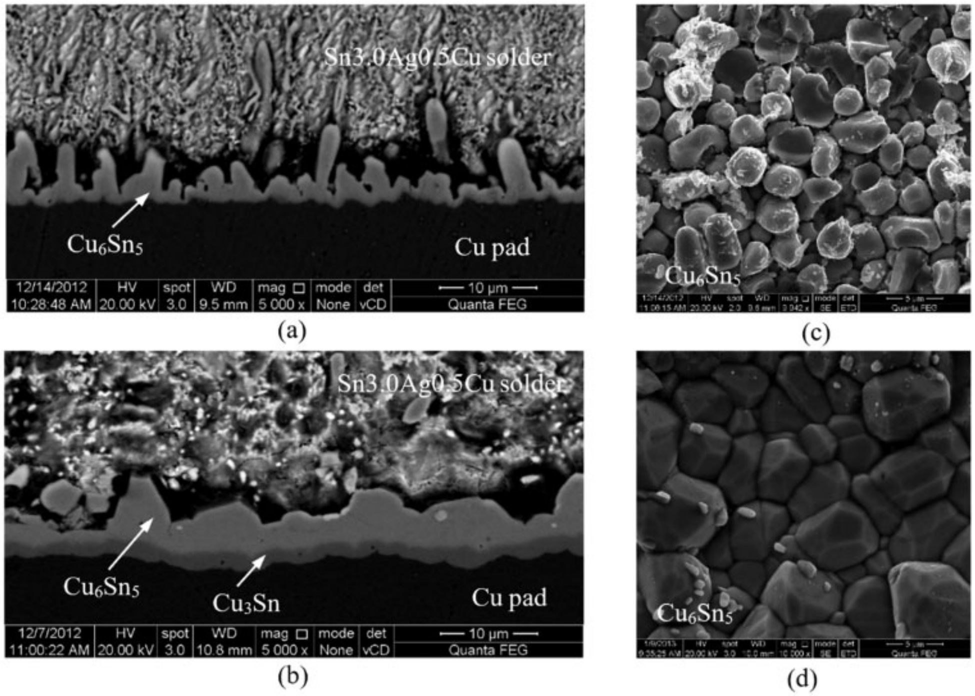

Figure 2: SEM images of the Sn3.0Ag0.5Cu/Cu interface aged at 150°C for (a) 0 h, (b) 500 h and the top views of the IMC layer aged for (c) 0 h and (d) 500 h

2.2 Geometrical Features of Grain-Level Modeling

Voronoi tessellation is widely applied to generate the geometry of the grain microstructure of polycrystalline materials [28,29]. Suppose p_i is a point in a plane that can be called a nucleus, and P represents a set of n points. To divide the plane into n cells, the voronoi tessellation of P is

$$V(p_i) = \left\{ q \in \text{Plane} \,\middle|\, \mathrm{d}(q, p_i) \le \mathrm{d}\left(q, p_j\right) \ \text{ for each } p_i \in P,\ j \neq i \right\} \tag{1}$$

where q is a point lying in the cell, and $\mathrm{d}(q, p_i)$ denotes the Euclidean distance between q and p_i.

The shape and aggregate morphology of the grains are defined by the nuclei; thus, the distribution of nuclei should be predefined carefully. The center points of the regular polygon were (x_i, y_i). The coordinates of the nuclei (a_i, b_i) were chosen randomly around the center points, which were $a_i \in (x_i - \alpha x_i, x_i + \alpha x_i)$ and $b_i \in (y_i - \beta y_i, y_i + \beta y_i)$. The α and β were applied to control the location of the nucleus within the polygon. Here, the models of regular polygon (Fig. 3a) and irregular polygon (Fig. 3b) are established. The vertex coordinates of the cells generated by MATLAB, and the geometric model of the polycrystalline microstructure were established by Python scripting language and ABAQUS/CAE.

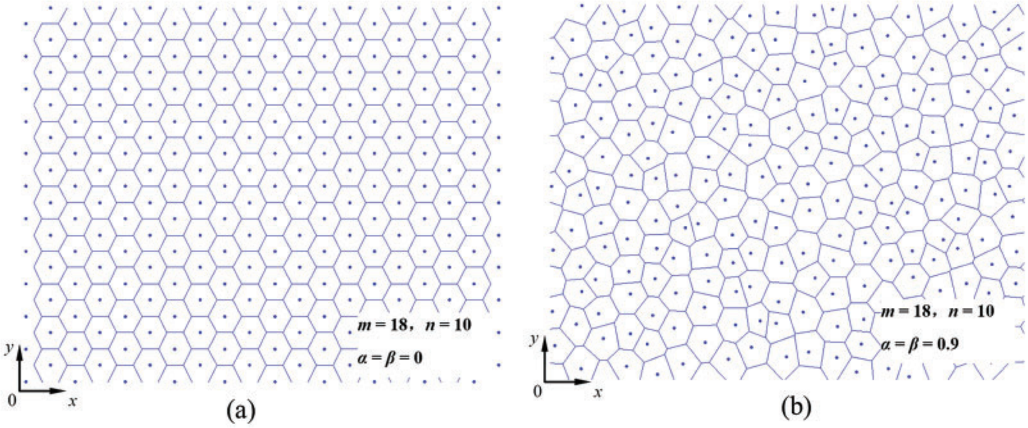

Figure 3: Voronoi tessellations with (a) Regular hexagonal grains and (b) Irregular polygonal grains

2.3 Constitutive Behavior of the Cohesive Zone Element

Cohesive zone law. A cohesive zone law is described by the relation between the traction **T** on the interface and the corresponding separating displacement $\boldsymbol{\delta}$ [30–32]. Here, a modified exponential cohesive zone law [33] was applied, as shown in Fig. 4. The normal traction T_n and the tangential traction T_t are expressed as

$$T_\mathrm{n} = \frac{\phi_\mathrm{n}}{\delta_\mathrm{cr,n}}\left(\frac{\delta_\mathrm{n}}{\delta_\mathrm{cr,n}}\right)\exp\left(-\frac{\delta_\mathrm{n}}{\delta_\mathrm{cr,n}}\right)\exp\left(-\frac{\delta_\mathrm{t}^2}{\delta_\mathrm{cr,t}^2}\right), \qquad \delta_\mathrm{n} \geq 0, \quad \Delta\delta_\mathrm{n} \geq 0 \tag{2a}$$

$$T_\mathrm{t} = 2\frac{\phi_\mathrm{t}}{\delta_\mathrm{cr,t}}\left(\frac{\delta_\mathrm{t}}{\delta_\mathrm{cr,t}}\right)\left(1 + \frac{\delta_\mathrm{n}}{\delta_\mathrm{cr,n}}\right)\exp\left(-\frac{\delta_\mathrm{n}}{\delta_\mathrm{cr,n}}\right)\exp\left(-\frac{\delta_\mathrm{t}^2}{\delta_\mathrm{cr,t}^2}\right), \quad \Delta\delta_\mathrm{t} \geq 0 \tag{2b}$$

where δ_n and δ_t are separating displacements in the normal and tangential directions, respectively; $\delta_\mathrm{cr,n}$ and $\delta_\mathrm{cr,t}$ are the critical separating displacements; $\Delta\delta_\mathrm{n}$ and $\Delta\delta_\mathrm{t}$ are the increments of the separating displacement; ϕ_n and ϕ_t are the cohesive energies under opening and shearing failure, respectively. The modified cohesive zone law preserves most features of the original exponential cohesive zone law proposed by Xu et al. [30] and includes a more advantageous controllable coupling effect. This modified cohesive zone law describes the mixed-mode decohesion process better and provides the possibility to account for different values for ϕ_n and ϕ_t [33].

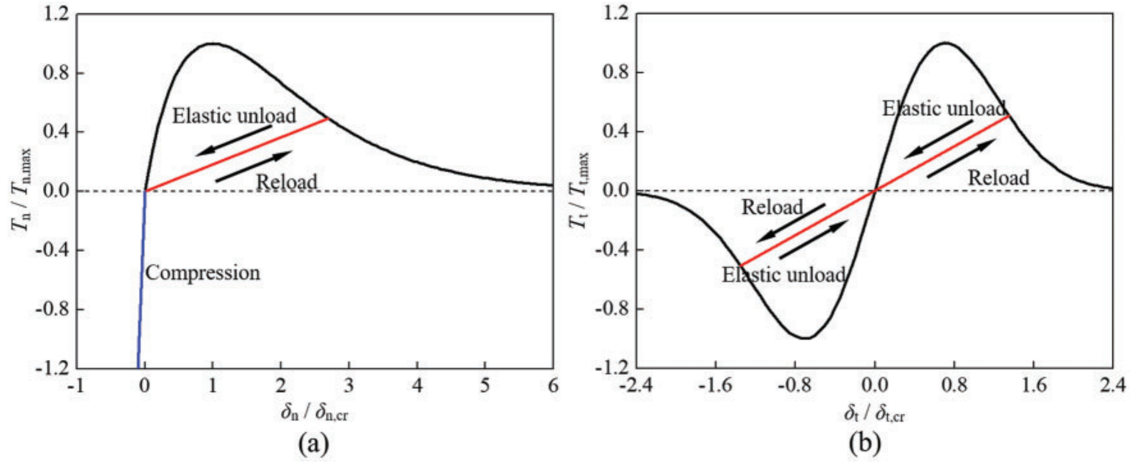

Figure 4: The cohesive zone law: (a) The normal traction-separation relationship; (b) The tangential traction-separation relationship

Unloading and reloading. In the cohesive zone element, after the maximum traction is reached, the cohesive zone element shows an irreversible response, and the traction-separation curve for unloading/reloading shows an elastic relation, as shown in Fig. 3, i.e.,

$$\Delta T_n = k_n \Delta \delta_n, \quad \Delta \delta_n < 0 \tag{3a}$$

$$\Delta T_t = k_t \Delta \delta_t, \quad \Delta \delta_t < 0 \tag{3b}$$

where ΔT_n and ΔT_t are the increments of the normal and tangential tractions, respectively, and k_n and k_t are the unloading/reloading stiffnesses in the normal and tangential directions, respectively.

Compression. When the cohesive zone element is under compression, the interpenetration of the two volume elements which connected by the cohesive zone elements may occur. To ensure that the interpenetration is tolerable, some efforts have been made, including applying a contact algorithm at the interfaces [34], choosing the normal stiffness value carefully [35], and modifying the constitutive equation in compression [36]. Here, when the normal displacement is negative, an extra compressive traction T_c is applied, i.e., if $\delta_n < 0$,

$$T_c = -\alpha \left(\frac{\delta_n}{\delta_{tol}} \right)^2, \delta_n < 0 \tag{4}$$

where α is the contact stiffness and δ_{tol} is a specific interpenetration tolerance. This extra compressive traction improves the compressive capacity of the cohesive zone element, and interpenetration can be prevented.

2.4 Cohesive Zone Element

The cohesive zone element connects the two adjacent volume elements during the fracture process. In this section, the basic formulation of the cohesive interface element used in this paper is presented [37,38].

Fig. 5 shows a two-dimensional quadrilateral cohesive zone element with two integration points, four nodes, and a local element coordinate ξ $(-1 \le \xi \le 1)$ defined along the midline of the element. The initial thickness of the cohesive zone element is zero, as shown in Fig. 5a. When the adjacent volume elements deform, the two surfaces of the cohesive zone element separate, and the midline deforms. Another local coordinate system (n, t) connected with the deformed midline is defined in order to describe the traction-separation relation, as shown in Fig. 5b.

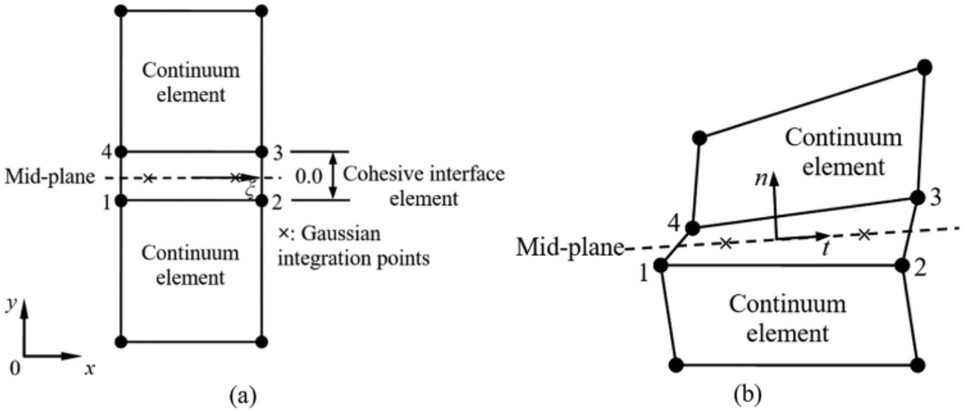

Figure 5: The cohesive interface element in (a) The initial configuration and (b) The deformed configuration

The nodal displacement vector of the four-node cohesive zone element is

$$\mathbf{u}_I = (u_1, v_1, u_2, v_2, u_4, v_4, u_3, v_3)^{\mathrm{T}} \tag{5}$$

The nodal displacements of the bottom and top nodes are

$$\mathbf{u}_I^{\mathrm{bottom}} = (u_1, v_1, u_2, v_2)^{\mathrm{T}}, \mathbf{u}_I^{\mathrm{top}} = (u_4, v_4, u_3, v_3)^{\mathrm{T}} \tag{6}$$

The separating displacement of the element is then expressed as

$$\Delta\mathbf{u}_I = \mathbf{u}_I^{\mathrm{top}} - \mathbf{u}_I^{\mathrm{bottom}} \tag{7}$$

The continuous separating displacement field within the element is

$$\begin{aligned}\Delta\mathbf{u}(\xi) &= \begin{pmatrix}\Delta u_x(\xi)\\ \Delta u_y(\xi)\end{pmatrix} = \mathbf{H}(\xi)\,\Delta\mathbf{u}_I\\ &= \mathbf{H}(\xi)\,\mathbf{u}_I^{\mathrm{top}} - \mathbf{H}(\xi)\,\mathbf{u}_I^{\mathrm{bottom}} = \mathbf{B}(\xi)\,\mathbf{u}_I\end{aligned} \tag{8}$$

With

$$\mathbf{B}(\xi) = [-\mathbf{H}(\xi)\ |\mathbf{H}(\xi)] \tag{9}$$

where $\mathbf{H}(\xi)$ is a matrix of the shape function.

The nodal force vector is

$$\mathbf{F}^{\mathrm{el}} = \int_{A_{\mathrm{el}}} \mathbf{B}^{\mathrm{T}}\mathbf{T}\,\mathrm{d}A \tag{10}$$

where the tractions, $\mathbf{T}$, are computed from the separating displacements via the cohesive zone law, which is shown in Section 2.3, and A_{el} is the area of the cohesive zone element. The tangential stiffness is computed by

$$\mathbf{K}^{\mathrm{el}} = \frac{\partial \mathbf{F}^{\mathrm{el}}}{\partial \mathbf{u}_I} = W \int_{-1}^{1} \mathbf{B}^{\mathrm{T}} \mathbf{D} \mathbf{B} \det(\mathbf{J})\, \mathrm{d}\xi \tag{11}$$

where **D** is the cohesive constitutive tangent stiffness matrix derived by differentiating the traction with respect to the separation.

3 Result and Discussion

3.1 Effect of the Grain Aggregate Morphology on the Failure Behavior

Two-dimensional finite element models including a Cu pad, Sn3.0Ag0.5Cu solder and Cu_6Sn_5 grains were constructed, as presented in Fig. 5. To investigate the effect of the grain aggregate morphology, voronoi tessellations were utilized to generate three models with different shape coefficients: Model I with $\alpha_1 = \beta_1 = 0$ (Fig. 6a), Model II with $\alpha_2 = \beta_2 = 0.3$ (Fig. 6b), and Model III with $\alpha_3 = \beta_3 = 0.9$ (Fig. 6c). An increase in the coefficients α and β indicates an increase in the irregularity of the grain aggregate morphology. The list of the related finite element models is given in Table 1. The average thickness of the IMC (Cu_6Sn_5) layer t_m was defined by dividing the area A by its width L, i.e., $t_m = A/L$, which were 9.5, 9.4 and 9.3 µm in the models. 48 grains and 138 grain boundaries were applied in each model.

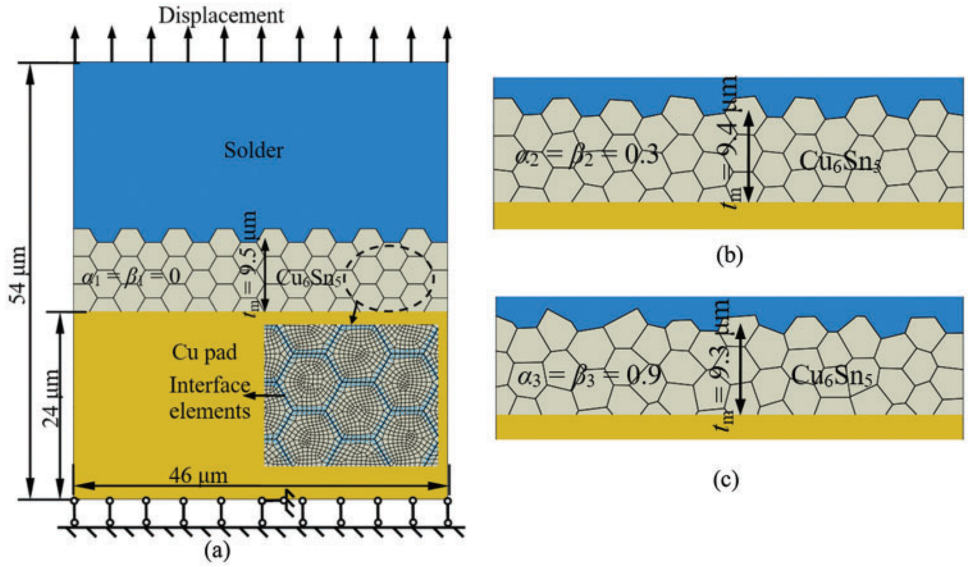

Figure 6: Models of solder/Cu_6Sn_5 grains/Cu pad structure with different grain aggregate morphologies: (a) Model I ($\alpha_1 = \beta_1 = 0$), (b) Model II ($\alpha_2 = \beta_2 = 0.3$), and (c) Model III ($\alpha_3 = \beta_3 = 0.9$)

Table 1: Outline of the finite element analyses

Mode	t_m (µm)	Shape coefficient	Grain interface properties strategy	Maximum grain interface tractions (MPa)
Model I	9.5	$\alpha_1 = \beta_1 = 0$	Homogeneous	$T_{n,max} = 68$, $T_{t,max} = 28$
Model II	9.4	$\alpha_2 = \beta_2 = 0.3$	Homogeneous	$T_{n,max} = 68$, $T_{t,max} = 28$

(Continued)

Table 1 (continued)

Mode	t_m (μm)	Shape coefficient	Grain interface properties strategy	Maximum grain interface tractions (MPa)
Model III	9.3	$\alpha_3 = \beta_3 = 0.9$	Homogeneous	$T_{n,max} = 68$, $T_{t,max} = 28$
Model I-W1	9.5	$\alpha_1 = \beta_1 = 0$	Weibull $\kappa_1 = 5$, $\lambda_1 = 1$	$T_{n,max} = 68$, $T_{t,max} = 28$
Model I-W2	9.5	$\alpha_1 = \beta_1 = 0$	Weibull $\kappa_2 = 2.5$, $\lambda_2 = 0.8$	$T_{n,max} = 68$, $T_{t,max} = 28$
Model I-W3	9.5	$\alpha_1 = \beta_1 = 0$	Weibull $\kappa_3 = 5$, $\lambda_3 = 1.5$	$T_{n,max} = 68$, $T_{t,max} = 28$
Model III-W1	9.3	$\alpha_3 = \beta_3 = 0.9$	Weibull $\kappa_1 = 5$, $\lambda_1 = 1$	$T_{n,max} = 68$, $T_{t,max} = 28$
Model III-W2	9.3	$\alpha_3 = \beta_3 = 0.9$	Weibull $\kappa_2 = 2.5$, $\lambda_2 = 0.8$	$T_{n,max} = 68$, $T_{t,max} = 28$
Model III-W3	9.3	$\alpha_3 = \beta_3 = 0.9$	Weibull $\kappa_3 = 5$, $\lambda_3 = 1.5$	$T_{n,max} = 68$, $T_{t,max} = 28$
Model IV-N	15.5	$\alpha_3 = \beta_3 = 0.9$	Homogeneous	$T_{n,max} = 68$, $T_{t,max} = 28$
Model IV-T	15.5	$\alpha_3 = \beta_3 = 0.9$	Homogeneous	$T_{n,max} = 27$, $T_{t,max} = 60$

The CPE4 elements in ABAQUS were used to mesh the interior of the Cu_6Sn_5 grains, the solder, and the Cu pad. The cohesive zone elements described above were embedded along the grain boundaries. The boundary condition of the model is shown in Fig. 6a.

The Young's modulus E, Poisson's ratio ν, and the stress intensity factor K_I of Cu_6Sn_5 are 119 GPa, 0.31, and 2.1 MPa·m$^{1/2}$, respectively [39]. The critical energy release rate G^c of Cu_6Sn_5 can be calculated by

$$G^c = \frac{(1-\nu^2)\,K_I^2}{E} \tag{12}$$

The cohesive energies are assumed to be equal to the critical energy release rate, i.e., $\phi_n = \phi_t = G^c = 33.52$ N/m. The maximum normal and tangential tractions are $T_{n,max} = 68$ MPa [40] and $T_{t,max} = 28$ MPa [41], respectively. The Young's modulus and Poisson's ratio of the Cu pad are 117 GPa and 0.34, respectively; The Young's modulus and Poisson's ratio of the Sn3.0Ag0.5Cu solder are 54 GPa and 0.36, respectively.

Fig. 7a shows the force-displacement response curves. The overall responses of the three models were almost the same, indicating that the overall response is not sensitive to the grain aggregate morphology. The results of the models with different grain aggregate morphologies show various possible crack configurations (Figs. 6c, 7b and 7d). The general direction of the three crack paths was normal to the loading axis. However, some noticeable deviations were produced by the irregular grain aggregate morphology. In Model I with $\alpha_1 = \beta_1 = 0$ (Fig. 7b), the grain interfaces perpendicular to the loading direction were subjected to almost the same stress; thus, the microcracks initiated at those interfaces simultaneously. The crack configuration had a regular zigzag shape, and it remained perpendicular to the loading direction. In Model II with $\alpha_2 = \beta_2 = 0.3$ (Fig. 7c), the main crack path was prone to be perpendicular to the loading direction, as in Model I, while the crack configuration was much more random due to the irregular grain aggregate morphology. Model III with $\alpha_3 = \beta_3 = 0.9$ had the most random crack configuration among the three models (Fig. 7d). This indicates that the regular grain aggregate morphology can bias the propagation direction of the microcracks, and the irregular aggregate morphology results in a more random crack configuration.

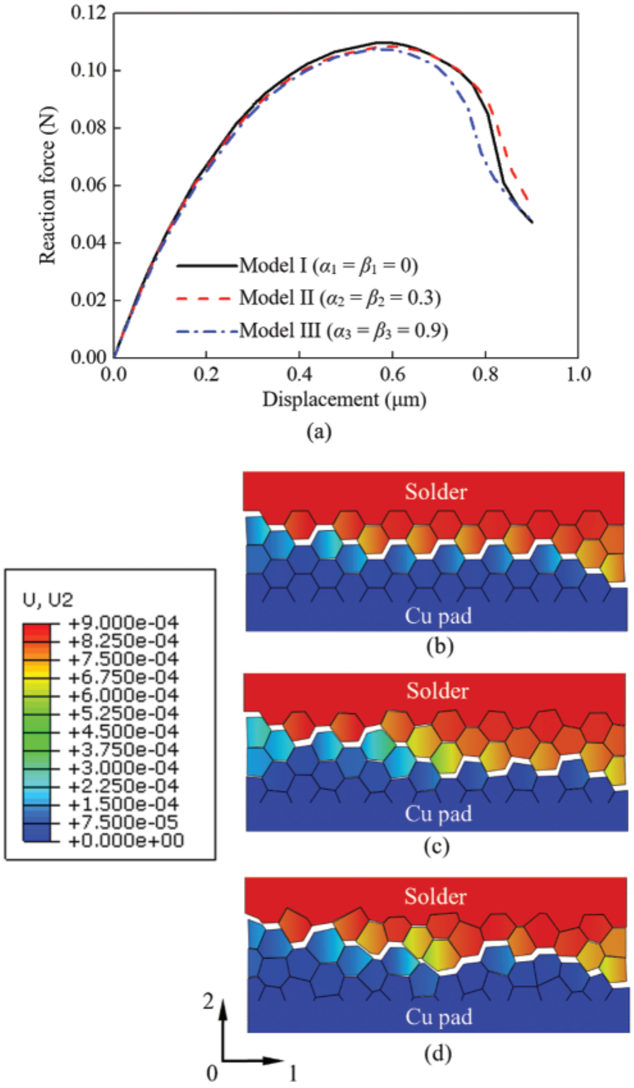

Figure 7: (a) Effect of the grain aggregate morphology on the overall force-displacement response, (b) Crack configuration of Model I ($\alpha_1 = \beta_1 = 0$), (c) Crack configuration of Model II ($\alpha_2 = \beta_2 = 0.3$), and (d) Crack configuration of Model III ($\alpha_3 = \beta_3 = 0.9$)

3.2 Effect of the Grain Boundary Defects on the Failure Behavior

To consider the grain boundary defects, a Weibull distribution [42] was applied to each of the parameters of the grain interfacial material. The four parameters of the cohesive zone law, the cohesive energies ϕ_n and ϕ_t, and the maximum tractions $T_{n,max}$ and $T_{t,max}$, were all described by Weibull distributions according to the following probability density functions:

$$f\left(\varphi_{\mathrm{n}}^{i}\right)=\frac{\kappa}{\lambda^{\kappa}}\left(\frac{\phi_{\mathrm{n}}^{i}}{\phi_{\mathrm{n}}}\right)^{\kappa-1}\exp\left[-\left(\frac{\phi_{\mathrm{n}}^{i}}{\phi_{\mathrm{n}}}\right)^{\kappa}\right] \tag{13a}$$

$$f\left(\varphi_{\mathrm{t}}^{i}\right)=\frac{\kappa}{\lambda^{\kappa}}\left(\frac{\phi_{\mathrm{t}}^{i}}{\phi_{\mathrm{t}}}\right)^{\kappa-1}\exp\left[-\left(\frac{\phi_{\mathrm{t}}^{i}}{\phi_{\mathrm{t}}}\right)^{\kappa}\right] \tag{13b}$$

$$f\left(T_{\mathrm{n,\ max}}^{i}\right)=\frac{\kappa}{\lambda^{\kappa}}\left(\frac{T_{\mathrm{n,\ max}}^{i}}{T_{\mathrm{n,\ max}}}\right)^{\kappa-1}\exp\left[-\left(\frac{T_{\mathrm{n,\ max}}^{i}}{T_{\mathrm{n,\ max}}}\right)^{\kappa}\right] \tag{13c}$$

$$f\left(T_{\mathrm{t,\ max}}^{i}\right)=\frac{\kappa}{\lambda^{\kappa}}\left(\frac{T_{\mathrm{t,\ max}}^{i}}{T_{\mathrm{t,\ max}}}\right)^{\kappa-1}\exp\left[-\left(\frac{T_{\mathrm{t,\ max}}^{i}}{T_{\mathrm{t,\ max}}}\right)^{\kappa}\right] \tag{13d}$$

in which κ and λ are the Weibull parameters, which are measures of the variability in the material parameters.

The grain boundary defect effect for both the regular grain aggregate morphology model, Model I-W1∼W3 with $\alpha_1 = \beta_1 = 0$, and the irregular grain aggregate morphology model, Model III-W1∼W3 with $\alpha_3 = \beta_3 = 0.9$, was investigated. The list of the related models is given in Table 1. Models I and III, which have homogeneous grain interface properties, were used for comparison. In the models with material parameters with Weibull distributions, the grain facet was stochastically assigned a set of four parameters according to Eqs. (13a), (13b), (13c) and (13d) the four material parameters changed in a range from 0.5 to 1.5 of the values employed in Model I or III. Each grain facet had the same value of the parameters, and in this way, there were N_{f} different interface elements (N_{f} = number of facets in the microstructure). Three groups of Weibull parameters, W1 with $\kappa_1 = 5$ and $\lambda_1 = 1$, W2 with $\kappa_2 = 2.5$ and $\lambda_2 = 0.8$, and W3 with $\kappa_3 = 5$ and $\lambda_3 = 1.5$, were used. Fig. 8 shows the histogram for the number of grain facets with different maximum tractions.

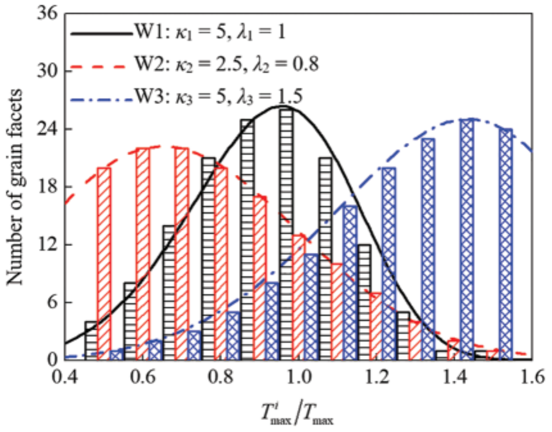

Figure 8: Weibull distribution of the grain interfacial maximum tractions

The overall force-displacement responses of the models with the interfacial material parameters with Weibull distributions are compared with that of the model with homogeneous interfacial material properties in Fig. 9. In Model I-W1 and Model III-W1 with Weibull parameters $\kappa_1 = 5$ and $\lambda_1 = 1$, 29% of the interface elements had higher interfacial strengths than those in Model I and Model III, and 52% of the interface elements had lower interfacial strengths. As a result, for both the regular grain aggregate morphology model (Fig. 9a) and the irregular grain aggregate morphology model (Fig. 9b), the overall strengths of Model I-W1 and Model III-W1 were approximately 14% lower than those of Model I and Model III, even though one-third of the total interfaces were stronger in Model I-W1 and Model III-W1 than in Model I and Model III. In Model I-W2 and Model III-W2 with Weibull parameters $\kappa_2 = 2.5$ and $\lambda_2 = 0.8$, 17% of the interface elements had higher interfacial strengths than those in Model I and Model III, and 73% of the interface elements had lower interfacial strengths. Since more weak interfaces existed in these models, the overall strengths of Model I-W2 and Model III-W2 were approximately 30% lower than those of Model I and Model III. Model I-W3 and Model III-W3 with Weibull parameters $\kappa_3 = 5$ and $\lambda_3 = 1.5$ had the strongest interfaces among the models, 78% of the interface elements had higher interfacial strengths than those in Model I and Model III, and only 14% of the interface elements had lower interfacial strengths. However, the overall strengths of Model I-W3 and Model III-W3 were only approximately 7% higher than those of Model I and Model III. The results indicate that the weak grain interfaces play a crucial role in the overall strength of the model.

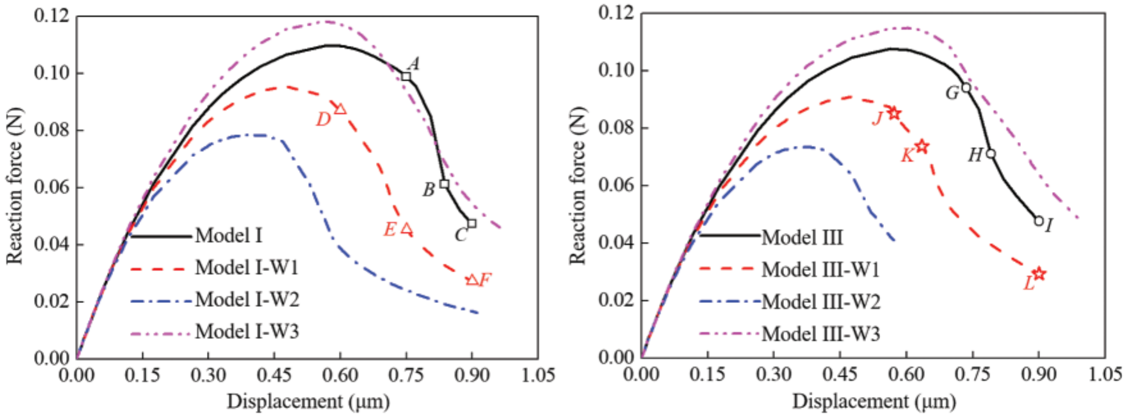

(a) (b)

Figure 9: Effect of the grain interface property strategies on the overall force-displacement response: (a) Model with shape coefficients $\alpha_1 = \beta_1 = 0$ and (b) Model with shape coefficients $\alpha_3 = \beta_3 = 0.9$

To examine the difference in the crack configuration for the regular grain aggregate morphology model (shape coefficients $\alpha_1 = \beta_1 = 0$) with different grain interface property strategies, three points labeled A, B and C for Model I in Fig. 9a were chose, and the corresponding crack configurations are shown in Figs. 10a–10c. Similarly, the crack configurations corresponding to points D, E and F for Model I-W1 in Fig. 9a are shown in Figs. 10d–10f.

At point A, the microcracks initiated at the bottom right and top left of the grain layer (Fig. 10a). At point B, the microcracks occurred in the central region of the grain layer initiated almost simultaneously since the grain interfaces perpendicular to the loading direction were subjected to almost the same stress. The microcracks propagated and coalesced to form a main crack across the grain layer (Fig. 10b). At point C, the path of the main crack showed a regular zigzag shape, and the stress contours were generally symmetrical (Fig. 10c). In Model I, the crack configuration is determined by only the grain aggregate morphology, as all the grain interfaces have the same strength.

Figs. 10d–10f show the crack configuration and the vertical normal stress σ_{22} of Model I-W1. Owing to the existence of weak grain interfaces, the crack configuration of Model I-W1 was quite different from that of Model I, even though the same grain aggregate morphology was applied in the two models. At point D, the microcracks initiated at random grain interfaces (Fig. 10d). Although the grain interfaces perpendicular to the loading direction underwent a similar stress, the microcracks propagated along a random path rather than failed simultaneously, and with the development of the microcracks, the stress in the adjacent elements was released (Fig. 10e). The final crack configuration of Model I-W1 was much more irregular, and the stress contours were nonsymmetrical (Fig. 10f). In Model I-W1, the crack configuration is determined by both the grain aggregate morphology and the grain interface properties.

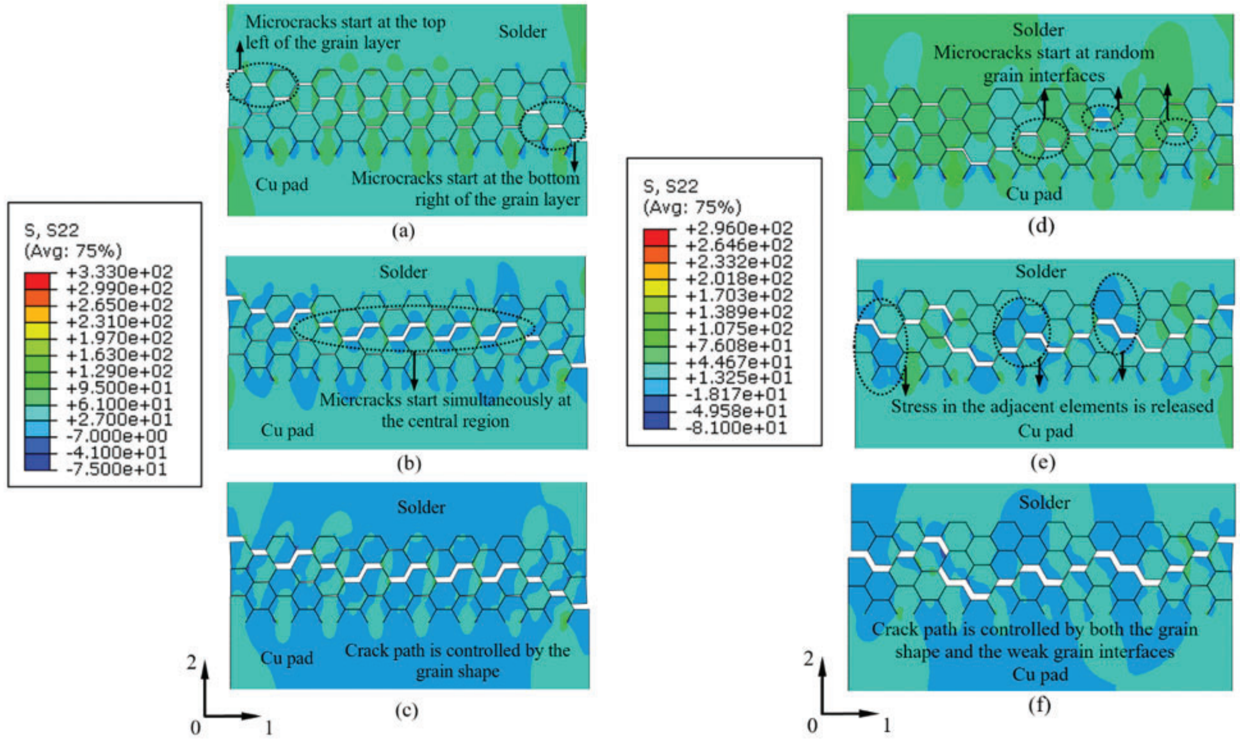

Figure 10: Crack configuration and stress σ_{22} of Model I at (a) Point A, (b) Point B, and (c) Point C, and Model I-W1 at (d) Point D, (e) Point E and (f) Point F in Fig. 9a

The effect of the grain boundary defects on the crack configuration for the irregular grain aggregate morphology model (shape coefficients $\alpha_3 = \beta_3 = 0.9$) has been studied. Three points labeled G, H and I for Model III in Fig. 9b were chosen, and the corresponding crack configurations are shown in Figs. 11a–11c. Similarly, the crack configurations corresponding to points J, K and L for Model III-W1 in Fig. 9b are shown in Figs. 11d–11f.

Defining φ as the angle between the grain facet and the 1-axial direction, at load step G, the angles of the cracking grain interfaces were $\varphi_1 = 0.65°$, $\varphi_2 = 3.0°$ and $\varphi_3 = 3.7°$. These grain interfaces were approximately perpendicular to the loading direction (Fig. 10a). This suggests that microcracks are prone to initiate at grain interfaces whose angle φ is small. This can be explained by Fig. 12. As shown in Fig. 12a, when the displacement in the y direction is u, the normal opening separation between two grains is $\delta_n = u$. When the same displacement u is applied in the grains in Fig. 11b, in which the local reference frame is not superposed with the global frame, the normal opening separation is $\delta_n = u{\cdot}\cos\varphi$. Therefore, the normal opening separation at the grain interface decreases with increasing grain facet angle φ. This indicates that microcracks are prone to occur in the grain interfaces that are perpendicular to the loading direction, and it is more difficult for an oblique grain interface to start cracking. At point H, the microcracks propagated, and more grain interfaces opened (Fig. 11b). The microcracks coalesced to form a main crack, and the crack path was random due to the irregular grain aggregate morphology (Fig. 11c).

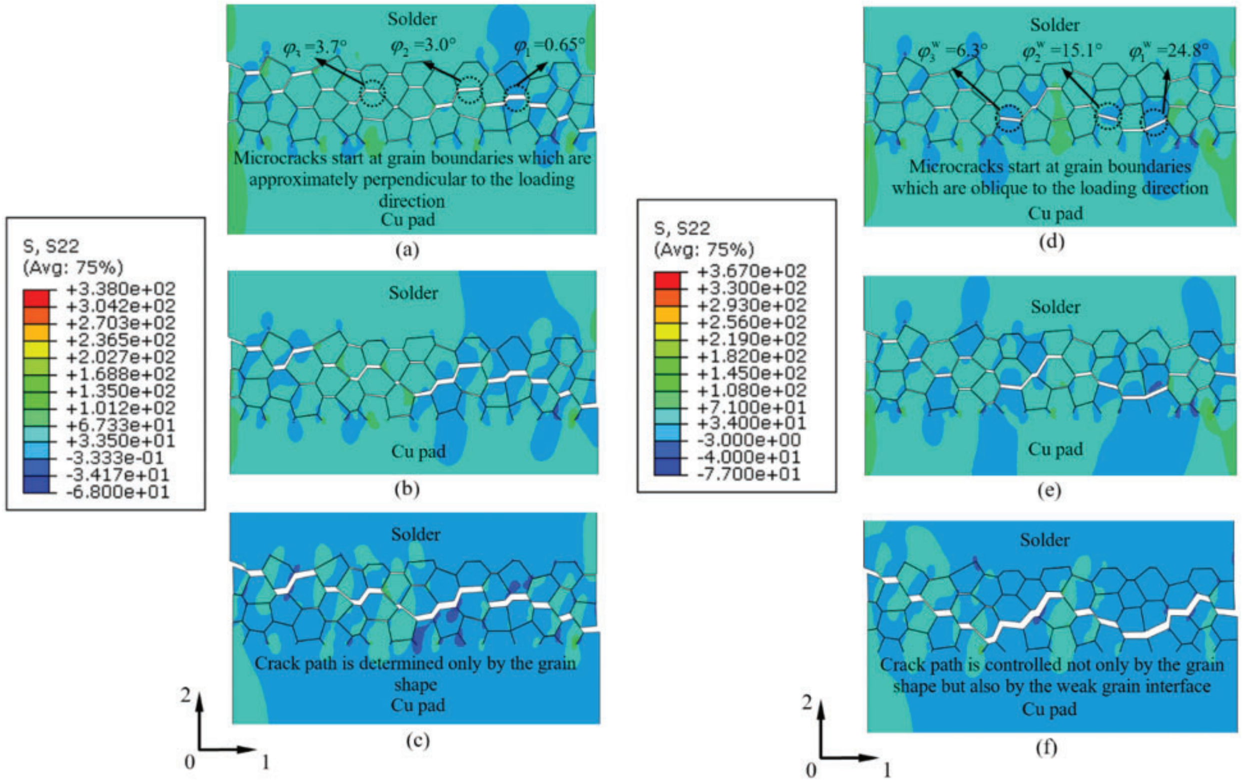

Figure 11: Crack configuration and stress σ_{22} of Model III at (a) Point G, (b) Point H and (c) Point I, and Model III-W1 at (a) Point J, (b) Point K and (c) Point L in Fig. 9b

Figs. 11d–11f show the crack configuration and the vertical normal stress σ_{22} of Model III-W1. At load step J, the microcracks initiated at different locations from those in Model III. The angles of the cracking grain interfaces were $\phi_1^w = 24.8°$, $\phi_2^w = 15.1°$ and $\phi_3^w = 6.3°$, which were much greater than those in Model III (Fig. 11d). These more tilted grain interfaces did not easily crack; however, the microcracks started at these grain interfaces due to their lower interfacial strength. Comparing the crack configurations at the final point of the two models, as shown in Figs. 10c and 10f, although the same grain shape and aggregate morphology were adopted, their final crack configurations were apparently different due to the existence of the weak interfaces in Model III-W1. This suggests that in Model III-W1, the crack path was controlled by not only the grain aggregate morphology but also the weak grain interfaces.

3.3 Effect of the Normal and Tangential Strengths of the Grain Interfaces on the Failure Behavior of the IMC

The normal and tangential traction-separation laws control the normal opening separation between grains and the grain boundary sliding, respectively. There are two possible grain motions, as demonstrated in Fig. 13. At one extreme, when the normal strength is low, the two grains may separate directly without any tangential sliding displacement (Fig. 13a). At the other extreme, when the tangential strength is low, the two grains may slide along their boundary without any normal opening separation (Fig. 13b). For most cases, both the normal and tangential strengths exist at grain interfaces, but their magnitudes in the two directions are different. The lowest strength always controls the mechanical behavior of the grains.

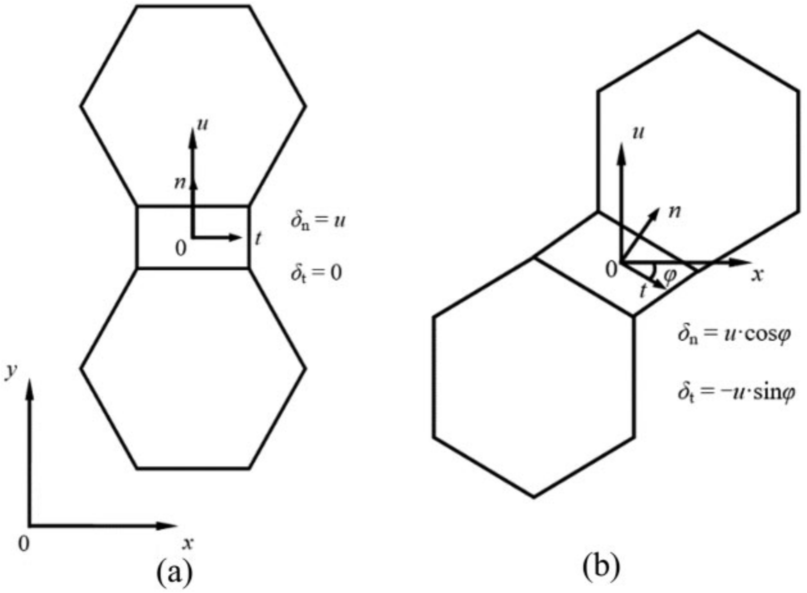

Figure 12: Effect of the grain facet angle on the separation: (a) The grain facet is perpendicular to the loading direction; (b) The grain facet is oblique to the loading direction

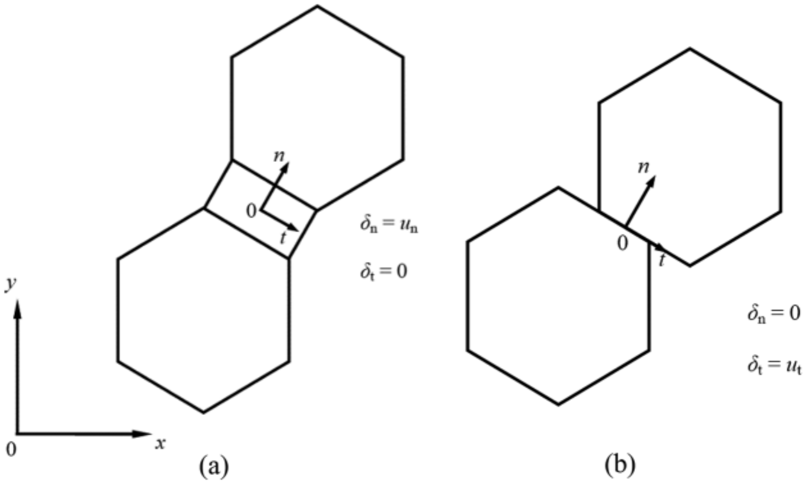

Figure 13: Deformation modes of the interface element: (a) Pure normal opening separation and (b) Pure tangential sliding separation

The thickness of IMC layer in the finite element model applied here was 15.5 μm. Model IV-N and Model IV-T were used in this study, as depicted in Fig. 14. In Model IV-N, the maximum traction in the normal direction was larger than that in the tangential direction, and the parameters of the cohesive zone law were $\phi_n = \phi_t = 33.52$ N/m, $T_{n,max} = 68$ MPa and $T_{t,max} = 28$ MPa. In contrast, in Model IV-T, the maximum traction in the tangential direction was larger than that in the normal direction, and the parameters of the cohesive zone law were $\phi_n = \phi_t = 33.52$ N/m, $T_{n,max} = 27$ MPa and $T_{t,max} = 60$ MPa [43].

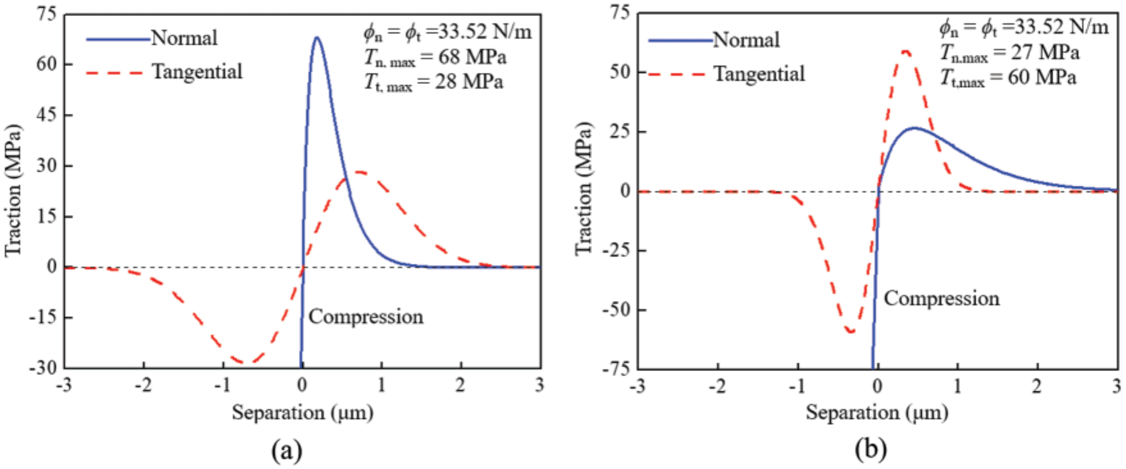

Figure 14: Normal and tangential traction-separation curves of (a) Model IV-N with $\phi_n = \phi_t = 33.52$ N/m, $T_{n,max} = 68$ MPa, and $T_{t,max} = 28$ MPa and (b) Model IV-T with $\phi_n = \phi_t = 33.52$ N/m $T_{n,max} = 27$ MPa, and $T_{t,max} = 60$ MPa

Fig. 15a gives the overall responses of the two models. The force-displacement curve of Model IV-N is very similar to a typical stress-strain curve for ductile materials, which shows a large amount of plastic deformation before failure. The force-displacement curve of Model IV-T shows features of brittle materials, which are characterized by sudden and rapid failure with little plastic deformation.

To examine the difference in the crack configuration for Model IV-N and Model IV-T, load steps labeled *M* and *N* for Model IV-N and *O* and *P* for Model IV-T in Fig. 15a were selected, and the corresponding crack configurations are shown in Figs. 15b∼15e.

Fig. 15b shows the displacement results u_1 of Model IV-N at load step *M*. The grains were prone to slide along boundaries due to the low strength in the tangential direction of the grain interfaces; as a result, the grain region contracted, analogous to the necking phenomenon in ductile materials. Fig. 15c gives the displacement results u_1 of Model IV-T at load step *O*. In this model, the grains were prone to separate directly from each other due to the low strength in the normal direction of the grain interfaces. The grains were extruded in this way because it was difficult for them to slide past the adjacent grains, which led to expansion of the grain region. This phenomenon is quite analogous to the dilatancy effect in rock-like materials.

Fig. 15d shows the displacement results u_2 of Model IV-N at load step *N*. As the grains in Model IV-N were prone to slide along boundaries, the microcracks propagated along a zigzag path across the grain region. Fig. 15e shows the displacement results u_2 of Model IV-T at load step *P*. Compared to Model IV-N, the main crack path in Model IV-T was straight and perpendicular to the loading direction. This is because the strength in the normal direction of the grain interfaces was lower in Model IV-T, and the low strength direction in the grain interfaces was the same direction as the loading direction; thus, most of these grain interfaces cracked and coalesced to form a relatively straight crack path.

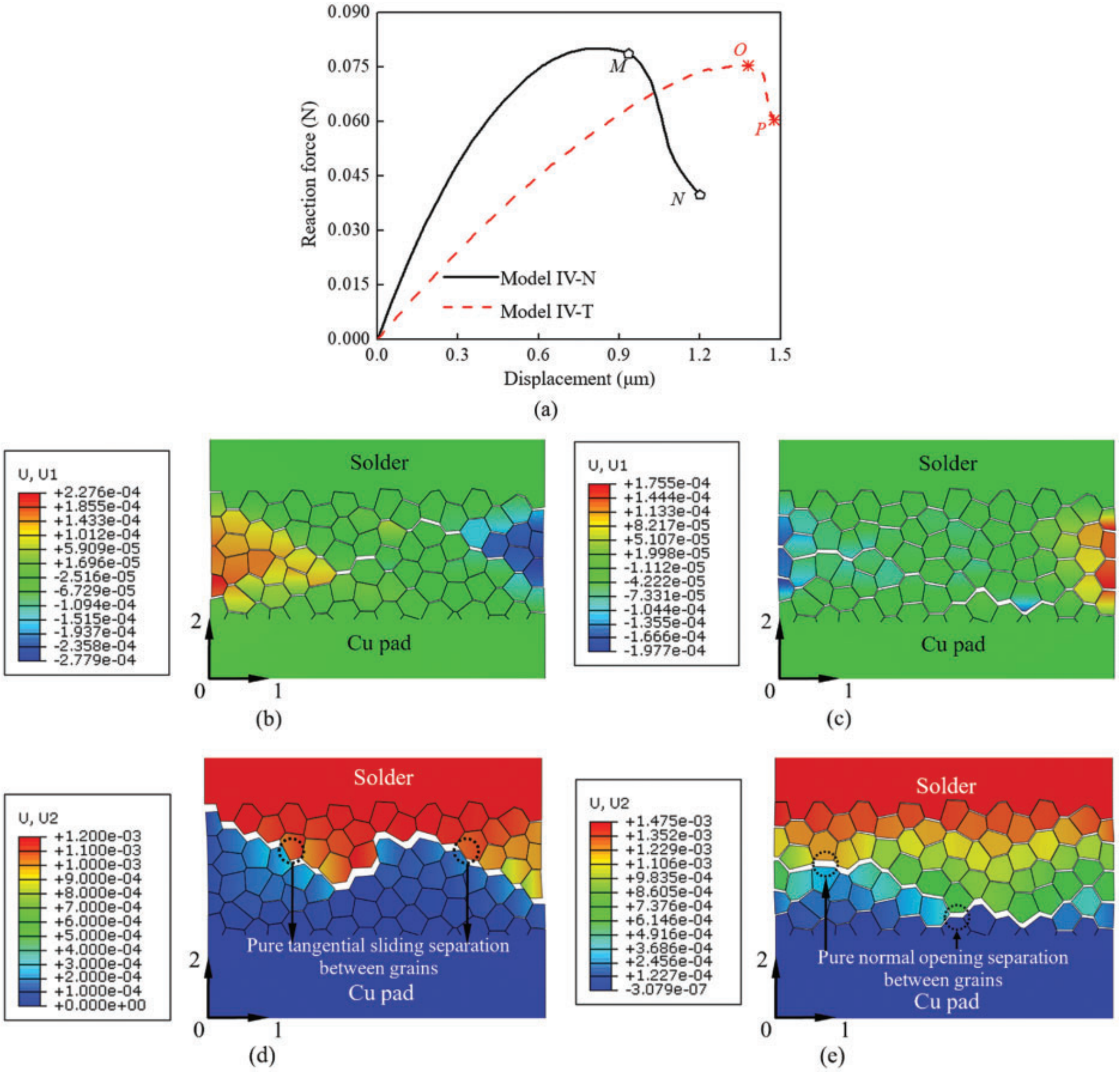

Figure 15: (a) Effect of the cohesive zone law parameters on the overall force-displacement response, crack configuration and displacement result u_1 at (b) Point M in (a) for model IV-N, and (c) Point O in (a) for model IV-T, crack configuration and displacement result u_2 at (d) Point N in (a) for model IV-N and (e) Point P in (a) for model IV-T

The overall strains ε_{11} of the grain region in the two models are compared in Fig. 16. In Model IV-N, the grains were prone to slide along grain boundaries due to the low strength in the tangential direction of grain interfaces. Therefore, a contracting deformation was observed under tensile loading, and ε_{11} of Model IV-N was negative. In contrast, in Model IV-T, the grains were prone to separating rather than tangential sliding due to the low strength in the normal direction of the grain interfaces. The grains pushed against each other instead of sliding along the grain boundaries; as a result, the model expanded, and ε_{11} of Model IV-T was positive.

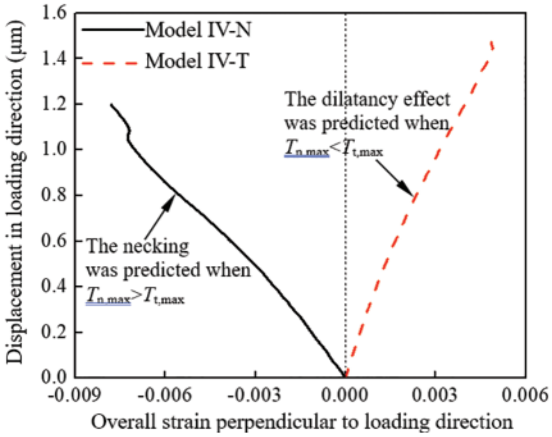

Figure 16: Effect of the cohesive zone law parameters on the overall strain of the grain region, ε_{11}

4 Conclusion

In this paper, a micromechanical model was constructed to explicitly predict the microcrack initiation, random crack path morphology and failure mode of the IMC. The influences of the grain aggregate morphology, the grain boundary defects and the sensitivity of the various cohesive zone parameters in predicting the overall mechanical response were investigated, and the following important points were derived:

(1) The overall mechanical strength of the IMC is not sensitive to the grain aggregate morphology, but the crack configuration depends greatly on the grain aggregate morphology. In the regular grain model, the crack path is relatively regular, while in the irregular grain model, the crack path is much more random.

(2) The overall strength of the model is determined dominantly by the weak grain interfaces. In the model with material parameters described by Weibull distributions, the crack configuration is controlled by not only the grain aggregate morphology but also the weak grain interfaces.

(3) The maximum tractions in the normal and tangential directions of the grain interfaces are critical in determining the overall strength, deformation, microcrack propagation and failure mode of the model. When the maximum traction in the normal direction is larger than that in the tangential direction, the necking phenomenon occurs during model deformation. When the maximum traction in the normal direction is smaller than that in the tangential direction, the dilatancy effect can be predicted by the model.

To close, it is necessary to mention that the role of the Cu_3Sn layer was neglected in this study, and the effect of the Cu_3Sn layer will be considered in the future modeling work.

Funding Statement: This research was supported by the National Natural Science Foundation of China (NSFC) under Grant 11872078, and Beijing Natural Science Foundation No. 3222005.

Conflicts of Interest: The authors declare that they have no conflicts of interest to report regarding the present study.

References

1. Bang, W. H., Moon, M. W., Kim, C. U., Kang, S. H., Jung, J. P. et al. (2008). Study of fracture mechanics in testing interfacial fracture of solder joints. *Journal of Electronic Materials, 37(4),* 417–428. DOI 10.1007/s11664-008-0393-8.
2. Jing, J. P., Gao, F., Johnson, J., Liang, F. Z., Williams, R. L. et al. (2009). Simulation of dynamic fracture along solder-pad interfaces using a cohesive zone model. *Engineering Failure Analysis, 16,* 1579–1586. DOI 10.1016/j.engfailanal.2008.10.019.
3. Alam, M. O., Lu, H., Bailey, C., Chan, Y. C. (2009). Fracture mechanics analysis of solder joint intermetallic compounds in shear test. *Computational Materials Science, 45(2),* 576–583. DOI 10.1016/j.commatsci.2008.12.001.
4. Zavattieri, P. D., Espinosa, H. D. (2003). A grain level model for the study of failure initiation and evolution in polycrystalline brittle materials. Part I: Theory and numerical implementation. *Mechanics of Materials, 35(3–6),* 333–364. DOI 10.1016/S0167-6636(02)00285-5.
5. Zavattieri, P. D., Espinosa, H. D. (2003). A grain level model for the study of failure initiation and evolution in polycrystalline brittle materials. Part II: Numerical examples. *Mechanics of Materials, 35(3–6),* 365–394. DOI 10.1016/S0167-6636(02)00287-9.
6. Onck, P., van der Giessen, E. (1998). Micromechanics of creep fracture: Simulation of intergranular crack growth. *Computational Materials Science, 13(1–3),* 90–102. DOI 10.1016/S0927-0256(98)00049-4.
7. Ghosh, S., Liu, Y. (1995). Voronoi cell finite element model based on micropolar theory of thermoelasticity for heterogeneous materials. *International Journal for Numerical Methods in Engineering, 38(8),* 1361–1398. DOI 10.1002/(ISSN)1097-0207.
8. Wu, M. S., Niu, J. (1995). Micromechanical prediction of the compressive failure of ice: Model development. *Mechanics of Materials, 20(1),* 9–32. DOI 10.1016/0167-6636(94)00047-K.
9. Wu, M. S., Niu, J. (1995). Micromechanical prediction of the compressive failure of ice: Numerical simulations. *Mechanics of Materials, 20(1),* 33–58.
10. Toi, Y., Kiyosue, T. (1995). Damage mechanics models for brittle microcracking solids based on three-dimensional mesoscopic simulations. *Engineering Fracture Mechanics, 50(1),* 11–27. DOI 10.1016/0013-7944(94)00160-J.
11. Barbe, F., Decker, L., Jeulin, D., Cailletaud, G. (2001). Intergranular and intragranular behavior of polycrystalline aggregates. Part 1: F.E. model. *International Journal of Plasticity, 17(4),* 513–536. DOI 10.1016/S0749-6419(00)00061-9.
12. Barbe, F., Forest, S., Cailletaud, G. (2001). Intergranular and intragranular behavior of polycrystalline aggregates. Part 2: Results. *International Journal of Plasticity, 17(4),* 537–563. DOI 10.1016/S0749-6419(00)00062-0.
13. Musienko, A., Cailletaud, G. (2009). Simulation of inter-and transgranular crack propagation in polycrystalline aggregates due to stress corrosion cracking. *Acta Materialia, 57(13),* 3840–3855. DOI 10.1016/j.actamat.2009.04.035.
14. An, T., Qin, F. (2013). Intergranular cracking simulation of the intermetallic compound layer in solder joints. *Computational Materials Science, 79,* 1–14. DOI 10.1016/j.commatsci.2013.05.044.
15. Zeng, X., Li, S. (2010). A multiscale cohesive zone model and simulations of fracture. *Computer Methods in Applied Mechanics and Engineering, 199(9–12),* 547–556. DOI 10.1016/j.cma.2009.10.008.
16. Li, S., Zeng, X., Ren, B., Qian, J., Zhang, J. et al. (2012). An atomistic-based interphase zone model for crystalline solids. *Computer Methods in Applied Mechanics and Engineering, 229,* 87–109. DOI 10.1016/j.cma.2012.03.023.
17. Hosford, W. (2010). *Solid mechanics*. New York, USA: Cambridge University Press.
18. Zavattieri, P. D. (2000). *Computational modeling for bridging size scales in the failure of solids (Ph.D. Thesis)*. Purdue University, West Lafayette, IN, USA.

19. Barenblatt, G. I. (1962). Mathematical theory of equilibrium cracks. *Advances in Applied Mechanics, 7,* 56–129.
20. Dugdale, D. S. (1960). Yielding of steel sheets containing slits. *Journal of the Mechanics and Physics of Solids, 8(2),* 100–104. DOI 10.1016/0022-5096(60)90013-2.
21. Needleman, A. (1987). A continuum model for void nucleation by inclusion debonding. *Journal of Applied Mechanics, 54,* 525–531. DOI 10.1115/1.3173064.
22. Chandra, N., Li, H., Shet, C., Ghonem, H. (2002). Some issues in the application of cohesive zone models for metal-ceramic interfaces. *International Journal of Solids and Structures, 39(10),* 2827–2855. DOI 10.1016/S0020-7683(02)00149-X.
23. Salih, S., Davey, K., Zhenmin, Z. (2019). A computationally efficient cohesive zone model for fatigue. *Fatigue & Fracture of Engineering Materials & Structures, 42(2),* 518–532. DOI 10.1111/ffe.12927.
24. Li, H., Li, L., Fan, J. K., Yue, Z. F. (2021). Verification of a cohesive model-based extended finite element method for ductile crack propagation. *Fatigue & Fracture of Engineering Materials & Structures, 44(3),* 762–775. DOI 10.1111/ffe.13392.
25. Maio, U. D., Greco, F., Leonetti, L., Luciano, R., Blasi, P. N. et al. (2019). A refined diffuse cohesive approach for the failure analysis in quasibrittle materials–part II: Application to plain and reinforced concrete structures. *Fatigue & Fracture of Engineering Materials & Structures, 42(12),* 2764–2781. DOI 10.1111/ffe.13115.
26. Yu, D. Q., Wang, L. (2008). The growth and roughness evolution of intermetallic compounds of Sn-Ag-Cu/Cu interface during soldering reaction. *Journal of Alloys and Compounds, 458(1–2),* 542–547. DOI 10.1016/j.jallcom.2007.04.047.
27. Yazzie, K. E., Xie, H. X., Williams, J. J., Chawla, N. (2012). On the relationship between solder-controlled and intermetallic compound (IMC)-controlled fracture in Sn-based solder joints. *Scripta Materialia, 66(8),* 586–589. DOI 10.1016/j.scriptamat.2012.01.009.
28. Qian, J., Li, S. (2011). Application of multiscale cohesive zone model to simulate fracture in poly-crystalline solids. *ASME Journal of Engineering Materials and Technology, 133(1),* 011010. DOI 10.1115/1.4002647.
29. Fan, H., Shi, C., Li, S. (2013). Application of multiscale process zone model to simulate fracture in polycrystalline solids. *Journal of Multiscale Modeling, 5(4),* 1350015. DOI 10.1142/S1756973713500157.
30. Xu, X. P., Needleman, A. (1993). Void nucleation by inclusion debonding in a crystal matrix. *Modelling and Simulation in Materials Science and Engineering, 1(2),* 111–132. DOI 10.1088/0965-0393/1/2/001.
31. Tvergaard, V., Hutchinson, J. W. (1992). The relation between crack growth resistance and fracture process parameters in elastic-plastic solids. *Journal of the Mechanics and Physics of Solids, 40(6),* 1377–1397. DOI 10.1016/0022-5096(92)90020-3.
32. Geubelle, P. H., Baylor, J. S. (1998). Impact-induced delamination of composites: A 2D simulation. *Composites Part B: Engineering, 29(5),* 589–602. DOI 10.1016/S1359-8368(98)00013-4.
33. van den Bosch, M. J., Schreurs, P. J. G., Geers, M. G. D. (2006). An improved description of the exponential Xu and needleman cohesive zone law for mixed-mode decohesion. *Engineering Fracture Mechanics, 73(9),* 1220–1234. DOI 10.1016/j.engfracmech.2005.12.006.
34. Espinosa, H. D., Zavattieri, P. D., Emore, G. L. (1998). Adaptive FEM computation of geometric and material nonlinearities with application to brittle failure. *Mechanics of Materials, 29(3–4),* 275–305. DOI 10.1016/S0167-6636(98)00018-0.
35. Luther, T., Könke, C. (2009). Polycrystal models for the analysis of intergranular crack growth in metallic materials. *Engineering Fracture Mechanics, 76(15),* 2332–2343. DOI 10.1016/j.engfracmech.2009.07.006.
36. Van den Bosch, M. J., Schreurs, P. J. G., Geers, M. G. D. (2007). A cohesive zone model with a large displacement formulation accounting for interfacial fibrillation. *European Journal of Mechanics-A/Solids, 26(1),* 1–19. DOI 10.1016/j.euromechsol.2006.09.003.

37. Qiu, Y., Grisfield, M. A., Alfano, G. (2001). An interface element formulation for the simulation of delamination with buckling. *Engineering Fracture Mechanics, 68(16),* 1755–1776. DOI 10.1016/S0013-7944(01)00052-2.
38. Gao, Y. F., Bower, A. F. (2004). A simple technique for avoiding convergence problems in finite element simulations of crack nucleation and growth on cohesive interfaces. *Modelling and Simulation in Materials Science and Engineering, 12(3),* 453–463. DOI 10.1088/0965-0393/12/3/007.
39. Ghosh, G. (2004). Elastic properties, hardness, and indentation fracture toughness of intermetallics relevant to electronic packaging. *Journal of Materials Research, 19(5),* 1439–1454. DOI 10.1557/JMR.2004.0193.
40. Prakash, K. H., Sritharan, T. (2004). Tensile fracture of tin-lead solder joints in copper. *Materials Science and Engineering: A, 379(1–2),* 277–285. DOI 10.1016/j.msea.2004.02.049.
41. Zhao, J., Cheng, C. Q., Qi, L., Chi, C. Y. (2009). Kinetics of intermetallic compound layers and shear strength in bi-bearing SnAgCu/Cu soldering couples. *Journal of Alloys and Compounds, 473(1–2),* 382–388. DOI 10.1016/j.jallcom.2008.05.082.
42. Weibull, W., Sweden, S. (1951). A statistical distribution function of wide applicability. *Journal of Applied Mechanics, 18,* 293–297. DOI 10.1115/1.4010337.
43. Lee, H. T., Chen, M. H., Jao, H. M., Liao, T. L. (2003). Influence of interfacial intermetallic compound on fracture behavior of solder joints. *Materials Science and Engineering: A, 358(1–2),* 134–141. DOI 10.1016/S0921-5093(03)00277-6.

Computer Modeling in
Engineering & Sciences

Tech Science Press

DOI: 10.32604/cmes.2022.022823

ARTICLE

Earth Pressure of the Trapdoor Problem Using Three-Dimensional Discrete Element Method

Qizhi Chen[1], Chuli Xu[1], Baoping Zou[1,*], Zhanyou Luo[2], Changjie Xu[3] and Xu Long[4,*]

[1]School of Civil Engineering and Architecture, Zhejiang University of Science and Technology, Hangzhou, 310023, China

[2]School of Civil and Environmental Engineering, Ningbo University, Ningbo, 315211, China

[3]School of Civil Engineering and Architecture, East China Jiaotong University, Nanchang, 330013, China

[4]School of Mechanics, Civil Engineering and Architecture, Northwestern Polytechnical University, Xi'an, 710072, China

*Corresponding Authors: Baoping Zou. Email: zoubp@zust.edu.cn; Xu Long. Email: xulong@nwpu.edu.cn

Received: 28 March 2022 Accepted: 27 June 2022

ABSTRACT

Load transformation from the yielding part of the soil to the adjacent part is known as the soil arching effect, which plays an important role in the design of various geotechnical infrastructures. Terzaghi's trapdoor test was an important milestone in the development of theories on soil arching. The research on earth pressure of the trapdoor problem is presented in this paper using the three-dimensional (3D) discrete element method (DEM). Five 3D trapdoor models with different heights are established by 3D DEM software PFC 3D. The variation of earth pressure on the trapdoor with the downward movement of the trapdoor, the distribution of vertical earth pressure along the horizontal direction, the distribution of vertical earth pressure along the vertical direction, the distribution of lateral earth pressure coefficient along the depth direction, the magnitude and direction of contact force chain are studied, respectively. Related research results show that the earth pressure on the trapdoor decreases rapidly after the downward movement of the trapdoor, and then reaches the minimum earth pressure. After that, the earth's pressure will rise slightly, and whether this phenomenon occurs depends on the depth ratio. For the bottom soil, due to the stress transfer caused by the soil arching effect, the ratio of earth pressure in the loose area decreases, while the ratio of earth pressure in the stable area increases. With the trapdoor moving down, the vertical earth pressure along the depth in the stable zone is basically consistent with the initial state, which shows an approximate linear distribution. After the trapdoor moves down, the distribution of earth pressure along with the depth in the loose area changes, which is far less than the theoretical value of vertical earth pressure of its self-weight. Because of the compression of the soil on both sides, the lateral earth pressure coefficient of most areas on the central axis of the loose zone is close to the passive earth pressure coefficient K_{p}. The existence of a 'soil arch' can be observed intuitively from the distribution diagram of the contact force chain in the loose zone.

KEYWORDS

Soil arching effect; three dimensional discrete element; earth pressure; contact force chain

1 Introduction

Soil arching effect refers to the phenomenon of relative displacement and stress redistribution of soil, which widely exists in geotechnical engineering. Lai et al. [1] pointed out that soil arching effect is the key to the load transfer of high pile embankment. Liang et al. [2] pointed out that it is the main reason why the earth pressure on the shield tunnel far less than its theoretical value. Jiao et al. [3] considered soil arching effects on the distribution of earth pressure on rigid retaining walls and reported that it also affects the active earth pressure acting on the rigid retaining wall. The above is enough to illustrate the importance of studying the soil arching effect, which makes many scholars participate in the research of soil arching effect.

In terms of model test, Terzaghi [4] first conducted the famous trapdoor model test to study the soil arching effect. Based on the test results, the famous theoretical formula of Terzaghi loose earth pressure which is widely used in geotechnical engineering practice was put forward. After that, Iglesia et al. [5,6] made a series of centrifuge tests and presented the expressions of earth pressure acting on the trapdoor evolving from an initially curved state to a triangular shape and ultimately to a prism with a rectangular cross-section. Dewoolkar et al. [7] conducted a series of axisymmetric centrifuge model tests and investigated the failure mechanisms of soil mass above a trapdoor with different buried depth and stress levels. Costa et al. [8] carried out a similar investigation with centrifuge model tests under plane strain conditions. Rui et al. [9–12] conducted a series of multi trapdoor model tests in dense sands and found three different forms of slip surface evolution types. Chevalier et al. [13] and Chevalier et al. [14] studied the influencing factors of stress transfer and stress distribution in trapdoor problems through experiment and simulation.

Some researchers use numerical simulation to study the soil arching effect. Lai et al. [15,16] and Rui et al. [9,10] used the discrete element method (DEM) to study the soil arching effect of pile supported embankments. Lai et al. [1] revealed the morphological features and mobilization mechanism of soil arcing using the DEM modeling. Pardo et al. [17] simulated the trapdoor tests through a 2D finite element model with two different kinds of constitutive models. Sloan et al. [18], Martin [19], and Keawsawasvong et al. [20] obtained the upper and lower bound solutions of a strip trapdoor problem under different conditions through the finite element limit analysis method.

In theoretical studies, Liang et al. [2] proposed an analytical model to estimate the average loosening earth pressure acting on the trapdoor and the stress distribution in the loose area under the limit state. Based on the experimental observation, Liang et al. [21] proposed an analytical solution considering the deflection of the principal stress axis to predict the minimum and residual value of the loose earth pressure acting on the top of the trapdoor. Aubertin et al. [22–25] proposed a series of analytical or semi-analytical solutions to calculate the earth pressure generated by backfill in backfilled stopes. Eekelen et al. [26] put forward the limit-state equilibrium model with a concentric arch for pile-supported embankments design. Qian et al. [27,28] used the spatial discretization technique to study the active and passive earth pressure of sloping backfills. Li et al. [29] pointed out a novel method of calculating active earth pressure on laggings between piles considering the soil arching effect.

It can be found that many scholars have used different research methods to study the soil arching effect, but there are relatively few studies on the soil arching effect in trapdoor problems by using the three-dimensional (3D) DEM. In order to better reveal the change of earth pressure caused by the soil arching effect in the sand and the failure mode in loose areas, it is necessary to carry out a numerical simulation based on meso-structure. In this paper, a trapdoor model is established through the 3D DEM software PFC3D. The relative displacement of the particles is caused by moving the trapdoor down, which results in the soil arching effect. Further, the magnitude and distribution of the loose earth pressure and the distribution of the force chain between the particles are studied.

2 3D DEM Model of Soil Arching Effect

2.1 Description of 3D Discrete Element Method

The discrete element method was firstly introduced by Cundall et al. [30] and has been gradually applied in the fields of geotechnical engineering. In this paper, the simulations of the soil arching effect were implemented using commercial DEM software PFC3D developed by Itasca Consulting Group Inc. (USA) [31]. The discrete element method is based on the theory of non-continuum mechanics, which is suitable for granular materials. The basic idea of the discrete element method is to simulate the physical and mechanical properties of granular materials through the motion and interaction of granular media. In PFC3D, particles are considered rigid but small overlaps are allowed at the contact points. The size of the overlapping area is related to the contact force and follows the force-displacement law. The overlapping area is much smaller than the particle size. In PFC3D, particles are considered to be connected by springs, visco-pots, slides and couplers as shown in Fig. 1. Moreover, the motion of the particles obeys Newton's second law. The forces and displacements are related by the contact stiffness in normal and shear directions as follows:

$$F_i^n = K_n U^n n_i \tag{1}$$

$$\Delta F_i^s = -K_s \Delta U^s \tag{2}$$

where n_i is the unit normal vector in $i = x, y, z$ directions. F_n is the normal force to the normal displacement U^n. F_s is the shear force to the shear displacement U^s. K_n is normal stiffness and K_s is shear stiffness.

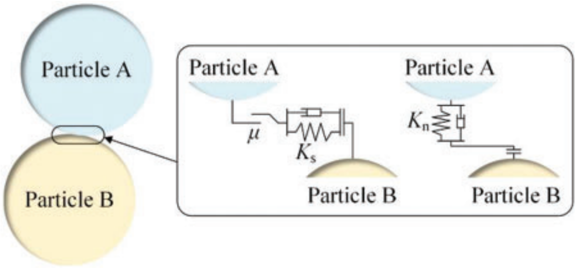

Figure 1: Interaction between two particles

During each calculation cycle, all contact information is updated according to the position of the particles and the wall. According to the force-displacement law, the contact force between the contact particles is calculated. After the contact force is obtained, the force and moment acting on the particles are calculated. According to Newton's second law, the velocity and acceleration of each particle are obtained. At the end of each calculation cycle, the displacement and rotation angle of the particles are obtained, and then the position of the particles and the wall is updated to form new contacts, and then the next calculation cycle is carried out.

In this paper, spheres are used in 3D DEM modeling for granular materials. Additionally, the linear contact model is chosen for DEM simulations in PFC3D. The linear contact model provides the relation between contact force and relative displacement of the particles as shown in Eqs. (1) and (2). In addition, the tangential contact force is limited by a friction coefficient μ [31]. Because the three contact parameters (K_n, K_s, and μ) in the linear contact model are all constant values, it can provide high computing efficiency.

2.2 3D DEM Model and Parameters

Referring to the typical trapdoor experimental model, a 3D trapdoor model is established in PFC3D. Typical calculation model diagram shows in Fig. 2a, the model consisting of 9 walls, the width of model is 1.5 m, the length of model is 3 m, and the width of middle moving door is 0.6 m, except for the intermediate trapdoor, the rest of the wall remains immobile in the simulation process.

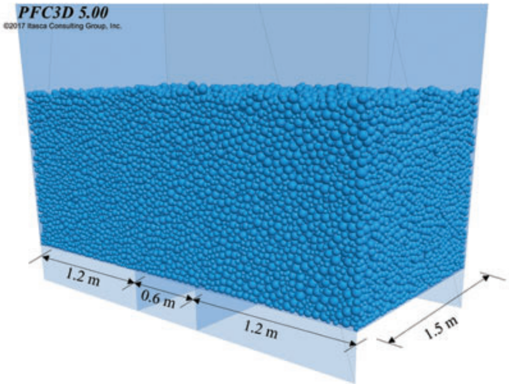

(a) Schematic diagram of calculation model

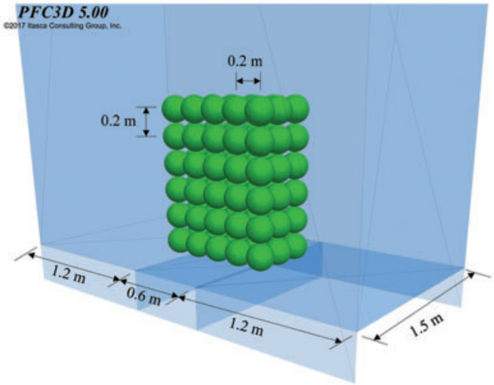

(b) Schematic diagram of measurement spheres

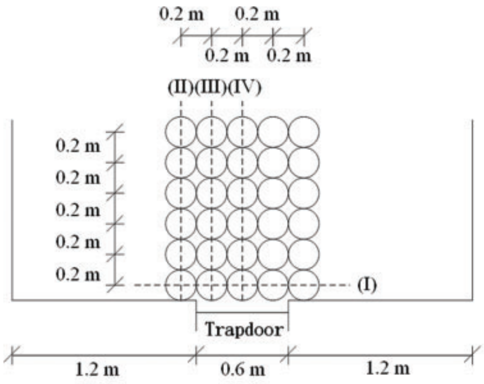

(c) Front view of calculation model and measurement spheres

Figure 2: DEM model and arrangement of measurement spheres

In the DEM model, the soil is simulated by spherical particles. The particle micro parameters used in this simulation are mainly obtained by reference, and do not rely on specific projects or tests. The particle density is $G_s = 2600\,\text{kg/m}^3$, the particle radius is 12 to 30 mm evenly distributed, the particle normal stiffness is $K_n = 1.5 \times 10^8$ N/m, and the particle shear stiffness is $K_s = 1.0 \times 10^8$ N/m, the friction coefficient is $\mu = 0.25$. The soil of the model is generated by gravity settling (gravity acceleration is $g = 9.8\,\text{m/s}^2$) and the particles are balanced under its self-weight stress.

The calibration method of macro parameters corresponding to particle micro parameters refers to the method described by Chen et al. [32]. A calibration model with a length of 50 cm, width of 50 cm and height of 80 cm is established. Using the aforementioned particle micro parameters and particle generation method, 2778 particles are generated. The resulting soil specimen porosity rate measured by the measurement spheres is $n = 0.36$. The unit weight can be obtained by follows:

$$\gamma = G_s g (1 - n) \tag{3}$$

Therefore, the unit weight is 16.31 kN/m^3. Jaky [33] proposed the coefficient of earth pressure at rest, which is wildly used in geotechnical engineering. In Jack's formulation, the earth pressure coefficient at rest has the following relationship with the internal friction angle:

$$K_0 = 1 - \sin\varphi \tag{4}$$

where K_0 is the earth pressure coefficient at rest and φ is the internal friction angle. The calibration of the coefficient of friction between particles is realized according to the relationship between the lateral earth pressure acting on the wall at rest and the angle of internal friction. According to Eq. (4), the internal friction angle can be shown as follows:

$$\varphi = \arctan(1 - K_0) \tag{5}$$

The lateral earth pressure acting on the wall per unit length E_0 can be shown as follows:

$$E_0 = 0.5\left(\gamma H^2 K_0\right) \tag{6}$$

where H is depth. So the relationship between the lateral earth pressure acting on the wall at rest and the internal friction angle can be drawn as follows:

$$\varphi = \arcsin\left(1 - 2E_0/\gamma H^2\right) \tag{7}$$

The lateral earth pressure acting on the wall per unit length can be measured by measuring spheres at different depths. The variation of lateral earth pressure per unit length at different depths in calibration is shown in Fig. 3. In this way, the distribution of lateral earth pressure acting on the wall is obtained, and then the angle of internal friction can be obtained by Eq. (7). Through the calibration model, the angle of internal friction is 12.2 degrees.

Taking the effect of depth ratio (H/B) act on the soil arching effect into account, the filling height (H) was selected as 0.4, 0.8, 1.2, 1.5, 2.1 m, corresponding to five groups of different buried depth ratios (H/B). 0.67, 1.33, 2.00, 2.50, 3.50. The number of particles generated are 25,000 ($H/B = 0.67$), 50,000 ($H/B = 1.33$), 75,000 ($H/B = 2.00$), 93,750 ($H/B = 2.50$) and 131,250 ($H/B = 3.50$). The relative displacement in particles is caused by controlling the slow downshift of the trapdoor, which results in the soil arch effect. In the simulation process, each movement of the trapdoor displacement is 1.0×10^{-4} m. In each cycle, the unbalanced force is generated after the trapdoor is lowered and then eliminated by equilibrium calculation. The calculation is carried out on a computer with dual Intel Xeon E5-2678 v3 CPUs and 128 G RAM. The calculation time varies from several hours to hundreds of hours depending on the number of particles. The earth pressure at a different place of soil is measured by measurement spheres arranged above the trapdoor during the process of the trapdoor moving down. The diameter of each measurement sphere is 0.2 m. Five measurement spheres are arranged in the length direction of the model, and 3 measurement spheres are arranged in the width direction. The number of measurement spheres in the height direction is determined according to the height of the soil, and the typical measurement spheres arrangement schematic is shown in Figs. 2b and 2c.

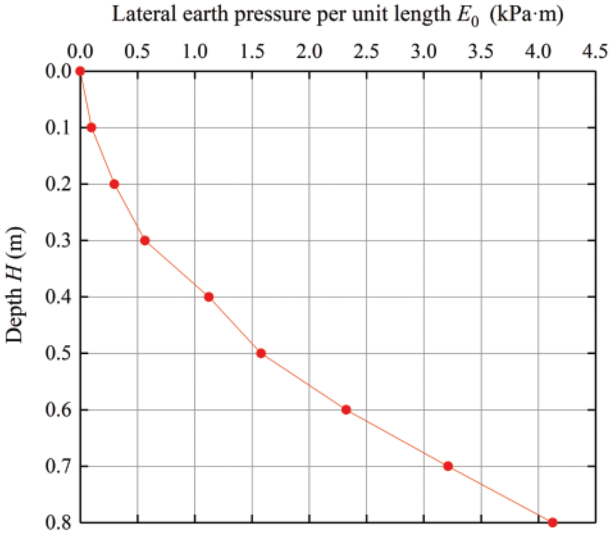

Figure 3: Variation of lateral earth pressure per unit length acting on the wall of unit length at different depth in calibration

3 Analysis of 3D DEM Calculation Results

3.1 Variation Law of Earth Pressure on the Trapdoor with the Downward Movement of the Trapdoor

Equilibrium calculation of the particles is carried out after the generation of particle, and then the earth pressure acting on the trapdoor is recognized. Then moving down the trapdoor, the displacement of each movement is 1.0×10^{-4} m, and after the movement, the unbalanced force is eliminated by equilibrium calculation, and then the soil earth pressure acting on the trapdoor is recorded.

The displacement of each movement is 1.0×10^{-4} m, 500 cycles in total, and the downward movement of the trapdoor is 0.05 m, which is 8.33% of the trapdoor width. The simulation results of five groups under of different buried depth ratios are shown in Fig. 4. It can be seen from the results that for the simulation results of different buried depth ratios, the earth pressure on the trapdoor decreases rapidly after the first few cycles of simulation, and then reaches the minimum earth pressure. For the case of the deep buried depth ratio, the earth pressure on the trapdoor remains basically unchanged, while for the case of shallow buried depth, the earth pressure will rise slightly.

The minimum value of earth pressure is related to the buried depth ratio. In the case of $H/B = 0.67$, the minimum earth pressure is 71.8% of the initial value, in the case of $H/B = 1.33$, the minimum earth pressure is 45.1% of the initial value, in the case of $H/B = 2.00$, the minimum earth pressure is 28.1% of the initial value, $H/B = 2.50$, the minimum earth pressure is 25.4% of the initial value, and in the case of $H/B = 3.50$, the minimum earth pressure is 18.2% of the initial value. It can be found that the larger the buried depth ratio is, the smaller the value of earth pressure in the loose zone relative to the initial earth pressure will be. And the soil arching effect in the overlying soil is more obvious, mainly because with the increasing of the depth of the upper soil, the formation of a longer slip surface makes the stress more easily transmitted to the none loose areas on both sides.

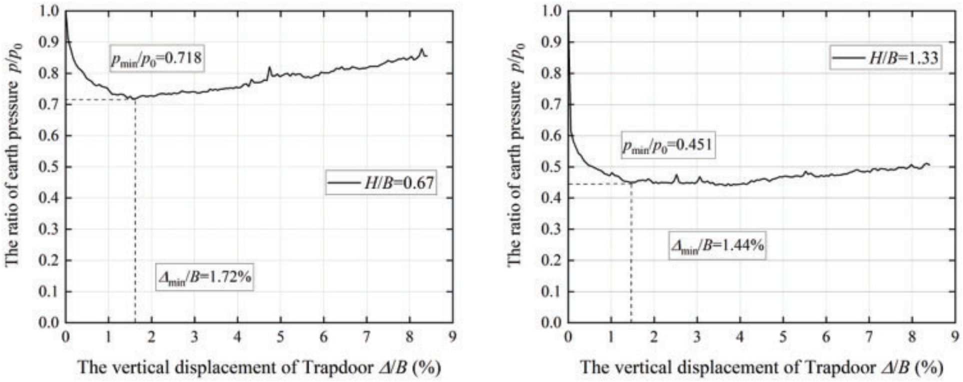

(a) H/B=0.67 (b) H/B=1.33

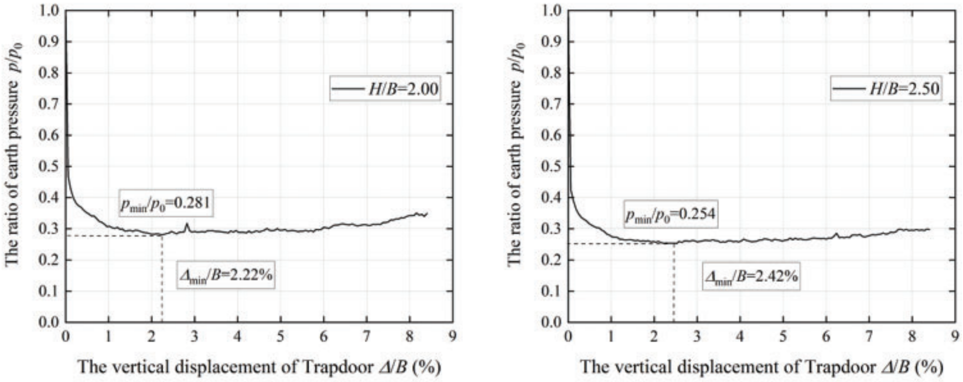

(c) H/B=2.00 (d) H/B=2.50

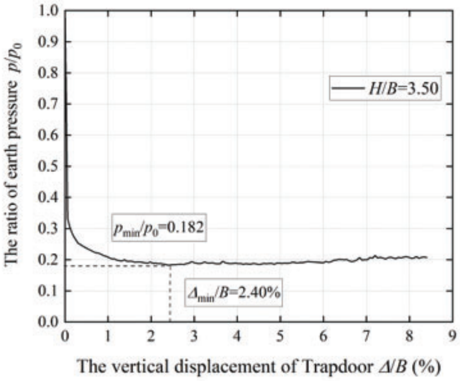

(e) H/B=3.50

Figure 4: Variation curve of the ratio of earth pressure with the downward movement of trapdoor

From the simulation results, it can also be found that the minimum earth pressure occurs at the moment when the vertical displacement reaches 1.72%, 1.44%, 2.22%, 2.42% and 2.40% of the trapdoor width for 5 different depth ratio, respectively. Dewoolkar et al. [7] concluded that the minimum earth pressure usually occurs when the vertical displacement of the trapdoor is 0.1% to 9% of the trapdoor width and the average is about 2% based on a large number of trapdoor model tests. The simulation results in this paper are consistent with this conclusion.

3.2 Distribution Law of Vertical Earth Pressure along Horizontal Direction

Fig. 5 shows the change of vertical earth pressure along the I line with trapdoor moving down, the position of the line (I) is shown in Fig. 2c, with five measurement spheres in the length direction, three in the middle above the moving trapdoor and two on both sides in the stable area. The earth pressure result is the average value of each measuring spheres on line (I).

It can be seen from the results that the downward movement of the trapdoor causes the soil arching effect in the loose area, and the ratio of earth pressure in the middle loose area is significantly lower than the initial ratio of 1. The ratio of earth pressure measured in the stable area on both sides will be higher than the initial ratio as the trapdoor moves down, mainly due to the soil arching effect, and the earth pressure in the middle loose area will transfer to the stable area on both sides. For Fig. 5a the depth ratio $H/B = 0.67$, the data have greater discreteness compared with the simulation results of larger relative depth due to the shallow soil thickness.

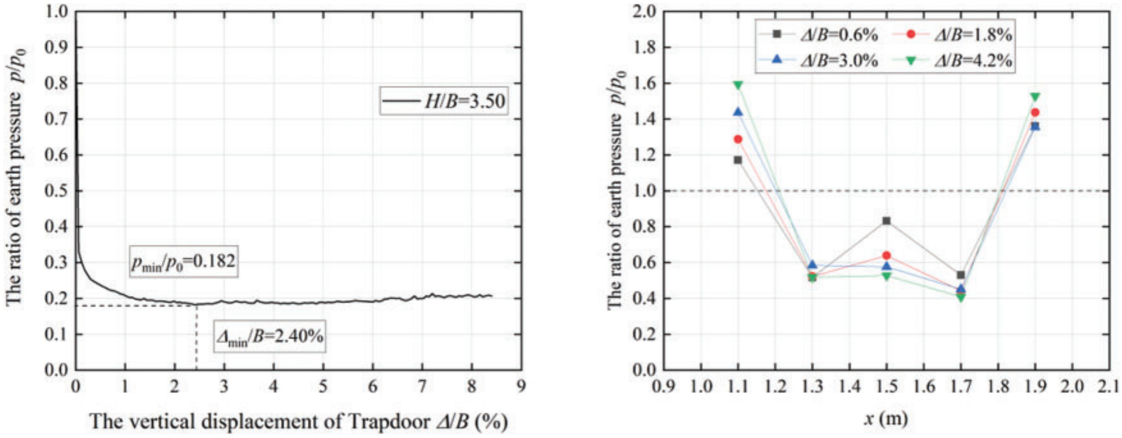

(a) *H/B*=0.67 (b) *H/B*=1.33

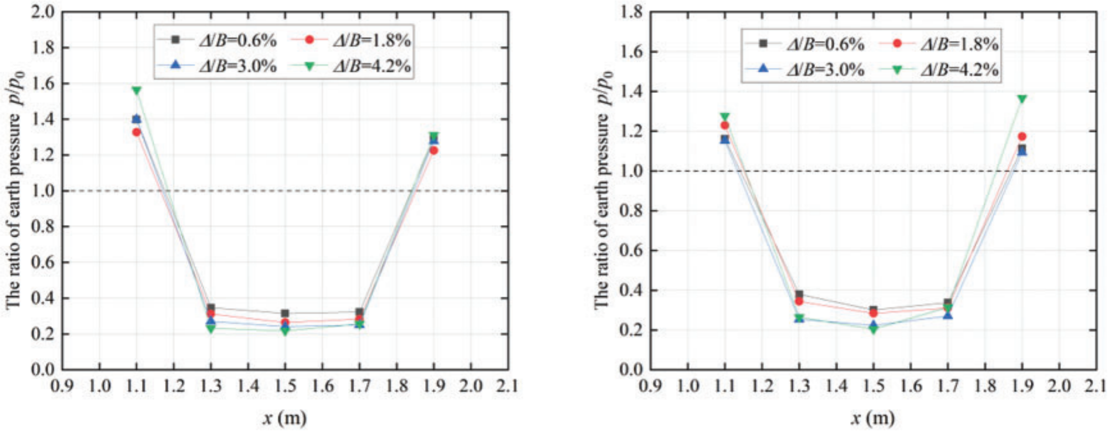

(c) *H/B*=2.00 (d) *H/B*=2.50

Figure 5: (Continued)

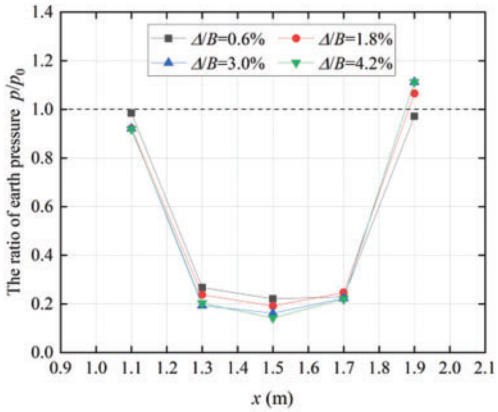

(e) H/B=3.50

Figure 5: Variation of vertical earth pressure on line (I) with the downward movement of trapdoor

In addition, it can be seen from the results that with the increase of the displacement of the trapdoor, the soil arching effect becomes more obvious. The more stress transfer occurs, the ratio of earth pressure decreases in the loose area, and the ratio of earth pressure in the stable area increases. Taking Fig. 5b for example, when the vertical displacement of the trapdoor reaches 0.6%, 1.8%, 3.0% and 4.2% of the trapdoor width, the ratios of earth pressure at the middle position are 0.83, 0.64, 0.58 and 0.53, respectively. The ratio of earth pressure decreases in turn and remains stable. The ratios of earth pressure in the measuring balls of the left stability zone are 1.29, 1.37, 1.45 and 1.44, respectively, which increase in turn and finally remain stable.

3.3 *Distribution law of Vertical Earth Pressure along Vertical Direction*

The calculation results of vertical earth pressure distribution of lines (II), (III) and (IV) along the vertical direction with the downward movement of the trapdoor are shown in Figs. 6 to 8. The simulation results of the vertical distribution of earth pressure of group which H/B is 0.67 is not analyzed because the depth is too shallow.

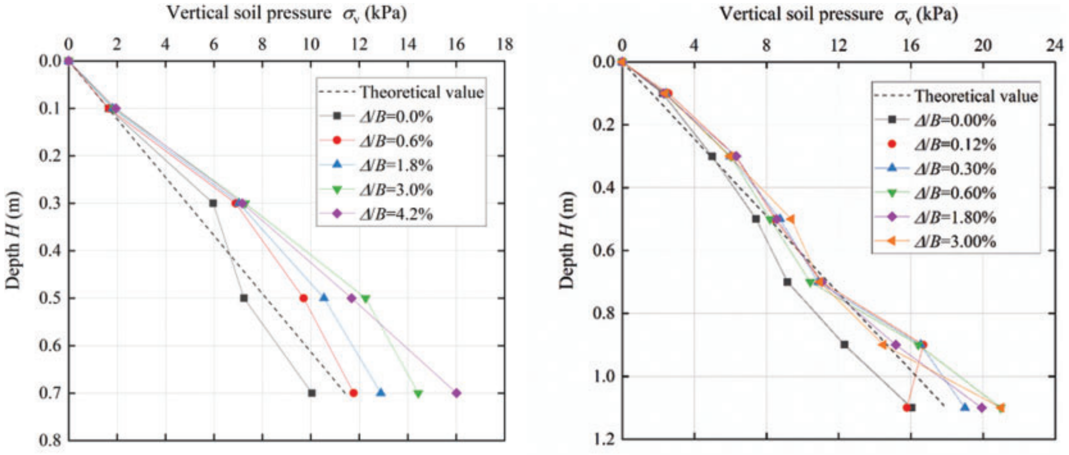

(a) H/B=1.33 (b) H/B=2.00

Figure 6: (Continued)

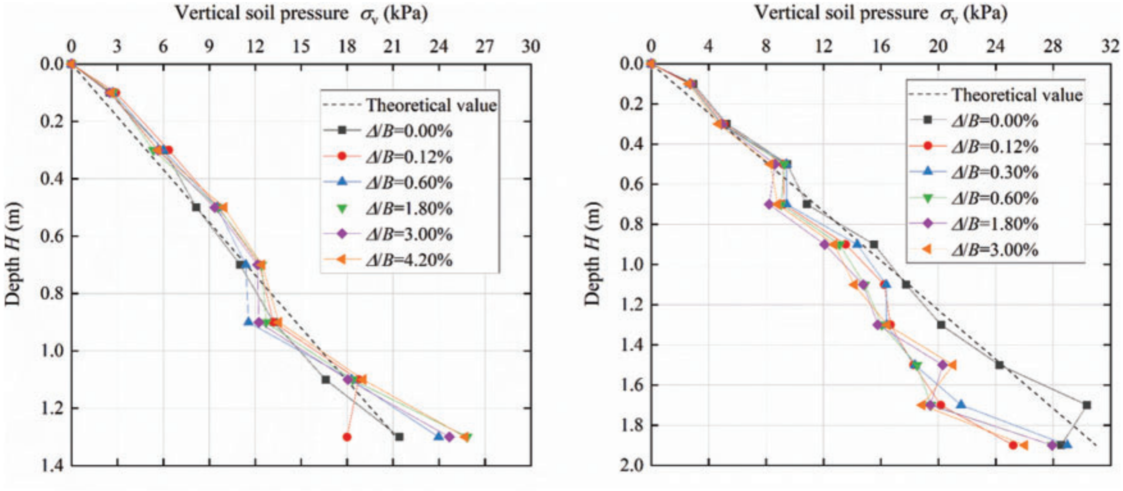

(c) H/B=2.50 (d) H/B=3.50

Figure 6: Variation of vertical earth pressure on line (II) with the downward movement of trapdoor

The vertical earth pressure results located on lines (II), (III) and (IV) can be seen from Figs. 6 to 8. The initial vertical earth pressure at the beginning of the simulation is comparable to the theoretical value of the earth's self-gravity stress which increases linearly along the depth.

Fig. 6 shows the distribution change of vertical earth pressure along the depth line (II) in the stability zone with the trapdoor moving down. It can be seen from the results that after the trapdoor moves down, the vertical distribution of earth pressure in the stability zone still maintains an approximate linear distribution. For different displacement of the trapdoor, the earth pressure of the shallow part of soil basically does not change because it is less affected by the loosening area. While the deep part of the soil is relatively affected by the loosening area.

For the soil in the loose zone, with the moving down of the trapdoor, the variations of the earth pressure distribution along the depth on line (III) and line (IV) are shown in Figs. 7 and 8. It can be found that after the downward of the trapdoor, the earth pressure in the loose area changes along the depth distribution is different from the linear distribution of the initial state because of the soil arching effect. The earth pressure of the deep part of the soil will be much smaller than the theoretical value of the vertical earth pressure of its self-weight because of the stress redistribution in the loose area. Taking the simulation results of $H/B = 3.50$ in Fig. 7d as an example, when the trapdoor displacement reaches 0.3% width of the trapdoor, the measured vertical earth pressure at the depth of 1.9 m is 8.21 kPa, which is far less than the theoretical value of self-weight vertical earth pressure 30.98 kPa. The vertical earth pressure is only 26.5% of the theoretical self-weight. The vertical earth pressure at the depth of 1.9 m is even equivalent to the earth pressure at 0.7 m.

In addition, the results of Figs. 7 and 8 show that with the increasing of trapdoor displacement, the soil arching effect becomes more and more significant which means the earth pressure in the loose area is smaller. Still taking the simulation result of $H/B = 3.50$ in Fig. 7d as an example, when the trapdoor displacement reaches 0.12%, 0.30%, 0.60%, 1.80% and 3.00% of the trapdoor width, the vertical earth pressure at 1.7 m is 8.44, 7.55, 5.81, 5.08 and 4.37 kPa, which shows a gradually decreasing trend and a steady trend.

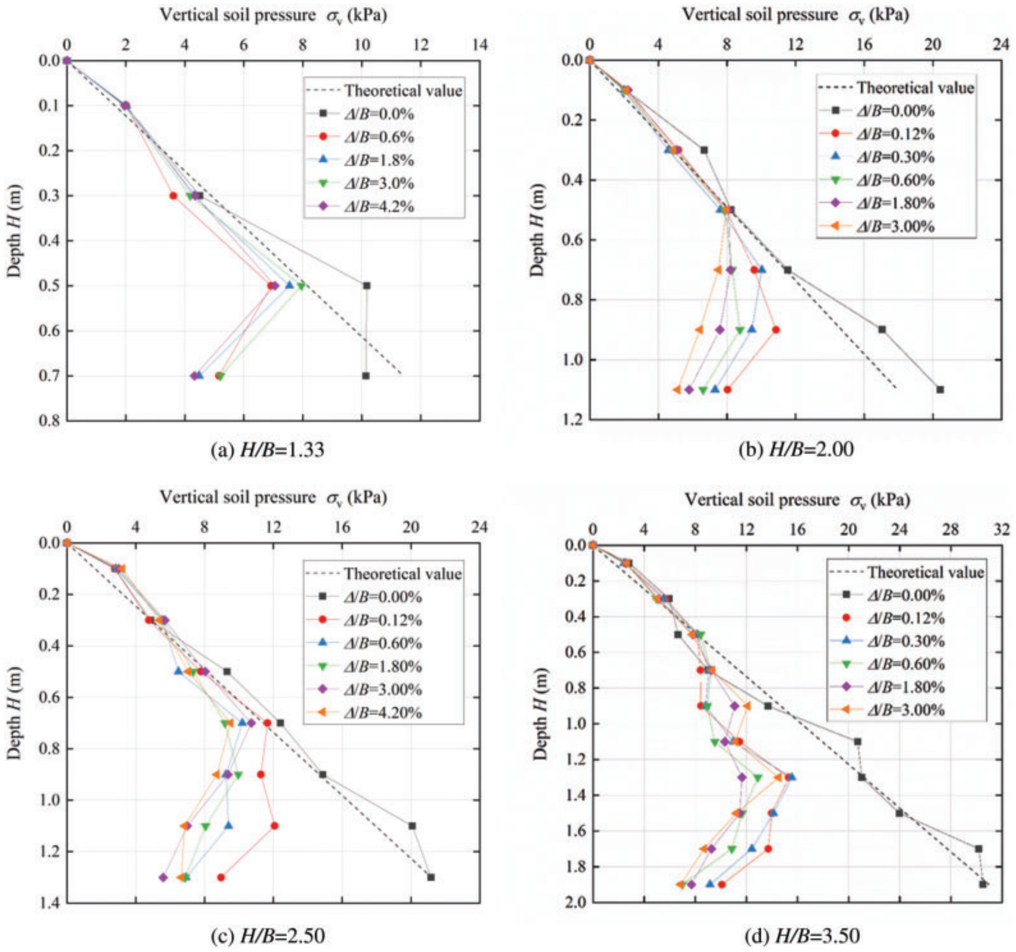

(a) H/B=1.33 (b) H/B=2.00

(c) H/B=2.50 (d) H/B=3.50

Figure 7: Variation of vertical earth pressure on line (III) with the downward movement of trapdoor

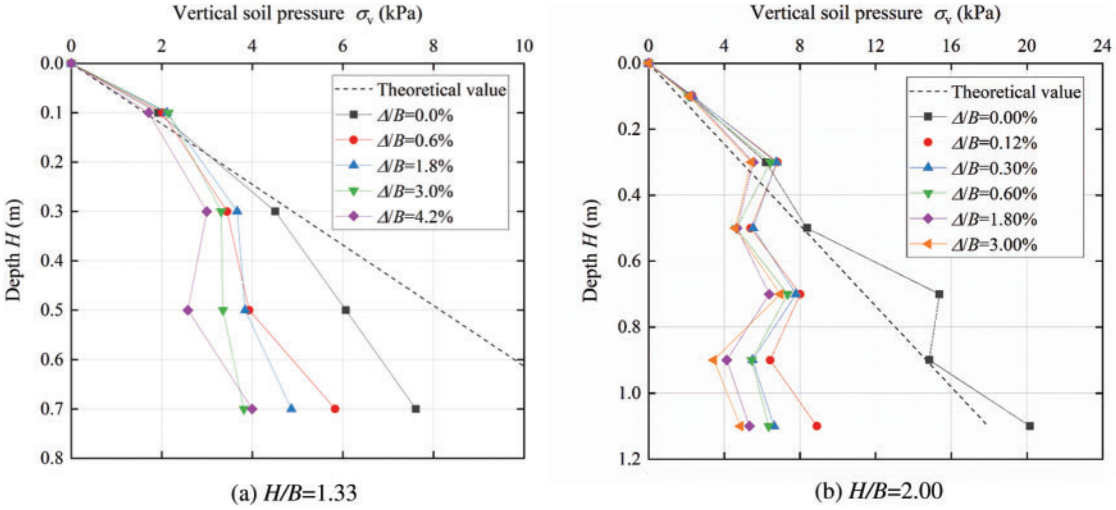

(a) H/B=1.33 (b) H/B=2.00

Figure 8: (Continued)

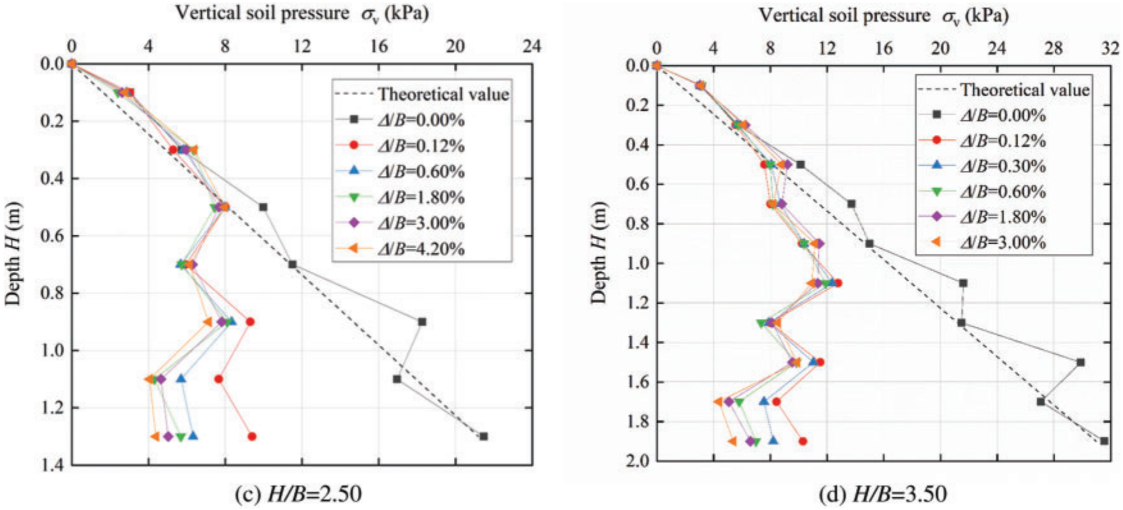

(c) *H*/*B*=2.50 (d) *H*/*B*=3.50

Figure 8: Variation of vertical earth pressure on line (IV) with the downward movement of trapdoor

3.4 Distribution Law of Lateral Earth Pressure Coefficient along Depth Direction

The simulation results of lateral earth pressure coefficient on the central axis (IV) of loose zone are shown in Fig. 9. It can be found that when the soil arching effect occurs in the loose area, the horizontal earth pressure will be greater than vertical earth pressure and the lateral earth pressure coefficient of most areas on the axis of the loose area will be closer to the passive earth pressure coefficient Kp because of the extrusion of the soil on both sides. There will be some deviation in the shallow soil and the bottom soil, mainly due to the impact of the boundary. At the same time, it can be found that with the increase of trapdoor displacement, the ratio of earth pressure trends to increase. It is speculated that the main reason is that as the downward movement of the trapdoor, the squeezing effect of the soil on both sides acting on the soil on the central axis is intensified.

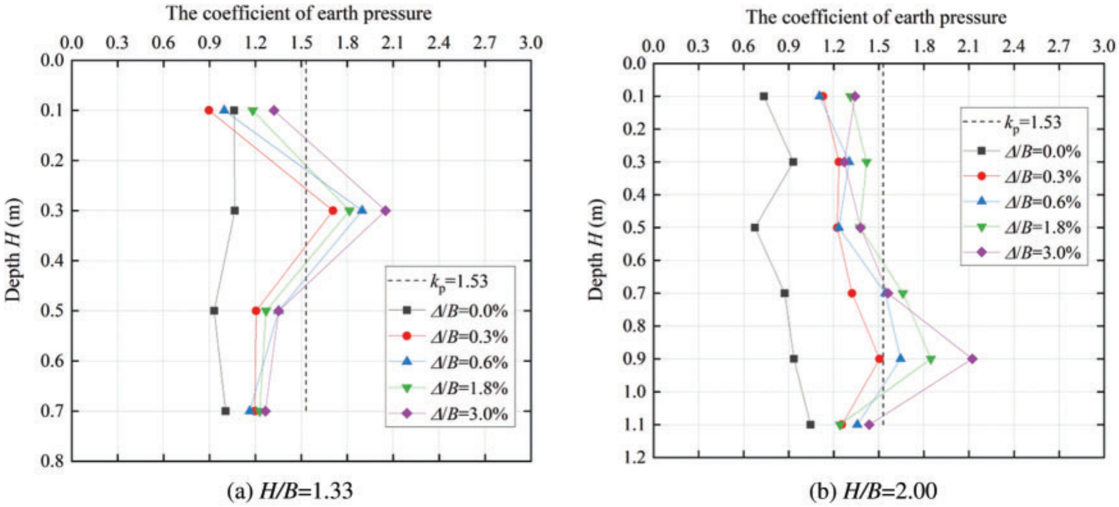

(a) *H*/*B*=1.33 (b) *H*/*B*=2.00

Figure 9: (Continued)

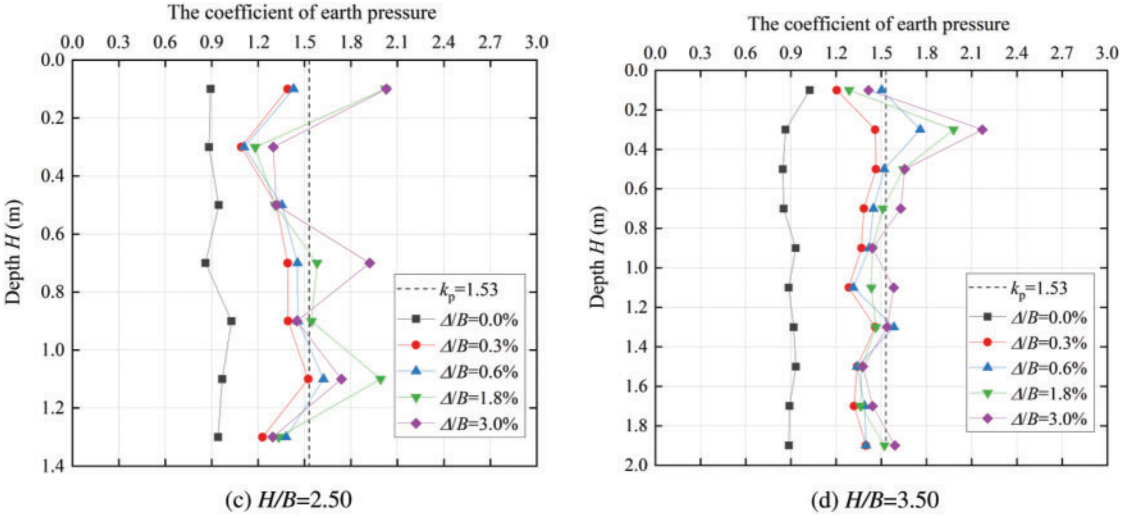

(c) H/B=2.50 (d) H/B=3.50

Figure 9: Variation of lateral earth pressure coefficient along the line (IV) with the downward movement of trapdoor

3.5 Size and Distribution Law of Contact Force Chain

According to the simulation results of five groups of different buried depth ratios, the distribution of contact force chain can be observed by cross sections. The front section view is shown in Fig. 10. It can be clearly seen that the soil stress in the loose zone transfers to the stable zone on both sides of the loose zone, and the contact force of particles on the central axis is mainly in the horizontal direction. Through the distribution diagram of contact force chain, the existence of "soil arch" can be observed intuitively.

(a) H/B=0.67

Figure 10: (Continued)

(b) *H/B*=1.33

(c) *H/B*=2.00

(d) *H/B*=2.50

Figure 10: (Continued)

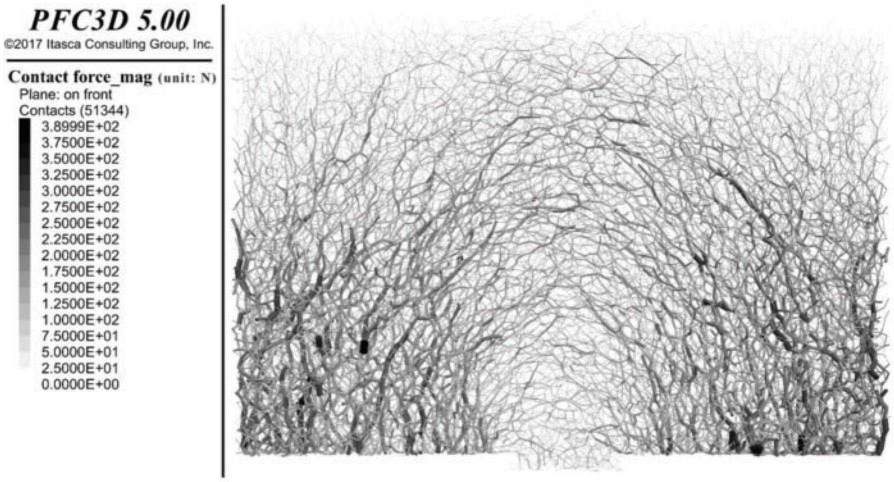

(e) H/B=3.50

Figure 10: Front view of contact force chain

Fig. 11 is a vertical cross section view at 0.1 m from the bottom of the contact force chain of the simulation group with $H/B = 1.33$. It can be found from the results that the contact force in the loose area is significantly less than that in the stable area on both sides, mainly due to the soil arching effect, the stress is transmitted to the stable area on both sides through the arched force chain formed above. The distribution results of the contact force chain in Fig. 11 are consistent with the conclusion that the earth pressure above the bezel is much less than the pressure of its self-weight.

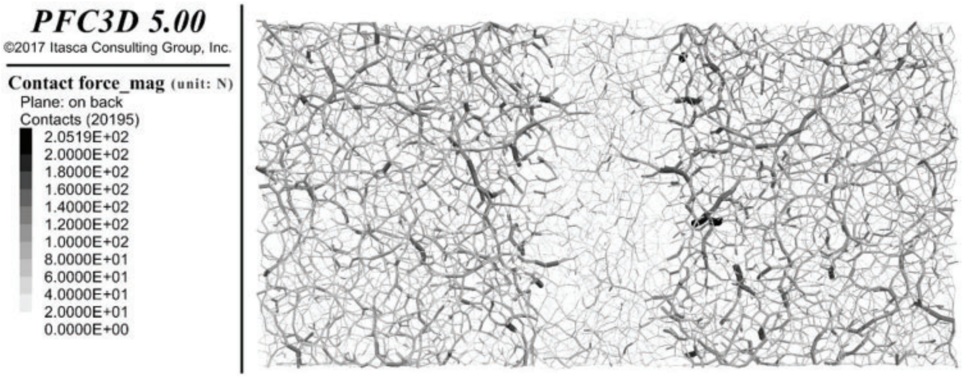

Figure 11: Top view of contact force chain

4 Conclusion

The 3D DEM software PFC3D is used to study the trapdoor problem, the change of earth pressure and the lateral ratio of earth pressure in loose and stable areas is studied, and the preliminary conclusions and suggestions were as follows:

1) Due to the presence of the soil arching effect, the earth pressure on the trapdoor decreases rapidly after the simulation begins, and then reaches the minimum earth pressure. The earth pressure on the trapdoor then remains basically unchanged for the large buried depth ratio,

while the earth pressure will rise slightly for shallow burial depth. The larger the depth ratio is, the smaller the earth pressure in the loose zone relative to the initial earth pressure will be.

2) For the bottom soil, due to stress transfer caused by the soil arching effect, the ratio of earth pressure in the loose area decreases, while the ratio of earth pressure in the stable area increases.
3) As the trapdoor moves down, the vertical earth pressure in the stable area is basically the same along the depth distribution as the initial state, showing an approximate linear distribution. After the trapdoor moves down, the earth pressure in the loose area changes along the depth distribution; unlike the linear distribution of the initial state, the deep earth pressure will be much smaller than the theoretical value of its self-weight earth pressure.
4) When the soil arching effect occurs in the loose area, the lateral earth pressure coefficient of most areas on the axis of the loose area is close to the passive earth pressure coefficient K_p due to the extrusion of the soil on both sides.
5) The contact force chain in the loose zone shows that the soil stress is transferred to the stable zone on both sides of the loose zone through the distribution diagram of the contact force.

Funding Statement: The financial supports from National Natural Science Foundation of China (NSFC Grant No. 52008373) and Natural Science Foundation of Zhejiang Province of China (No. Q22E080445) are greatly acknowledged.

Conflicts of Interest: The authors declare that they have no conflicts of interest to report regarding the present study.

References

1. Lai, H. J., Zheng, J. J., Cui, M. J. (2021). Improved analytical soil arching model for the design of piled embankments. *International Journal of Geomechanics, 21(3),* 04020261. DOI 10.1061/(ASCE)GM.1943-5622.0001929.
2. Liang, L., Xu, C. (2019). Numerical and theoretical research on stress distribution in the loosening zone of the trapdoor problem. *International Journal for Numerical and Analytical Methods in Geomechanics, 43(7),* 1426–1447. DOI 10.1002/nag.2906.
3. Jiao, Y. Y., Zhang, Y., Tan, F. (2020). Estimation of active earth pressure against rigid retaining walls considering soil arching effects and intermediate principal stress. *International Journal of Geomechanics, 20(11),* 04020217. DOI 10.1061/(ASCE)GM.1943-5622.0001865.
4. Terzaghi, K. (1936). Stress distribution in dry and in saturated sand above a yielding trap-door. *1st International Conference on Soil Mechanics and Foundation Engineering*, pp. 307–311. Harvard University Cambridge, Mass.
5. Iglesia, G. R., Einstein, H. H., Whitman, R. V. (2011). Validation of centrifuge model scaling for soil systems via trapdoor tests. *Journal of Geotechnical & Geoenvironmental Engineering, 137(11),* 1075–1089. DOI 10.1061/(ASCE)GT.1943-5606.0000517.
6. Iglesia, G. R., Einstein, H. H., Whitman, R. V. (2014). Investigation of soil arching with centrifuge tests. *Journal of Geotechnical & Geoenvironmental Engineering, 140(2),* 04013005. DOI 10.1061/(ASCE)GT.1943-5606.0000998.
7. Dewoolkar, M. M., Kitidech, S., Hon-Yim, K. O. (2007). Centrifuge modeling of granular soil response over active circular trapdoors. *Soil and Foundation, 47(5),* 931–945. DOI 10.3208/sandf.47.931.
8. Costa, Y. D., Zornberg, J. G., Bueno, B. S., Costa, C. L. (2009). Failure mechanisms in sand over a deep active trapdoor. *Journal of Geotechnical & Geoenvironmental Engineering, 135(11),* 1741–1753. DOI 10.1061/(ASCE)GT.1943-5606.0000134.

9. Rui, R., Tol, F. V., Xia, X. L., Eekelen, S. V., Xia, Y. Y. (2016a). Evolution of soil arching; 2D DEM simulations. *Computers and Geotechnics, 73,* 199–209. DOI 10.1016/j.compgeo.2015.12.006.
10. Rui, R., van Tol, A. F., Xia, Y. Y., van Eekelen, S. J. M., Hu, G. (2016b). Investigation of soil-arching development in dense sand by 2D model tests. *Geotechnical Testing Journal*, *39(3),* 20150130. DOI 10.1520/GTJ20150130.
11. Rui, R., Tol, F. V., Xia, Y. Y., Eekelen, S. V., Hu, G. (2018). Evolution of soil arching: 2D analytical models. *International Journal of Geomechanics, 18(6),* 04018056. DOI 10.1061/(ASCE)GM.1943-5622.0001169.
12. Rui, R., Han, J., van Eekelen, S. J. M., Wan, Y. (2019). Experimental investigation of soil-arching development in unreinforced and geosynthetic-reinforced pile-supported embankments. *Journal of Geotechnical and Geoenvironmental Engineering, 145(1),* 04018103. DOI 10.1061/(ASCE)GT.1943-5606.0002000.
13. Chevalier, B., Otani, J. (2011). Arching observation in three-dimensional trapdoor problem with X-ray CT and discrete element method. *Soils & Foundations, 51(3),* 459–469. DOI 10.3208/sandf.51.459.
14. Chevalier, B., Combe, G., Villard, P. (2012). Experimental and discrete element modeling studies of the trapdoor problem: Influence of the macro-mechanical frictional parameters. *Acta Geotechnica, 7(1),* 15–39. DOI 10.1007/s11440-011-0152-5.
15. Lai, H. J., Zheng, J. J., Zhang, J., Zhang, R. J., Lan, C. (2014). Dem analysis of "soil"-arching within geogrid-reinforced and unreinforced pile-supported embankments. *Computers & Geotechnics, 61,* 13–23.
16. Lai, H. J., Zheng, J. J., Zhang, R. J., Cui, M. J. (2016). Visualization of the formation and features of soil arching within a piled embankment by discrete element method simulation. *Journal of Zhejiang University-SCIENCE A, 17(10),* 803-817. DOI 10.1631/jzus.A1500302.
17. Pardo, G. S., Sáez, E. (2014). Experimental and numerical study of arching soil effect in coarse sand. *Computers and Geotechnics, 57(4),* 75–84. DOI 10.1016/j.compgeo.2014.01.005.
18. Sloan, S. W., Purushothaman, N., Assadi, A. (1990). Undrained stability of a trapdoor. *Géotechnique, 40(1),* 45–62. DOI 10.1680/geot.1990.40.1.45.
19. Martin, C. M. (2009). Undrained collapse of a shallow plane-strain trapdoor. *Géotechnique, 59(10),* 855–863. DOI 10.1680/geot.8.T.023.
20. Keawsawasvong, S., Ukritchon, B. (2017). Undrained stability of an active planar trapdoor in non-homogeneous clays with a linear increase of strength with depth. *Computers and Geotechnics, 81,* 284–293. DOI 10.1016/j.compgeo.2016.08.027.
21. Liang, L., Xu, C., Chen, Q., Chen, Q. (2020). Experimental and theoretical investigations on evolution of soil-arching effect in 2D trapdoor problem. *International Journal of Geomechanics, 20(6),* 06020007. DOI 10.1061/(ASCE)GM.1943-5622.0001643.
22. Aubertin, M., Li, L., Arnoldi, S., Belem, T., Bussière, B. et al. (2003). Interaction between backfill and rock mass in narrow stopes. *Soil and Rock America, 1(2),* 1157–1164.
23. Li, L., Aubertin, M. (2008). An improved analytical solution to estimate the stress state in subvertical backfilled stopes. *Canadian Geotechnical Journal, 45(10),* 1487–1496. DOI 10.1139/T08-060.
24. Li, L., Aubertin, M. (2009). Horizontal pressure on barricades for backfilled stopes. Part I: Fully drained conditions. *Canadian Geotechnical Journal, 46(1),* 37–46. DOI 10.1139/T08-104.
25. Li, L., Aubertin, M. (2009). Horizontal pressure on barricades for backfilled stopes. Part II: Submerged conditions. *Canadian Geotechnical Journal, 46(1),* 47–56. DOI 10.1139/T08-105.
26. Eekelen, S. V., Bezuijen, A., van Tol, A. F. (2013). An analytical model for arching in piled embankments. *Geotextiles & Geomembranes, 39,* 78–102. DOI 10.1016/j.geotexmem.2013.07.005.
27. Qian, Z. H., Zou, J. F., Tian, J., Pan, Q. J. (2020). Estimations of active and passive earth thrusts of non-homogeneous frictional soils using a discretisation technique. *Computers and Geotechnics, 119,* 103366. DOI 10.1016/j.compgeo.2019.103366.

28. Qian, Z. H., Zou, J. F., Pan, Q. J., Chen, G. H., Liu, S. X. (2020). Discretization-based kinematical analysis of three-dimensional seismic active earth pressures under nonlinear failure criterion. *Computers and Geotechnics, 126,* 103739. DOI 10.1016/j.compgeo.2020.103739.
29. Li, F., Hong, Z., Yu, J., Sun, L., Wang, L. (2020). A novel method of calculating active earth pressure on laggings between piles considering the soil arching effect. *European Journal of Environmental and Civil Engineering,* 1–15. DOI 10.1080/19648189.2020.1852603.
30. Cundall, P. A., Strack, O. D. (1979). A discrete numerical model for granular assemblies. *Geotechnique, 29(1),* 47–65. DOI 10.1680/geot.1979.29.1.47.
31. Itasca (2008). *Particle flow code in 3 dimensions (PFC3D), User's guide.* Minneapolis: Itasca Consulting Group.
32. Chen, Y. D., Yu, Y., She, Y. X. (2013). Method for determining mesoscopic parameters of sand in three-dimensional particle flow code numerical modeling. *Chinese Journal of Geotechnical Engineering, 35(S2),* 88–93.
33. Jaky, J. (1944). The coefficient of earth pressure at rest. *Journal of the Society of Hungarian Architects and Engineers, 22,* 355–358.

Computer Modeling in
Engineering & Sciences

Tech Science Press

DOI: 10.32604/cmes.2023.025749

ARTICLE

Numerical Simulation of Low Cycle Fatigue Behavior of Ti_2AlNb Alloy Subcomponents

Yanju Wang[1], **Zhenyu Zhu**[2], **Aixue Sha**[1] **and Wenfeng Hao**[3,*]

[1]Materials Evaluation Center for Aeronautical and Aeroengine Application, AECC Beijing Institute of Aeronautical Materials, Beijing, 100095, China

[2]Faculty of Civil Engineering and Mechanics, Jiangsu University, Zhenjiang, 212013, China

[3]College of Mechanical Engineering, Yangzhou University, Yangzhou, 225127, China

*Corresponding Author: Wenfeng Hao. Email: hwf@yzu.edu.cn

Received: 28 July 2022 Accepted: 12 October 2022

ABSTRACT

Many titanium alloy subcomponents are subjected to fatigue loading in aerospace engineering, resulting in fatigue failure. The fatigue behavior of Ti_2AlNb alloy subcomponents was investigated based on the Seeger fatigue life theory and the improved Lemaitre damage evolution theory. Firstly, the finite element models of the standard open-hole specimen and Y-section subcomponents have been established by ABAQUS. The damage model parameters were determined by fatigue tests, and the reliability of fatigue life simulation results of the Ti_2AlNb alloy standard open-hole specimen was verified. Meanwhile, the fatigue life of Ti_2AlNb alloy Y-section subcomponents was predicted. Under the same initial conditions, the average error of fatigue life predicted by two different models was 20.6%. Finally, the effects of loading amplitude, temperature, and Y-interface angle on fatigue properties of Ti_2AlNb Y-section subcomponents were investigated. These results provide a new idea for evaluating the fatigue life of various Ti_2AlNb alloy subcomponents.

KEYWORDS

Fatigue life prediction; stiffness degeneration; Ti_2AlNb alloy; continuous damage mechanics; numerical simulation

1 Introduction

Advances in the aerospace industry require new lightweight materials and complex integral component forming technologies to improve fuel efficiency and payloads. Ti_2AlNb alloy has good plasticity and fracture toughness at room temperature, creep and fatigue resistance at a high temperature, high Young's modulus, and specific strength. Compared with the traditional high-temperature titanium alloy, the upper limit of application temperature of Ti_2AlNb alloy exceeds 600°C and reaches 650°C∼700°C [1–4].

Many titanium alloy subcomponents are subjected to fatigue loading in aerospace engineering, resulting in fatigue failure. The fatigue behavior of Ti_2AlNb alloy subcomponents is fundamental. The fatigue properties of Ti_2AlNb alloy were mainly studied by analyzing the influence of microstructure, alloy composition and surface treatment. Through the study of the Orthorhombic structure (O phase), the formation mechanism of Ti_2AlNb alloy is diverse and complex, and the formation of the material is strongly dependent on the thermal machining process [5–8]. When the O phase layer is thick, the longer the slip path, the lower the fatigue life. The thin O phase layer and the dense O/B2 phase interface can improve the fatigue crack initiation resistance. By adjusting the ratio of Al/Nb or adding alloying elements, such as Mo, Zr, Fe, Ta, W, Si and V, the mechanical properties of Ti_2AlNb alloy, such as strength, plasticity, oxidation resistance and creep resistance, have been significantly changed [9–12]. For instance, W effectively improves the high temperature tensile strength of Ti_2AlNb alloy from 752 to 1123 MPa [13]. Zhang et al. [14,15] studied the effect of cooling rate on the microstructure and tensile properties of Ti_2AlNb alloy. Chen et al. [16] studied the effect of shot peening on the fatigue performance of Ti_2AlNb. They measured the residual stress of the specimen after glass fine shot peening by X-ray diffraction and electropolishing. Based on the image crystal plasticity model, Fu et al. [17] studied the influence of size and distribution for the O phase on the fracture properties of Ti_2AlNb superalloy. After shot peening, residual compressive stress was introduced into the surfaces of samples, which offset part of the tensile stress, delayed the initiation and propagation of cracks, and significantly increased the fatigue strength limit from 170 to 360 MPa and the high cycle fatigue life is prolonged more than 25 times [16,18]. The study of fatigue properties and deformation behaviour of Ti_2AlNb alloy focuses on the material parts, and the fatigue behavior of subcomponents needs further study.

The fatigue life prediction of titanium alloy can be divided into three main criteria: stress criteria [19,20], energy criteria [21–23] and strain criteria [24–26]. The stress criterion is suitable for the life prediction of High Cycle Fatigue (HCF). The energy criterion considers that material damage accumulates strain energy caused by stress. When the energy reaches the critical value, the material will fail, and it cannot reflect the difference in the influence of various stress (strain) components on the material failure. The strain criterion of Morrow et al. [22] has been widely applied to the fatigue life prediction of elastic-plastic materials under Low Cycle Fatigue (LCF). Based on the strain criterion, Bäumel et al. [27] first found that a uniform description of fatigue parameters of different types of metal materials would lead to errors, so fatigue parameter expressions of steel, titanium and aluminium were given respectively. Seeger theory general slope method has significant advantages in the fatigue life prediction of titanium alloys. Continuum Damage Mechanics (CDM) has been rapidly developed and applied in recent years. CDM theory connects fatigue with microcrack evolution and further develops the traditional fatigue theory [28–31]. Compared with the classical fatigue theory, CDM theory is more consistent with the microscopic mechanism of the fatigue process observed in the experiments. The damage variable can measure the fatigue damage process more directly, which is convenient for considering the fatigue damage. Zhou et al. [32,33] improved the Lemaitre damage evolution model and applied the CDM method to fatigue damage and life prediction of titanium alloy TC4 materials and components, achieving excellent accuracy.

To sum up, the fatigue behavior of Ti_2AlNb alloy subcomponents is still an open question. Seeger fatigue life theory and the improved Lemaitre damage evolution theory are used to predicting the fatigue life of Ti_2AlNb alloy standard open-hole specimen and Y-section subcomponents. The research method has a particular reference significance for predicting the fatigue life of Ti_2AlNb alloy subcomponents and provides a new idea for evaluating the fatigue life of various engineering structures.

2 Methodology

2.1 Seeger Theory

Seeger theory has been widely used to estimate the elastic-plastic stress and strain of notched parts under uniaxial or multiaxial stress (monotone and cyclic loading). Its accuracy has also been verified in relevant experiments [34].

$$\varepsilon = \frac{\sigma}{E} + \left(\frac{\sigma}{K'}\right)^{\frac{1}{n'}} \tag{1}$$

where K' is the strain hardening coefficient, and n' is the strain hardening exponent.

The relation between the real local stress amplitude and durability is:

$$\frac{\Delta\sigma}{2} = \sigma_f' \left(2N_f\right)^b \tag{2}$$

where b is the fatigue strength exponent (Basquin's exponent), σ_f' is the fatigue strength coefficient and N_f is the number of cycles to failure.

The true fracture strength (or stress) is shown to be:

$$\sigma_f = \frac{P_f}{A_f} \tag{3}$$

where P_f is the load at fracture, and A_f is the cross-sectional area at fracture.

The fatigue ductility coefficient, ε_f', is approximately equal to the true fracture ductility ε_f. The true fracture ductility was shown to be:

$$\varepsilon_f = ln\left(\frac{A_0}{A_f}\right) \tag{4}$$

where A_0 is the original cross-sectional area.

Fatigue life can also be approximated by Eq. (5).

$$2N_f = \left(\frac{\varepsilon_f' E}{\sigma_f'}\right)^{\frac{1}{b-c}} \tag{5}$$

The fatigue strength exponent will usually be between −0.05 and −0.12. The fatigue ductility exponent, c, will usually be between −0.5 and −0.7.

From Eqs. (1) and (2), the following relation can be deduced:

$$K' = \frac{\sigma_f'}{\left(\varepsilon_f'\right)^{n'}} \tag{6}$$

$$n' = \frac{b}{c} \tag{7}$$

Seeger theory involves fatigue parameters as shown in Table 1, $a = 1.0$ when σ_b/E is less than 0.003, otherwise $a = 1.375 – 125\sigma_b/E$. σ_b is tensile strength.

2.2 The Improved Lemaitre Damage Evolution Theory

In the framework of CDM, damage is defined as the development of pores in microscopic, submicroscopic, and macroscopic fracture processes of materials, which is accompanied by the deterioration of the mechanical properties of materials. The 'damage' does not correspond to the actual crack. In metallic materials, the damage usually has no directivity, called isotropic damage, and can be expressed as a scalar quantity.

Table 1: Seeger theoretical method fatigue parameters of titanium alloy

σ_f'	ε_f'	b	c	n'	K'
$1.67\sigma_u$	0.35	−0.095	−0.69	0.11	$1.61\sigma_u$

According to the equivalent strain hypothesis proposed by Lemaitre and Desmorat, the effective stress acting on the effective area can be defined as:

$$\widetilde{\sigma}_{ij} = \frac{\sigma_{ij}}{1 - D} \tag{8}$$

where σ_{ij} is the nominal stress, without considering the influence of damage, D is the damage variable.

According to the constitutive damage model proposed by Krajcinovic and Lemaitre, the fatigue damage of metal materials in LCF is mainly caused by accumulated plastic strain. The greater the cumulative plastic deformation, the more excellent the energy dissipation caused by damage.

Damage increment, $\dot{D}$, can be expressed as:

$$\dot{D} = \frac{Y}{S}\dot{p} \tag{9}$$

Damage strain energy release rate, Y, can be expressed as:

$$Y = \frac{\sigma_{eq}^2 R_V}{2E\,(1 - D)^2} \tag{10}$$

where S is material constant, $\dot{p}$ is cumulative plastic strain increment, σ_{eq} is Von Mises stress, and R_V is stress triaxiality. In uniaxial state, R_V is 1.

Substitute Eq. (10) into Eq. (9)

$$\dot{D} = \frac{\sigma_{eq}^2 R_V}{2ES\,(1 - D)^2}\dot{p} \tag{11}$$

According to the study of Zhou et al. [32], Eq. (11) cannot sufficiently describe the phenomenon of a sharp increase in damage of titanium alloy materials before failure. Eq. (11) is improved as:

$$\dot{D} = \frac{\sigma_{eq}^2 R_V}{2ES\,(1 - D)^{\alpha}\,(1 - D/D_c)}\dot{p} \tag{12}$$

where α is the material constant, and D_c is damage limit.

For the LCF behavior of metal materials, the Ramberg-Osgood cycle is usually adopted. Within a stable cycle, the plastic strain can be expressed as:

$$\frac{\Delta p}{2} = \left(\frac{\Delta\sigma_{eq}}{2K\,(1 - D)}\right)^{1/n} \tag{13}$$

where Δp is the change of cumulative plastic strain in a cycle, K is the cyclic strengthening coefficient, n is the cyclic strain hardening exponent.

The equivalent stress difference, $\Delta\sigma_{eq}$, can be expressed as:

$$\Delta\sigma_{eq} = \Delta\sigma_{eq}^{'} - \Delta\sigma_{eq}^{''} < \sigma_{m}^{''} > \tag{14}$$

where $\Delta\sigma_{eq}^{'}$ is the peak equivalent stress, $\Delta\sigma_{eq}^{''}$ is the valley equivalent stress, $\sigma_{m}^{''}$ is the average stress.

Assuming that the damage changes very little in a cycle, it can be approximated that the damage variable D in Eq. (13) is a specific value. By differentiating both ends of Eq. (13), the plastic strain rate can be obtained:

$$dp = \frac{1}{nK\left(1-D\right)}\left(\frac{\sigma_{eq}}{K\left(1-D\right)}\right)^{\frac{1}{n}-1} d\sigma_{eq} \tag{15}$$

By using the established damage constitutive relation Eqs. (13), (15), and damage evolution Eq. (12), the change process of D at any point in the whole fatigue process can be theoretically given through numerical analysis. When D reaches D_c at the danger point, fatigue failure occurs in the subcomponents, which can be expressed as follows:

$$\int_{0}^{N_f} \frac{\delta D}{\delta N} dN = D_c \tag{16}$$

where $\frac{\delta D}{\delta N}$ is the damage increment within a cycle.

In order to calculate $\frac{\delta D}{\delta N}$ quickly and accurately, the following two assumptions are proposed:

A. Within a cycle, the damage changes, ΔD, very little, and D can be approximated as a constant;
B. When D_c is small, D is a small quantity, so the stress field variation between different cycles can be ignored.

By differentiating both ends of Eq. (12):

$$dD = \frac{\sigma_{eq}^{2} R_V}{2ES\left(1-D\right)^{\alpha}\left(1-D/D_c\right)} dp \tag{17}$$

For symmetric fatigue cycles, the hysteresis loop is central symmetry:

$$\frac{\delta D}{\delta N} = \oint dD = \int_{A}^{B} dD + \int_{B}^{A} dD = 2\int_{A}^{B} dD \tag{18}$$

By substituting Eqs. (14), (15) and (17) into Eq. (18) and integrating them, the fatigue damage within a cycle can be obtained, that is, the cumulative damage of Ti_2AlNb alloy in each loading cycle is:

$$\frac{\delta D}{\delta N} = \frac{\left(\Delta\sigma_{eq}/2\right)^{2+1/n} R_V}{ES\left(K\right)^{1/n}\left(1-D\right)^{\alpha+1/n}\left(1-D/D_c\right)\left(1+2n\right)} \tag{19}$$

where S is a variable mainly related to $\Delta\sigma_{eq}$:

$$S = Ae^{\left(B\frac{\Delta\sigma_{eq}}{2}\right)} \tag{20}$$

Material parameters involved in the damage model are shown in Table 2 [35].

Table 2: Damage parameters of Ti_2AlNb alloy

A	B	K	n	α	D_c
77.62	0.0023	2104	0.133	4.1	0.06

2.3 *Material Parameters of Ti_2AlNb Alloy*

2.3.1 *Young's Modulus and Poisson's Ratio*

In order to measure the Elastic modulus and Poisson's ratio of Ti_2AlNb alloy, the bar specimens were tested using the dynamic (acoustic resonance) method according to ASTM E1875-20. The data required for the excerpt is shown in Table 3.

Table 3: Elastic modulus, shear modulus and Poisson's ratio of Ti_2AlNb alloy

Temperature, T(°C)	E(GPa)	G(GPa)	ν
24	113.2	43.5	0.301
500	103.7	39.5	0.313
600	99.7	37.9	0.315
700	95.0	36.1	0.316

2.3.2 *High Temperature Fatigue Tests of Standard Open-Hole Specimens*

As the operating temperature range of Ti_2AlNb alloy subcomponents includes 500°C∼700°C, the standard open-hole specimen was selected for the test, as shown in Fig. 1. The machine used in high temperature tensile test is shown in Fig. 2. The results of the static tensile test are shown in Fig. 3, the tensile strength of 550°C and 650°C is 990 and 908 MPa, respectively. The machine used in high temperature fatigue tensile test is shown in Fig. 4. The fatigue test results are shown in Table 4, where R is stress ratio, F is the maximum tensile force, ε is the maximum strain, and N_f is fatigue life. In this paper, the LCF life of subcomponents is mainly studied. Therefore, the failure cycles of Ti_2AlNb alloy standard open-hole specimens are all lower than 10^4.

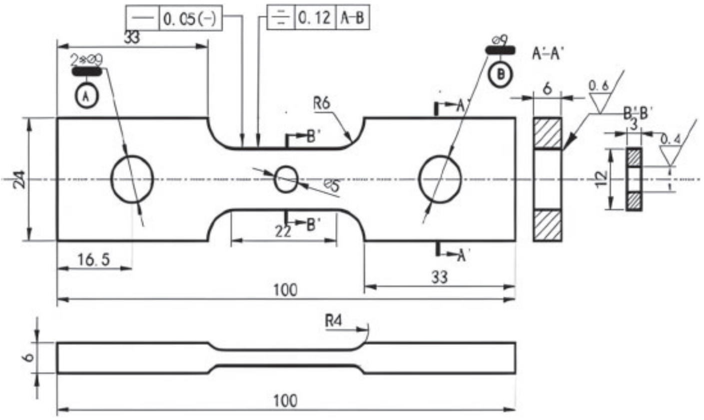

Figure 1: The size of Ti_2AlNb alloy standard open-hole specimen

Figure 2: High temperature tensile testing machine (Tinius Olsen 100ST)

3 Numerical Simulations of Ti_2AlNb Alloy Subcomponents

Numerical methods to simulate the behavior of materials can reduce the design and experimental costs, and the combination of experimental and simulated data is more consistent with the actual situation [36]. Firstly, the finite element model (FEM) of Ti_2AlNb alloy standard open-hole specimens were analyzed for grid convergence. Then, the fatigue life of Ti_2AlNb alloy standard open-hole specimens was predicted. The reliability of the two theoretical methods was analyzed and the fatigue parameters were determined. Finally, the two theoretical methods were used to predict the fatigue life of Ti_2AlNb alloy Y-section subcomponents.

3.1 Mesh Size of Standard Open-Hole Specimens

The FEM model of Ti_2AlNb alloy standard open-hole specimen was established in ABAQUS software. Three-dimensional four-node linear solid elements (C3D4) were used in the model. The element is defined by four nodes with three degrees of freedom for each node: translations in the nodal directions, x, y and z. To accurately obtain the local stress field of the specimen under cyclic loading, high-quality mesh discretization is needed [37].

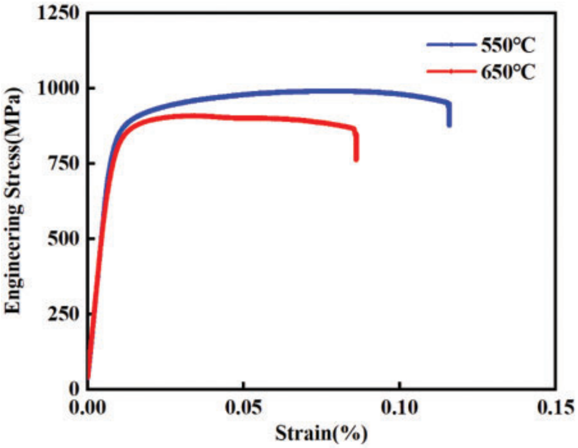

Figure 3: Tensile stress-strain curve

Figure 4: High temperature fatigue tensile testing machine (Instron 8801)

Table 4: Fatigue test data of Ti_2AlNb alloy standard open-hole specimen

T(°C)	R	F(kN)	ε(%)	N_f
550	−1	12.84	1.353	492
		10.52	1.057	1357
		9.25	0.931	2467
		7.16	0.718	5298
		6.73	0.592	7627
650	−1	8.56	0.992	714
		7.75	0.668	1861
		6.41	0.616	3634
		6.05	0.583	6923

The convergence solution independent of the mesh size is obtained in the numerical calculation after the mesh sensitivity analysis, as shown in Fig. 5. When the global mesh size (GS) is 2 mm, and the local mesh size (LS) is 0.2 mm, the numerical calculation accuracy and calculation time are the best for the Seeger fatigue life theory. A total of 31,765 elements are created, as shown in Fig. 6a. When the GS is 2 mm, and the LS is 1 mm, the numerical calculation accuracy and calculation time are the best for the improved Lemaitre damage evolution theory. A total of 15,265 elements are created, as shown in Fig. 6b.

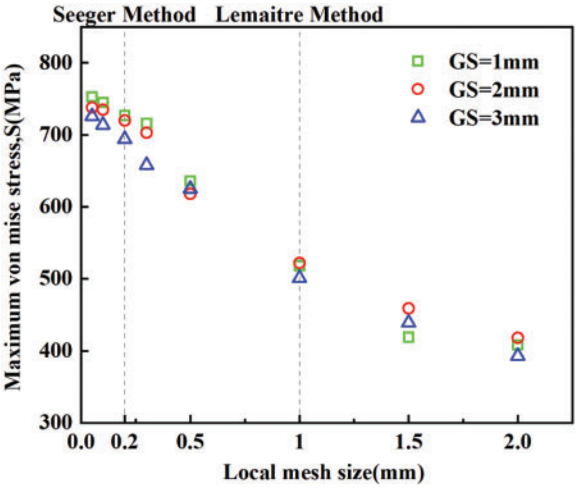

Figure 5: Scatter diagrams of trend of solution convergence of Ti_2AlNb alloy standard open-hole specimens model based on mesh size (Initial conditions: $T = 550°C$, $F = 7.16$ kN)

(a) Seeger fatigue life theory grid

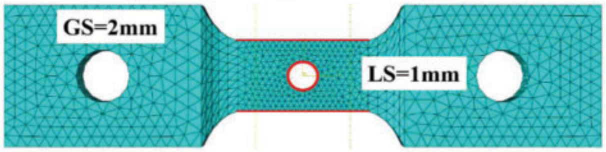

(b) The improved Lemaitre damage evolution theory grid

Figure 6: Grid size of Ti_2AlNb alloy standard open-hole specimen

Seeger method is to directly predict the fatigue life through empirical formulas based on the stress calculation results, so selecting finer grid elements is useful to improve the accuracy. The improved Lemaitre method calculates the cumulative damage according to the average stress of the grid. If the grid elements are selected too fine, the grid stiffness at the stress concentration will degrade rapidly until failure, leading to a large error in the predicted fatigue life. Therefore, selecting an appropriate grid element density can reduce the error.

3.2 Predicting Fatigue Life of Standard Open-Hole Specimen by Seeger Theory

Based on Seeger fatigue life theory, the static tensile results of the Ti_2AlNb alloy standard open-hole specimen of FEM were post-processed in FE-SAFE software. The fatigue cloud diagram of the FEM was generated, and showed the predicted fatigue life of a finite element structure at different positions. According to Fig. 7a, when $F = 12.84$ kN, the fatigue life of the most dangerous point $N_f = 10^{2.782}$, that is, failure after 605 cycles. According to Fig. 7b, when $F = 6.73$ kN, the fatigue life of the most dangerous point $N_f = 10^{3.908}$, that is, failure after 8,090 cycles.

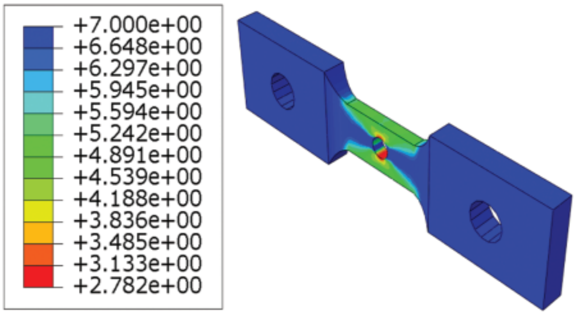

(a) Initial conditions: *T*=550°C, *F*=12.84 kN

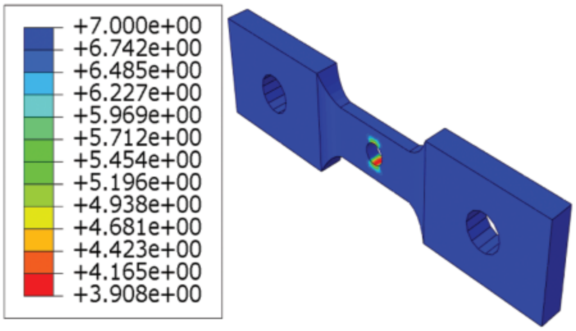

(b) Initial conditions: *T*=550°C, *F*=6.73 kN

Figure 7: Seeger theoretical fatigue life cloud diagram of Ti_2AlNb alloy standard open-hole specimens

Seeger theoretical error w_{Seeger} calculation formula is introduced:

$$w_{Seeger} = \frac{\left|N_{f-Seeger} - N_{f-Test}\right|}{N_{f-Test}} \times 100\% \tag{21}$$

where $N_{f-Seeger}$ is the maximum failure cycle number of Seeger theory, and N_{f-Test} is the maximum failure cycle number of tests. The maximum number of failure cycles is the number of cycles a subcomponent undergoes when it fails ($D = D_c$) under periodic load.

The fatigue life of Ti_2AlNb alloy standard open-hole specimens was calculated at 550°C under five different forces: 12.84, 10.52, 9.25, 7.16 and 6.73 kN. When the temperature is 650°C, the fatigue life was calculated under five forces: 8.56, 7.75, 6.41 and 6.05 kN. Seeger fatigue life prediction value (Seeger) and test fatigue life value (Test) are summarized, as shown in Fig. 8. Eq. (21) is used for error analysis when the initial conditions are identical. The average error of maximum failure cycles at 550°C and 650°C is 12.4% and 15.2%, respectively. The nine-point average error between the Seeger theory and the test value is 13.8%.

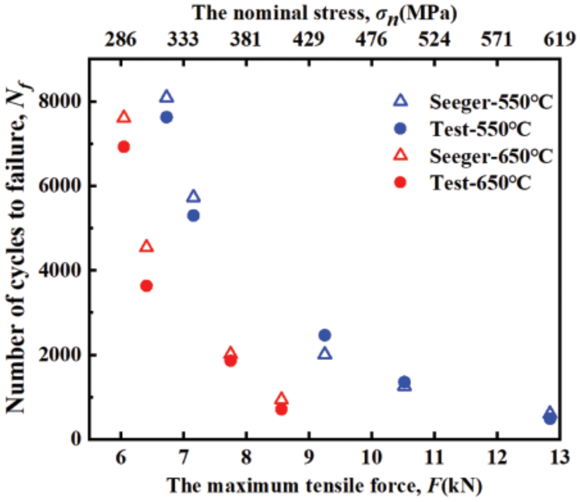

Figure 8: Scatter diagrams of Seeger theoretical fatigue life and test fatigue life of Ti_2AlNb alloy standard open-hole specimens

Although Seeger theory can predict the fatigue life of Ti_2AlNb alloy specimens within the allowable error range, there are still some defects. Seeger theory gives fatigue parameters based on many fatigue tests of Al-Ti alloy. Still, it is not rigorous enough to adopt uniform titanium alloy parameters for Ti_2AlNb alloy. Seeger theory read the equivalent stress of all grids in a static tensile process of the FEM. It calculates the fatigue life by using titanium alloy's approximate fatigue life formula, which could not show the complete stiffness degradation process.

3.3 Predicting Fatigue Life of Standard Open-Hole Specimen by the Improved Lemaitre Theory

The FEM of Ti_2AlNb alloy standard open-hole specimen is subjected to axial loads on both cross-sections. The periodic, constant amplitude load adopts the loading method of the triangular wave, and each analysis step carries out a complete tension and compression process. The specific amplitude is shown in Fig. 9.

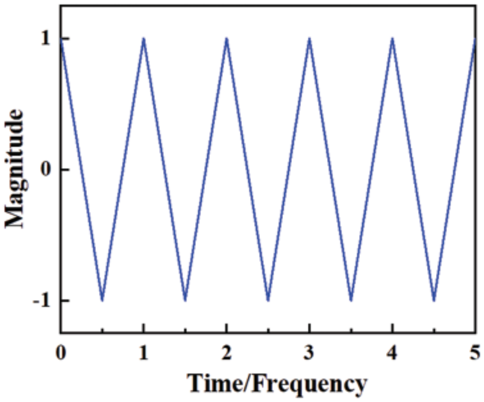

Figure 9: The smooth analysis step periodic triangular wave load

The improved Lemaitre damage evolution theory is coupled to ABAQUS through the UMAT subroutine to simulate the low cycle fatigue damage of Ti_2AlNb alloy standard open-hole specimen. Firstly, the stress-strain field is calculated, and then the damage of elements is calculated according to the global element stress. With the increase in the number of cycles, the damage to elements accumulates continuously. When the damage of elements reaches critical damage ($D_c = 0.06$), the element fails and loses its load-carrying capacity. The specific process is shown in Fig. 10. The maximum number of failure cycles equals the total analysis step time multiplied by the number of loading cycles per analysis step.

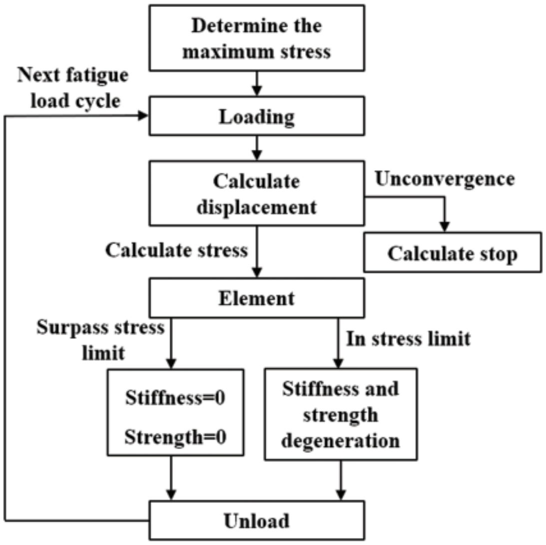

Figure 10: Flow chart of fatigue life calculated by the improved Lemaitre theory

When the initial condition is $T = 550°C$ and $F = 12.84$ kN, Fig. 11 shows the fatigue damage process of Ti_2AlNb alloy standard open-hole specimen under cyclic loading. Figs. 11a–11c show fatigue damage accumulation, and Figs. 11d–11e show the rapid expansion of fatigue damage.

The error of the improved Lemaitre damage evolution theory $w_{Lemaitre}$ is introduced:

$$w_{Lemaitre} = \frac{\left|N_{f-Lemaitre} - N_{f-Test}\right|}{N_{f-Test}} \times 100\% \tag{22}$$

where $N_{f-Lemaitre}$ is the maximum number of failure cycles of the improved Lemaitre damage evolution theory.

The improved Lemaitre prediction value (Lemaitre) and test fatigue life value (Test) are summarized, as shown in Fig. 12. Eq. (22) is used for error analysis when the initial conditions are identical. The average error of maximum failure cycles at 550°C and 650°C is 21.4% and 12.5%, respectively. The stiffness of the grid element degrades rapidly when the cyclic stress is high, resulting in a significant error at 550°C. The nine-point average error between the improved Lemaitre theory and the Test value is 16.9%.

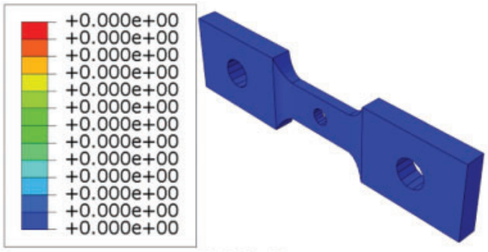

(a) N=0

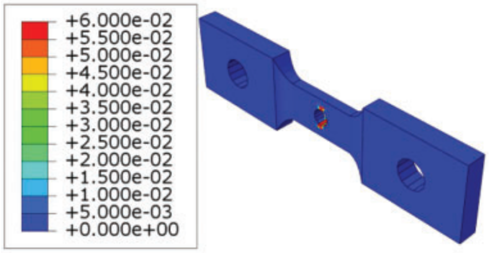

(b) N=200

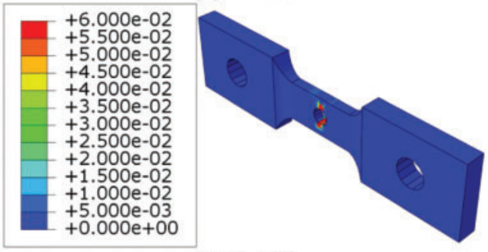

(c) N=400

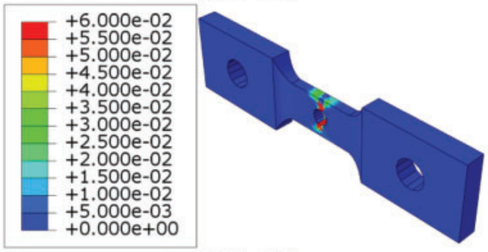

(d) N=415

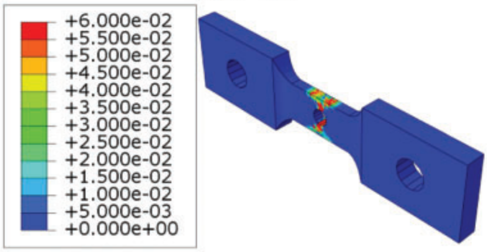

(e) N_f=426

Figure 11: Damage evolution of Ti_2AlNb alloy standard open-hole specimen (Initial conditions: $T =$ 550°C, $F = 12.84$ kN)

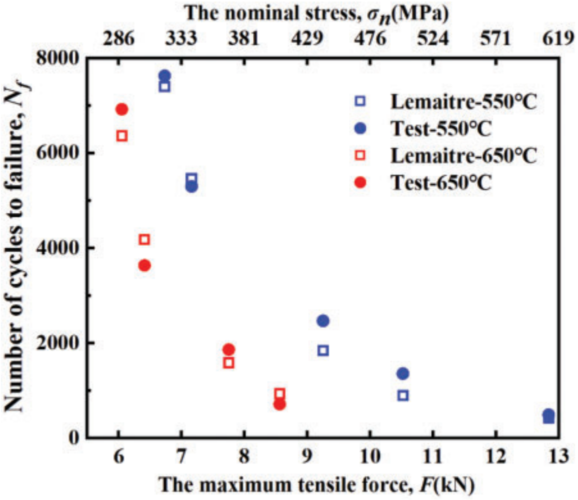

Figure 12: Scatter diagrams of the improved Lemaitre theoretical fatigue life and Test fatigue life of Ti_2AlNb alloy standard open-hole specimens

The difference between Seeger theory method and the improved Lemaitre damage evolution theory in predicting the fatigue life of structural parts can be understood through the simulation in 3.2 and 3.3. The advantage of Seeger method is that it can quickly predict the fatigue life of structural parts through empirical formulas by using the stress calculation results. The disadvantage is that it cannot show the damaging effect of fatigue load on structural parts. The advantage of the improved Lemaitre method is that it can fully show the damage process of fatigue load on structural parts, while the disadvantage is that it needs a long calculation time. The UMAT subroutine must be modified when different metal materials are switched.

3.4 Predicting Fatigue Life of Y-Section Subcomponents

For feature extraction of structural parts of integral investment casting casing of Ti_2AlNb alloy, there are many Y-shaped areas with three interface interactions in the casing section, as shown in Fig. 13. According to this characteristic, the fatigue properties of the simulated subcomponents were tested at the interface angles of 30°, 40° and 60°, respectively. The fatigue properties of the subcomponents with different interface angles were compared and analyzed. Fig. 14 shows the dimensions of the three Y-section subcomponents.

The fatigue life of the Ti_2AlNb alloy Y-section subcomponents with the interface angle of 30° was calculated under five different loads: 22, 20, 18, 16 and 14 kN. The fatigue life of the Y-section subcomponents with the angle of 40° was calculated under five loads: 20, 18, 16, 14 and 12 kN. The fatigue life of the Y-section subcomponents with the angle of 60° was calculated under five loads: 18, 16, 14, 12 and 10 kN. Fatigue life values predicted by Seeger theory (Seeger) and fatigue life values predicted by the improved Lemaitre damage evolution theory (Lemaitre) are summarized, as shown in Fig. 15.

The error between Seeger and the improved Lemaitre method, w_Y, is introduced:

$$w_Y = \frac{\left|N_{f-Seeger} - N_{f-Lemaitre}\right|}{N_{f-Lemaitre}} \times 100\% \tag{23}$$

When the initial conditions are identical, Eq. (23) is used to analyze the predicted life values of the two fatigue theories. At 550°C, the average errors of the maximum failure cycles of Y-section subcomponents are 15.1%, 25.0% and 15.4% when the angle of the interface area is 30°, 40° and 60°, respectively. At 650°C, the average errors are 19.8%, 26.8% and 21.6% when the angle is 30°, 40° and 60°, respectively.

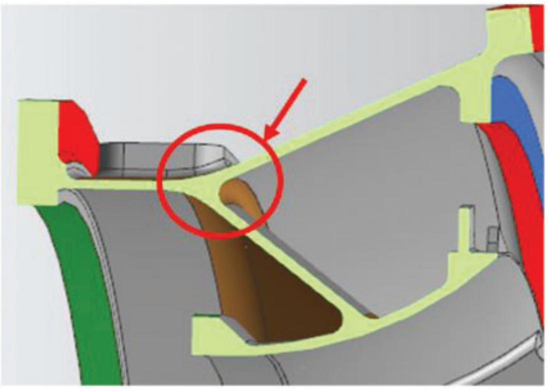

Figure 13: Y-shaped area of aviation components

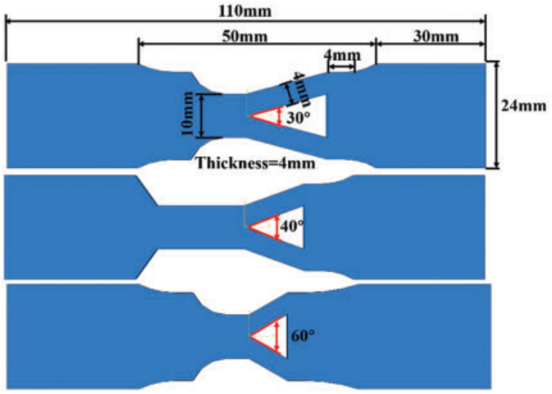

Figure 14: Dimension drawings of three Y-section subcomponents

Fig. 15 shows that when the maximum failure cycles are identical, the periodic loads carried by Ti_2AlNb alloy Y-section subcomponents at 650°C are all smaller than those carried at 550°C. Temperature is negatively correlated with the fatigue life of the subcomponents. When the temperature is constant, decreasing the load amplitude will increase the number of failure cycles of Ti_2AlNb alloy Y-section subcomponents. The load amplitude is negatively correlated with the fatigue life of the subcomponents.

The effect of interface angle on the fatigue life of Ti_2AlNb alloy Y-section subcomponents is studied by two theoretical methods. When the initial conditions are $T = 550°C$ and $F = 14$ kN, Seeger theoretical fatigue life cloud diagrams of the three subcomponents are observed, as shown in Fig. 16. When the interface angle is 30°, 40° and 60°, the maximum failure cycles are 3047, 1896 and 706, respectively. The larger the interface angle, the smaller the fatigue life. When the initial conditions are $T = 550°C$ and $F = 14$ kN, the stiffness degeneration process of Ti_2AlNb alloy Y-section subcomponents at different interface angles is shown in Figs. 17–19, respectively. By observing the failure position of the structures, it is found that the increase of the angle of the interface area will amplify the stress concentration effect, thus reducing the fatigue life, which is consistent with the Seeger theory results.

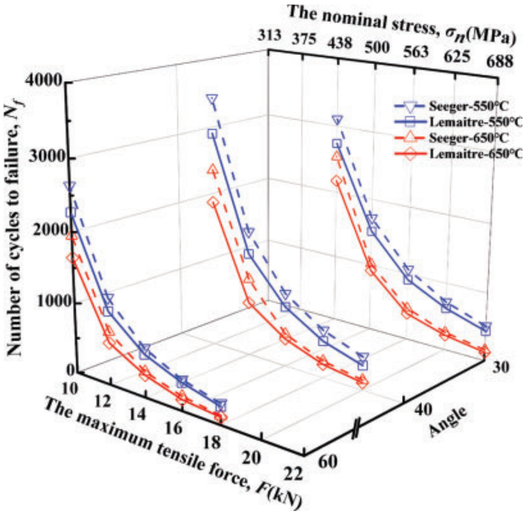

Figure 15: The maximum failure cycles of Ti_2AlNb alloy Y-section subcomponents at different interface angles, loads and temperatures

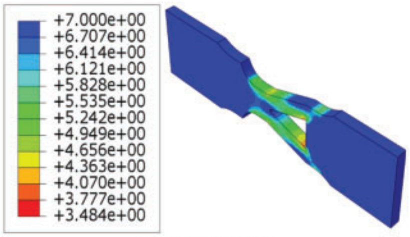

(a) Angle=30°

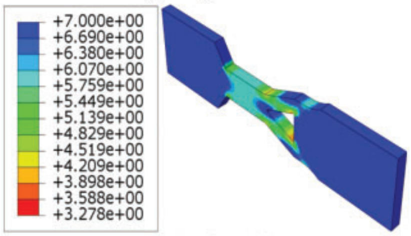

(b) Angle=40°

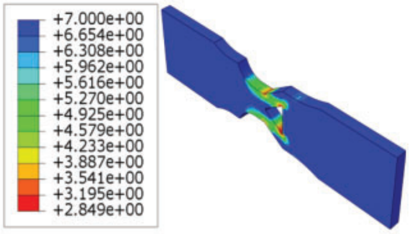

(c) Angle=60°

Figure 16: Seeger theoretical fatigue life cloud diagram of Ti_2AlNb alloy Y-section subcomponents (Initial conditions: $T = 550°C$, $F = 14$ kN)

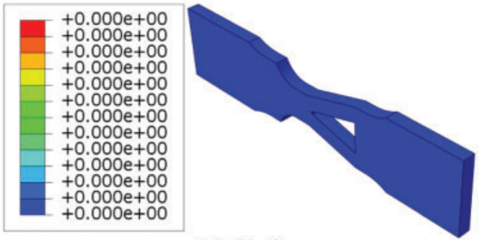

(a) N=0

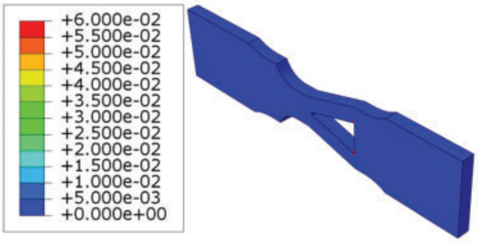

(b) N=1000

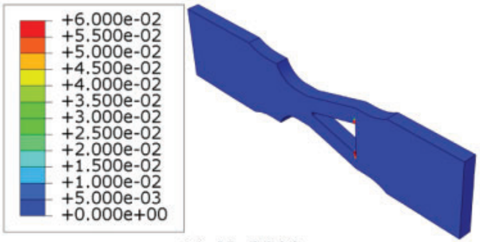

(c) N=2000

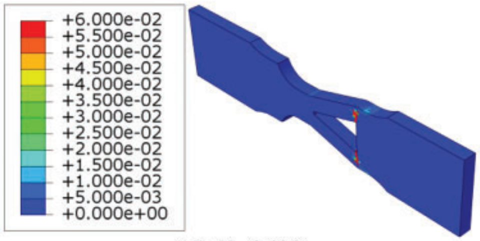

(d) N=2600

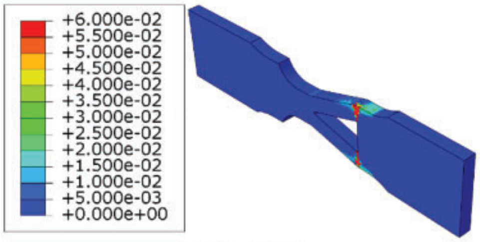

(e) N_f=2740

Figure 17: Damage evolution of Ti_2AlNb alloy 30° Y-section subcomponents (Initial conditions: $T =$ 550°C, $F = 14$ kN)

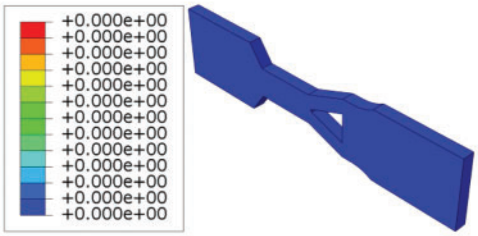

(a) N=0

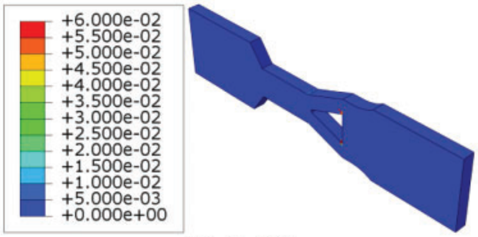

(b) N=500

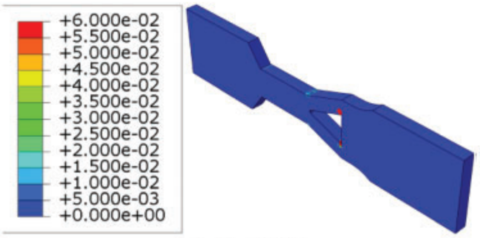

(c) N=1000

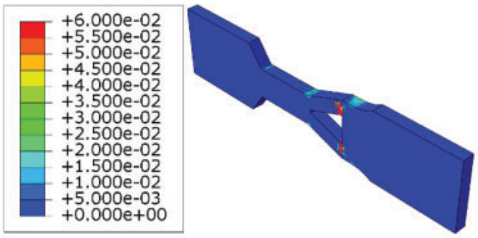

(d) N=1400

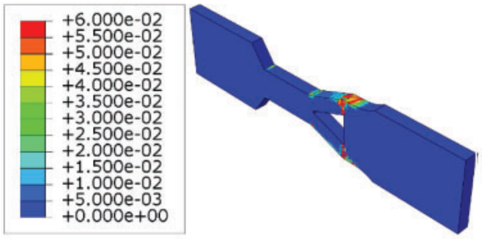

(e) N_f=1492

Figure 18: Damage evolution of Ti_2AlNb alloy 40° Y-section subcomponents (Initial conditions: T = 550°C, F = 14 kN)

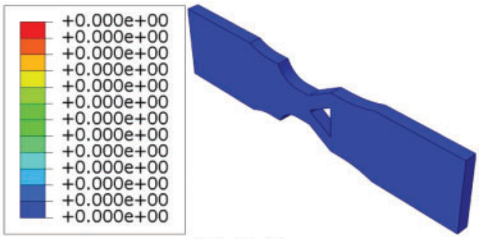

(a) N=0

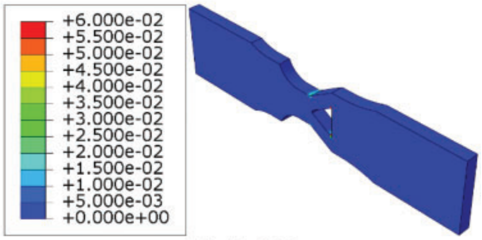

(b) N=200

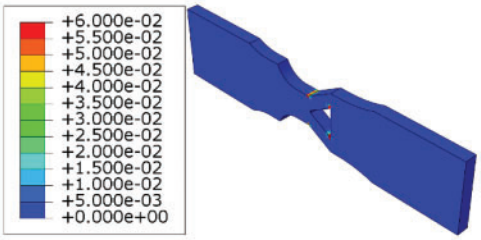

(c) N=400

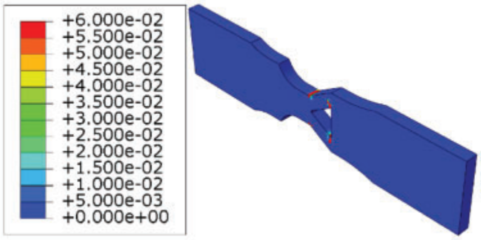

(d) N=580

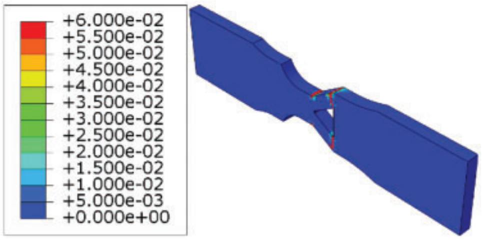

(e) N_f=602

Figure 19: Damage evolution of Ti_2AlNb alloy 60° Y-section subcomponents (Initial conditions: $T = 550°C$, $F = 14$ kN)

When the improved Lemaitre damage evolution theory is used to predict the fatigue life of subcomponents, the maximum number of failure cycles is far less than expected, but the failure cycle cannot converge. At this point, stiffness degradation has just begun, so the number of cycles applied at each analysis step needs to be adjusted. In addition, the unscientific division of the FEM grid will also lead to the appearance of some defective data.

4 Conclusion

In this paper, the low cycle fatigue behaviour of Ti_2AlNb alloy Y-section subcomponents has been studied experimentally and numerically. The finite element simulation parameters of Ti_2AlNb alloy standard open-hole specimen were determined based on the fatigue test data. The fatigue life of Ti_2AlNb alloy Y-section subcomponents was predicted, which solved the problem that it was difficult to conduct conventional fatigue tests for complex Ti_2AlNb alloy subcomponents. Some critical conclusions are summarized as follows:

(1) The convergence of the finite element model mesh of Ti_2AlNb alloy standard open-hole specimen was analyzed using fatigue test data at 550°C and 650°C. The optimal global mesh size of the Seeger theory and the improved Lemaitre theory is 2 mm, and the optimal local mesh size is 0.2 and 1 mm, respectively.

(2) The fatigue life of the Ti_2AlNb alloy standard open-hole specimen was predicted. The average error of maximum failure cycles of Ti_2AlNb alloy standard open-hole specimen at 550°C and 650°C between Seeger theory and test is 12.4% and 15.2%, respectively. The nine-point average error between the Seeger theory and the test value is 13.8%. The average error of maximum failure cycles of Ti_2AlNb alloy standard open-hole specimen at 550°C and 650°C between improved Lemaitre damage evolution theory and test is 21.4% and 12.5%, respectively. The stiffness of the grid element degrades rapidly when the cyclic stress is high, resulting in a significant error at 550°C. The nine-point average error between the improved Lemaitre theory and the test value is 16.9%. The average errors of fatigue life predicted by the Seeger theory and the improved Lemaitre theory are 13.8% and 16.9%, respectively.

(3) The load amplitude, temperature, and Y-interface angle are negatively correlated with the fatigue life of the Ti_2AlNb alloy Y-section subcomponents. The average error of fatigue life of Ti_2AlNb alloy Y-section subcomponents predicted by two theoretical methods is 20.6%. By observing the failure position of the structures, it is found that the increase of the angle of the interface area will amplify the stress concentration effect, thus reducing the fatigue life, which is consistent with the Seeger theory results.

Funding Statement: The authors are grateful for the financial support provided by the National Science and Technology Major Project (No. J2019-VI-0003-0116) and the Six Talent Peaks Project in Jiangsu Province (Grant No. 2019-KTHY-059).

Conflicts of Interest: The authors declare that they have no conflicts of interest to report regarding the present study.

References

1. Kumpfert, J. (2001). Intermetallic alloys based on orthorhombic titanium aluminide. *Advanced Engineering Materials, 3(11),* 851–864. https://doi.org/10.1002/1527-2648(200111)3:11<851::Aid-adem851>3.0.Co;2-g
2. Boehlert, C. J. (2001). Part III. The tensile behavior of Ti-Al-Nb O+Bcc orthorhombic alloys. *Metallurgical and Materials Transactions A, 32(8),* 1977–1988. https://doi.org/10.1007/s11661-001-0010-4

3. Zhou, Y., Wang, D., Song, L., Mukhtar, A., Huang, D. et al. (2021). Effect of heat treatments on the microstructure and mechanical properties of Ti_2AlNb intermetallic fabricated by selective laser melting. *Materials Science and Engineering A, 817*. https://doi.org/10.1016/j.msea.2021.141352
4. Li, Z., Cui, Y., Yu, Z., Liu, C. (2021). In-situ fabrication of Ti_2AlNb-based alloy through double-wire arc additive manufacturing. *Journal of Alloys and Compounds, 876*. https://doi.org/10.1016/j.jallcom.2021.160021
5. Zhang, H., Li, C., Ma, Z., Yu, L., Liu, Y. (2019). Effect of dual aging treatments on phase transformation and microstructure in a pre-deformed Ti_2AlNb-based alloy containing $O + \beta/B2$ structures. *Vacuum, 164,* 175–180. https://doi.org/10.1016/j.vacuum.2019.03.022
6. Huang, Y., Liu, Y., Zhang, Y., Liang, H. (2020). Thermal stability and mechanical properties of Ti-22Al-25Nb alloy with different initial microstructures. *Journal of Alloys and Compounds, 842*. https://doi.org/10.1016/j.jallcom.2020.155794
7. Zheng, Y., Zeng, W., Zhang, P., Ma, H., Li, D. et al. (2020). Anti-correlation between solution strengthening and precipitation strengthening in lamellar O microstructures of a Ti_2AlNb based alloy. *Journal of Alloys and Compounds, 847*. https://doi.org/10.1016/j.jallcom.2020.156470
8. Zhang, H., Zhang, Y., Liang, H., Yu, L., Liu, Y. (2020). Effect of the primary O phase on thermal deformation behavior of a Ti_2AlNb-based alloy. *Journal of Alloys and Compounds, 846*. https://doi.org/10.1016/j.jallcom.2020.156458
9. Dang, W., Li, J., Zhang, T., Kou, H. (2015). Oxidation behavior of Zr-containing Ti_2AlNb-based alloy at 800°C. *Transactions of Nonferrous Metals Society of China, 25(3),* 783–790. https://doi.org/10.1016/s1003-6326(15)63664-0
10. Germann, L., Banerjee, D., Guedou, J. Y., Strudel, J. L. (2005). Effect of composition on the mechanical properties of newly developed Ti_2AlNb-based titanium aluminide. *Intermetallics, 13(9),* 920–924. https://doi.org/10.1016/j.intermet.2004.12.003
11. Du, Z., Ma, S., Han, G., Wei, X., Han, J. et al. (2021). The parameter optimization and mechanical property of the honeycomb structure for Ti_2AlNb based alloy. *Journal of Manufacturing Processes, 65,* 206–213. https://doi.org/10.1016/j.jmapro.2021.03.031
12. Zhang, Y., Cai, Q., Ma, Z., Li, C., Yu, L. et al. (2019). Solution treatment for enhanced hardness in Mo-modified Ti_2AlNb-based alloys. *Journal of Alloys and Compounds, 805,* 1184–1190. https://doi.org/10.1016/j.jallcom.2019.07.149
13. Tang, F., Nakazawa, S., Hagiwara, M. (2002). The effect of quaternary additions on the microstructures and mechanical properties of orthorhombic Ti_2AlNb-based alloys. *Materials Science and Engineering A, 329,* 492–498. https://doi.org/10.1016/s0921-5093(01)01626-4
14. Zhang, H., Zhang, Y., Liang, H., Liu, Y. (2021). Influence of cooling rates on microstructure and tensile properties of a heat treated Ti_2AlNb-based alloy. *Materials Science and Engineering A, 817*. https://doi.org/10.1016/j.msea.2021.141345
15. Bu, Z., Zhang, Y., Yang, L., Kang, J., Li, J. (2022). Effect of cooling rate on phase transformation in Ti_2AlNb alloy. *Journal of Alloys and Compounds, 893*. https://doi.org/10.1016/j.jallcom.2021.162364
16. Chen, Y., Wang, J., Gao, Y., Feng, A. (2019). Effect of shot peening on fatigue performance of Ti_2AlNb intermetallic alloy. *International Journal of Fatigue, 127,* 53–57. https://doi.org/10.1016/j.ijfatigue.2019.05.034
17. Fu, Y., Lv, M., Zhao, Q., Zhang, H., Cui, Z. (2021). Investigation on the size and distribution effects of O phase on fracture properties of Ti_2AlNb superalloy by using image-based crystal plasticity modeling. *Materials Science and Engineering A, 805*. https://doi.org/10.1016/j.msea.2021.140787
18. Chen, Y., Gao, Y. (2019). Simulation of the residual stress and fatigue prediction of Ti_2AlNb intermetallic compound under shot peening. *Surface Technology, 48,* 167–172+188. https://doi.org/10.16490/j.cnki.issn.1001-3660.2019.06.019
19. Basquin, O. (1910). The exponential law of endurance tests. *Proceedings-American Society for Testing and Materials,* vol. 10, pp. 625–630.

20. Morrow, J. (1965). Cyclic plastic strain energy and fatigue of metals. *ASTM, 45–87.* https://doi.org/10.1520/STP378-EB
21. Coffin, L. (1954). A study of the effects of cyclic thermal stresses on a ductile metal. *Transactions of the American Society of Mechanical Engineers, 76(6),* 931–949. https://doi.org/10.1115/1.4015020
22. Morrow, J., Raske, D. (1969). *Mechanics of materials in low cycle fatigue testing*. Dordrecht, Netherlands: Kluwer Academic Publishers-Plenum Publishers.
23. Zhang, Y., Chen, Z., Qu, S., Feng, A., Mi, G. et al. (2020). Microstructure and cyclic deformation behavior of a 3D-printed Ti-6Al-4 V alloy. *Journal of Alloys and Compounds, 825*. https://doi.org/10.1016/j.jallcom.2020.153971
24. Smith, K., Watson, P., Topper, T. (1970). A stress-strain functions for the fatigue of metals (stress-strain function for metal fatigue including mean stress effect). *Journal of Materials Science & Technology, 5,* 767–778.
25. Lorenzo, F., Laird, C. (1984). A new approach to predicting fatigue life behavior under action of mean stresses. *Materials Science and Engineering A, 62,* 205–210. https://doi.org/10.1016/0025-5416(84)90223-4
26. Ince, A., Glinka, G. (2014). A generalized fatigue damage parameter for multiaxial fatigue life prediction under proportional and non-proportional loadings. *International Journal of Fatigue, 62,* 34–41. https://doi.org/10.1016/j.ijfatigue.2013.10.007
27. Bäumel, A., Seeger, T., Boller, C. (1987). *Materials data for cyclic loading*. Amsterdam, Netherlands: Elsevier Science Publishers.
28. Lemaitre, J. (1996). *A course on damage mechanics*. Berlin, Germany: Springer-Verlag.
29. Ellyson, B., Chekir, N., Brochu, M. (2017). Characterization of bending vibration fatigue of WBD fabricated Ti-6A1-4 V. *International Journal of Fatigue, 101,* 36–44. https://doi.org/10.1016/j.ijfatigue.2017.03.045
30. Long, X., Guo, Y., Su, Y., Siow, K. S., Chen, C. (2022). Constitutive, creep, and fatigue behavior of sintered Ag for finite element simulation of mechanical reliability: A critical review. *Journal of Materials Science: Materials in Electronics, 33(5),* 2293–2309. https://doi.org/10.1007/s10854-021-07474-1
31. Yang, B., Luo, J., Wan, B., Su, Y., Fu, G. et al. (2022). Numerical and experimental investigations of the thermal fatigue lifetime of CBGA packages. *Computer Modeling in Engineering & Sciences, 130(2),* 1113–1134. https://doi.org/10.32604/cmes.2022.018037
32. Zhou, S., Liu, J., Huang, B. (2008). Continuum damage mechanics study on low-cycle fatigue damage of Ti alloy TC4. *Journal of Mechanical Strength, 30,* 798–803. https://doi.org/10.16579/j.issn.1001.9669.2008.05.009
33. Song, S., Han, Y., Xu, L. (2019). The research of low cycle fatigue damage of Ti-6Al-4 V titanium alloy based on combined hardening model. *Transactions of the China Welding Institution, 40,* 43–48. https://doi.org/10.12073/j.hjxb.2019400009
34. Yang, S., Yang, L., Wang, Y. (2020). Determining the fatigue parameters in total strain life equation of a material based on monotonic tensile mechanical properties. *Engineering Fracture Mechanics, 226*. https://doi.org/10.1016/j.engfracmech.2019.106866
35. Jing, H., Pan, S., Xu, L., Zhao, L., Han, Y. (2021). Bending fatigue behavior and damage mechanism of the Ti-6Al-4 V titanium alloy. *Journal of Tianjin University: Natural Science & Engineering Technology, 54,* 942–949. https://doi.org/10.11784/tdxbz202006023
36. Poursan Dalir, M., Hedayati, E., Hedayati, A. (2021). Detection and identification of subcutaneous defects using ultrasonic waves in reflective test. *Journal of Mechanical Engineering and Sciences, 15(2),* 8003–8015. https://doi.org/10.15282/jmes.15.2.2021.06.0631
37. Hedayati, E., Vahedi, M. (2017). Numerical investigation of penetration in Ceramic/Aluminum targets using smoothed particle hydrodynamics method and presenting a modified analytical model. *Computer Modeling in Engineering & Sciences, 113(3),* 295–323. https://doi.org/10.3970/cmes.2017.113.307

Tech Science Press
2520 St. Rose Parkway,
Suite 108D, Henderson, Nevada,
USA

www.techscience.com

CMES Editorial Office
E-mail: cmes@techscience.com
www.techscience.com/journal/CMES

Tech Science Press

Tech Science Press